

# Electronic structure and dynamics of photoactive yellow protein chromophores

Alice Henley

A thesis submitted for the degree of  
Doctor of Philosophy

University College London (UCL)  
August 2020

I, Alice Henley, confirm that the work presented in this thesis is my own. Where information has been derived from other sources, I confirm that this has been indicated in the thesis.

# Abstract

Photoactive yellow protein (PYP) is responsible for the negative phototactic response of *Halorhodospira halophila* to blue light. At the heart of PYP lies the anionic *para*-coumaric acid chromophore that initiates the response by photoisomerisation. The work presented in this thesis aimed to improve our understanding of the electronic structure and dynamics of the chromophore using photoelectron spectroscopy techniques and quantum chemistry calculations.

Model chromophore analogues with molecular tethers hindering rotation about single or double bonds within the chromophore were studied in the gas phase with anion photoelectron spectroscopy. These studies aimed to investigate the role of torsional motion in controlling the competition between electronic relaxation processes, following photoexcitation in the range 400–310 nm. Evidence was found to suggest that single bond rotation about either site adjacent to the central C=C bond enabled efficient conversion from the first excited state to the ground state and locking the central C=C bond effectively turned off this conversion to the ground state.

Later in this thesis, a protocol for simulating photodetachment from an anionic chromophore in solution is illustrated with phenolate – a molecular building block common to many biological molecules including the photoactive yellow protein chromophore. This computational approach is then applied to simulate electron detachment from a photoactive yellow protein chromophore in aqueous solution. These computational results are presented with, and provide molecular-level insight into, a liquid micro-jet x-ray photoelectron spectrum (recorded by collaborators). The energy required for the lowest energy electron detachment process is found to blue-shift dramatically upon solvation compared to the gas phase.

## Impact Statement

Photoactive proteins receive a great deal of interest due to their efficient and selective functions and have applications in bioimaging of cells, photovoltaic materials and molecular photoswitches. The work in this thesis contributes to an international effort to improve our understanding of how such photoactive proteins function at a molecular level. Specifically, this thesis focusses on photoactive yellow protein by employing photoelectron spectroscopy techniques to investigate the electronic structure and dynamics of the isolated chromophore. The insights presented are of interest to those studying the protein in its native environment, but also have the potential to guide future rational design of bio-inspired molecular devices. The analyses presented in this thesis also contribute to more fundamental research in the area of spectroscopy and dynamics of isolated anionic molecules in the gas phase and will complement future work on similar exotic species and benchmarking of theoretical approaches.

The work described later in the thesis illustrates how gas-phase photoelectron spectra may be compared to similar measurements made in solution to unravel the role that an aqueous environment has on the electronic structure of a photoactive protein chromophore. Also presented is a method to simulate large-scale solute-solvent systems at ambient temperature effectively and efficiently. This work is of immense current interest to researchers as photoelectron spectroscopy measurements recorded in solution are receiving increasing interest. Additionally, these developments could potentially have a broader reach within the scientific community as a similar approach may be used to calculate other photochemical or electrochemical properties of aqueous solutes. There is also potential to expand on the techniques used to describe dynamic processes in solution such as the evolution of an excited state population or how bonds break and form in chemical reactions.



**The work presented in this thesis is based upon the following publications:**

Chapter 1

Alice Henley and Helen H. Fielding, “Anion photoelectron spectroscopy of protein chromophores”, *Int. Rev. Phys. Chem.*, 2019, **38**, 1, 1-34.

Chapter 4

Alice Henley, Matus E. Diveky, Anand M. Patel, Michael A. Parkes, James C. Anderson and Helen H. Fielding, “Electronic structure and dynamics of torsion-locked photoactive yellow protein chromophores”, *Phys. Chem. Chem. Phys.*, 2017, **19**, 31572-31580.

Chapter 5

Alice Henley, Anand M. Patel, Michael A. Parkes, James C. Anderson and Helen H. Fielding, “Role of photoisomerisation on the photodetachment of the photoactive yellow protein chromophore”, *J. Phys. Chem. A*, 2018, **122**, 8222-8228.

Chapter 7

Alice Henley, Claudia Kolbeck, Sebastian Malerz, Anastasia V. Bochenkova, Bernd Winter and Helen H. Fielding, “Investigating the effect of solvation on the electron detachment from the photoactive yellow protein chromophore”, *in preparation*.

**Contributions were also made to the following publications:**

1. Michael A. Parkes, Jonathan Crellin, Alice Henley and Helen H. Fielding, "A photoelectron imaging and quantum chemistry study of the deprotonated indole anion", *Phys. Chem. Chem. Phys.*, 2018, **20**, 15543-15549.
2. Joanne L. Woodhouse, Alice Henley, Michael A. Parkes and Helen H. Fielding, "A photoelectron imaging and quantum chemistry study of phenolate, difluorophenolate and dimethoxyphenolate anions", *J. Phys. Chem. A*, 2019, **123**, 2709-2718.
3. Alice Henley, Jamie W. Riley, Binxing Wang and Helen H. Fielding, "An experimental and computational study of the effect of aqueous solution on the multiphoton ionisation photoelectron spectrum of phenol", *Faraday Discuss.*, 2020, **221**, 202-218.
4. Anand M. Patel, Alice Henley, Michael A. Parkes, Mariana Assmann, Graham A. Worth, James C. Anderson and Helen H. Fielding, "Shining light on the electronic structure and relaxation dynamics of the isolated oxyluciferin anion", *Phys. Chem. Chem. Phys.*, 2020, **22**, 19022-19032.
5. River Riley, Alice Henley, Anton N. Boichenko, Nadezhda N. Kleshchina, Bingxing Wang, Danielle Winning, Omri Tau, Ross Lewin, John M. Ward, Helen C. Hailes, Anastasia V. Bochenkova and Helen H. Fielding, "Liquid-microjet photoelectron spectroscopy of the green fluorescent protein chromophore", *submitted*.
6. Joanne L. Woodhouse, Alice Henley, Michael A. Parkes, Ross Lewin, John M. Ward, Helen C. Hailes, Anastasia V. Bochenkova and Helen H. Fielding, "Photoelectron angular distributions of the deprotonated GFP chromophore anion and RNA fluorescent tags", *in preparation*.
7. Joanne L. Woodhouse, Alice Henley, Ross Lewin, John M. Ward, Helen C. Hailes, Anastasia V. Bochenkova and Helen H. Fielding, "Enhanced internal conversion in a locked green fluorescent protein chromophore", *in preparation*.
8. William G. Fortune, Omri Tau, Alice Henley and Helen H. Fielding, "Liquid-microjet photoelectron spectroscopy of the phenolate anion", *in preparation*.

# Acknowledgements

First and foremost, I thank my supervisor Prof Helen Fielding for consistently providing me with guidance, helpful suggestions, timely feedback and more over the last four years. Thank you for allowing me to not take myself too seriously and for your endless reminders that yellow is never a valid choice. For the many opportunities you have offered or helped me to gain, I am very grateful for your immeasurable efforts and support. I would also like to thank you for reading through chapters of this thesis and always providing helpful suggestions for improvements.

I have had the great pleasure of working (and not working!) with so many fantastic scientists during my PhD. I thank Dr Mike Parkes for showing me the ropes in the lab and being an ever-dependable wealth of knowledge - I will perpetually owe you a pint. Dr River Riley and Dr Joanne Woodhouse both helped me tremendously with lab work and I have had so much fun working with you both; having such great friends really helped me build confidence living in London and in my work, too. I thank the students I have supported for enabling me to procrastinate from my own work and help them engage in their projects. I thank (but also apologise to) Joseph Broughton for listening to my rants in recent years and I thank Dr Lily Ellis-Gibbings for her friendship and for sending me motivation (literally) to get on with my thesis.

I extend my gratitude to all occupants of 123 over the years as well as colleagues and collaborators I have worked with at UCL and beyond: Anand Patel and Prof James Anderson for synthesising the locked chromophores; Dr Bernd Winter and his group for providing a liquid-microjet x-ray photoelectron spectrum; and Prof Graham Worth, Dr Jörg Sassmannshausen, Dr Mariana Assmann and Dr Frank Otto for discussions, computational support and plenty of patience. I also thank Prof Anastasia Bochenkova for introducing me to new theoretical techniques and her group for welcoming me so well on my visit to Moscow. A special thank you to Dr June McCombie for highlighting the PhD position to me originally and generally being so kind and supportive throughout my time in academia.

Finally, I thank Saddam (Dad and Sam) for supporting me throughout my studies, particularly over the last year ... and Jack, of course.

# Contents

<b>Outline of the thesis</b>	<b>19</b>
<b>1 Introduction</b>	<b>21</b>
1.1 Anion photoelectron spectroscopy	24
1.2 Photoactive yellow protein	30
1.2.1 Background	30
1.2.2 Deprotomers of the chromophore	32
1.2.3 Dynamics of the first electronically excited state	35
1.2.4 Higher lying electronically excited states	38
1.2.5 Tuning the electronic structure and dynamics	40
1.2.6 Effect of solvation	42
1.3 Summary	47
<b>2 Experimental methods</b>	<b>49</b>
2.1 Electrospray anion source	50
2.2 Mass-selection and ion accumulation	52
2.3 Velocity map imaging spectrometer	57
2.4 Image reconstruction	61
2.5 Light sources	64
2.6 Overall operation	65
2.7 Calibration of the spectrometer	68
2.8 Summary	72
<b>3 Computational methods</b>	<b>73</b>
3.1 Introduction	73
3.2 Detachment energies	80

3.2.1	Energy difference	80
3.2.2	Electron propagator theory	81
3.2.3	Equations-of-motion coupled-cluster methods	82
3.3	Vertical excitation energies	84
3.3.1	Time-dependent density functional theory	84
3.3.2	Equations-of-motion coupled-cluster methods	86
3.3.3	Algebraic diagrammatic construction methods	87
3.4	Inclusion of an environment	88
3.4.1	Microsolvation	88
3.4.2	Implicit solvent models	89
3.4.3	Quantum mechanics/molecular mechanics	90
3.4.4	Effective fragment potential methods	92
3.5	Summary	95
<b>4</b>	<b>Electronic structure and dynamics of torsion-locked photoactive yellow protein chromophores</b>	<b>96</b>
4.1	Introduction	96
4.2	Methods	99
4.2.1	Chromophores	99
4.2.2	Photoelectron spectroscopy	99
4.2.3	Calculations	100
4.3	Results and discussion	101
4.3.1	Photoelectron spectra	101
4.3.2	Computational results	106
4.3.3	Interpreting the spectra	115
4.3.4	The role of torsional motion	117
4.4	Outlook and conclusion	120
<b>5</b>	<b>The role of photoisomerisation on the photodetachment of the photoactive yellow protein chromophore</b>	<b>122</b>
5.1	Introduction	122
5.2	Methods	124

5.2.1	Chromophores	124
5.2.2	Photoelectron spectroscopy	124
5.2.3	Calculations	125
5.3	Results and discussion	126
5.3.1	Photoelectron spectra	126
5.3.2	Computational results	129
5.3.3	The importance of double bond rotation	133
5.4	Conclusions and outlook	138
<b>6</b>	<b>A procedure for calculating the electronic structure of an anionic solute in aqueous solution</b>	<b>140</b>
6.1	Introduction	140
6.2	Methods	143
6.3	Results and discussion	146
6.4	Conclusions and outlook	164
<b>7</b>	<b>Investigating the effect of solvation on the electron detachment from the photoactive yellow protein chromophore</b>	<b>166</b>
7.1	Introduction	167
7.2	Methods	170
7.2.1	Experimental details	170
7.2.2	Computational details	171
7.3	Results and discussion	174
7.3.1	Experimental results	174
7.3.2	Computational results	178
7.3.3	Role of an aqueous environment	191
7.4	Conclusions and outlook	197
<b>8</b>	<b>Summary and Outlook</b>	<b>199</b>
8.1	Anion photoelectron spectroscopy of photoactive yellow protein chromophore analogues	200
8.2	Photodetachment from chromophores in aqueous solutions	202

<b>Appendices</b>	<b>204</b>
A	Supporting material for Chapter 2
B	Supporting material for Chapter 4
C	Supporting material for Chapter 5
D	Supporting material for Chapter 6
E	Supporting material for Chapter 7
<b>Bibliography</b>	<b>223</b>

## List of Figures

1.1	General Jablonski diagram illustrating various electronic relaxation processes	22
1.2	PYP structure highlighting the chromophore within	23
1.3	Schematic showing the transitions associated with the ADE and VDEs	25
1.4	Jablonski diagram illustrating possible photodetachment pathways	26
1.5	Characteristic features present in anion photoelectron spectra recorded with different photon energies	28
1.6	Resonance characters with respect to the detachment continuum	29
1.7	Structure of $pCA^-$	31
1.8	Photocycle of PYP	31
1.9	Electronic absorption spectra of model PYP chromophore analogues $pCA^-$ and $pCTP^-$	33
1.10	Isomers of $pCA^-$	33
1.11	Structure of $pCK^-$	35
1.12	Pump-probe photoelectron spectra of $pCK^-$	36
1.13	Schematic potential energy surface illustrating photoisomerisation of $pCK^-$	37
1.14	Action-absorption spectrum of gas-phase $pCE^-$	38

1.15	Orbitals associated with VEEs calculated for $p\text{CA}^-$	39
1.16	Modified PYP chromophore structures	40
1.17	Photoelectron spectra of $p\text{CE}^-$ and $p\text{CT}^-$	42
1.18	Absorption spectra of aqueous anionic $p\text{CA}$ at various pH	43
1.19	Absorption spectra of methylated chromophore analogues in methanol	44
2.1	Schematic diagram of the anion photoelectron spectrometer	50
2.2	Schematic illustration of an electrospray ionisation anion source	51
2.3	Schematic illustrating the operation of a QMF	52
2.4	$a$ - $q$ stability diagram and bandpass region for a QMF	54
2.5	$U$ - $V$ stability diagram and mass-filtering resolution	55
2.6	Schematic diagram of the linear hexapole ion trap	56
2.7	Typical potentials within the linear hexapole ion trap	57
2.8	Schematic of the colinear VMI photoelectron spectrometer	58
2.9	Simulated trajectories within a VMI spectrometer illustrating velocity mapping	59
2.10	Simulated ion trajectories within the potential switch and VMI optics	60
2.11	Schematic illustrating a forward Abel transform of a photoelectron Newton sphere	62
2.12	Beam line setup used for nanosecond laser pulses	64
2.13	Beam line setup used for femtosecond laser pulses	65
2.14	Schematic showing typical experimental timings used	67
2.15	Pixel to eV calibration using the photoelectron spectrum of iodide	70
2.16	Pixel to eV calibration using the photoelectron spectrum of indole	71
2.17	Pixel to eV calibration using the photoelectron spectrum of $p\text{HBDI}^-$	71
3.1	CCSD excitations included within EOM-IP-CCSD	84
3.2	CCSD excitations included within EOM-EE-CCSD	87
3.3	Example microsolvated phenol structure	88
3.4	Example QM/MM simulation geometry	90
4.1	Torsional motions within the PYP chromophore	97
4.2	Structures of $p\text{CA}^-$ , $p\text{CE}^-$ , $Pp\text{CE}^-$ and $Np\text{CE}^-$	99



4.3	Photoelectron spectra of $pCA^-$ , $pCE^-$ , $PpCE^-$ and $NpCE^-$	102
4.4	400nm photoelectron spectra of $pCA^-$ , $pCE^-$ , $PpCE^-$ and $NpCE^-$	104
4.5	Photoelectron images of $pCA^-$ , $pCE^-$ , $PpCE^-$ and $NpCE^-$	105
4.6	Anisotropy parameters measured for $NpCE^-$	106
4.7	Structural comparisons of the model chromophores in reference to $pCA^-$	107
4.8	Orbitals associated with the calculated VEEs of $pCA^-$	109
4.9	Orbitals associated with the calculated VEEs of $pCE^-$	110
4.10	Orbitals associated with the calculated VEEs of $PpCE^-$	111
4.11	Orbitals associated with the calculated VEEs of $NpCE^-$	112
4.12	Simplification of the state characters for the PYP chromophores and electronic configurations of relevant states	114
4.13	Photoelectron spectra of $pCA^-$ highlighting the major features	116
5.1	Structures of $pCE^-$ and $EBpCE^-$	124
5.2	Photoelectron spectra of $pCE^-$ and $EBpCE^-$	127
5.3	Photoelectron images for $pCE^-$ and $EBpCE^-$	128
5.4	Anisotropy parameters measured for $EBpCE^-$	129
5.5	Structural comparisons of $pCE^-$ and $EBpCE^-$	131
5.6	Orbitals associated with the calculated VEEs of $EBpCE^-$	131
5.7	400 nm photoelectron spectra of $pCE^-$ and $EBpCE^-$	135
6.1	Structure of phenolate (within the PYP chromophore structure)	143
6.2	Flowchart outlining the general approach used to simulate the photoelectron spectrum of aqueous phenolate	144
6.3	MD simulation cell of aqueous phenolate	147
6.4	MM energy over the time evolution in the MD trajectory	147
6.5	Column chart describing the number of solute-solvent hydrogen bonds	148
6.6	RDFs between the phenolate oxygen atom and solvent atoms	150
6.7	Convergence of VDE with expanding QM or EFP subsystems	151
6.8	Example QM/EFP constructions of aqueous phenolate	152
6.9	QM/EFP energies <i>vs.</i> MM/MM energies	153

6.10	$S_0$ and $D_0$ energies and VDEs calculated for 300 snapshot geometries	154
6.11	Sampling representative configurations of aqueous phenolate at room temperature	155
6.12	Charge distributions within the QM subsystem	156
6.13	Convergence of VDEs with increasing number of sampled configurations	159
6.14	EOM-IP-CCSD VDEs <i>vs.</i> DFT VDEs	160
6.15	Photodetachment cross-sections for gas-phase and aqueous phenolate	163
7.1	MD simulation cell of aqueous $p\text{CE}^-$	172
7.2	Example QM/EFP constructions of aqueous $p\text{CE}^-$	173
7.3	Valence photoelectron spectrum of a 5 mM $p\text{CE}^-$ aqueous solution measured at 180 eV	175
7.4	Fitting attempts made to construct a reference spectrum	176
7.5	Fitting attempts made to the difference valence spectrum of aqueous $p\text{CE}^-$	177
7.6	$S_0$ and $D_0$ energies and VDEs calculated for 300 snapshot geometries	179
7.7	Sampling representative configurations of aqueous $p\text{CE}^-$ at room temperature	180
7.8	Simulated absorption spectra using TD-DFT results of a single geometry	185
7.9	Simulated absorption spectrum using twenty snapshot structures	186
7.10	Convergence of average VDE with increasing sample size of configurations	191
7.11	Comparison of absorption maxima and VDEs of a PYP chromophore in different environments	195
7.12	Correlation in the electronic configurations of $S_{0-2}$ with $D_{0-1}$	197
A.1	Schematic illustrating typical times used on the delay generators	205
E.2	MM/MM energy calculated over evolution of the MD trajectory for aqueous $p\text{CE}^-$	214
E.3	Convergence of VDE with an increasing QM subsystem size	215
E.4	Convergence of VDE with an expanding EFP subsystem size	216

E.5	Column chart illustrating the number of $p\text{CE}^-$ -solvent hydrogen bonds over the MD trajectory	216
E.6	QM/EFP energy <i>vs.</i> MM/MM energy for aqueous $p\text{CE}^-$	217

## List of Tables

1.1	SA-CASSCF(14,12)-PT2/cc-pVDZ calculated vertical excitation energies of gaseous and aqueous $p\text{CE}^-$	44
2.1	Typical voltages applied to the potential switch	66
2.2	Typical voltages applied to the 2D detector	67
3.1	Calculated VIEs of microsolvated phenol clusters	89
4.1	Benchmarking methods for VEE calculations using a PYP chromophore	100
4.2	VDEs and ADEs of $p\text{CA}^-$ , $p\text{CE}^-$ , $Pp\text{CE}^-$ and $Np\text{CE}^-$	107
4.3	$p\text{CA}^-$ calculated VEEs	109
4.4	$p\text{CE}^-$ calculated VEEs	110
4.5	$Pp\text{CE}^-$ calculated VEEs	111
4.6	$Np\text{CE}^-$ calculated VEEs	112
4.7	VEEs for $p\text{CA}^-$ , $p\text{CE}^-$ , $Pp\text{CE}^-$ and $Np\text{CE}^-$	113
4.8	Calculated $D_0$ dipole moments of $p\text{CA}^-$ , $p\text{CE}^-$ , $Pp\text{CE}^-$ and $Np\text{CE}^-$	120
5.1	VDEs of $p\text{CE}^-$ and $\text{EB}p\text{CE}^-$	130
5.2	$\text{EB}p\text{CE}^-$ calculated VEEs	132
5.3	Calculated VEEs of $p\text{CE}^-$ and $\text{EB}p\text{CE}^-$	133
5.4	$D_0$ dipole moments of $p\text{CE}^-$ and $\text{EB}p\text{CE}^-$	138
6.1	Benchmarking of the DFT theory level used within the DFT/EFP calculations	145
6.2	VDEs of aqueous phenolate	158
6.3	EOM-IP-CCSD transition orbitals for the first VDE	161

6.4	EOM-IP-CCSD transition orbitals for the second VDE	162
7.1	QM/EFP VEEs calculated using an unoptimised geometry	182
7.2	QM/EFP VEEs calculated using a QM/EFP-optimised geometry	183
7.3	TD-DFT VEEs calculated with various theory levels for aqueous $p\text{CE}^-$	184
7.4	TD-DFT and EOM-EE-CCSD VEEs compared to those reported in the literature	188
7.5	EOM-EE-CCSD/EFP VEEs from a single optimised geometry	189
7.6	Calculated and experimental VDEs of aqueous $p\text{CE}^-$	190
7.7	EOM-IP-CCSD/EFP transition orbitals of aqueous $p\text{CE}^-$	190
B.1	Optimised co-ordinates of $p\text{CA}$ in $S_0$ and $D_0$	206
B.2	Optimised co-ordinates of $p\text{CE}$ in $S_0$ and $D_0$	207
B.3	Optimised co-ordinates of $Pp\text{CE}$ in $S_0$ and $D_0$	208
B.4	Optimised co-ordinates of $Np\text{CE}$ in $S_0$ and $D_0$	209
C.5	Optimised co-ordinates of $EBp\text{CE}$ in $S_0$ and $D_0$	210
E.6	B3LYP/6-311++G**//EFP VEEs of aqueous $p\text{CE}^-$	218
E.7	$\omega$ -B97X-D/6-31+G*//EFP VEEs of aqueous $p\text{CE}^-$	219
E.8	$\omega$ -B97X-D/6-311++G**//EFP VEEs of aqueous $p\text{CE}^-$	220
E.9	CAM-B3LYP/6-31+G*//EFP VEEs of aqueous $p\text{CE}^-$	221
E.10	CAM-B3LYP/6-311++G**//EFP VEEs of aqueous $p\text{CE}^-$	222

# Acronyms

<b>ADC</b>	Algebraic diagrammatic construction
<b>ADE</b>	Adiabatic detachment energy
<b>AEE</b>	Adiabatic excitation energy
<b>AIE</b>	Adiabatic ionisation energy
<b>ASEP</b>	Averaged solvent electrostatic potential
<b>B3LYP</b>	Becke, 3-parameter, Lee–Yang–Parr functional
<b>BASEX</b>	Basis set expansion
<b>BBO</b>	$\beta$ -barium borate
<b>BLYP</b>	Becke Lee–Yang–Parr functional
<b>CAM</b>	Coulomb-attenuating method
<b>CAS</b>	Complete active space
<b>CASPT2</b>	Multiconfigurational second-order perturbation theory
<b>CCD</b>	Charge-coupled device
<b>CHARMM</b>	Chemistry at Harvard macromolecular mechanics
<b>CI</b>	Conical intersection
<b>DC</b>	Direct current
<b>DCM</b>	para–hydroxybenzylidene–dimethylimidazolinone
<b>DFT</b>	Density functional theory
<b>DNA</b>	Deoxyribonucleic acid
<b>eBE</b>	Electron binding energy
<b>EFP</b>	Effective fragment potential
<b>eKE</b>	Electron kinetic energy
<b>EOM-CC</b>	Equation-of-motion coupled-cluster
<b>EOM-CCSD</b>	EOM-CC with single and double excitations
<b>EOM-EE-CCSD</b>	EOM-CCSD for electronic excited states
<b>EOM-IP-CCSD</b>	EOM-CCSD for ionisation potentials
<b>EPT</b>	Electron propagator theory
<b>ESI</b>	Electrospray ionisation
<b>FADH</b>	Flavin adenine dinucleotide

**FC** Franck-Condon  
**FWHM** Full width at half maximum  
**GGA** Generalised gradient approximation  
**HF** Hartree-Fock  
**HOMO** Highest occupied molecular orbital  
**IC** Internal conversion  
**ISR** Intersystem crossing  
**IVR** Intramolecular vibrational relaxation  
**LDA** Local-density approximation  
**LUMO** Lowest unoccupied molecular orbital  
**MCP** Microchannel plate  
**MD** Molecular dynamics  
**MM** Molecular mechanics  
**MP** Møller-Plesset  
**MS** Mass spectrometer  
**NAMD** Nanoscale molecular dynamics  
**Nd:YAG** Neodymium-doped yttrium aluminium garnet  
**Nd:YLF** Neodymium-doped yttrium lithium fluoride  
**PAD** Photoelectron angular distribution  
**pBASEX** Polar basis set expansion  
*p***HBDI**<sup>−</sup> 4-hydroxybenzylidene-1,2-dimethylimidazolinone  
**PCM** Polarisable continuum model  
**PD** Photodetachment  
**PS** Potential switch  
**PYP** Photoactive yellow protein  
**QM** Quantum mechanics  
**QMF** Quadrupole mass filter  
**RDF** Radial distribution function  
**REMPI** Resonance-enhanced multiphoton ionisation  
**RF** Radio frequency  
**RMSD** Root-mean-square deviation

**SA-CAS** State-averaged complete active space  
**SCF** Self consistent field  
**SVWN** Slater, Vosko, Wilk, Nusair functional  
**TD-DFT** Time-dependent density functional theory  
**TE** Thermionic emission  
**TIP3P** Transferable intermolecular potential with 3 points  
**TOF** Time-of-flight  
**TR-PES** Time-resolved photoelectron spectroscopy  
**UV** Ultraviolet  
**VDE** Vertical detachment energy  
**VEE** Vertical excitation energy  
**VIE** Vertical ionisation energy  
**VMD** Visual molecular dynamics  
**VMI** Velocity map imaging  
**XPS** X-ray photoelectron spectroscopy  
 $\omega$ -**B97X-D** Range-separated hybrid exchange-correlation functional with dispersion correction  
 $\omega$ **PBE** Range-separated Perdew–Burke–Ernzerhof functional

# Outline of the thesis

Chapter 1 describes how anion photoelectron spectroscopy measurements and computational methods may be used to improve our understanding of the electronic structure and relaxation dynamics of photoactive protein chromophores. A background on photoactive yellow protein (PYP) and a review of previous studies that focussed on the photochemistry of PYP or the chromophore within the protein is also provided.

Chapter 2 describes the anion photoelectron spectrometer employed to record the measurements presented in this thesis. Details are provided on the function of each of the major components within the apparatus and the procedures used to calibrate the instrument.

Chapter 3 provides a background on the computational methods employed to complement the gas-phase anion photoelectron spectroscopy measurements. Various possible approaches to extend upon the calculation of isolated gas-phase chromophores to include a solvent environment are described, including those employed in later Chapters of the thesis.

Chapters 4 and 5 describe studies combining anion photoelectron spectroscopy measurements and quantum chemistry calculations to investigate the competing electronic relaxation pathways of model PYP chromophores isolated in the gas phase. The work in Chapter 4 aimed to investigate the role of single bond torsional motion in guiding the relaxation dynamics by studying four model PYP chromophores: *para*-coumaric acid, its methyl ester and two analogues with aliphatic bridges hindering torsional motions around the single bonds adjacent to the alkene group. The work in Chapter 5 sought to probe the importance of double bond rotation (isomerisation) within the chromophore by comparing the measurements and calculations performed



on a model PYP chromophore unable to rotate about the double bond to those performed on an unlocked reference chromophore. In both studies, photoexcitation of 400 nm light was used to directly access the  $S_1$  band and wavelengths in the range 346–310 nm were used to explore the higher-lying electronically excited states of the chromophores.

Chapter 6 details a protocol for modelling an organic anion in bulk aqueous solution and calculating the electronic structure of the large-scale system. The method is illustrated using aqueous phenolate as an example. Phenolate is a molecular building block common to many biologically relevant molecules, including the PYP chromophore.

In Chapter 7, a liquid micro-jet x-ray photoelectron spectrum of a PYP chromophore in aqueous solution is presented and a computational approach similar to that described in the previous chapter is employed to simulate photodetachment from the PYP chromophore in solution. Thus, a comparison is made between the gas-phase measurements to highlight the effect of a polar solvent on the electronic structure of the chromophore.

Chapter 8 summarises the work presented within this thesis and suggests potential directions for future development.

# Chapter 1

## Introduction

In nature, many organisms have evolved to perform biological processes using photoactive proteins that efficiently and selectively transfer light energy into a physical response. Well-known examples include photosynthesis, vision and the production of vitamin D. At the heart of these proteins is a small chromophore that absorbs the light and undergoes small-scale structural changes, which are then captured and amplified by the protein around it, cascading to a macroscopic response.

Generally, when a photoactive protein chromophore absorbs a photon it is excited from its electronic ground state,  $S_0$ , to an electronically excited singlet state,  $S_n$ , in which the nuclei may no longer be in their equilibrium positions. Subsequent redistribution of internal energy may then occur in a number of ways (Figure 1.1).<sup>1</sup> The coupling between vibrational modes of the chromophore may lead to intramolecular vibrational energy redistribution (IVR), typically on a timescale of 1 – 100 ps. The chromophore may then relax from the excited singlet state back to the electronic ground state by emitting a photon,  $S_n \rightarrow S_0 + h\nu$  (fluorescence), on a timescale of 100 ps – 100 ns. However, ultrafast non-radiative relaxation processes often compete with radiative relaxation; for example, the chromophore can relax from an excited singlet state to a lower-lying excited singlet state or the electronic ground state by undergoing internal conversion (IC) on a timescale of approximately 10 fs – 10 ps. Alternatively, the chromophore may undergo an intersystem crossing (ISC) from the excited singlet state to a lower lying triplet state, typically on a longer timescale of 100 ps – 10  $\mu$ s, depending on the strength of the spin-orbit coupling between the

singlet and triplet states. The chromophore can then relax back to the electronic ground state from the triplet state by emitting a photon,  $T_n \rightarrow S_0 + h\nu$  (phosphorescence), on a timescale of  $1\ \mu\text{s} - 1\ \text{s}$ , or undergo reverse ISC back to a singlet state (the electronic ground state, as shown) typically on a timescale of  $1\ \mu\text{s} - 10\ \text{ms}$ .<sup>2</sup>

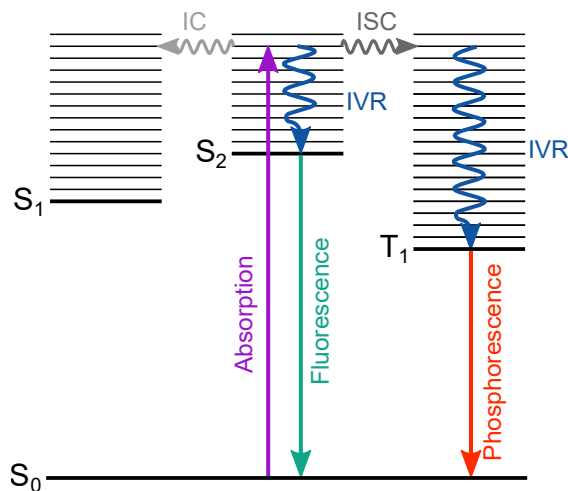


**Figure 1.1:** Jablonski diagram illustrating some of the possible relaxation processes following the absorption of light including intramolecular vibrational energy redistribution (IVR), fluorescence, internal conversion (IC), intersystem crossing (ISC) and phosphorescence.

Such protein chromophores often exist as closed-shell anions following deprotonation during proton-transfer reactions within their proteins; one such example is the chromophore that lies at the heart of the photoactive yellow protein (PYP), illustrated in Figure 1.2.<sup>3</sup> For deprotonated chromophore anions, electron emission is another common relaxation process. Photoinduced electron emission is a pertinent process in biology; a particularly well-known example is the repair mechanism for photodamaged DNA, which involves photoinduced electron transfer from the electronically excited cofactor of DNA photolyase, flavin adenine dinucleotide ( $\text{FADH}^-$ ).<sup>4</sup>

Understanding the competition between the many possible electronic relaxation processes in a photoactive protein requires a detailed understanding of the electronic structure of the chromophore. Experimentally, the most direct way of determining electronic structure is through the measurement of electron binding energies using photoelectron spectroscopy. Measuring the electron binding energies of isolated

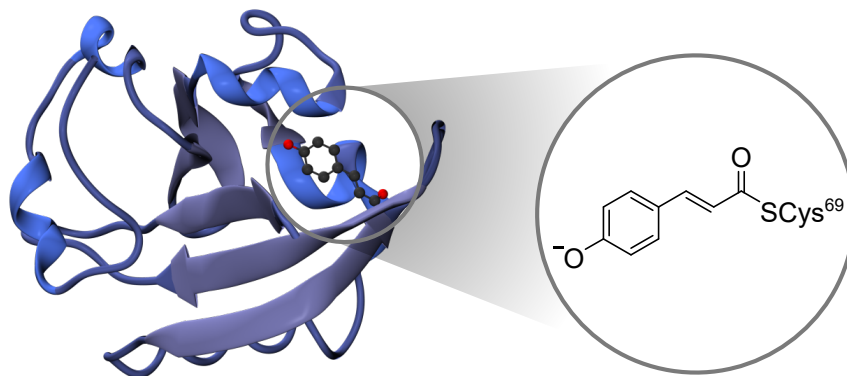


**Figure 1.2:** Structure of the photoactive yellow protein, PYP (left) highlighting the chromophore within (right). Protein structure taken from the Protein Data Bank ID 1NWZ.<sup>5</sup>

protein chromophores in the gas phase, free from interactions with their protein environment, allows the intrinsic electronic structure of the chromophore to be determined in detail. Comparing the electronic structure and dynamics of the isolated chromophore with those of the chromophore in solution or its protein environment then sheds light on the role of the interactions between the chromophore and a surrounding solvent or protein environment.

The work described in this thesis highlights the important role that photoelectron spectroscopy has played, and continues to play, in improving our understanding of the electronic structure and relaxation dynamics of deprotonated protein chromophore anions in the gas phase. The remainder of this chapter begins with an overview of anion photoelectron spectroscopy in the gas phase and a discussion of how we interpret photoelectron spectra. It then reviews the literature regarding the electronic structure and dynamics of the isolated photoactive yellow protein chromophore in both the gas phase and in aqueous solution. The work presented in later chapters focusses largely on the photoactive yellow protein chromophore and phenolate - a motif present in the PYP chromophore and also in numerous other photoactive biological molecules.

## 1.1 Anion photoelectron spectroscopy

Photoelectron spectroscopy is a powerful technique for probing the relaxation dynamics and electronic structures of photoactive chromophores. Employing photoelectron spectroscopy in the gas phase ensures that we can determine the intrinsic photophysics of the chromophores without any complication of an environment or solvent. Moreover, gas-phase measurements provide access to the higher lying electronically excited states of protein chromophores that cannot always be measured easily in their native protein environments because the UV absorption of the chromophores often overlap with those of aromatic amino acid residues. Anion photoelectron spectroscopy can be used to improve our understanding of the electronic structure and relaxation dynamics of deprotonated protein chromophore anions in the gas phase.

Anion photoelectron spectroscopy involves recording the electron kinetic energy (eKE) distribution following photodetachment of an electron,  $e^-$ , from an anion. For a closed-shell molecular anion,  $M^-$ , the photodetachment process may be represented simply as the following.



Here,  $M^\bullet$  is the neutral radical formed by removing an electron. If we consider the electrons as independent, photodetachment occurs without any reorganisation of the remaining electrons, *i.e.* Koopmans' picture.<sup>6</sup> Hence, the eKE distribution of photoelectrons allows us to determine the electron binding energy (eBE) of an electron detached from a particular molecular orbital, with respect to the electronic state of the resultant neutral radical, using  $eBE = h\nu - eKE$ . The detachment process is effectively instantaneous compared to the timescale for nuclear rearrangement. Therefore the spectral profile is determined by the Franck-Condon overlap of the vibrational wave functions of the two electronic states - *i.e.* the anion before photodetachment and the neutral radical following detachment. For a photodetachment process from a closed-shell anion in its electronic ground state to the electronic ground state of the neutral radical, the states are  $S_0$  and  $D_0$ , respectively.

Important quantities are the adiabatic detachment energy (ADE) and the vertical

detachment energy (VDE); and are illustrated in Figure 1.3. These detachment energies are analogous to adiabatic and vertical ionisation energies (AIE and VIEs) when considering photoelectron spectroscopy of neutral molecules. The ADE is the difference between the electronic energies of the anion and the corresponding neutral radical in their ground vibrational states. The VDE is the difference between the electronic energies of the anion and the corresponding neutral at the geometry of the anion in its ground vibrational state, where the Franck-Condon overlap is greatest. Experimentally, the ADE and VDE are approximately equivalent to the photon energies corresponding to the onset of the photoelectron spectrum and the maximum in the photoelectron distribution intensity, respectively.

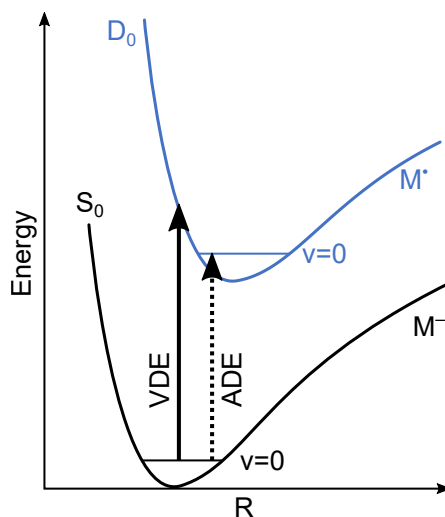


**Figure 1.3:** A schematic illustration of the potential energy curves for a molecular anion,  $M^-$ , in its closed shell ground electronic state,  $S_0$ , and the corresponding neutral radical,  $M^\bullet$ , in its ground electronic state,  $D_0$ , as a function of a single vibrational mode coordinate,  $R$ . Vertical arrows represent the experimental vertical detachment energy (VDE) and adiabatic detachment energy (ADE).

The valence electrons of a gas-phase molecular anion are weakly-bound and so a single UV photon is often sufficient to overcome the detachment threshold. In addition, almost all excited electronic states,  $[M^-]^*$ , lie above the ADE and so populations of such excited states may lead to indirect, delayed detachment. As a result, UV photoelectron spectra of anions have features that arise due to direct detachment and indirect detachment processes, as illustrated in Figure 1.4. Direct photodetachment from  $S_0$  to the  $D_0$  continuum gives photoelectrons with  $eKE \sim h\nu - VDE(D_0)$ , determined by the Franck-Condon overlap of the vibrational wave

functions of  $S_0$  and  $D_0$  (shown in purple in Figure 1.4). Indirect photodetachment is represented as

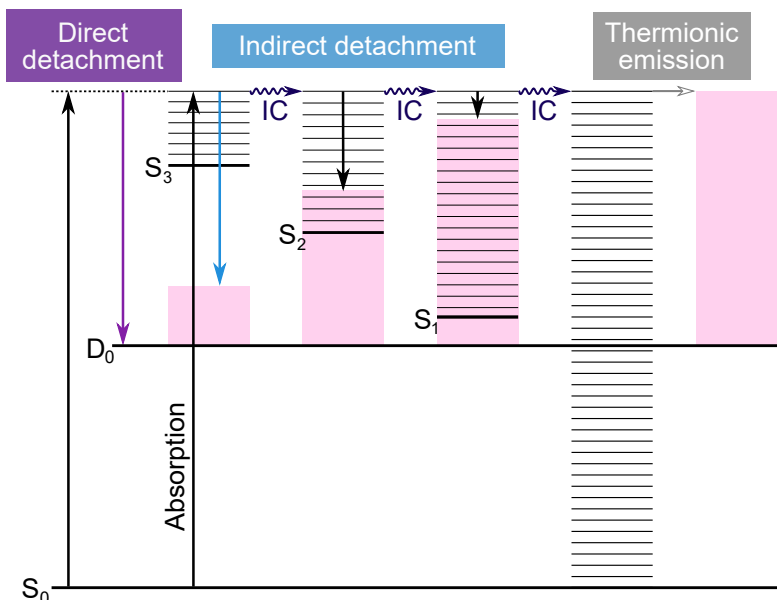
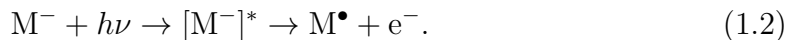


**Figure 1.4:** Jablonski diagram illustrating the major photodetachment pathways possible for a closed-shell anion following UV photoexcitation. Thin horizontal black lines represent the vibrational levels of the anion and pink shaded areas represent the vibrational energy left with the neutral radical (determined by the propensity for the conservation of vibrational energy). Arrows pointing downwards represent the eKE release on detachment, horizontal wavy blue arrows indicate possible internal conversion (IC) processes between singlet states and the horizontal grey arrow indicates eKE release on thermionic emission. Colours of the eKE release arrows and the labels above correspond to the features in Figure 1.5.

For molecular anions that do not undergo large geometry changes during photodetachment, there is a propensity for conserving vibrational energy. Hence, indirect photodetachment following photoexcitation of  $S_3$  (shown in blue in Figure 1.4) with excess vibrational energy,  $E_{\text{vib}} = h\nu - E(S_3)$  gives photoelectrons with  $\text{eKE} \sim h\nu - E(D_0) - E_{\text{vib}}$ , where  $E(D_0)$  is the adiabatic detachment energy of  $D_0$  and  $E(S_3)$  is the adiabatic excitation energy of  $S_0 \rightarrow S_3$ . Or, more consisely,  $\text{eKE} \sim E(S_3) - E(D_0)$  *i.e.* photoelectrons leave with eKE corresponding to the  $S_3$ - $D_0$  energy difference. Alternatively, photoexcitation of  $S_3$  may be followed by internal conversion to  $S_2$  and subsequent indirect photodetachment from  $S_2$  which gives rise to photoelectrons with lower eKEs as a higher vibrational level of  $S_2$  is

populated and so more vibrational energy remains with the neutral radical on detachment. Similarly, indirect photodetachment following internal conversion into  $S_1$  at the same photon energy would give rise to photoelectrons with even lower eKEs. If the anion undergoes internal conversion back to  $S_0$ , vibronic coupling between the ground electronic states of the anion and neutral radical may result in vibrational autodetachment.<sup>7</sup> Alternatively, coupling between the very high density of vibrational states with energy,  $E_{vib} \sim h\nu$ , may result in a statistical redistribution of vibrational energy and a delayed emission of electrons known as thermionic emission (shown in grey in Figure 1.4) with an eKE profile,  $P(\epsilon)$ , defined by Klots' formula<sup>8,9</sup>

$$P(\epsilon) \propto \epsilon^{1/2} \exp(-\epsilon/k_B T_{M\bullet}) \quad (1.3)$$

where  $k_B$  is Boltzmann's constant and  $T_{M\bullet}$  is the temperature of the neutral radical,<sup>10–12</sup>

$$T_{M\bullet} = T_{M-} + (h\nu - \text{ADE})/C_V. \quad (1.4)$$

$T_{M-}$  is the microcanonical temperature of the anions before photoexcitation and  $C_V$  is the microcanonical heat capacity.

Direct and indirect photodetachment processes can be identified by monitoring how features in the photoelectron spectra, plotted as functions of eKE and eBE, vary with photon energy, as shown in Figure 1.5. Direct photodetachment (purple) from the ground electronic state of the anion,  $S_0$ , to the ground electronic state of the neutral radical,  $D_0$ , gives rise to a photoelectron distribution whose eKE increases linearly with photon energy but whose eBE is constant and corresponds to the  $S_0$ - $D_0$  VDE. Indirect photodetachment (blue) from a resonance in the detachment continuum,  $S_n$  (*e.g.*  $S_3$ , as discussed above), gives rise to a photoelectron distribution whose eKE remains constant with increasing photon energy and corresponds to the energy difference,  $E(S_n) - E(D_0)$ . Thermionic emission from hot  $S_0$  (grey), populated by IC from an electronically excited state of the anion, is characterised by a photoelectron distribution with a profile defined by Equation (1.3) with  $\text{eKE} \sim 0$  ( $\text{eBE} \sim h\nu$ ).

The competition between indirect detachment and internal conversion is gov-



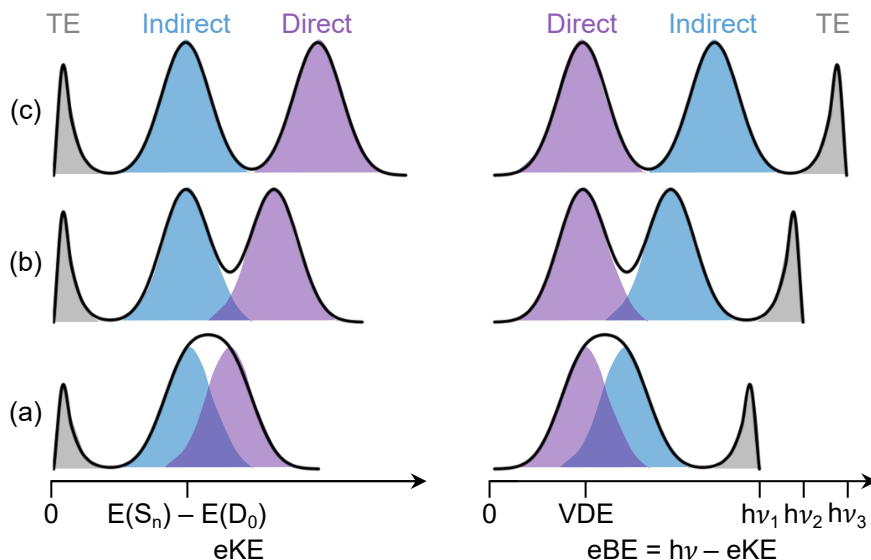


**Figure 1.5:** Cartoon illustrating how features corresponding to direct (purple) and indirect (blue, grey) photodetachment processes appear in photoelectron spectra plotted as functions of  $eKE$  (left) and  $eBE$  (right) for three photon energies, (a)  $h\nu_1$ , (b)  $h\nu_2$  and (c)  $h\nu_3$ , where  $h\nu_1 < h\nu_2 < h\nu_3$ . Direct photodetachment from  $S_0$  to  $D_0$  gives rise to photoelectrons with a maximum situated at an  $eBE$  that corresponds to the  $S_0$ - $D_0$  VDE (purple). Indirect photodetachment following photoexcitation of a resonance in the detachment continuum,  $S_n$ , gives rise to photoelectrons with a maximum  $eKE$  corresponding to  $E(S_n) - E(D_0)$  (blue). Thermionic emission from  $S_0$  following photoexcitation of an electronically excited state of the anion and subsequent IC back to  $S_0$  gives electrons with a characteristic energy distribution profile defined by Equation (1.3) (grey).

erned by their timescales. The timescale for indirect electron detachment is typically in the range 10 fs – 10 ps, depending on the strength of the coupling between the electronically excited state and the detachment continuum. Excited electronic states embedded in the detachment continuum are classified either as shape or Feshbach resonances (Figure 1.6).

Shape resonances only require the loss of a single electron to generate the neutral electron configuration, whereas Feshbach resonances require concerted electronic reconfiguration and loss of an electron to generate the neutral electron configuration. Consequently, electronically excited states with shape resonance character are coupled more strongly to the detachment continuum than those with Feshbach resonance character. Therefore, electron detachment from a shape resonance is much faster than that from a Feshbach resonance. Electron detachment from an excited-shape resonance (Figure 1.6) is even faster.

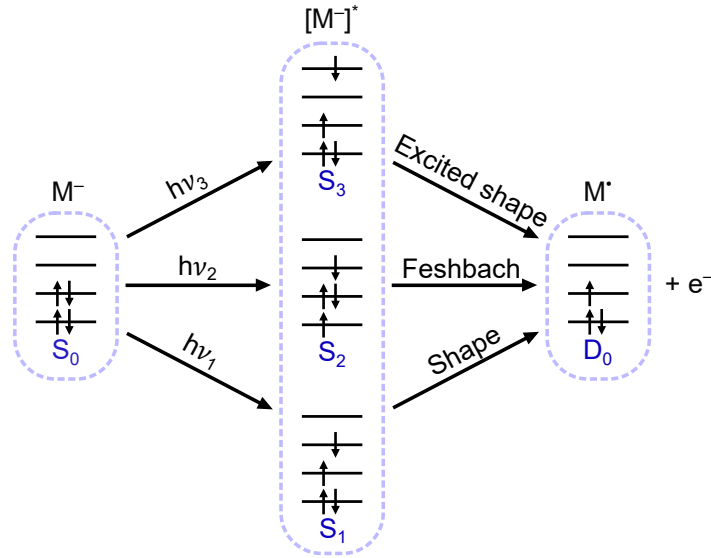


**Figure 1.6:** Electronic configurations of electronically excited states of an anion,  $[M^-]^*$ , with shape, Feshbach and excited-shape resonance characters with respect to the detachment continuum associated with the neutral radical,  $M^\bullet$ , in its electronic ground-state,  $D_0$ .

Photoelectron angular distributions (PADs) may be measured experimentally as well as the eKE distribution, which provides additional information on the symmetry of the molecular orbital from which the electron is detached.<sup>13,14</sup> As an electron leaves a molecular anion, its wavefunction reflects the electronic and nuclear configurations of the anion. PADs are generally measured in the lab frame with the anions aligned randomly relative to the electric field vector of the photodetaching laser light. Hence, the measured PAD will reflect the overlap between the electric field and the transition dipole moments for photodetachment. For a one-photon detachment process, the PAD can be expressed as

$$I(\theta) \propto 1 + \beta_2 P_2(\cos \theta) \quad (1.5)$$

where  $I(\theta)$  is the probability of photoelectron emission at a particular angle  $\theta$ , defined as the angle between the laser polarisation and the velocity vector of the photoelectron.  $P_2(\cos \theta)$  is the second-order Legendre polynomial and  $\beta_2$  is the anisotropy parameter.  $\beta_2$  ranges from  $-1$  to  $+2$ , with the limits corresponding to photoelectron emission perpendicular ( $\sin^2 \theta$  distribution) or parallel ( $\cos^2 \theta$  distribution) to

the laser polarisation, respectively. With purely direct photoelectron detachment processes, photoelectrons with different anisotropies can be assumed to arise from orbitals of different electronic characters. In general, a negative  $\beta_2$  can be attributed to photodetachment from a  $p$  or  $\pi$  character orbital and a positive  $\beta_2$  can be attributed to photodetachment from an  $s$  or  $\sigma$  character orbital. PADs can be very sensitive to continuum resonances and molecular conformations and can provide valuable information of the anion electronic and nuclear structure.<sup>15–17</sup>

Pump-probe techniques may also be employed to study the evolution of the excited state dynamics of anions. In a time-resolved anion photoelectron spectroscopy (TRPES) experiment, an ultrashort pump laser pulse (typically  $\sim 100$  fs) promotes an anion to an excited electronic state and a second ultrashort probe laser pulse then detaches an electron from the evolving excited state of the anion. The photoelectron spectra are then measured at a series of precisely timed pump-probe time intervals. One of the advantages of TRPES over other pump-probe methods, such as transient absorption spectroscopy or time-resolved fluorescence spectroscopy, is that electron detachment is always an allowed process because there are no stringent selection rules for photodetachment. However, it should be noted that the detachment cross-section,  $\sigma \propto eKE^{l+1/2}$ ,<sup>18,19</sup> where  $l$  is the orbital angular momentum of the outgoing electron wave, shows that  $\sigma \rightarrow 0$  as  $eKE \rightarrow 0$ . One of the advantages of anion TRPES over neutral-molecule TRPES is that the low photodetachment energies of only a few eV make it relatively straightforward to monitor repopulation of the ground state of the anion using UV laser pulses.

## 1.2 Photoactive yellow protein

### 1.2.1 Background

Photoactive yellow protein (PYP) is the primary photoreceptor responsible for the negative phototactic response of the *Halorhodospira halophila* bacterium.<sup>20–23</sup> The chromophore that lies at the heart of PYP is *trans-para*-coumaric acid (*pCA*). In its unactivated (dark) resting state the chromophore exists in its deprotonated anionic *trans* form, as shown in Figure 1.7.

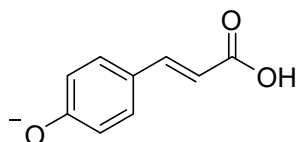


**Figure 1.7:** Structure of the deprotonated PYP chromophore anion,  $pCA^-$ .

In PYP, the chromophore is covalently bound to the protein at the carbonyl terminus by a thio-ester link with a cysteine residue. The negative charge on the chromophore is stabilised by a network of hydrogen bonds with surrounding amino acid residues. Following photoexcitation with blue light, the deprotonated chromophore anion undergoes rapid *trans-cis* isomerisation to generate a red-shifted intermediate, pR, in which the chromophore is in a strained *cis* conformation (Figure 1.8).<sup>3</sup> A series of thermal reactions then follow. The hydrogen-bond network reorganises to accommodate the *cis* conformation, the protein partially unfolds and the chromophore is protonated, generating a blue-shifted intermediate, pB, which is the signalling state. This long-lived signalling state is what the host organism responds to and triggers the bacterium to move to avoid potentially-harmful UV light. Subsequent *cis-trans* isomerisation of the chromophore, refolding of the protein and deprotonation of the chromophore complete the photocycle by regenerating the protein in its initial state, pG.

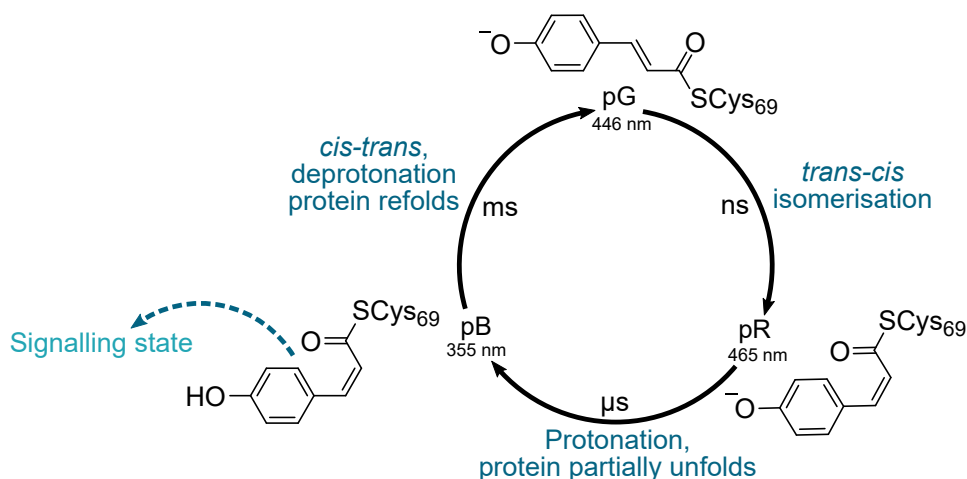


**Figure 1.8:** Photocycle of photoactive yellow protein (PYP) showing the major intermediates, their absorption maxima and time-scales.

PYP is an ideal candidate for studying biological photoreceptors as a result of its

small size (125 residues), stability and ease of crystallisation.<sup>21,24–27</sup> Chromophores with similar structures to the PYP chromophore have also been found to function as ultrafast photoprotective sunscreens in the leaves of plants.<sup>28,29</sup> Moreover, PYP has been shown to be useful as a tag for small molecule imaging of live cells.<sup>30</sup> Numerous spectroscopic and computational chemistry studies of the electronic structure and relaxation dynamics of isolated model PYP chromophores in the gas phase have been aimed at understanding the role of the chromophore and its environment in determining the function of this important photoreceptor.<sup>31–39</sup>

### 1.2.2 Deprotomers of the chromophore

The first experimental investigation of the electronic structure of gas-phase  $pCA^-$  was an action-absorption spectroscopy study.<sup>31</sup> The spectra were measured by irradiating anions stored in an electrostatic storage ring with a tunable laser pulse and recording the yield of neutral fragments formed as a function of wavelength to indicate the relative absorption cross-section. The action-absorption band (Figure 1.9) was found to have a maximum around 430 nm (2.88 eV). The authors also reported spectra for  $pCTP^-$ , a phenyl-thioester analogue which was found to have a gas-phase absorption maximum of 460 nm. Both absorption maxima are close to the absorption maximum of the protein (446 nm).<sup>20</sup> Conversely, the absorption maxima of the chromophores in solution were significantly blue-shifted from the gas-phase, or protein, measurements. This led to the suggestion that the electrostatic environment of the PYP chromophore in the protein is closer to that of the chromophore *in vacuo* than the chromophore in aqueous solution.

There has been some discussion about the deprotonated form of the  $pCA$  chromophore *in vacuo*<sup>31,33,34,36</sup> as it has acidic hydrogen sites on the phenol and carboxylic acid groups and can therefore exist as a phenolate or carboxylate anion (Figure 1.10). In this early study, it was originally thought that the deprotonation of  $pCA^-$  would primarily occur at the carboxylate, as shown by the structure in 1.9A. In the gas phase, the phenolate isomer is more stable than the carboxylate isomer because the negative charge is delocalised throughout the anion, but in polar solvents, the carboxylate form is more stable than the phenolate because the localised

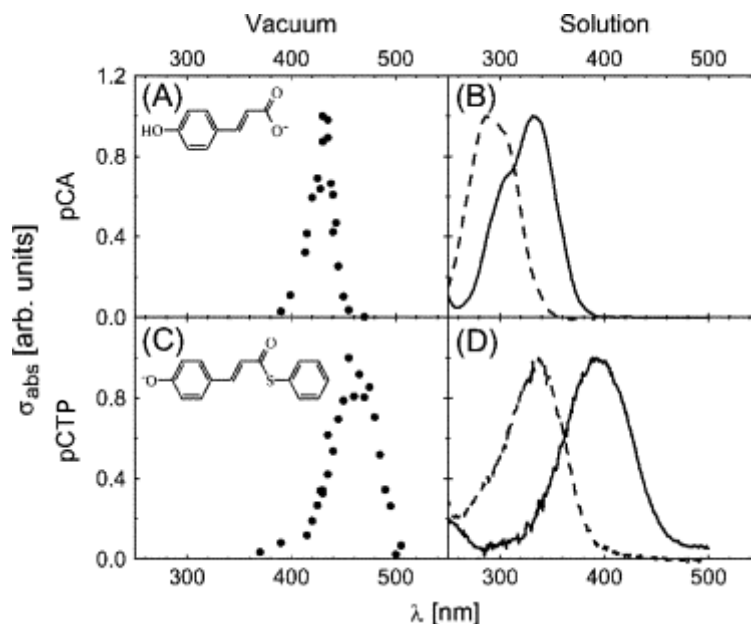


**Figure 1.9:** Absorption curves of two model PYP chromophores,  $pCA^-$  and  $pCTP^-$ . (A)  $pCA^-$  in vacuum. (B)  $pCA$  in aqueous solution. The dashed line is for a neutral solution, and the solid line is for a solution with NaOH added, pH > 11. (C)  $pCTP^-$  in vacuum. (D)  $pCTP$  in aqueous solution. The dashed line is for a neutral solution, and the solid line is for a borate (III) buffer, pH 10.2. Adapted from Reference 31.

charge can be solvated more efficiently. Within the protein, the chromophore exists in the phenolate form as the carbonyl terminus is covalently connected to the protein structure *via* a thioester linkage. Hence the phenolate deprotomer is more desirable to study as a model of the PYP chromophore.

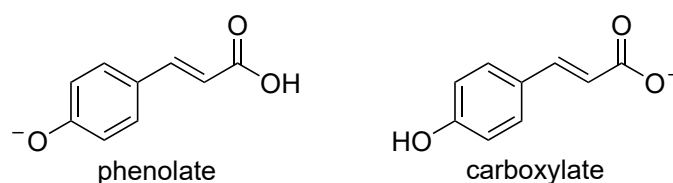


**Figure 1.10:** Phenolate and carboxylate deprotonated forms of  $pCA^-$ .

The conditions used in an electrospray ion source have been found to play an important role in determining which deprotomer may form in the gas phase. Using gas-phase IR spectroscopy techniques, Almasian *et al.* found evidence for both isomers forming from an electrospray ionisation source and they were able to maximise the fraction of the phenolate isomer by using an aprotic solvent (dry acetonitrile).<sup>36</sup>

SA-CAS(14,12)-PT2/cc-pVDZ calculations have predicted gas-phase vertical ex-

citation energies of 2.89 eV and 3.86 eV for the phenolate and carboxylate forms, respectively,<sup>40</sup> suggesting that the early action-absorption spectra were dominated by the phenolate form of  $pCA^-$ . Rocha-Rinza *et al.* reported action-absorption spectra of analogues of  $pCA^-$  with methyl groups terminating either deprotonation site.<sup>33</sup> Interestingly, the spectra look remarkably similar with very little difference in the maxima of the  $S_1$  band ( $430 \pm 3$  nm for both species). This disagrees with the SA-CAS(14,12)-PT2 calculations that calculated vertical excitation energies differing by  $\sim 1$  eV for the two deprotonomers.<sup>40</sup> It was unclear whether there was some contamination present in the measurements, or the calculated predictions simply do not agree. This highlights the importance of detailed supporting computational studies and reporting the conditions used when producing the anions.

Recently, Bull *et al.*<sup>41</sup> used ion mobility techniques in tandem with photoexcitation to study  $pCA^-$  and methylated analogues, similar to those used by Rocha-Rinza *et al.*<sup>33</sup> The authors found that the two methylated analogues had different photophysical responses; the phenoxide and carboxylate methylated analogues had action-absorption maxima of 430 and 360 nm, respectively. These findings correlate well with the theoretical predictions,<sup>40</sup> but poorly with previous action-absorption measurements of the two analogues.<sup>33</sup> The authors also found evidence supporting the generation of the phenolate deprotonomer of  $pCA^-$  from the carboxylate deprotonomer *via* a multistep photoinitiated proton transfer.

The photodetachment process in gas-phase  $pCA^-$  has been measured in several photoelectron spectroscopy studies<sup>37,38</sup> and the VDE has been measured as  $2.91 \pm 0.05$  eV.<sup>38</sup> The VDEs of the two isomers of  $pCA^-$  calculated using the EPT/6-311++G(3df,3pd) method were found to be 3.00 eV for the phenolate form and 4.68 eV for the carboxylate form, suggesting that the photoelectron spectra were dominated by the phenolate form of  $pCA^-$ .<sup>37</sup>

Other model chromophores have also been used such as the methylated analogues described above that help to reduce structure ambiguity upon deprotonation,<sup>33,34,41,42</sup> or thioester derivatives of the chromophore which strengthen the likeness to the protein environment,<sup>31,38,43–46</sup> or chromophores with molecular tethers restricting rotational motion.<sup>47–52</sup>

There have also been numerous gas-phase spectroscopic studies of neutral model chromophores and fragments of *pCA*.<sup>35,53–56</sup> The electronic structure of the neutral *pCA* chromophore differs greatly from that in its deprotonated, anionic form; the vertical ionisation energy is greater than double that of the VDE of isolated *pCA*<sup>−</sup>.<sup>35</sup> However, it is of greater biological relevance to study the deprotonated, anionic form of the chromophore as that is how it exists in the resting state of the protein and hence more relevant to help interpret the initial steps of the photocycle.

### 1.2.3 Dynamics of the first electronically excited state

The timescales associated with electronic relaxation following photoexcitation of the  $S_1$  state of a model ketone PYP chromophore, *pCK*<sup>−</sup> (Figure 1.11), *in vacuo* have been determined using time-resolved photoelectron spectroscopy.<sup>32</sup> Gas-phase anions were excited with 400 nm (3.10 eV) femtosecond pump pulses, close to the absorption maximum of the  $S_1$  band. The evolution of the population on the excited state was monitored by firing 800 nm (1.55 eV) femtosecond probe pulses at a series of pump-probe delays to project the excited state population onto the photodetachment continuum.

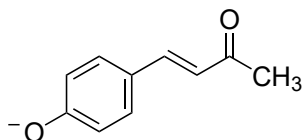


**Figure 1.11:** Structure of the model ketone PYP chromophore, *pCK*<sup>−</sup>, used in time-resolved photoelectron spectroscopy experiments in Reference 32.

The pump-only spectrum was observed to have an intense peak around 0.2 eV eKE, arising from one-photon direct photodetachment from the ground state (Figure 1.12). In the pump-probe spectrum at 200 fs delay, the peak around 0.2 eV eKE partially depleted and a broad peak centred around 0.9 eV appeared. With increasing pump-probe delay, the low energy feature around 0.2 eV (labelled I in Figure 1.12) was observed to be recovered on timescales of 4 ps and 52 ps. The broad peak around 0.9 eV was separated into two regions (labelled II and III in Figure 1.12). The higher eKE region II was observed to decay on timescales of 1 ps



and 4 ps. The lower eKE region III was observed to rise on a timescale of 1 ps and then decay on a timescale of 52 ps.

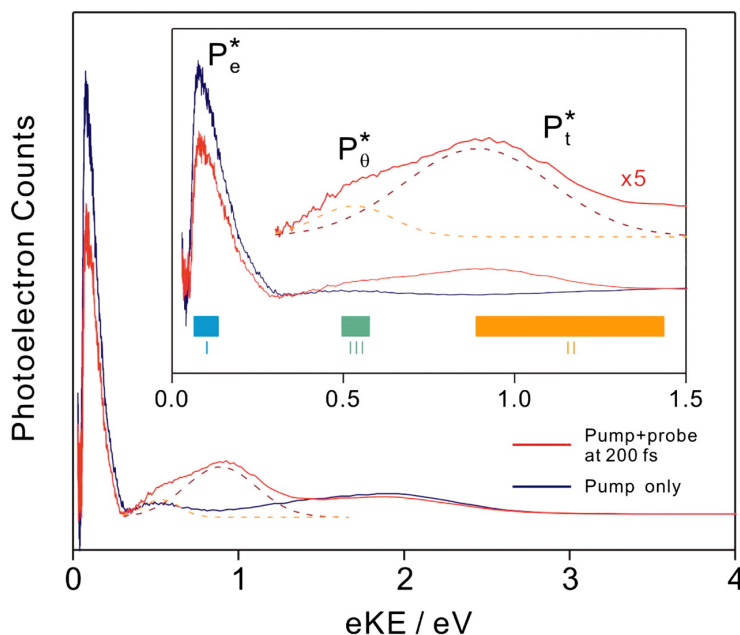


**Figure 1.12:** Pump-only (blue) and pump-probe (200 fs delay; red) photoelectron spectra of  $pCK^-$ . Inset: 0-1.5 eV eKE region with eKE windows I, II and III, corresponding to  $P_e^*$ ,  $P_t^*$  and  $P_\theta^*$ , respectively (see text) Reproduced from Reference 32.

It was concluded that these TRPES spectra showed that following photoexcitation, population in the excited  $S_1$  state initially bifurcated with 80% of the population remaining on the excited state with the chromophore in its *trans* form,  $P_t^*$  (region II), and 20% of the population undergoing autodetachment to form a low eKE electron and neutral radical,  $P_e^*$  (region I), on a 4 ps timescale.  $P_t^*$  then evolved to form a twisted intermediate,  $P_\theta^*$  (region III), on a 1 ps timescale, which then underwent internal conversion, on a 52 ps timescale, back to the electronic ground state as a vibrationally-hot *cis* conformer,  $P_c$ . The decay of  $P_\theta^*$  was accompanied by a damped oscillation with period corresponding to  $\sim 40\text{ cm}^{-1}$ , a low-frequency motion involved in the isomerisation.

The timescale for *trans-cis* isomerisation of this particular chromophore in the gas phase (52 ps) is an order of magnitude slower than isomerisation in the protein; this was explained in terms of IVR through coordinates orthogonal to the reaction path (Figure 1.13). It was concluded that one of the roles of the microen-

environment within the PYP protein is therefore to direct excited state population towards the conical intersection with the *cis* ground-state with high quantum yield ( $\Phi \sim 0.35^{57-61}$ ). This also supported an earlier theoretical study that predicted that the conical intersection between  $S_1$  and the *cis* ground state lay further from the global minimum on the  $S_1$  potential energy surface for the chromophore *in vacuo* than in the protein (Figure 1.13 inset).<sup>62</sup>

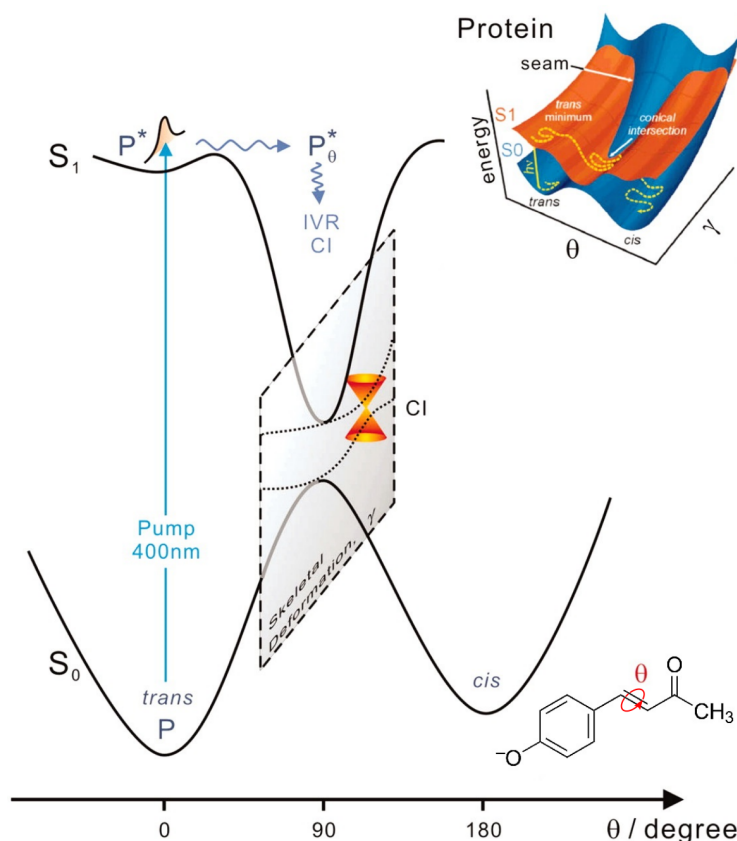


**Figure 1.13:** Schematic potential energy surface illustrating photoisomerisation of  $pCK^-$ . The photoisomerisation coordinate is  $\theta$  and orthogonal coordinates are  $\gamma$ , represented by the perpendicular plane labelled skeletal deformation and containing the conical intersection (CI) with the *cis* ground-state. Following photoexcitation from  $S_0$  to  $S_1$ , population on the excited state ( $P^*$ ) bifurcates to  $P_e^*$  (20 %) and  $P_t^*$  (80 %). Inset: illustration of the dynamics of the chromophore in PYP with a cut in the 3D surface showing a similar  $\theta$  dependence but having a CI much closer to the reaction coordinate. Reproduced from Reference 32.

### 1.2.4 Higher lying electronically excited states

Photoabsorption of higher energy photons can result in electron emission creating radicals and free electrons potentially harmful to biological systems by mutation of DNA. Electron emission has been observed from the protein following multiphoton excitation of a high-lying excited state when irradiated by high intensity light of wavelength  $\sim 400$  nm.<sup>63–65</sup> This has been proposed to occur *via* an excited state absorption from the first excited state to a high-lying excited state from which there is sufficient energy to overcome the detachment threshold.<sup>64</sup> Interestingly, the absorption band of the detached electron within the protein cavity was found to be similar to that of the solvated electron. This led to the suggestion that the protein environment provides a water-like local environment for the electron.

One of the first gas-phase experimental investigations of higher lying electronically excited states of an isolated PYP chromophore was an action-absorption spectrum of  $pCE^-$ , the methyl ester analogue of  $pCA^-$ .<sup>34</sup> Several electronically excited states were found above the detachment threshold (Figure 1.14).

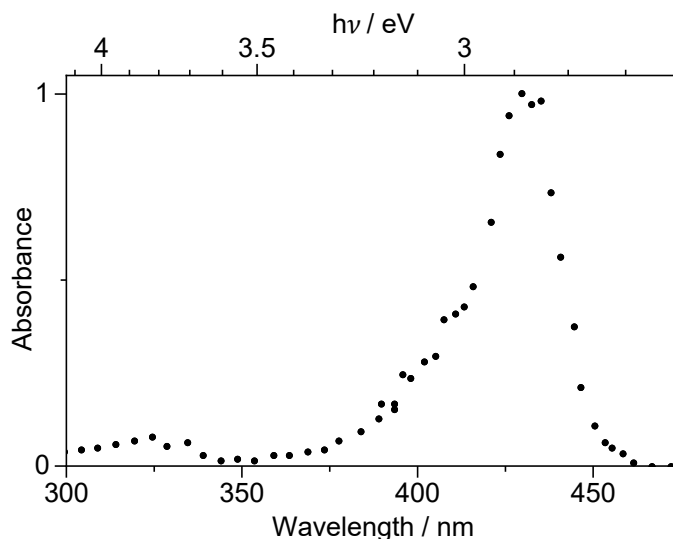


**Figure 1.14:** Action-absorption spectrum of gas-phase  $pCE^-$  adapted from Reference 34.

Anion photoelectron spectra of  $pCA^-$  recorded at photon energies in the range 364–315 nm have been shown to broaden considerably with increasing photon energy, indicative of autodetachment from a resonant high lying electronically excited state in the continuum.<sup>37</sup> SA-CASSCF(14,12)-PT2 calculations found the vertical

excitation energies (VEEs) of the first three singlet electronically excited states of  $p\text{CA}^-$  to be 419 nm (2.96 eV), 339 nm (3.65 eV) and 325 nm (3.82 eV),<sup>42</sup> in agreement with the action-absorption measurement.<sup>34</sup> The oscillator strength of  $S_1$  was near unity, while that of  $S_2$  was zero (a dark state) and that of  $S_3 \sim 10\%$ . These electronically excited states were dominated by excitations of  $S_1(\pi\pi_1^*)$ ,  $S_2(n\pi_1^*)$  and  $S_3(\pi\pi_2^*)$  character, respectively. The relevant orbitals calculated using TD-CAM-B3LYP/6-311++G(3df,3pd)<sup>38</sup> are shown in Figure 1.15 and are similar to those calculated with SA-CASSCF(14,12)-PT2.<sup>42</sup> The first two singlet excited states lying above the detachment threshold,  $S_2$  and  $S_3$ , have Feshbach and excited-shape resonance character with respect to the  $D_0$  continuum, respectively. This suggests that the broadening of photoelectron spectra following excitation around 320 nm arises from fast autodetachment from the  $S_3$  excited-shape resonance as this would outcompete the relatively slow autodetachment from  $S_2$ .

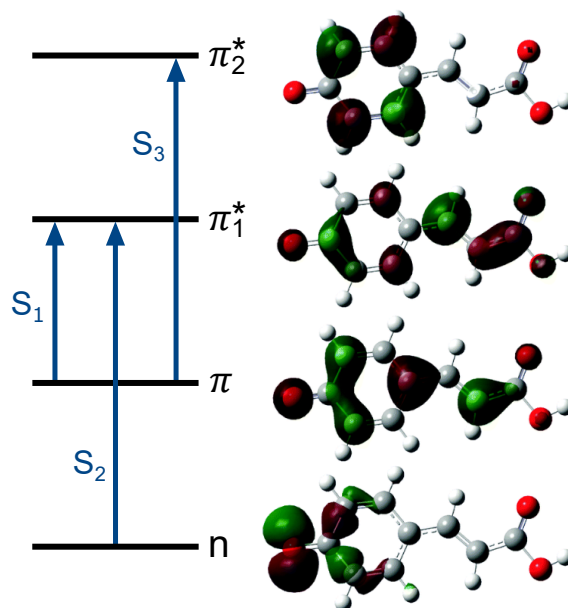


**Figure 1.15:** The first three singlet electronic excited state transitions and the main contributing orbitals for model PYP chromophore  $p\text{CA}^-$  calculated at the CAM-B3LYP/6-311++G(3df,3pd) level. Orbitals taken from Reference 38.

Since the excited-shape resonance is strongly coupled to the detachment continuum in the gas phase, it is expected that resonant electron transfer from this  $S_3$  state of the chromophore in aqueous solution, or in PYP, would also be efficient and could be responsible for the generation of solvated electrons. In the gas phase, an

additional feature with  $eKE \sim 0$  has been observed in anion photoelectron spectra recorded at wavelengths resonant with  $S_3$ . This low  $eKE$  feature has been attributed to thermionic emission from  $S_0$ , suggesting that internal conversion from  $S_3$  to the ground state competes with autodetachment.<sup>37,38</sup>

### 1.2.5 Tuning the electronic structure and dynamics

Knowing that the structure of the chromophore and the protein environment play an important role in guiding the electronic relaxation dynamics has inspired several combined anion photoelectron spectroscopy and quantum chemistry investigations of structurally-modified chromophores; examples include changing the position of the phenoxide group ( $oCA^-$  and  $mCA^-$ )<sup>37</sup> or substitution at the coumaryl tail ( $pCT^-$  and  $pCE^-$ ).<sup>38</sup>

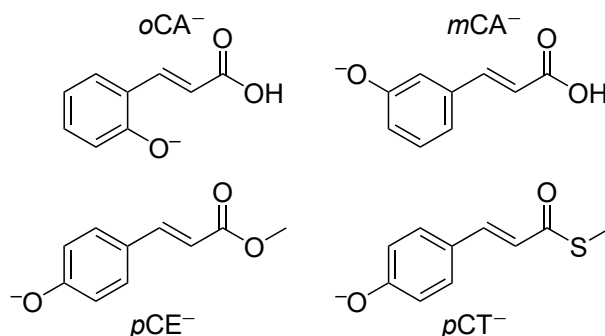


**Figure 1.16:** Model deprotonated chromophores with the phenoxide group moved to *ortho* ( $oCA^-$ ) and *meta* ( $mCA^-$ ) positions or substitution of ester ( $pCE^-$ ) and methyl-thioester ( $pCT^-$ ) groups at the coumaryl tail.

A study of  $oCA^-$ ,  $mCA^-$  and  $pCA^-$  chromophores showed that moving the position of the  $O^-$  group on the phenoxide moiety changed the branching ratio between direct photodetachment and indirect photodetachment. In agreement with action absorption spectra,<sup>34</sup> TD-CAM-B3LYP/6-311++G(3df,3pd) calculated VEEs showed that the  $S_3$  state was much higher in energy for the *ortho* isomer than the other isomers and that the  $S_1$  state was significantly lower and had almost negligible oscillator strength for the *meta* isomer. Thus, following photoexcitation in the range 364-315 nm, the  $S_3$  state of  $oCA^-$  was inaccessible so the spectra did not show the broadening characteristic of indirect detachment observed in  $mCA^-$  and  $pCA^-$ .

Moreover, the longer wavelength photoelectron spectra of  $mCA^-$  were found to be completely dominated by direct photodetachment.

A separate study of  $pCA^-$ ,  $pCE^-$  and  $pCT^-$  aimed to investigate how substitution at the coumaryl tail of the chromophore may control competing relaxation pathways following UV photoexcitation in the range 350-315 nm.<sup>38</sup> The photoelectron spectra were found to be dominated by electrons arising from direct detachment and indirect detachment from the  $S_3(\pi\pi^*)$  state, but some spectra also had a low eKE component arising from autodetachment from lower lying electronically excited states or thermionic emission (TE) from the electronic ground state (Figure 1.17). Substituting the hydrogen atom of the carboxylic acid group ( $pCA^-$ ) with a methyl group ( $pCE^-$ ) was found to lower the threshold for electron detachment but had very little effect on the competition between the different relaxation pathways. However, substituting with a thioester group ( $pCT^-$ ) raised the threshold for electron detachment and appeared to ‘turn off’ the competing electron emission processes from lower lying electronically excited states. This has potential implications in terms of tuning the light-induced electron donor properties of PYP.

There have been both experimental<sup>51</sup> and theoretical<sup>61,62,66</sup> investigations aimed at better understanding the role of torsional rotations in the photochemistry of the PYP chromophore. It is well-understood that the initial *trans-cis* isomerisation step in the PYP photocycle involves secondary nuclear motions at the chromophore-level.<sup>67</sup> Stahl *et al.* employed time-resolved spectroscopic techniques to study the photophysics of a reconstructed PYP with a chromophore rotation-locked by an ethane bridge across the phenolate-ethene single bond.<sup>51</sup> Comparing to wild-type PYP, the authors reported that the excited state dynamics of the locked chromophore were accelerated but that the isomerisation yield reduced by  $\sim 60\%$ , implying that the phenolate rotation is not an alternative to *trans-cis* isomerisation but it does help facilitate the isomerisation with some coupled movement.

Computational studies of  $S_1$  dynamics have found a minimum on the  $S_1$  potential energy surface involving a twist around the single bond connecting the phenolate and C=C bond moieties, in addition to the minimum along the isomerisation coordinate.<sup>39,45,62,68-71</sup> This led to the suggestion that single-bond rotation may compete

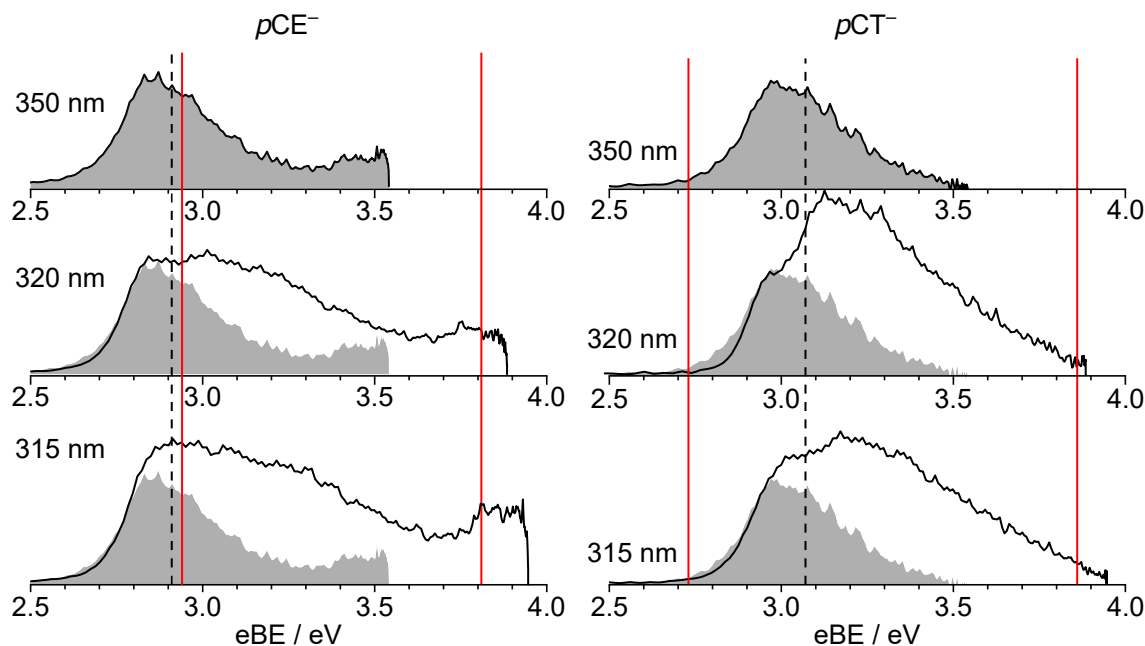


**Figure 1.17:** Photoelectron spectra of  $pCE^-$  and  $pCT^-$  recorded at 350 nm (3.54 eV), 320 nm (3.87 eV) and 315 nm (3.94 eV) presented as a function of electron binding energy (eBE). The 350 nm spectra are superimposed on the 310 and 315 nm spectra, as shown in shaded grey. Intensities have been scaled to align the rising edges. Dashed black lines mark the calculated VDEs (EPT/6-311++G(3df,3pd)) and solid red lines mark the VEEs of the  $S_1$  and  $S_3$  states calculated using SA-CASSCF(14,12)-PT2/cc-pVDZ by Garcia-Prieto *et al.*<sup>42</sup> Taken from Reference 38.

with isomerisation (double-bond rotation) and therefore impact the relaxation pathway following photoexcitation of the chromophore in the gas phase.

### 1.2.6 Effect of solvation

As described in Section 1.2.2, the  $pCA^-$  monoanion exists preferentially as the carboxylate in polar solvents as the localised charge can be more effectively stabilised by surrounding water molecules, whereas the phenolate deprotomer is the more stable deprotomer *in vacuo*.<sup>33,72,73</sup> Absorption spectra for  $pCA^-$  in aqueous solutions of various pH were recorded by Cunha *et al.* and are presented in Figure 1.18.<sup>74</sup> At high pH, it is possible to afford the dianionic species in which both the phenolate and carboxylate ends are deprotonated.<sup>74,75</sup> It is clear from the absorption maxima that the electronic structures differ greatly between the three forms, which is expected due to the vast differences in conjugation.

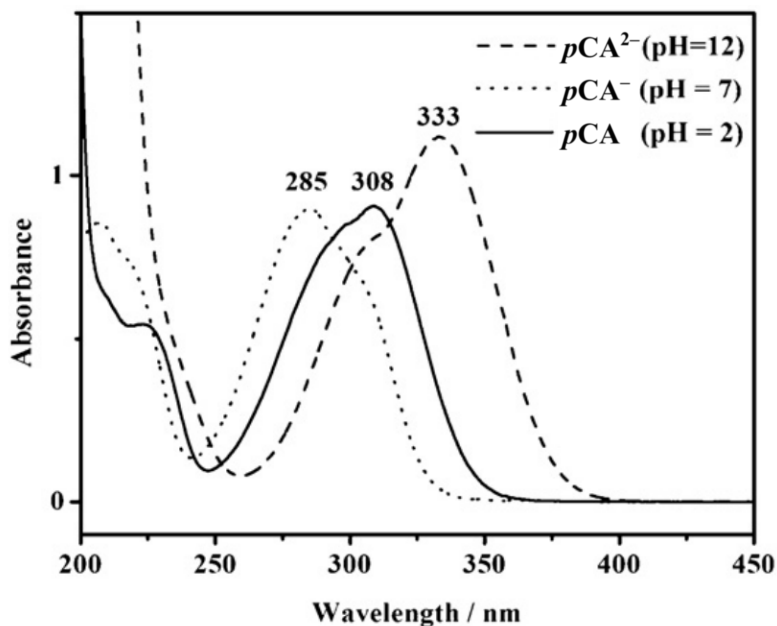


**Figure 1.18:** UV-visible absorption spectra recorded by Cunha *et al.* of *pCA* in aqueous solutions at pH 2, 7 and 12. Absorption maxima of the three solutions are labelled (in nm). Adapted from Reference 74.

Figure 1.19 shows absorption spectra recorded by Rocha-Rinza *et al.* of methylated chromophore analogues, which ensure complete formation of either the phenolate form or the carboxylate form.<sup>33</sup> The  $\lambda_{\max}$  of the carboxylate isomer, labelled **B**, (282 nm) is similar to that of the *pCA*<sup>−</sup> monoanion in aqueous solution (285 nm, Figure 1.18),<sup>74</sup> while the  $\lambda_{\max}$  of the phenolate isomer, labelled **C** (or *pCE*<sup>−</sup>), is 356 nm. Ester analogues of the PYP chromophore, such as *pCE*<sup>−</sup>, are desirable to use in solution studies in order to eliminate ambiguity surrounding which deprotonomer is present and ensure the deprotonation occurs at the phenol site, to best mimic the chromophore in its natural form in PYP.<sup>43,46,49,76,77</sup>

Upon solvation, the  $\lambda_{\max}$  for *pCE*<sup>−</sup> red-shifts significantly from the gas-phase value of 432 nm (Figure 1.14) to 356 nm (in methanol).<sup>34</sup> Garcia-Prieto *et al.* compared the calculated vertical excitation energies to the first three electronically excited states of *pCE*<sup>−</sup> in the gas phase and aqueous solution,<sup>42</sup> as shown in Table 1.1. The main contributions to the character of each transition are also shown and it can be seen that there is significantly more mixing with the  $\pi\pi^*$  states in solution than in the gas phase. Upon solvation, the  $n\pi^*$  state blue-shifts significantly more than the  $\pi\pi^*$  states such that the three electronically excited states reorder in



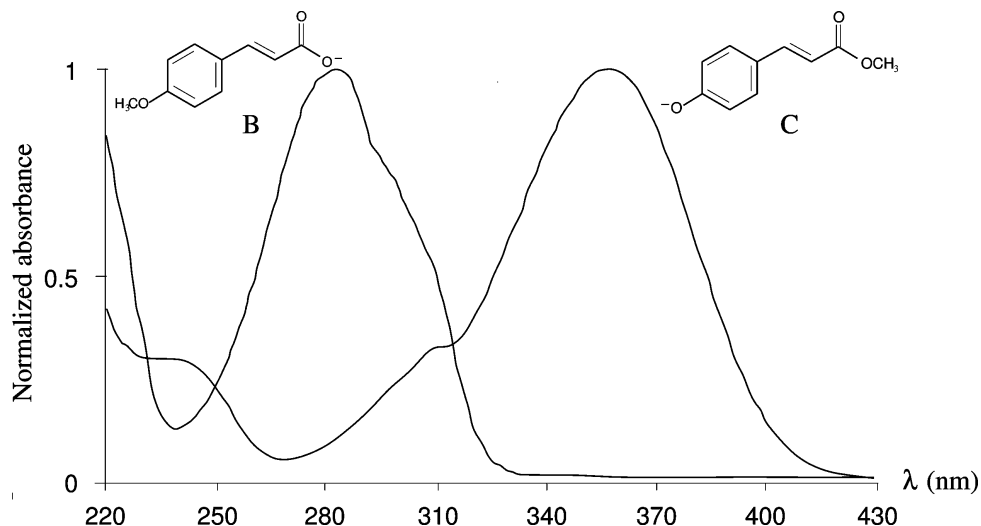


**Figure 1.19:** UV-visible absorption spectra of methylated chromophore analogues as shown by the structures recorded in methanol. Reproduced from Reference 33.

energy. The orbitals of the solvated chromophore are similar to those of the chromophore in the gas phase (Figure 1.15). The  $n\pi^*$  state blue-shifts to such an extent in a polar solvent because the electron density moves from being largely localised at the phenolate oxygen to being much more evenly spread across the chromophore. Conversely, transitions to the  $\pi\pi^*$  states involve excitations between orbitals that share a similar extent of delocalisation in the molecule and hence have much smaller solvatochromic shifts.

		$S_0-S_1$	$S_0-S_2$	$S_0-S_3$
(g)	Character	$\pi\pi_1^*$	$n\pi_1^*$	$\pi\pi_2^*$
	VEE / eV	2.94	3.65	3.81
	Experiment	2.88 <sup>33</sup>		
(aq)	Character	39% $\pi\pi_2^*$ 18% $\pi\pi_1^*$	49% $\pi\pi_1^*$ 13% $\pi\pi_2^*$	76% $n\pi_1^*$
	VEE / eV	3.76	3.81	5.00
	Experiment	3.48-3.54 <sup>33</sup>		
	Osc. strength	0.18	0.60	$\sim 0$
	Solvent shift	-0.05	+0.87	+1.35

**Table 1.1:** SA-CASSCF(14,12)-PT2/cc-pVDZ calculated vertical excitation energies, oscillator strengths and solvent shifts for  $pCE^-$  in the gas (g) and aqueous (aq) phases, adapted from Reference 42.

There have been numerous studies using PYP chromophore analogues in solution

aimed at better understanding the role of the functional group at the carbonyl terminus of the chromophore,<sup>48,77–81</sup> the deprotonation state of the chromophore,<sup>43,49,76,82</sup> the role of specific bond rotations within the chromophore<sup>43,49,77,83</sup> and the properties of the solvent surrounding the chromophore.<sup>76,77,81,84</sup> Chagenet-Barret and coworkers used transient absorption spectroscopy on PYP chromophore analogues including the dianion  $pCA^{2-}$  as well as monoanionic analogues with amide, ketone and phenyl-thioester functionalities.<sup>77,79–81</sup> The authors reported a strong dependence on electron accepting properties of the functionality at the carbonyl tail of the chromophore. For weakly electron accepting groups like the dianion or amide, evidence was found for the production of the *cis* product after  $\sim 10$  ps but no detectable intermediates were found. Whereas with strongly electron accepting groups like the thioester analogue, the authors found evidence for an intermediate state that preferably relaxes back to the *trans* ground state on timescales of  $\sim 1$  ps. This led to the suggestion that the native chromophore in PYP, similar to the thioester studied, successfully isomerises as the positively-charged neighbouring Arg52 residue counteracts the large photoinduced charge shift. However, later work by Stahl *et al.* found little difference in photoisomerisation yields between native PYP and a mutant PYP with the Arg52 residue exchanged for a neutral Alanine residue.<sup>51</sup> Several groups have compared the non-radiative relaxation of neutral chromophores and their deprotonated anionic counterparts to report that the anionic chromophores relax *via* an isomerisation involving mainly the double bond while the neutral chromophores undergo a relaxation mechanism with both double and single bond rotations.<sup>49,76</sup> Many groups have employed various solvents to study the effect of viscosity and polarity on the relaxation pathways and isomerisation coordinate because the viscosity hinders the nuclear motions necessary for isomerisation and solvent polarity effects the charge distribution in the electronically excited state.<sup>76</sup> Solvent properties can make dramatic differences to the photophysical behaviour of the chromophore; one study reported that for  $pCK^-$ , a chromophore analogue that cannot photoisomerise in aqueous solutions, can in decanol (a very viscous solvent with low polarity).<sup>84</sup> Hence, it is interesting to consider both perturbation of the internal structure of the chromophore as well as its surrounding environment when studying the relaxation

dynamics of PYP chromophores in solution.

There has been relatively little exploration of the effect of solvation on the VDE of the PYP chromophore. Due to its anionic nature, it will be much more stable in aqueous solvent than in the gas phase and hence require more energy to remove an electron. In the gas phase, the detachment threshold is so low that many of the excited states lie above the detachment continuum and so autodetachment occurs readily following photoexcitation of these excited states. Whereas, in aqueous solution, the detachment threshold is likely to blue-shift to a much greater extent than the excitation energies and so the electronically excited states will be more stable with respect to detachment. Hence, the UV photoelectron spectrum of the PYP chromophore in aqueous solution is expected to involve multiphoton processes in order to surpass the detachment barrier.

Several transient absorption spectroscopy studies on PYP and isolated PYP chromophores in solution have found evidence for the production of solvated electrons.<sup>44,63–65,79,80,85,86</sup> Electron ejection was proposed to occur *via* a two-photon ( $\sim 400$  nm) process: first a ground state absorption into the first electronically excited state and then an excited state absorption. Zhu *et al.* studied this photoionisation process in PYP in greater detail.<sup>63</sup> The authors found evidence to suggest that electron ejects to a distance of  $\sim 3$  Å from the ionisation point and geminate electron-radical recombination then occurs at a distance of  $\sim 2$  Å and is controlled by diffusion, similar to that of hydrated electrons in water.

Gromov *et al.* calculated the detachment threshold for  $pCT^-$  (Figure 1.16) and the  $pCT^- \cdot (H_2O)_2$  complex in the gas phase using EPT with the aug-cc-pVDZ basis set.<sup>45</sup> The authors found that the addition of two water molecules blue-shifted the detachment energy from 2.90 eV to 3.58 eV. Similarly, Zuev *et al.* calculated the VDEs of the two deprotonomers of isolated  $pCA^-$  and when complexed with two water molecules ( $pCA^- \cdot (H_2O)_2$ ) in various conformations at the EOM-IP-CCSD/6-31+G\* level.<sup>72</sup> They reported blue-shifts of  $\sim 0.4$  - 0.8 eV on the inclusion of the two water molecules. The authors also reported VEEs calculated using EOM-EE-CCSD/6-31+G\* and found that the first electronically excited state was bound with respect to the first detachment continuum. Microsolvation studies such as these pro-

vide a gradual step towards solvation; with extrapolation, these blue-shifts serve as an indication of how dramatic the blue-shift may extend to in a bulk environment. Microsolvation models are also useful to investigate the effects of local hydrogen bonding with a relatively small system, perhaps modelling an environment similar to that within the protein pocket, and hence have been used to study the photoisomerisation mechanism in great detail.<sup>87–90</sup>

## 1.3 Summary

This chapter has outlined how photoelectron spectroscopy may be used to determine the electronic structure and relaxation dynamics of a biological chromophore anion in the gas phase. Studying isolated chromophores in the gas phase enables us to determine the intrinsic properties of the isolated chromophore and hence develop our understanding of the complete protein. A background into the photoactive yellow protein was also given, a photoactive protein that has an anionic chromophore within it which undergoes a *trans-cis* photoisomerisation following the absorption of blue light. This small-scale nuclear motion propagates to large-scale structural changes and the protein unfolds partially. The process is reversible and briefly describes the stages of the photocycle of PYP. The initial photoisomerisation step and the role of the protein in guiding the photocycle is not completely understood. While various groups have studied analogues of the PYP chromophore in solution, there are many factors such as the choice of analogue and solvent that make comparisons difficult. Hence, studying the isolated chromophores in the gas phase using photoelectron spectroscopy would be useful in affording a direct comparison between various chromophore structures. Moreover, such gas-phase experiments are useful as a comparison to experiments of the PYP chromophore in solution and so could help solve many of the open questions about the production of solvated electrons observed in spectroscopy measurements of PYP chromophores in solution.

The PYP chromophore is the molecule of focus for this thesis and Chapters 4 and 5 detail photoelectron spectroscopy studies using rotation-locked analogues of the chromophore. Chapters 6 and 7 then detail a protocol for calculating elec-

tronic structures of organic chromophores in aqueous solution at room temperature, ultimately describing such an approach for the PYP chromophore.

The next chapter outlines the key components of the anion photoelectron spectrometer used for the work presented in this thesis. Accurate quantum chemistry calculations were used to help analyse the spectra and a background into the methods used and how these could be extended to accommodate solvent will be covered in greater detail in Chapter 3.

# Chapter 2

## Experimental methods

This chapter provides a detailed description of the anion photoelectron spectrometer used to record the spectra presented in Chapters 4 and 5. The anions are produced with an electrospray anion source (Section 2.1), mass selected and collected in an ion trap, as described in Section 2.2. The pulsed anion beam interacts with laser light sources described in Section 2.5 and the photoelectrons are detected using velocity map imaging as described in Section 2.3. The three-dimensional distribution of initial electron velocities is recovered from a two-dimensional projection as described in Section 2.4 and the calibration methods used to obtain photoelectron spectra in energy are detailed in 2.7.

A schematic diagram of the anion photoelectron spectrometer apparatus is provided in Figure 2.1. The instrument was built from a modified Waters quadrupole time of flight (Q-TOF) mass spectrometer with the reflectron TOF removed and replaced with photoelectron velocity map imaging optics and with the hexapole collision cell converted to an ion trap.<sup>91</sup> Anions are produced using electrospray ionisation, mass-selected using a quadrupole mass selector, collected in a linear hexapole ion trap where they are thermalised by colliding with He or Ar gas before reaching the interaction region. The anions interact with a laser beam and photoelectrons are detected using a collinear velocity map imaging detector.

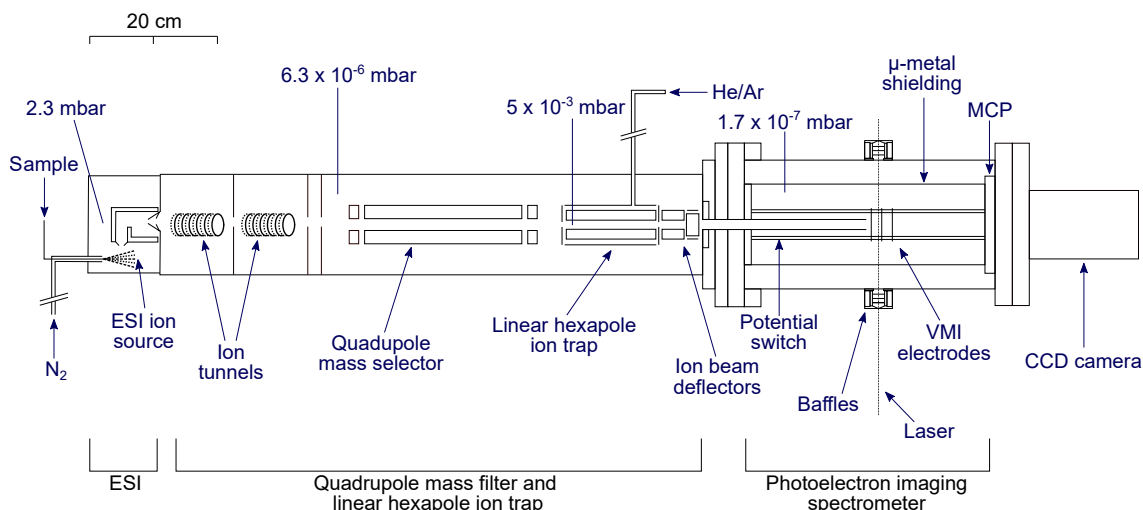


**Figure 2.1:** Schematic diagram of the electrospray ionisation (ESI) and photoelectron imaging apparatus. Not shown is a liquid N<sub>2</sub> cold trap which is positioned above the VMI electrodes, outside the  $\mu$ -metal shielding. Adapted from Reference 92.

## 2.1 Electrospray anion source

Electrospray ionisation (ESI) is a convenient technique that uses an electric charge to disperse a liquid to form isolated ions in the gas phase.<sup>93</sup> ESI is widely used in mass spectrometry and differs from alternative ion sources in that it may be used to produce multiply charged ions and is a soft ionisation technique as the ions are produced near room temperature and atmospheric pressure. Thus, fragmentation is less likely to occur which is attractive for the study of large biological molecules, such as proteins.<sup>94–96</sup>

Figure 2.2 illustrates the main stages of electrospray ionisation for the production of isolated anions. The analyte solution is expelled out of a high-voltage capillary at a rate of 1–20  $\mu$ L/min.<sup>97</sup> The charge at the capillary surface repels and the counter electrode attracts negatively charged ions, separating the charges in solution and producing a Taylor cone at the capillary tip.<sup>98</sup> A charged droplet separates off as the Coulombic repulsion between the charges at the surface equates to the surface tension of the solution. As the droplets travel towards the counter electrode, solvent evaporates leaving bare anions. There are two major mechanisms accepted for this process. The droplets fragment to increasingly smaller droplets as the charge density increases with solvent evaporation. Alternatively, once sufficient solvent

has evaporated, the charge density is high enough to cause a Coulomb explosion, ejecting the ions from the droplets.<sup>99</sup> The same ESI technique may be used to produce isolated cations with reversed polarity voltage applied across the capillary and counter electrode. Desolvation in ESI is often assisted with a nebulising and desolvation gas propelling coaxially with the capillary tip, not shown in Figure 2.2.

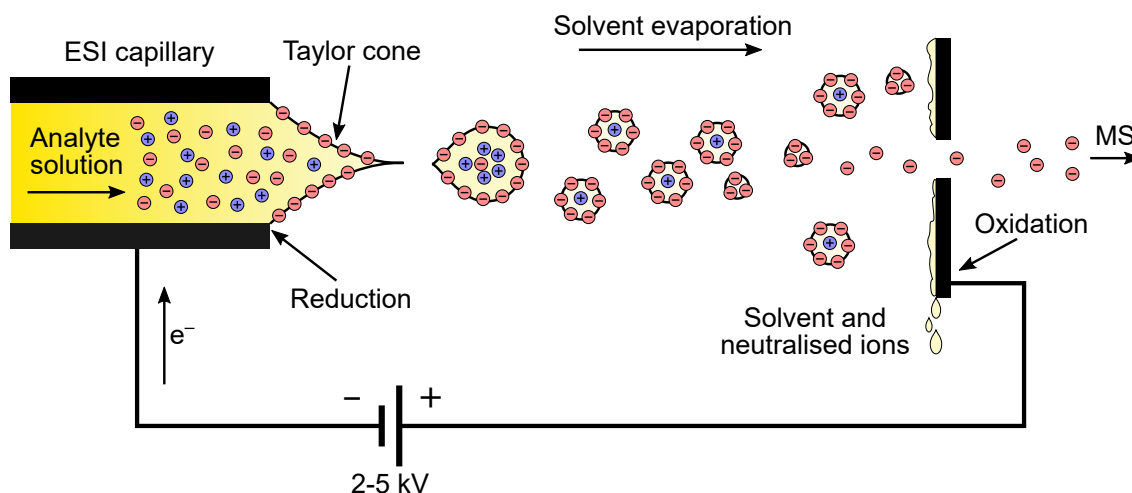


**Figure 2.2:** Schematic diagram of the electrospray ionisation process in negative mode. The analyte solution is pushed through a capillary held at high voltage, a Taylor cone is formed at the tip of the capillary with excess negative charge at the surface. Charged droplets are produced and travel towards the counter electrode and as the solvent evaporates, the droplets become smaller before leaving the naked analyte anions which then travel in to a mass spectrometer (MS).

For the experiments described in this thesis, analyte solutions were prepared in methanol at concentrations of  $\sim 1$  mM and a few drops of concentrated ammonia were added to encourage deprotonation. The solutions were sprayed from a syringe-pumped metal capillary maintained at high voltage (3-3.5 kV) *via* polyether ether ketone tubing, producing a continuous stream of anions. Solvent evaporation is assisted by a flow of heated nitrogen gas, typical in a standard z-spray ESI interface<sup>100</sup> (Figure 2.1). The sample and desolvation gas flow rates and the temperature and voltage of the capillary tip were optimised to give the most intense and stable ion beam, measured following mass selection at the detector. In our experiments, electrospray conditions were altered slightly from those used in prior work within the group<sup>37,38</sup> for the various PYP chromophore analogues. In the experiments presented in this thesis, optimal conditions were found with the capillary tip held at



voltages of 3-3.5 kV and a temperature of 180°C. Flow rates at the nebulising and desolvation N<sub>2</sub> gas outlets were typically < 150 L/hr and ~ 200 L/hr, respectively. The anions travel into the differentially-pumped vacuum chamber and are guided by radio frequency ion tunnels into the quadrupole mass filter (QMF).

## 2.2 Mass-selection and ion accumulation

The QMF is composed of four parallel cylindrical metal rods and each opposing rod pair is connected together with an applied radio frequency voltage (Figure 2.3).<sup>101</sup> For example, the electrodes in the  $xz$  plane have a positive direct current (DC) voltage bias applied,  $U$ . The electrodes in the  $yz$  plane have a negative DC bias applied,  $-U$ . With the DC potentials alone the anions entering the mass-filter would simply hit the positive electrodes, regardless of the mass of the anion. An additional oscillating radio-frequency (RF) voltage is applied to the electrodes ( $V\cos(\omega t)$ ) with amplitude  $V$ , angular frequency  $\omega$  over time  $t$  such that the two pairs of electrodes have waveforms completely out of phase. The oscillating field produced within the mass filter then focusses the ions or rejects ions from the centre axis depending on the mass-charge ratio of the ions, given particular voltages  $U$  and  $V$  as well as the radiofrequency of the oscillating potential,  $f$  (where  $\omega = 2\pi f$ ).

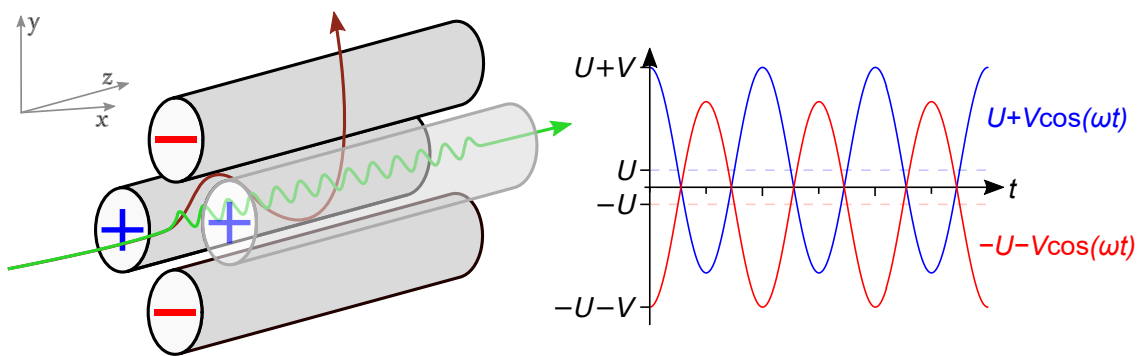


**Figure 2.3:** Left: simple cartoon illustrating the coordination of the applied voltages in the quadrupole mass filter with example trajectories of ions that have the selected mass-charge ratio (green) and an ion that is filtered out (maroon). Right: graphical representation of the voltages applied to the two pairs of electrodes where  $U$  is the DC voltage,  $V$  is the RF voltage waveform amplitude,  $\omega$  is the RF angular frequency and  $t$  is time.

Movement of the ions is not coupled between the  $xz$  and  $yz$  planes and so one

may consider the fields in the two planes independently. First, consider only the negative electrode pair, in the  $yz$  plane, with a singly-charged anion entering the scheme. If the anion is heavy (or the RF oscillation frequency is high), the ion will tend to be affected by the average potential, *i.e.* the DC voltage  $-U$  and so the anion remains close to the centre axis as it is equally repelled by each electrode. If the anion is light in mass (or the RF oscillation frequency is low), the ion will deviate from the centre axis as it is more sensitive to the defocusing RF voltage and steer into an electrode. The speed with which the ions can respond to the defocusing action provided by the transient attractive potentials (when  $-U - V\cos(\omega t) > 0$ ) is what determines the stability of the anion travelling in the  $yz$  plane. Hence, any ions with sufficient mass-charge successfully transmit through the field and so these negative electrodes filter out any anions with mass-charge below a certain value and act as a high mass filter. Now consider a singly-charged anion travelling in the  $xz$  plane between the positive electrodes. If the anion is heavy, the anion will tend to be more affected by the average potential,  $U$ . In this case, the DC voltage destabilises the anion and so heavier anions will intersect the electrodes. If the anion is light, it is more sensitive to the steering of the oscillating RF field and the transient repulsive potentials (when  $U + V\cos(\omega t) < 0$ ) focus the anion toward the centre axis. Hence, the positive pair of electrodes act as a low mass filter by rejecting anions with mass-charge ratios above a particular value. Therefore, the full quadrupole may filter a narrow band of mass-charge ratios in which there is mutual stability in both of the orthogonal planes.

The equations of motion for an anion in a quadrupole may be written in terms of the anion charge ( $Z$ ), the anion mass ( $m$ ) and the distance from the centre axis to an electrode surface ( $r_0$ ) as the following.

$$\frac{d^2x}{dt^2} + \frac{Zx}{mr_0^2} [U + V\cos(\omega t)] = 0 \quad (2.1)$$

$$\frac{d^2y}{dt^2} - \frac{Zy}{mr_0^2} [U + V\cos(\omega t)] = 0 \quad (2.2)$$

$$\frac{d^2z}{dt^2} = 0 \quad (2.3)$$

If we define parameters  $a$ ,  $q$  and  $\xi$  such that

$$a = \frac{4ZU}{\omega r_0^2 m}, \quad q = \frac{2ZV}{\omega r_0^2 m} \quad \text{and} \quad \xi = \frac{\omega t}{2} \quad (2.4)$$

the equations of motion may be rewritten as the following.

$$\frac{d^2 x}{d\xi^2} + [a + 2q \cos(2\xi)] x = 0 \quad (2.5)$$

$$\frac{d^2 y}{d\xi^2} - [a + 2q \cos(2\xi)] y = 0 \quad (2.6)$$

These equations are in the form of a canonical Mathieu's differential equation, which have either bounded or unbounded solutions.<sup>102,103</sup> Bounded solutions correspond to movement in  $x$  or  $y$  being finite and in regard of the quadrupole mass filter, these describe stable ion trajectories. In contrast, unbounded solutions correspond to ever-increasing displacement from the centre axis and so describe unstable trajectories of ions in the quadrupole. Stable solutions depend only on parameters  $a$  and  $q$  and there are various regions of  $a$ - $q$  space that correspond to stable solutions, as shown in Figure 2.4. Hence, the complex six-parameter problem is simplified into these two-parameter equations.

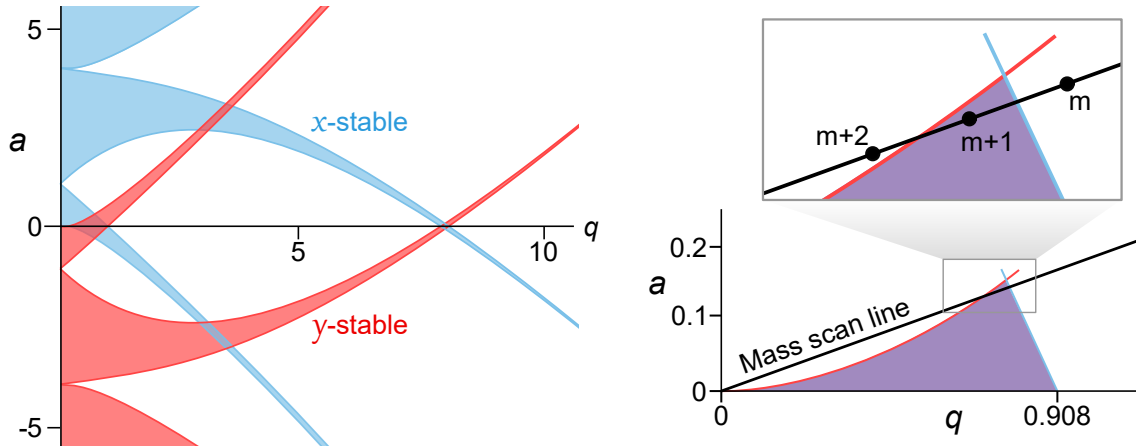


**Figure 2.4:** Left:  $a$ - $q$  stability diagram providing regions of  $a$  -  $q$  space that satisfy the Mathieu equations with finite solutions in  $x$  (blue) and  $y$  (red). Right: ion stability region with the lowest values of  $a$  and  $q$  (bottom) and the bandpass region (top). With three ions of equal charge but differing mass ( $m$ ,  $m + 1$  and  $m + 2$ ), a one amu width filter selects only the  $m + 1$  ions given  $\omega$ ,  $U$  and  $V$  remain fixed.

In practice, mass quadrupoles are operated with a constant  $a/q$  ratio which is equivalent to  $2U/V$  and so is established by always applying the DC potential as a fraction of the RF amplitude. In  $a-q$  space, the operation of the mass filter samples along a straight line with a zero intercept and a slope given by  $a/q = 2U/V$ , termed the mass scan line (Figure 2.4). If we consider a system in which  $Z$ ,  $\omega$ ,  $U$  and  $V$  are constant, the mass scan line may be thought of as a number line with discrete mass values lying along it. If the slope of the mass scan line is chosen such that only a small portion of the line falls within the stable boundary, only masses of a particular value will have stable trajectories within the quadrupole and hence narrow bandpass filtering is achieved.

Quadrupole mass analysers are commonly used in small mass spectrometers by scaling  $U$  and  $V$  over time while keeping the  $U/V$  ratio fixed. This sequentially filters ions of specific  $m/Z$  values and hence a mass spectrum is built up (Figure 2.5). As shown, the resolution of the spectrum is dependent on the slope of the mass scan line ( $U/V$  ratio).

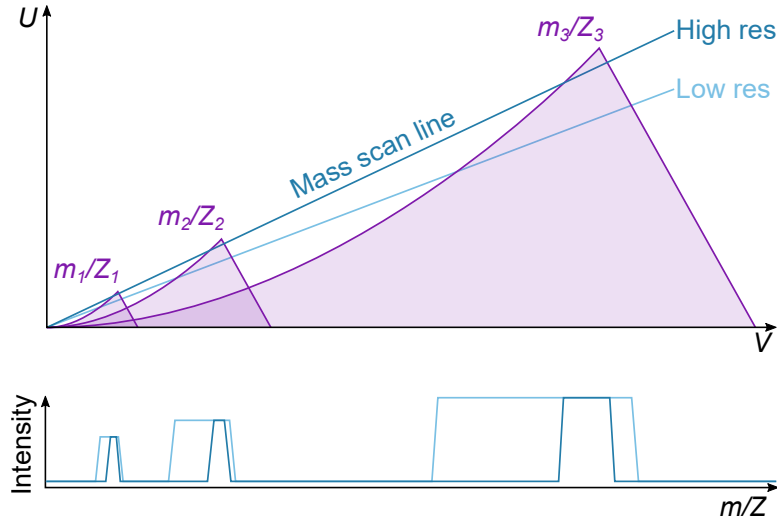


**Figure 2.5:** Schematic stability diagram in  $U - V$  space for three ions with mass-charge ratios with magnitudes such that  $m_1/Z_1 < m_2/Z_2 < m_3/Z_3$ . The shaded areas represent the regions of  $a - q$  space that satisfy Mathieu's differential equation with bound solutions for each of the ions. Two mass scan lines are shown with different slopes (given by  $U/V$ ) that afford high and low resolution mass filtering as shown by the spectra below.

With successful mass-selection, the continuous beam of ions enters a linear hexapole ion trap which bunches the ions into a pulsed beam, increasing the ion

density at the interaction region where the ions overlap with a pulsed laser beam. The trap consists of six parallel rods connected to a RF voltage supply (Figure 2.6). The rods are contained within an aluminium cylindrical sleeve with stainless steel entrance and exit lenses at either end of the trap (each with apertures  $\varnothing$  3 mm). There is a gas-inlet behind the entrance lens that allows the cell to be filled with a collision gas which thermalises the ions to room temperature. Ar or He were used as collision gases at pressures of  $\sim 10^{-5}$  mbar.

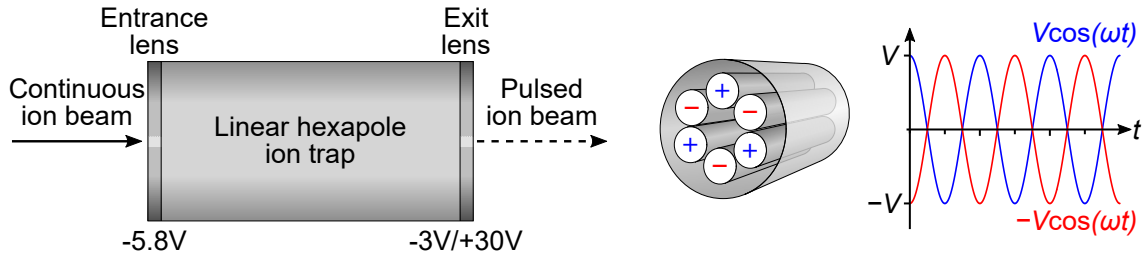


**Figure 2.6:** Left: schematic diagram of the ion trap consisting of a hexapole RF ion guide contained within an aluminium cylindrical sleeve capped with stainless steel entrance and exit lenses (each with apertures of 3 mm). Middle: electrode arrangement within the hexapole ion trap indicating the relative polarities of each electrode. Right: RF voltages applied to the electrodes within the hexapole.

Unlike the quadrupole mass filter described above, the equations that describe the ion motion in a hexapole contain cross-coordinate terms and so cannot be decoupled in  $x$  and  $y$ . This makes hexapole fields much more complex to describe mathematically. For a quadrupole linear ion trap, the ions are successfully trapped radially according to the solutions in  $a$ - $q$  space where  $U = a = 0$  (Figure 2.4) and the critical  $q$  value of 0.908 provides a distinct boundary for mass filtering. For a linear hexapole ion trap, there is not a clear boundary at the critical  $q$  value and so hexapole traps are able to contain ions with a wide range of mass-charge ratios. The hexapole electrodes confine the ions radially and a static potential is applied to the entrance and exit lenses to confine the ions axially. This creates a potential well along the axis of the trap, confining the ions in a linear arrangement.

Singly-charged ions enter the trap with a kinetic energy of 6.2 eV and most of this energy is removed by applying a voltage of -5.8 eV to the entrance lens (Figure 2.7). During ion accumulation in the trap, the exit lens is maintained at a voltage

of  $-3$  V which is sufficient to prevent ion leakage at either aperture. The ions are accumulated and held in the trap for approximately the interval of the repetition rate of the instrument (determined by the laser system, see Section 2.5). After exiting the trap, the ions travel into the photoelectron imaging spectrometer section of the apparatus (Figure 2.1) through the potential switch. The trap is opened for  $12\text{ }\mu\text{s}$  by increasing the exit lens voltage to  $+30$  V to expel the ions before returning to  $-3$  V for the next trapping cycle.

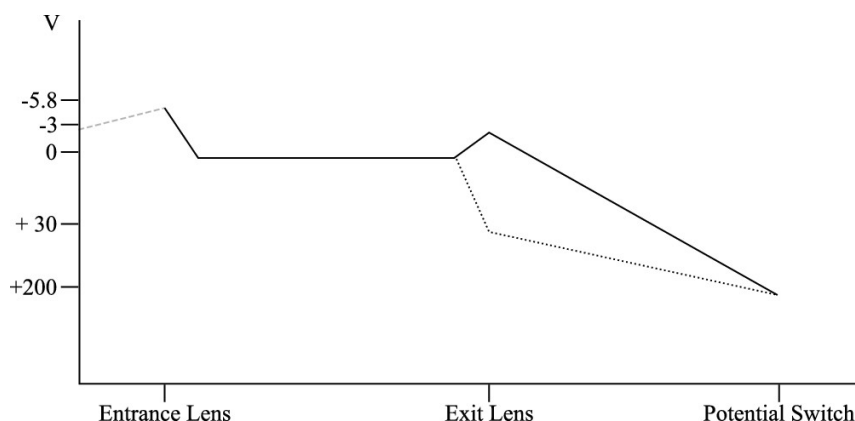


**Figure 2.7:** A schematic of the potentials experienced by the ions as they pass through the linear hexapole ion trap with the potential switch off. Solid lines show the trapping potentials and the dotted lines show the extraction potentials. The dashed line shows the potential experienced by an anion before it enters the linear hexapole ion trap. Plotted on a log scale. Reproduced from Reference 92.

## 2.3 Velocity map imaging spectrometer

Velocity map imaging (VMI) detection provides both photoelectron kinetic energy distributions and photoelectron angular distributions (PADs) simultaneously. From eKE distributions, we can determine a great deal of information on electronic and vibrational structure, as described in Section 1.1. The PADs give insight into the symmetry of the orbital from which the photoelectron was emitted, which can be of great value when interpreting spectra with several overlapping features, for example. Alternative photoelectron detection methods such as time-of-flight detection lack this angular information.

Photoelectrons from a single detachment process travel outwards from the in-

teraction region in all directions forming a sphere, termed a Newton sphere. The higher the eKE of the emitted electrons, the larger the radius of the sphere. In an experiment with several detachment processes, with each relating to a different eKE release, concentric spheres of different radii are produced. VMI employs an array of electrodes acting as an electrostatic lens to accelerate the electrons towards a position-sensitive detector (Figure 2.8). With optimised voltages on the electrodes, an inhomogeneous field is produced that allows for velocity-mapping to occur. In velocity-mapping, the Newton sphere(s) of photoelectrons expand and are focussed on to a two dimensional detector such that each electron with the same initial velocity vector maps on to the same point on the detector regardless of where they were emitted, this is shown in Figure 2.9. The resulting two-dimensional image generated is a projection of the original three-dimensional Newton sphere and so inversion is required to reconstruct this three-dimensional distribution (Section 2.4).

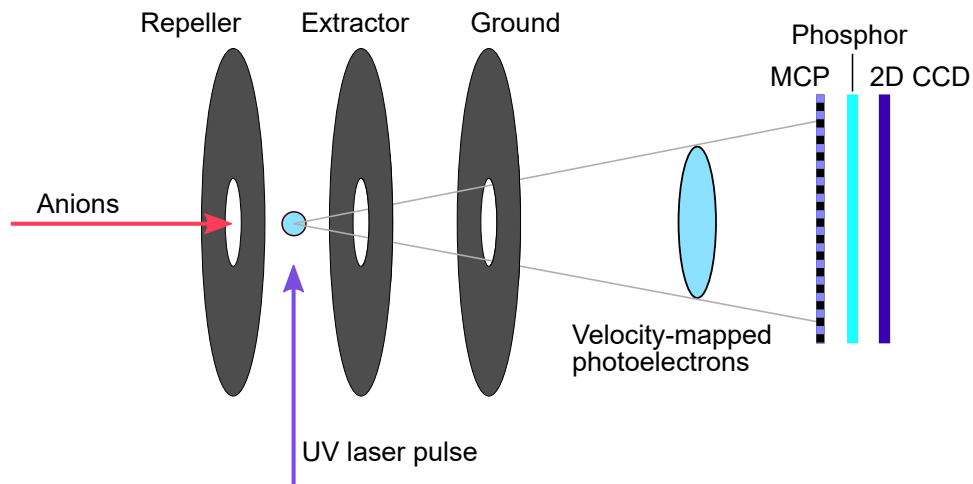


**Figure 2.8:** General structure of a velocity map imaging setup for photoelectron using the Eppink and Parker electrode configuration.<sup>104</sup> (MCP) Microchannel plate and (2D CCD) two-dimensional charge coupled device camera.

In our instrument, the VMI optics consist of three polished parallel field plates, the repeller, extractor and ground, as in the Eppink and Parker design (Figure 2.8).<sup>104</sup> The repeller plate is situated behind the laser interaction region and the anions enter the interaction region through an aperture 15 mm in diameter.<sup>92</sup> The plates are separated by 15 mm and each plate has a diameter of 105 mm with a 15 mm hole at its center. A negative voltage is applied to the repeller plate which

accelerates the photoelectrons towards the detector.

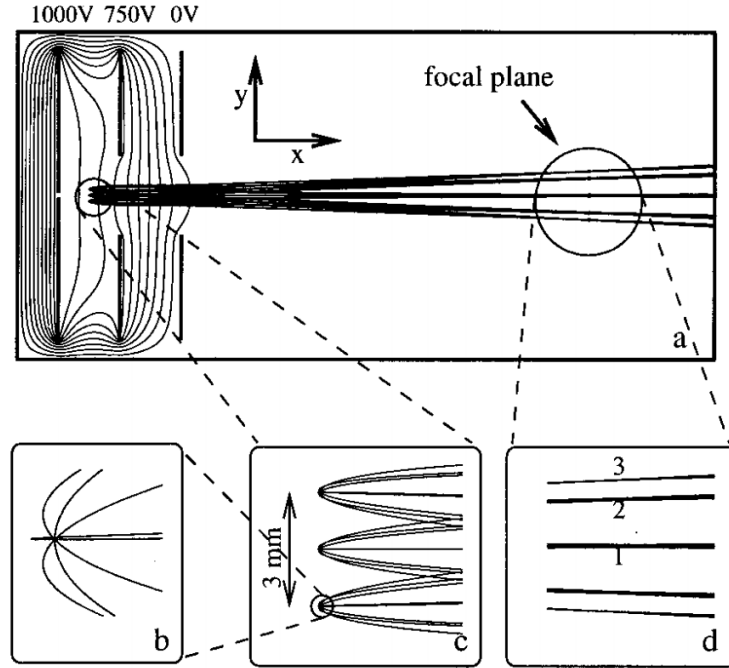


**Figure 2.9:** a. Simulated trajectories of charged particles in an inhomogeneous field generated by three plate electrodes. b. a model spherical distribution formed of 8 particles, each produced with a kinetic energy of 1 eV with an angular spacing of  $45^\circ$ . c. Starting points along a line of length 3 mm modelling the cylindrical shape of the interaction region between a laser beam and the ion packet. d. At the focusing plane (location of the detector), the trajectories of the particles emitted with the same ejection angle converge where 1, 2 and 3 correspond to particles emitted with ejection angles of  $0/180^\circ$  ( $x$ ),  $45/135^\circ$  and  $90^\circ$  ( $y$ ), respectively. Reproduced from Reference 104.

The anions may only overcome the strong negative potential at the repeller plate when the potential switch is on. The potential switch consists of a tube lens of 178 mm length and 10 mm internal diameter and is positioned so that the end of the tube lies within 3 mm of the repeller plate. A voltage supply is connected to the potential switch that allows for the low energy ions leaving the ion trap to enter the VMI optics, Figure 2.10. A voltage is applied to the extractor plate to provide a ratio between the voltages applied to the extractor and repeller plates such that the inhomogeneous field allows for velocity-mapping to occur. In practice this ratio was  $\sim 0.7$  and to calibrate the voltages for the best focusing at the detector, only the extractor voltage was altered while the other voltages were left fixed. The focusing was tested by recording a spectrum using iodide and finding the extractor voltage



that gave the narrowest peak (smallest FWHM) in the photoelectron spectrum. After passing through the ground electrode, the photoelectrons travel through a field-free region before hitting the detector. As shown in Figure 2.1, the interaction region, VMI optics and detector are surrounded by a  $\mu$ -metal shield. This acts to protect the spectrometer from stray magnetic fields that could deflect the electron trajectories.

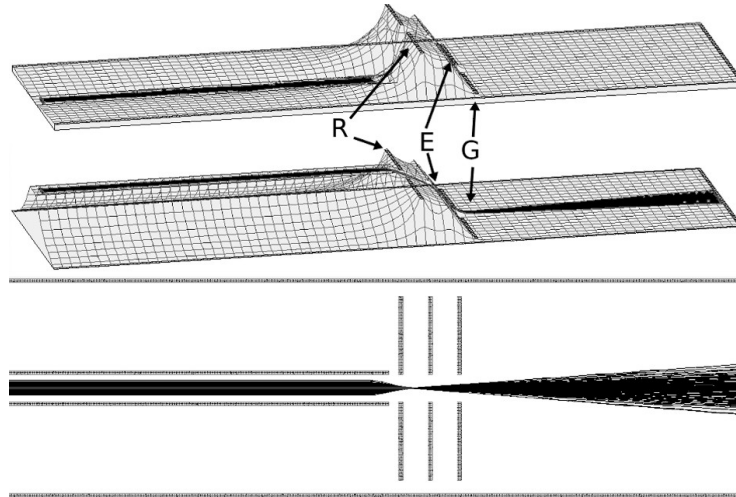


**Figure 2.10:** Simulated ion trajectories (SIMION) of iodide anions in the potential switch and VMI optics. The top and middle show 3D views of the ion trajectories (black) when the potential switch is off (+200 V) and on (-1000 V), respectively. Bottom shows a 2D view of the focussing of the ion beam in the interaction region. Repeller (R), extractor (E) and ground (G) plates are set at -870, -623 and 0 V, respectively. Reproduced from Reference 92.

The position-sensitive detector (Photek, East Sussex, UK) consists of a pair of microchannel plates (MCPs) backed by a phosphor screen and a charge-coupled device camera (CCD) detects the phosphorescent light emitted as the electrons hit the phosphor screen. The images were collected using commercial software (IFS32). An MCP is a thin plate constructed from a highly-resistive material with an array of densely-packed tiny tubes (microchannels). A potential difference is applied between the front and back faces to accelerate the electrons through the channels. The microchannels are angled off normal and so the incoming electrons collide with the inner surface of a microchannel which causes secondary electrons to be emitted which also collide with the channel walls creating an avalanche of electrons and hence amplifying the photoelectron signal at the detector. Using a pair of MCP

plates in tandem amplifies the signal further and readjusts the angle offset as the channels form a chevron shape.

Window baffles are fitted to the entrance and exit windows in the chamber where the laser passes through. These help reduce background signal at the detector from scattered electrons produced as the light passes through the windows. The detector is gated to a 50-75 ns window to minimise the inclusion of photoelectrons from scattered light and also prevent the detection of the much slower ion packet. This was tested by blocking the laser and minimising signal with the timing on the detector gate and in the experiments presented in this thesis, this ion-only signal was negligible. Similarly, the laser-only signal was minimised by blocking the ions entering the VMI optics and realigning the laser. Additionally, the liquid N<sub>2</sub> cold trap above the VMI optics was used to reduce laser-only background signal when necessary. Unlike the ion-only signal, the laser-only signal was often significant, particularly at higher photon energies at which ionisation of residual gas in the chamber or scattering are more prominent. Hence, during all data acquisition, laser-only images were recorded which were subtracted from the overall signal before image reconstruction.

## 2.4 Image reconstruction

The two-dimensional image captured at the detector is a projection of the three-dimensional distribution of photoelectron velocities (Figure 2.11). To obtain the velocities (and hence eKEs) and angular information of the photoelectrons, the three-dimensional distribution needs to be reconstructed. Assuming it has cylindrical symmetry about the laser polarisation axis (here denoted  $z$ ), the three-dimensional distribution may be obtained by performing an inverse Abel transform on the two-dimensional projection<sup>105</sup>

$$R(r, z) = -\frac{1}{\pi} \int_r^\infty \frac{\partial P(x, z)/\partial x}{\sqrt{(x^2 - r^2)}} dx \quad (2.7)$$

Where  $P(x, z)$  describes the intensities in the two-dimensional projection in the plane of the detector  $(x, z)$  and  $r$  denotes the radial coordinate that, along with the

$z$ -coordinate, describes the cylindrically-symmetric three-dimensional distribution,  $R(r, z)$ .

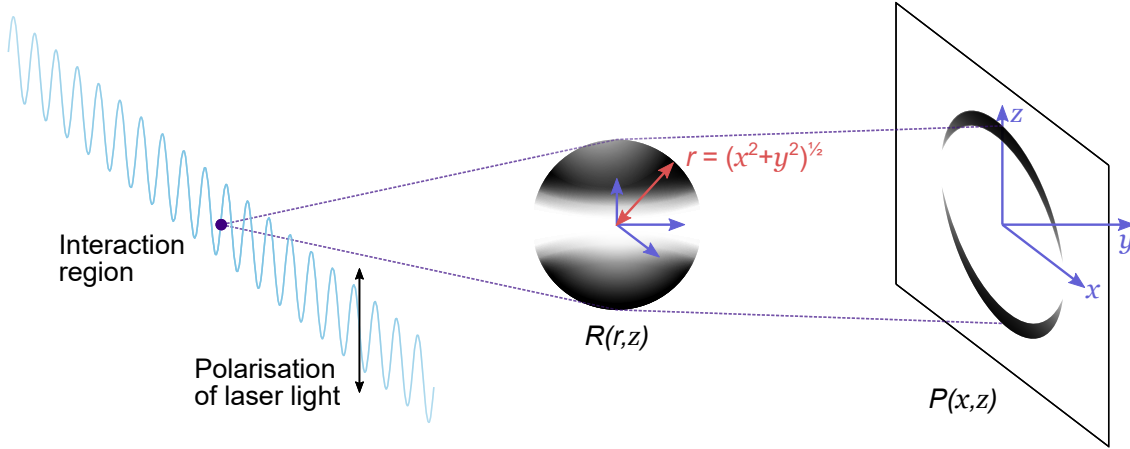


**Figure 2.11:** Schematic diagram of the Abel transform of the photoelectron Newton sphere,  $R(r, z)$ , originating from the interaction region with a UV laser pulse which then maps on to the detector a two-dimensional projection,  $P(x, z)$ .

However, practically this is difficult as there is a singularity point at the lower limit of the integral and the derivative of the projection distribution enhances experimental noise inevitable in any real measurement. In addition, experimentally  $P(x, z)$  is not a continuous function but is measured as an array of intensities at discrete points (pixels on the detector). Hence, smoothing, fitting or blurring of the data is required to employ an inverse Abel transform. There are various approaches available to circumvent the inverse Abel transform and reconstruct the three-dimensional distribution, each with different merits such as computational efficiency or robustness to noise. Early approaches of image inversion in the context of VMI used the Fourier-Hankel method<sup>105,106</sup> which is fast and reliable for near-perfect quality images but leads to the accumulation of noise along the centreline of the reconstructed image for lower quality data and can introduce large negative intensities that are physically meaningless. Onion-peeling<sup>107,108</sup> and back-tracking approaches<sup>109</sup> which involve reconstructing the image from the outside in by calculating the contribution of the most energetic particles and subtracting the contribution to the image for particles of this energy and iterating towards the centre of the image. Such methods are very fast to compute but are susceptible to oversubtracting and still suffer from

the amplification of noise towards the centreline. The iterative correction method first developed by Vrakking iteratively creates a guessed three-dimensional distribution, calculates its two-dimensional projection and compares this to the experimental data.<sup>110</sup> In this method, experimental noise is handled well by comparing the guessed distribution to the real data and so noise accumulates at the origin. However, the approach is very slow to converge and so proper prior information on the three-dimensional distribution is necessary to converge in a reasonable time. In the BASEX method (BASis Set EXpansion), the experimental projection is expanded to fit a set of basis set functions for which the inverse Abel integral can be calculated exactly.<sup>111</sup> The inverted image is found as the linear combination of Abel inverted basis functions with the same expansion coefficients. The calculation of both sets of basis functions are computationally expensive but are calculated and stored on disk prior to image inversion and so at the time of image reconstruction, the calculations are not intensive. BASEX uses functions similar to Gaussian functions in the basis sets defined at the pixel positions in Cartesian space. This method handles general noise better than the Fourier-Hankel or onion peeling approaches but still accumulates noise toward the centreline. pBASEX is an extension on the BASEX method in which the basis functions are in spherical polar coordinate space instead of pixel-orientated Cartesian space.<sup>112</sup> The use of polar coordinates simplifies the basis functions to only include a few (even order) Legendre polynomials to represent the angular distributions. pBASEX is less susceptible to aberrations in Cartesian space at the detector because the polar coordinates are fitted prior to conversion and so noise of this type is smoothed out radially. Similar to the iterative correction method, there is an accumulation of noise at the origin but this is minimal and not often a critical area of experimental interest.

This list is non-exhaustive and development into new algorithms for inverse Abel transforms remains an active area of research some thirty years later.<sup>113–116</sup> In this work, the polar basis set expansion (pBASEX) method is used due to its ability to handle noise, speed and ease of use.<sup>112</sup>

## 2.5 Light sources

In the experiments presented in this thesis, photoelectron spectra were recorded at wavelengths of 310–346 nm (ns pulses) and  $\sim 400$  nm (fs pulses).

Nanosecond laser pulses (duration  $\sim 6$  ns) were produced using the second harmonic of a dye laser (Sirah Cobra-Stretch D-24) pumped by the second harmonic, 532 nm, of a nanosecond Q-switched Nd:YAG laser (Continuum Powerlite Precision II), as shown in Figure 2.12. The Nd:YAG laser operates at a repetition rate of 20 Hz which dictates the repetition rate of the anion photoelectron spectrometer. Within the dye laser, dye solutions of Pyridine 1 and DCM in methanol were used to obtain wavelengths of 692 nm and 660–620 nm, respectively. The light was then doubled using a beta-barium borate (BBO) crystal and the doubled light was isolated from the fundamental using a set of Pellin-Broca prisms. The wavelengths were measured at the exit of the chamber using an interferometer wavelength meter (SNIIMS Type WS). The linewidth of the Sirah dye laser is quoted as  $\sim 0.05$   $\text{cm}^{-1}$  in the wavelength range used, which is less than the detector resolution.

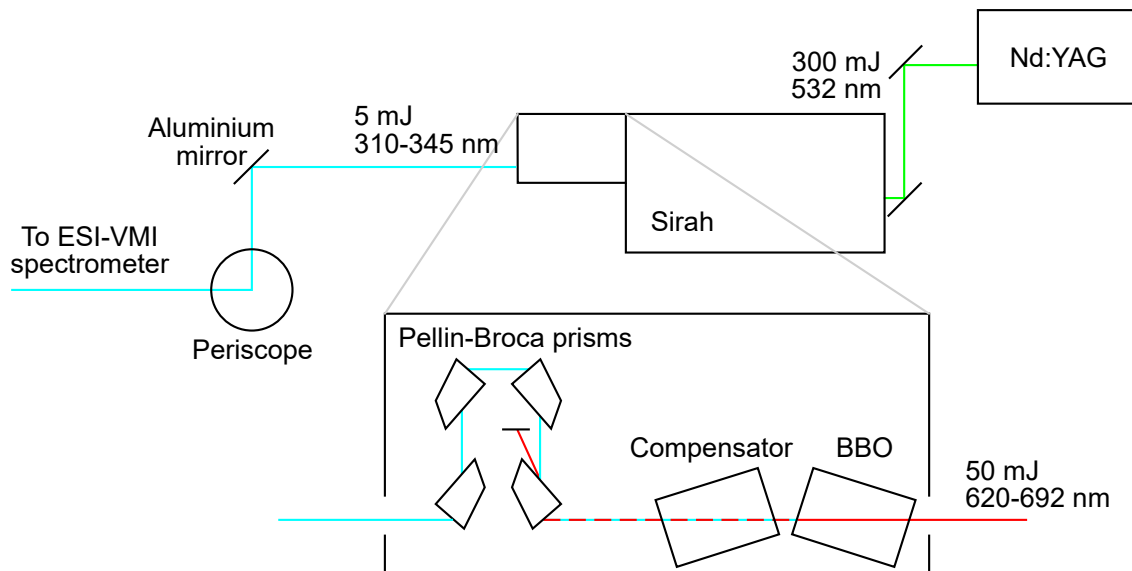


**Figure 2.12:** Schematic diagram of the beam line setup for the production of nanosecond laser pulses of wavelength 310–346 nm. Adapted from Reference 91.

Femtosecond pulses with wavelength centred at  $\sim 400$  nm were produced by frequency-doubling the output of a commercial amplified Ti:sapphire femtosecond laser system (Figure 2.13). Pulses were generated and enter the chamber at 1 kHz

while a synchronisation and delay generator was used so that on every fourth pulse, the anion photoelectron spectrometer was triggered. Hence, the instrument repetition rate was 250 Hz overall when recording spectra at this wavelength. A Ti:sapphire mode-locked oscillator (Coherent Mira), pumped by the second harmonic, 532 nm, of a continuous Nd:YAG (Coherent Verdi) provided an 800 nm seed beam for a Ti:sapphire regenerative amplifier (Coherent Legend). The Legend, pumped by the second harmonic of a Q-switched Nd:YLF (Coherent Evolution), generates high intensity femtosecond pulses of wavelength centred at  $\sim 800$  nm. Passing this through a BBO crystal creates a high intensity beam of short laser pulses ( $\sim 50$  fs) of wavelength  $\sim 400$  nm *via* second harmonic generation.

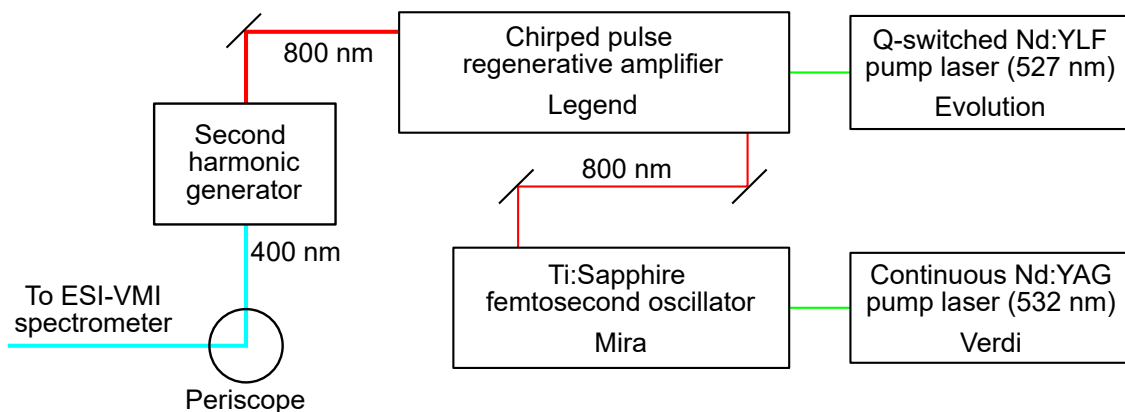


**Figure 2.13:** Schematic diagram of the beam line setup for the production of femtosecond laser pulses of wavelength  $\sim 400$  nm.

## 2.6 Overall operation

### Differential pumping

The full anion photoelectron spectrometer apparatus is comprised of three vacuum chambers; one housing the ESI ion source, another housing the quadrupole mass filter and ion trap and the third chamber housing the potential switch and VMI electrodes (Figure 2.1). Each of the chambers is held at a different pressure, with the ion source at the highest pressure and the spectrometer chamber at the lowest pressure. This is to allow the ESI ion source to spray at conditions close to ambient conditions and to minimise interference between the photoelectrons and background

gas in the VMI spectrometer. The pressure differences between the chambers are maintained by including only a small aperture between the chambers. The ESI chamber is pumped to a pressure of  $\sim 2.3$  mbar by a single scroll pump (Edwards XDS35i). The quadrupole mass filter/ion trap chamber is pumped to a pressure of  $6.3 \times 10^{-6}$  mbar with two 250 L/s turbomolecular pumps connected to the ion tunnels and quadrupole. Each of these turbomolecular pumps is backed by a scroll pump (Edwards XDS35i). The spectrometer chamber is pumped to a pressure of  $1.7 \times 10^{-7}$  mbar by a 1000 L/s turbomolecular pump (Leybold MAG W 1300 C) backed by a scroll pump (Edwards XDS35i).

### Typical voltages used

Typical voltages supplied to the potential switch and VMI electrodes (repeller, extractor and ground) are listed below in Table 2.1 for the detection of ions or electrons. The detection of ions was used to optimise the ESI and ion trap parameters to give a high ion-count that is closely focussed. For the detection of ions, a higher potential switch voltage is applied to overcome the higher potential at the repeller plate required to focus the ions and accelerate them towards the detector. Lower voltages are used for the detection of electrons to expand the Newton sphere more and so improve the resolution of the image at the detector.

	potential switch	extractor	repeller	ground
ions	+200/-1752	1060	1500	0
electrons	+200/-584	350	500	0

**Table 2.1:** Typical voltages applied to the potential switch (off/on) and the each of the VMI electrodes, in V.

Typical voltages applied to the detector are presented in Table 2.2 for the detection of ions or electrons. There are many more ions than photoelectrons present in the instrument and so lower voltages are applied for the detection of ions to protect the MCP from damage.

### Timing

The ion beam is controlled with software running on a PC and a variety of transistor-transistor logic pulses. There are many time delays to consider in order to trap and

	MCP front	MCP rear	phosphor
ions	350	750	4500
electrons	850	1300	5800

**Table 2.2:** Typical voltages applied to the front of the MCP, the rear of the MCP and the phosphor screen, in V.

release the ions effectively, time the potential switch, overlap the ion and laser pulses and time the detector. A DG535 delay generator (Stanford Research) was used as the master trigger to produce a 20 Hz pulse train for the nanosecond laser experiments. Delayed pulses from this master trigger were sent to the imaging electronics and two further DG535 delay generators, one triggering the ion trap and potential switch and the other triggering the nanosecond laser system. Figure 2.14 illustrates the timing sequence for the imaging of iodide ions (black) and photoelectrons (red) where the delay timings are relative to the onset of the ion trap opening. In practice, the master trigger sends a pulse to the laser delay generator (to trigger the flashlight pumping of the nanosecond laser medium) first and then the ion trap signal is sent  $\sim 250$   $\mu$ s later. A more detailed schematic of typical delay times used at each of the three delay generators may be found in Appendix A.1.

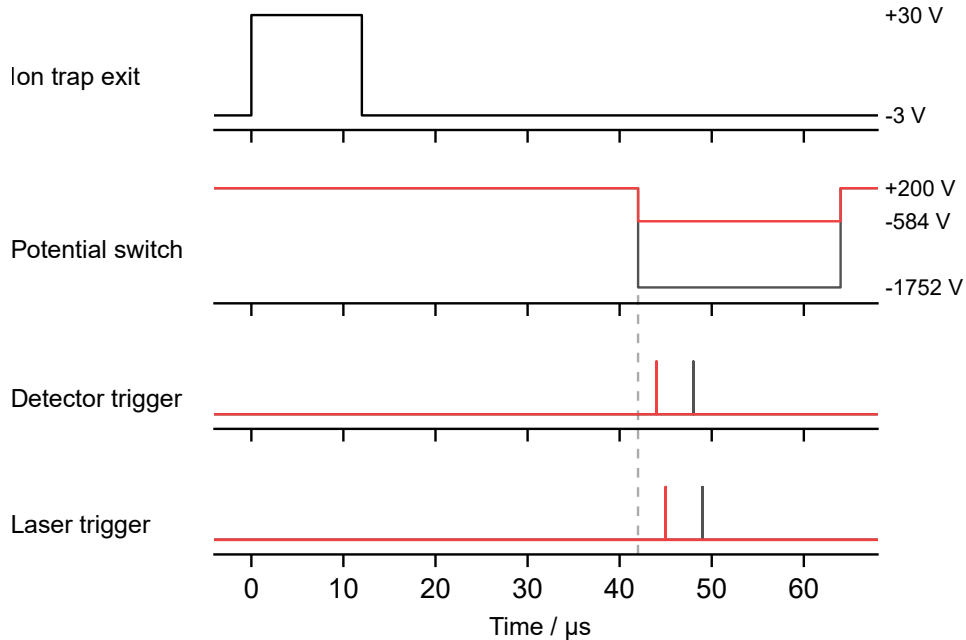


**Figure 2.14:** Schematic diagram of the delay times relative to the opening of the ion trap (0  $\mu$ s) for ion detection (black) and electron detection (red) for iodide.



As discussed in Section 2.2, the ions accumulate in the linear hexapole ion trap until the potential at the exit lens is switched to positive. The trap is open for 12  $\mu\text{s}$  and so ions are accumulated and held within the trap for approximately the remainder of the repetition rate interval. For a 20 Hz experiment, this would be  $50\text{ ms} - 12\text{ }\mu\text{s} = 49.988\text{ ms}$ . Following the ion trap, there is a delay before the potential switch is on and for iodide ions (Figure 2.14), this is 22  $\mu\text{s}$ . The potential switch is then turned on (voltage switched to negative) for 20  $\mu\text{s}$ , in which time the detector and laser are triggered. The potential switch voltages differ for the detection of electrons or anions as described in Table 2.1. The delay between the onset of the potential switch turning on to the camera trigger (here 2  $\mu\text{s}$  for electrons and 6  $\mu\text{s}$  for ions) is adjusted in order to overlap the camera window with the pulse of ions/photoelectrons. Likewise, the trigger to the laser is finely adjusted in order to find the best overlap of the ion and laser pulses at the interaction region. For other ion species, the time of flight of the ions will vary and hence the delays are adjusted for each molecule. The camera window is 50-75 ns to ensure that the photoelectron spectra have minimal ion signal.

## 2.7 Calibration of the spectrometer

The instrument is highly-sensitive to minute changes in experimental geometry such as laser alignment and VMI voltages. Hence, the instrument was calibrated daily or after any changes were made before a sample acquisition session. The velocity of a photoelectron is directly proportional to the distance between its position on the detector and the centre of the image ( $N$ , given in pixels). Therefore, the kinetic energy scales linearly with  $N^2$

$$v \propto N \Rightarrow eKE = \frac{1}{2}mv^2 = aN^2 \quad (2.8)$$

Where  $a$  is an experimentally determined calibration factor. The absolute uncertainty in  $N$  is constant across the detector ( $\Delta N = \pm 0.5\text{ pix}$ ) and hence the absolute uncertainty in velocity is also independent of the position on the detector. However, the energy width  $\Delta E$  scales linearly with  $N$ :

$$\Delta E = \frac{dE}{dN} \Delta N = 2aN\Delta N \quad (2.9)$$

Conversely, the relative error (or resolution) in velocity,  $\Delta v/v$  scales with  $1/N$ , while the energy resolution scales with  $2/N$ :

$$\frac{\Delta E}{E} = \frac{2aN\Delta N}{aN^2} = 2\frac{\Delta N}{N} \quad (2.10)$$

Hence, the energy resolution is better at positions on the detector further from the centre of the image. Therefore, it is best to calibrate with the visible circle of largest radius in the two-dimensional image.

To calibrate, a photoelectron image is recorded using a species with a well-defined photodetachment energy. Here, spectra were calibrated using the lowest energy electron detachment process in the photoelectron spectrum of iodide<sup>117</sup> (310–346 nm), deprotonated indole<sup>118</sup> (397.85 nm) or *p*HBDI<sup>-119</sup> (400 nm) and the calibration method used in each case is largely the same. For an iodide calibration, the lowest energy detachment transition is to the  $^2P_{3/2}$  state and is well-defined as 3.059 eV.<sup>117</sup> This transition shows as an atomically-sharp peak at the maximum intensity in the velocity spectrum (Figure 2.15). Before inversion, the centre position is found by fitting a circle to a ring within the image. To ensure the best centre position is found, many inversion attempts are made with different coordinates for the centre and the position that affords the smallest full-width half maximum of the peak is chosen. The calibration factor  $a$  (with units eV/pix<sup>2</sup>) may be determined using the following relationship.

$$eKE = h\nu - eBE = aN^2 \Rightarrow aN_{\text{peak}}^2 = h\nu - 3.059 \quad (2.11)$$

The value of  $a$  is then used to calibrate the sample spectra to an eKE scale. To preserve the total integrated signal in the eKE spectra following the conversion from pixels to eV, a Jacobian factor of  $1/2aN$  is applied to the intensities to account for the  $N \rightarrow N^2$  mapping. *i.e.* for  $eKE = \epsilon = aN^2$ .

$$\int_0^\infty y(N) dN = \int_0^\infty y(\epsilon) \frac{dN}{d\epsilon} d\epsilon = \int_0^\infty y(\epsilon) \frac{1}{2aN} d\epsilon \quad (2.12)$$

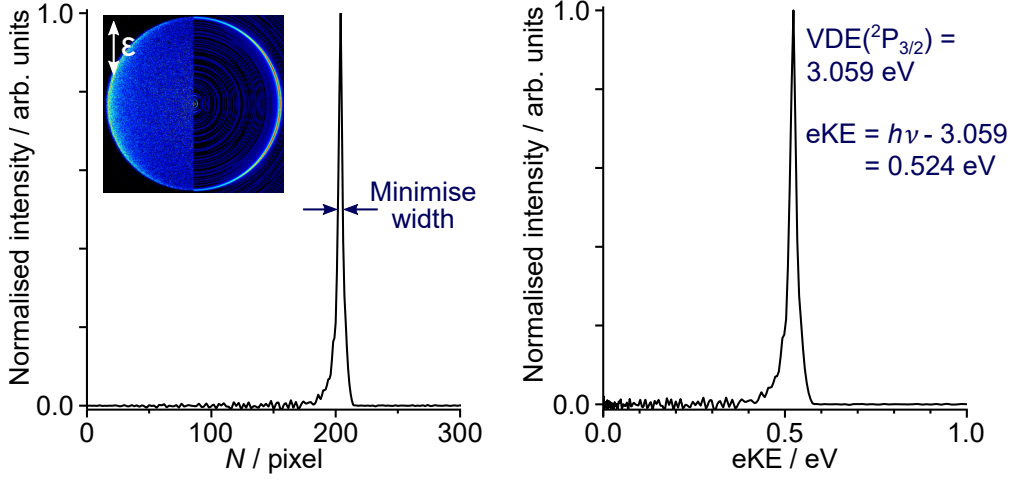


**Figure 2.15:** Left inset: Raw (left half) and inverted (right half) VMI images with the polarisation of the laser light shown by  $\epsilon$ . Left: Velocity spectrum. Right: eKE spectrum of iodide. All data shown here were measured at 346 nm.

The full-width half maximum of the iodide peak is used to determine the energy resolution ( $\Delta E/E < 5\%$ ). To calibrate the instrument for wavelengths  $\sim 400$  nm, iodide would not be appropriate to use as the photon energy is close to the detachment energy affording only very low eKE photoelectrons (eKE  $\sim 0.05$ ) eV and so very low resolutions as the intensity would be at the centre of the image. In the earlier experiments in this thesis,  $p\text{HBDI}^-$  was used to calibrate at 400 nm and later measurements used the much more resolved spectrum of indole. Calibrating the instrument with indole follows a similar approach to iodide (Figure 2.16).

For calibrations using  $p\text{HBDI}^-$ , the centre of the image was found in the same way by iteratively choosing different positions and selecting the position that gave the narrowest peak. To calibrate into energy space, the 400 nm spectrum was plotted in eBE space (as  $h\nu - aN^2$ ) and the calibration factor  $a$  was scaled to fit the rising edge of the 346 nm spectrum of  $p\text{HBDI}^-$ <sup>120</sup> (Figure 2.17). For the data recorded at wavelengths  $\sim 400$  nm, using a femtosecond laser, the energy resolution,  $\Delta E/E$ , is around 14%.

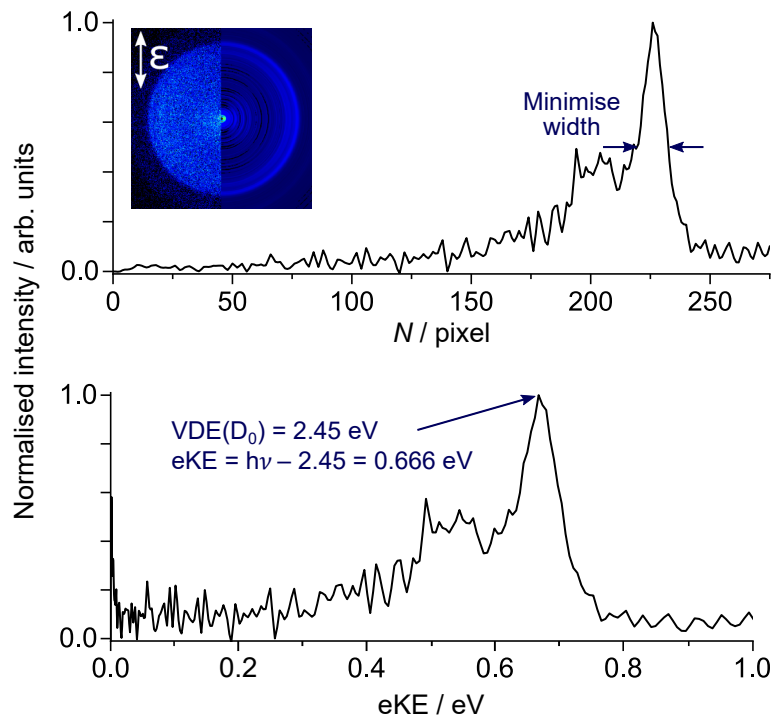


**Figure 2.16:** Top inset: Raw (left half) and inverted (right half) VMI images with the polarisation of the laser light shown by  $\epsilon$ . Top: Velocity spectrum. Bottom: eKE spectrum of indole. All data shown here were measured at 397.85 nm.

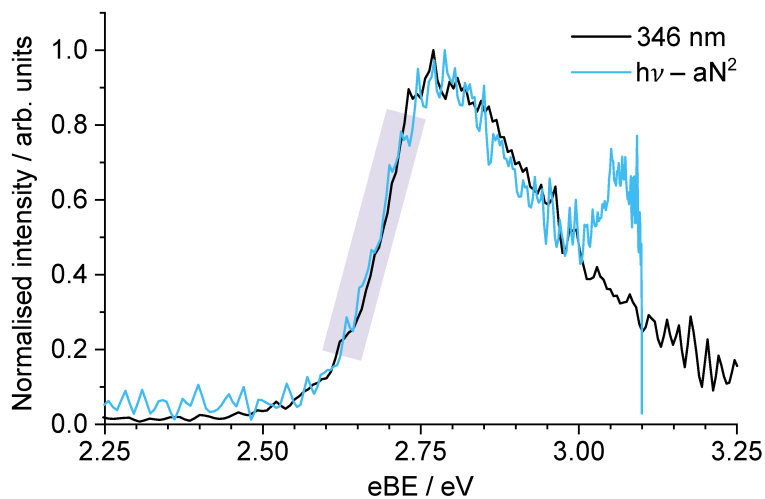


**Figure 2.17:** Calibration using  $p\text{HBDI}^-$  by scaling  $a$  in eBE space to fit the rising edge to the 346 nm spectrum.<sup>120</sup>

## 2.8 Summary

This chapter has focussed on describing the experimental method employed to record the spectra presented in Chapters 4 and 5. Details are provided on the function and employment of the major components of the apparatus. Section 2.1 outlined how a continuous beam of room temperature anions are produced in an electrospray anion source, while Section 2.2 described the mass selection and collection of anions to form a pulsed beam. Section 2.5 outlined the laser light sources used to produce wavelengths in the range 400–310 nm and Section 2.3 described how the photoelectrons are detected following the interaction of the laser with the pulsed ion beam, using velocity map imaging. Section 2.4 described how the three-dimensional distribution of photoelectron velocities is reconstructed from the two-dimensional projection at the detector. Finally, Sections 2.6 and 2.7 describe the overall timing and operation of the pulsed experiment and the various approaches used to calibrate. The following chapter describes the computational chemistry approaches used to aid in the analysis of the experimental measurements. Chapters 4 and 5 illustrate how such quantum chemical calculations and anion photoelectron spectroscopy measurements may be used to gain new insight into the electronic structure and dynamics of the photoactive yellow protein chromophore.

# Chapter 3

## Computational methods

To analyse photoelectron spectra, it is essential to make theoretical predictions of the electronic and nuclear structures of the chromophore before and after photodetachment. In this Chapter a description of the overall approach to calculate electronic structures of chromophores is given. Details of the computational techniques used in Chapters 4 and 5 to calculate ionisation potentials and excitation energies are provided. Section 3.4 outlines various possible approaches to extend upon the calculation of isolated gas-phase chromophores to include a solvent environment and introduces some of the techniques used in Chapters 6 and 7.

### 3.1 Introduction

The interpretation of anion photoelectron spectroscopy measurements frequently requires calculations to determine the ground electronic state of the anion, VDEs, ADEs and VEEs. Quantum-mechanical methods must be applied to appropriately model chromophores and accurately predict their electronic structures. Hence, the time-independent Schrödinger equation must be applied to the molecular system, modelled by the wavefunction,  $\Psi$

$$E\Psi = \hat{H}\Psi \tag{3.1}$$

where  $\hat{H}$  is the Hamiltonian operator and  $E$  is the eigenvalue energy.<sup>121</sup> The Hamiltonian includes both nucleic and electronic terms and may be written for an  $N$ -atom,  $n$ -electron system as

$$\hat{H} = -\sum_{I=1}^N \frac{\hbar}{2m_I} \nabla_I^2 - \sum_{i=1}^n \frac{\hbar}{2m_e} \nabla_i^2 - \sum_{I=1}^N \sum_{i=1}^n \frac{e^2 Z_I}{r_{i,I}} + \sum_{I<J} \frac{e^2 Z_I Z_J}{r_{I,J}} + \sum_{i<j} \frac{e^2}{r_{i,j}} \quad (3.2)$$

where subscript  $I$  and  $J$  relate to nuclei and subscript  $i$  and  $j$  relate to electrons,  $\hbar$  is reduced Planck's constant,  $m_I$  is the mass of nucleus  $I$ ,  $m_e$  is the mass of an electron,  $\nabla^2$  is the Laplacian operator,  $e$  is the charge of an electron,  $Z_I$  is the charge of nucleus  $I$  and  $r$  is the distance between two particles specified in its subscript. The first two terms are the translational energies of the nuclei and electrons, respectively. The latter three terms are the potential energies describing the electron-nuclear attraction, nuclear-nuclear repulsion and electron-electron interaction, respectively. This can be simplified by decoupling the nucleic and electronic terms into two separate Schrödinger equations; one for the electrons, the other for the nuclei. Generally this is a sensible approach as the electrons are much lighter in mass than the nuclei such that the nuclei are effectively stationary with respect to the electron motion *i.e.* the Born-Oppenheimer approximation is applied.<sup>122</sup> The electrons may be modelled in a fixed-frame nuclear configuration with an electronic Hamiltonian constructed as follows

$$\hat{H}_{\text{elec}} = -\sum_{i=1}^n \frac{\hbar}{2m_e} \nabla_i^2 - \sum_{I=1}^N \sum_{i=1}^n \frac{e^2 Z_I}{r_{i,I}} + \sum_{I<J} \frac{e^2 Z_I Z_J}{r_{I,J}} + \sum_{i<j} \frac{e^2}{r_{i,j}} \quad (3.3)$$

Here the nuclear geometry is constant and so the nuclear repulsion potential is a constant value. However, even with this simplification there are terms that are challenging to calculate. For simple systems like hydrogen it is possible to solve the Schrödinger equation exactly but complications arise for many-body systems. This is because the electron-electron interaction energy of each electron depends on the spatial arrangement of all other electrons in the system.

In a Hartree-Fock calculation, the wavefunction is constructed from the product of one-electron wavefunctions and the electronic Hamiltonian is reformulated into a

sum of Fock operators,  $\hat{f}_i$ , each relating to a single electron  $i$ .<sup>123–125</sup>

$$\hat{H}_{\text{HF}} = \sum_{i=1}^n \hat{f}_i \quad (3.4)$$

$$\hat{f}_i = -\frac{1}{2}\nabla_i^2 - \sum_{I=1}^N \frac{Z_I}{r_{i,I}} + 2\hat{J}_i - \hat{K}_i \quad (3.5)$$

$$\hat{J}_i = \iint \psi_i^*(\mathbf{r}_1)\psi_i(\mathbf{r}_1) \frac{1}{r_{12}} \psi_j^*(\mathbf{r}_2)\psi_j(\mathbf{r}_2) d\mathbf{r}_1 d\mathbf{r}_2 \quad (3.6)$$

$$\hat{K}_i = \iint \psi_i^*(\mathbf{r}_1)\psi_j(\mathbf{r}_1) \frac{1}{r_{12}} \psi_j^*(\mathbf{r}_2)\psi_i(\mathbf{r}_2) d\mathbf{r}_1 d\mathbf{r}_2 \quad (3.7)$$

The first two terms of the Fock operator relate only to electron  $i$  and describe the electronic translational energy and the electron-nuclear Coulombic attraction. The  $\hat{J}_i$  operator provides the Coulomb energy arising from the electron-electron interaction and when summed over all electron pairs, provides the total repulsion energy. The  $\hat{K}_i$  operator describes the exchange integrals and when summed up over all electron pairs, defines the exchange energy due to the antisymmetry of the total  $n$ -electron wavefunction. Hence, the Hartree-Fock energy may be calculated as

$$E_{\text{HF}} = \sum_{i=1}^n \epsilon_i - \sum_{i \neq j} [\hat{J}_i - \frac{1}{2}\hat{K}_i] \quad (3.8)$$

where  $\epsilon_i$  is the energy of electron  $i$  calculated from the one-electron terms in the Fock operator. However, for a many-body system, this is still not straightforward to solve. Typically, a suitable guess for the wavefunction is constructed from a linear combination of atomic orbitals described by known basis functions. This approximate wavefunction is then used to find the energy which will be greater than or equal to the true wavefunction energy,  $E_0$ , for the given Hamiltonian according to the variational principle.

$$E_0 \geq \frac{\langle \Psi | \hat{H} | \Psi \rangle}{\langle \Psi | \Psi \rangle} \quad (3.9)$$

For the Hartree-Fock Hamiltonian, the minimum reachable energy lies at what is known as the Hartree-Fock limit. An iterative self-consistent approach is then used to minimise the energy through variational optimisation of the wavefunction. In



most cases, the Hartree-Fock method is not sufficiently accurate, even at the Hartree-Fock limit. This is largely due to how the electron-electron interaction terms ( $\hat{J}_i$  and  $\hat{K}_i$ ) are calculated. The mean-field approximation is employed whereby the net repulsion on each electron is calculated by treating all of the other electrons within the molecule as a smooth distribution of negative charge. Deviations from this approximation are known as electron correlation and the difference between the Hartree-Fock limit and the true energy (within the basis set used) is known as the correlation energy and is often significant.

For any calculation, the quantum chemistry software package used constructs a wavefunction from a set of basis set functions chosen by the user. The basis functions have known analytical solutions to the integrals. For example, within any Pople (split-valence) type basis set, a contraction of a linear combination of Gaussian functions is used to represent each molecular orbital.<sup>126</sup> A complete basis set would represent the orbitals exactly but in practice this is not possible and a truncation of the full expansion is employed. This leads to inaccuracies in the calculation but these can be minimised by the use of large basis sets or by repeating the same calculation with increasing basis set size to estimate the converged value at the complete basis set limit. In practice, for medium to large molecular systems the latter would be too computationally expensive and so more commonly, a compromise is made with the use of a basis set that is benchmarked against a larger basis for a smaller representative molecular system. There are various basis sets available and careful consideration of the system is required when choosing which to use. For the calculation of anions, the choice of basis set is particularly important as the diffuse surplus charge must be described appropriately in order to obtain meaningful values.

For the calculation of detachment energies, for example, Hartree-Fock theory in its pure form would be insufficiently accurate as the correlation energy is not included. Post-Hartree-Fock methods may be employed in which the major approximations made in Hartree-Fock theory are relaxed with an increase in computational expense. Alternatively, density functional theory (DFT) methods may be used which include electron correlation and are inexpensive and hence very popular. Unlike Hartree-Fock, DFT employs functionals to determine the energy from the

electron density,  $\rho$ .<sup>127</sup>

$$E[\rho] = V_{\text{ne}}[\rho] + T[\rho] + V_{\text{ee}}[\rho] \quad (3.10)$$

Here, the energy is evaluated from three functionals describing the nuclear-electron interaction ( $V_{\text{ne}}[\rho]$ ), the electronic translational energy ( $T[\rho]$ ) and the electron-electron interaction ( $V_{\text{ee}}[\rho]$ ). Each functional is dependent on the electron density, which is spatially dependent. Kohn-Sham DFT is the form of DFT widely used today and assumes the system may be approximated such that the electrons are non-interacting.<sup>128</sup> The electronic translational functional is approximated to that of a system of non-interacting electrons ( $T_{\text{s}}[\rho]$ ) and the Coulomb interaction ( $J[\rho]$ ) is separated from the electron-electron interaction as follows.

$$\begin{aligned} E[\rho] &= V_{\text{ne}}[\rho] + T_{\text{s}}[\rho] + J[\rho] + (T[\rho] - T_{\text{s}}[\rho]) + (V_{\text{ee}}[\rho] - J[\rho]) \\ &= V_{\text{ne}}[\rho] + T_{\text{s}}[\rho] + J[\rho] + E_{\text{XC}}[\rho] \end{aligned} \quad (3.11)$$

The first three terms here may be computed and the unknown terms are collected into the exchange-correlation functional,  $E_{\text{XC}}[\rho]$ . The accuracy of DFT relies on how true this functional is to the system. There are a wide range of exchange-correlation functionals available that generally fit within three categories; local-density approximation (LDA), gradient generalisation approximation (GGA) or hybrid-type functionals.<sup>129,130</sup> In LDA, the electron density is dependent only on the coordinate at which the functional is evaluated. LDA functionals, such as SVWN (Slater Vosko-Wilk-Nusair), are widely used to calculate properties of solid-state materials.<sup>131,132</sup> GGA functionals are still local but include the gradient of the density at that coordinate. Hence, GGA functionals, such as BLYP (Becke Lee-Yang-Parr), often outperform LDA functionals for molecular geometries.<sup>133–136</sup> Hybrid functionals are the most popular type and include a component of exact Hartree-Fock exchange, making them no longer pure DFT but allow for a more accurate approximation of the exchange energy. One of the most popular hybrid functionals is B3LYP, denoting

Becke, 3-parameter, Lee-Yang-Parr.<sup>132–134,137</sup>

$$E_{\text{B3LYP}}[\rho] = a_0 E_{\text{HF}}^{\text{X}} + (1-a_0) E_{\text{LDA}}^{\text{X}} + a_{\text{x}} E_{\text{Becke}}^{\text{X}} \\ + (1-a_{\text{c}}) E_{\text{VWN}}^{\text{C}} + a_{\text{c}} E_{\text{LYP}}^{\text{C}} \quad (3.12)$$

The B3LYP functional is composed of various exchange (superscript X) and correlation (superscript C) functionals in different proportions defined by parameters  $a_0$ ,  $a_{\text{x}}$  and  $a_{\text{c}}$ . These parameters are chosen to provide the best approximation to a large set of experimental data. This functional has shown to perform well and efficiently for organic molecules. As a result of its popularity, the article describing this construction of the B3LYP functional has received more citations than any other article in the physical chemistry field.<sup>138</sup> The computational expense scales similarly for B3LYP and Hartree-Fock methods, but B3LYP is generally much more accurate.<sup>139–141</sup> For example, B3LYP can predict bond lengths to accuracies of  $\pm 0.008$  Å and bond angles to  $\pm 0.5^\circ$ ;<sup>142</sup> to improve on these would require a much more computationally-expensive method. A large set-back of DFT is that dispersion interactions are not accounted for intrinsically which can be important particularly with clusters or complexes, for example. However, an empirical correction to the energy may be implemented that incorporates an approximate dispersion energy.<sup>143</sup>

Before calculating the electronic structure of a molecule, it is important to determine the lowest energy conformation, or rather, any conformations likely to be populated under the experimental conditions. This is achieved by constructing the molecule (in various conformations, where necessary) and optimising the geometry. A geometry optimisation calculation uses an iterative approach to find a stationary point on the potential energy surface. In each iteration, the electronic energy and net inter-atomic force on each atom are calculated and the nuclear geometry changed to decrease the forces until the specified convergence criteria are met. Frequency calculations (vibrational analysis) are then used to confirm that a true minimum in the potential energy surface is reached. Generally, optimisation leads to the closest minimum on the potential energy surface to the initial geometry, which is not necessarily the global minimum. Hence, it is important to optimise from various

initial structures and in a deprotonated anion with several possible deprotonation sites, each of the various corresponding deprotomers need to also be tested. The relative energies of the various minima indicate which species may be expected in the experimental conditions.

There are various levels of theory available for geometry optimisation calculations at the quantum mechanics level but for all calculated results in this thesis, DFT with the B3LYP functional was used as this has been shown to work well for anionic chromophores.<sup>37,38,119,144–148</sup> For the results presented in Chapters 4 and 5, the Pople-type 6-311++G(3df,3pd) basis set<sup>126,149,150</sup> was employed for optimisation of geometries within the Gaussian09 software suite.<sup>151</sup> Whereas, for the much larger condensed-phase systems discussed in Chapters 6 and 7, a much smaller basis, 6-31+G(d), was used within the Firefly software package.<sup>152,153</sup> However, other basis sets including the Dunning (correlation-consistent) type<sup>154,155</sup> were used for testing and this is noted where appropriate.

Various computational chemistry software packages were used throughout this work and each differ slightly in the algorithms used to determine energies and optimise geometries. Hence, it is likely the energies and optimised geometries found will differ slightly between the software packages and care needs to be taken for inconsistencies when comparisons are made. Generally these discrepancies are small enough to be negligible. For example, the geometry of an isolated phenol molecule in the gas phase was optimised from the same initial geometry using B3LYP and the aug-cc-pVDZ basis set within two software packages, Gaussian09 and Firefly. With visualisation software, the structures appear identical by observation and following alignment, the root-mean-square deviation (RMSD) of the two structures was found to be only 0.001 Å. Similarly, the difference in the electronic energies calculated for phenol at B3LYP level with the 6-311++G(3df,3pd) basis set within the Gaussian09 and QChem<sup>156</sup> software packages was found to be < 0.001 eV.

## 3.2 Detachment energies

Koopmans' theorem assumes that the first ionisation energy of a molecule can be equated to the orbital energy of the HOMO using Hartree-Fock theory. However, this relies on the Hartree wavefunction being a reasonable representation of the orbitals and neglects any electronic relaxation or correlation. There are various approaches that may be used to calculate the detachment (ionisation) energies more accurately and several of which are used throughout the results chapters of this thesis. Here, detachment energies are discussed but it is worth noting that similar approaches may be used to find ionisation energies for neutral molecules.

### 3.2.1 Energy difference

A simple method for calculating a VDE of an anion is to take the difference between the energy of the initial anionic state in its optimal geometry and the energy of the final radical neutral state at the same geometry. Similarly, an ADE may be calculated from the difference of the energies of the two states at each of their optimised geometries. This is illustrated for a simple diatomic system in Figure 1.3. To calculate the VDE or ADE in this way requires two calculations but any theory level may be used and so if an inexpensive approach is used such as DFT, a VDE or ADE can be obtained very quickly. In Chapters 4 and 5, this method is used at the B3LYP/6-311++G(3df,3pd) theory level which has shown to reproduce similar energies to those found with higher-level theory.<sup>37,38,144,145</sup> In Chapters 6 and 7, this approach was used extensively to calculate VDEs for chromophores in aqueous environments using B3LYP/6-31+G(d) level theory because the calculations performed well and are much cheaper than alternatives. However, the detachment energies are relatively small and so inaccuracies in calculating the energies of either state may be significant when finding the difference. Hence, in all reported cases in this thesis comparisons were made with VDEs calculated using other methods where possible.

In Chapters 4 and 5, these calculations were performed using Gaussian09 and those in Chapters 6 and 7 were performed in the QChem software suite.

### 3.2.2 Electron propagator theory

Electron propagator theory (EPT) methods may be used to calculate vertical detachment energies directly by considering the interaction between the  $N$  and  $N - 1$  electron states, described by the Dyson orbital,  $\psi_i^{\text{Dyson}}$ .<sup>157–160</sup> For example, for the detachment of an electron from the  $\mathbf{r}_1$  position:

$$\psi_i^{\text{Dyson}}(\mathbf{r}_1) = N^{1/2} \int \Psi_N(\mathbf{r}_1, \mathbf{r}_2, \dots, \mathbf{r}_N) \Psi_{i,N-1}(\mathbf{r}_2, \mathbf{r}_3, \dots, \mathbf{r}_N) d\mathbf{r}_2 d\mathbf{r}_3 \dots d\mathbf{r}_N \quad (3.13)$$

Much like perturbative post-Hartree-Fock methods, EPT develops beyond Hartree-Fock through the introduction of an additional term to the Hamiltonian. For EPT, this term is the self-energy operator,  $\Sigma(\epsilon)$  and includes all relaxation and correlation effects.

$$\hat{H}\psi_i^{\text{Dyson}} = [F + \Sigma(\epsilon_i^{\text{Dyson}})]\psi_i^{\text{Dyson}} = \epsilon_i^{\text{Dyson}}\psi_i^{\text{Dyson}} \quad (3.14)$$

EPT methods employ Green's functions (correlation functions) to tackle the inhomogeneous differential equations. For a non-interacting single-particle system, the single-body Greens function (electron propagator) yields solutions equivalent to the orbital energies at the Hartree-Fock level. The Dyson equation relates the single-body propagator ( $G_0$ ) to the many-body propagator ( $G$ ).

$$\begin{aligned} G &= G_0 + G_0 \Sigma G \\ &= G_0 + G_0 \Sigma G_0 + G_0 \Sigma G_0 \Sigma G_0 + \dots \end{aligned} \quad (3.15)$$

Hence, the self-energy operator provides a link between many-body theory and a non-interacting system. The energies that produce singularities in  $G$  are known as the poles and these provide binding energies of orbitals. In practice, the self-energy is not known exactly but can be approximated by truncation of the full self-energy expression. The norms of the Dyson orbitals are known as pole strengths and are proportional to the transition probabilities (photodetachment cross-sections).

In Chapters 4 and 5, the outer-valence Green's function method<sup>157,158</sup> was used

with the 6-311++G(3df,3pd) basis within the Gaussian09 software suite to calculate the VDEs of deprotonated anionic chromophores in the gas phase. This approach has been shown to provide excellent agreement with experimentally measured values for the first detachment energy.<sup>37,38,145</sup>

### 3.2.3 Equations-of-motion coupled-cluster methods

Equations-of-motion coupled-cluster (EOM-CC) methods may be used to calculate properties of electronically-excited and open-shell species.<sup>161,162</sup> In the EOM formalism, target states  $|\Phi_f\rangle$ , are described as excitations from a reference state,  $|\Phi_0\rangle$

$$|\Phi_f\rangle = R(\Phi_f) |\Phi_0\rangle \quad (3.16)$$

where  $R$  is a general excitation operator. The reference state is solved at the Hartree-Fock level and so is described by a single Slater determinant. Hence, it is best to choose a well-behaved closed-shell system as the reference state. However, EOM-CC methods describe a variety of multiconfigurational target wavefunctions from this single reference wavefunction. The target EOM states are found by diagonalizing the similarity transformed Hamiltonian,  $\bar{H}$

$$\bar{H} = e^{-T} H e^T \quad (3.17)$$

$$\bar{H} R = E R \quad (3.18)$$

where  $H$  is the electronic Hamiltonian under the Born-Oppenheimer approximation and  $T$  is the coupled-cluster operator that constructs an exponential expansion of excited determinants from the reference wavefunction.

$$|\Psi_{CC}\rangle = e^T |\Psi_0\rangle \quad (3.19)$$

$$T = T_1 + T_2 + T_3 + \dots \quad (3.20)$$

$$e^T = 1 + T + \frac{1}{2!}T^2 + \frac{1}{3!}T^3 + \dots \quad (3.21)$$

Here,  $T_1$  includes all single excitations,  $T_2$  includes all double excitations and so on. Electronic correlation effects are accounted for within the exponential expansion of many determinants, making the coupled cluster approach more accurate than Hartree-Fock. To include all configurations in an  $N$ -electron system, excited determinants from singly-excited to  $N$ -order multiply excited configurations need to be included, as in full configuration-interaction (CI) theory. However, for larger systems with many electrons, this is not feasible. Commonly, operators  $T$  and  $R$  are truncated to include singly and doubly excited determinants in the target wavefunction (EOM-CCSD). Amplitudes for  $T$  are found which satisfy the CCSD equations as follows.

$$\langle \Phi_i^a | e^{-T} H e^T | \Phi_0 \rangle = \langle \Phi_i^a | \bar{H} | \Phi_0 \rangle = 0 \quad (3.22)$$

$$\langle \Phi_{ij}^{ab} | e^{-T} H e^T | \Phi_0 \rangle = \langle \Phi_{ij}^{ab} | \bar{H} | \Phi_0 \rangle = 0 \quad (3.23)$$

Here  $|\Phi_i^a\rangle$  describes the singly excited determinant in which an electron has been excited from an occupied orbital  $i$  to an unoccupied orbital  $a$  and  $|\Phi_{ij}^{ab}\rangle$  describes the doubly excited determinant in which one electron has been excited from  $i$  to  $a$  and another from  $j$  to  $b$ .

For the calculation of ionisation potentials (EOM-IP-CCSD), this operator removes an electron from the  $N$ -electron reference wavefunction to give the target wavefunction with  $N - 1$  electrons.<sup>163,164</sup>

$$|\Phi_f(N - 1)\rangle = R_{-1}(\Phi_f) |\Phi_0(N)\rangle \quad (3.24)$$

Examples of determinants for an ionising operator are illustrated in Figure 3.1. The reference wavefunction,  $\Psi_0$ , is the singlet ground state and the  $\Psi_i$  and  $\Psi_{ij}^a$  wavefunctions describe the single and double substitutions. Note that the spin is conserved between the single and double excitations.

The EOM-IP-CCSD approach has been shown to calculate VDEs of biological chromophores to a high level of accuracy for the first detachment energy and higher detachment continua.<sup>16,72,119,147,165–167</sup> In the later Chapters of this thesis, VDEs calculated using EOM-IP-CCSD were performed for both isolated chromophores in



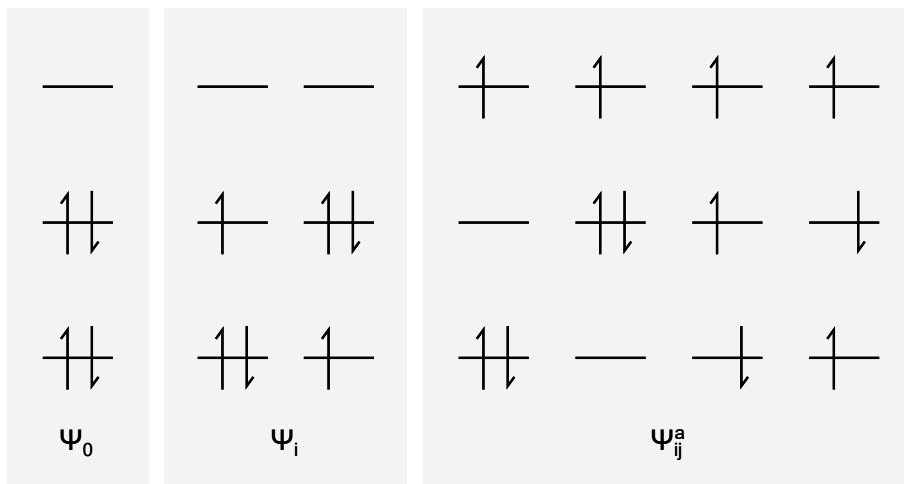


**Figure 3.1:** Example determinants included within the EOM-IP-CCSD method where  $|\Psi(N-1)\rangle = R_{-1}(\Psi) |\Psi_0(N)\rangle$

the gas phase and an aqueous environment. The calculations were performed within the Q-Chem software suite,<sup>162</sup> with a suitable basis set to accommodate for the system size and the core orbitals were frozen to lower the computational expense significantly.<sup>168</sup>

### 3.3 Vertical excitation energies

To interpret UV photoelectron spectra, it is invaluable to have an indication of the vertical excitation energies, the oscillator strengths of these transitions and the character of the transitions. There are various methods available for the calculation of electronically excited states varying in accuracy and expense. For anionic chromophores, the relatively low photodetachment thresholds make the treatment of the electronically excited states particularly challenging as these excited states generally lie in the detachment continuum and so the coupling between the quasi-bound valence state and the continuum needs to be accounted for appropriately.

#### 3.3.1 Time-dependent density functional theory

As described in Section 3.1, density functional methods are a powerful approach to model many-body systems in the ground state where the electron density is time-

independent. Time-dependent DFT (TD-DFT) extends the ideas of ground-state DFT to the treatment of time-dependent phenomena where the electron density is a function of position and time,  $\rho(\mathbf{r}, t)$ .<sup>169–171</sup> The total Hamiltonian in TD-DFT becomes  $\hat{H} = \hat{T} + \hat{V}(t) + \hat{V}_{ee}$  and the evolution of the system over time is governed by the time-dependent Schrödinger equation.

$$i\frac{\partial}{\partial t}\Psi(\mathbf{r}_1, \dots, \mathbf{r}_N, t) = \hat{H}(t)\Psi(\mathbf{r}_1, \dots, \mathbf{r}_N, t) \quad (3.25)$$

Runge and Gross showed that DFT can be extended to problems where a time-dependent external perturbation is present, such as the oscillating field of a laser.<sup>169</sup> The Runge-Gross theorem states that if two  $N$ -electron systems start from the same initial state,  $\Psi(t_0)$ , but are subject to different time-dependent potentials, their densities will be different. That is assuming that the potentials differ by more than just a time-dependent constant. *i.e.* there is a one-to-one mapping between the potential  $v(\mathbf{r}, t)$  and density  $\rho(\mathbf{r}, t)$ , for a given initial state. Hence, any observable of the system may be expressed as a functional of the density.

Much like with Kohn-Sham theory for ground-state systems, it is possible to reproduce the same density of a many-body interacting system using a non-interacting system for the treatment of time-dependent problems. The van Leeuwen theorem states that for a time-dependent density  $\rho(\mathbf{r}, t)$  associated with a given electron-electron interaction  $\hat{w}(|\mathbf{r} - \mathbf{r}'|)$ , external potential  $v(\mathbf{r}, t)$  and initial state  $\Psi_0$ , there exists a different many-body system ( $\Psi'(t)$ ) associated with an interaction  $\hat{w}'(|\mathbf{r} - \mathbf{r}'|)$  and unique external potential  $v'(\mathbf{r}, t)$  which reproduces the same time-dependent density  $\rho(\mathbf{r}, t)$ .<sup>172</sup> The initial state in this system,  $\Psi'(t_0)$  must be chosen such that it correctly derives the given density and its time-derivative at  $t = t_0$ . If one considers a non-interacting system, where  $w' = 0$ , the time-dependent interacting system density can be reproduced and so permits the use of a Kohn-Sham system in TD-DFT.

The Kohn-Sham system can then be propagated in time with an appropriate exchange-correlation functional,  $E_{XC}[\rho(\mathbf{r}, t)]$  in response to a time-varying applied electric field.<sup>170</sup> TD-DFT approaches are hugely popular due to the relatively low computational costs (scales as approximately the square of the system size) which

allows for the calculation of even large biomolecular systems.<sup>173,174</sup>

In later Chapters of this thesis, TD-DFT calculations were performed with the CAM-B3LYP functional<sup>175</sup> which employs a long-range correction (Coulomb-attenuating method) to the hybrid B3LYP functional described in Section 3.1. This CAM correction helps to describe diffuse excited states and charge-transfer states more accurately. In Chapters 4 and 5 TD-CAM-B3LYP calculations were performed with the 6-311++G(3df,3pd) basis set within the Gaussian09 software suite. In Chapter 7, TD-DFT calculations were performed to find the VEEs of  $p\text{CE}^-$  in aqueous solution within the QChem software. For these larger-scale systems, smaller basis sets (6-31+G\* and 6-311++G\*\*) were used and three functionals were tested: B3LYP, CAM-B3LYP and  $\omega$ -B97X-D.<sup>176,177</sup>  $\omega$ -B97X-D is another hybrid functional with an empirical dispersion correction that includes exchange *via* range separation - *i.e.* there are different contributions of exchange energy at short and long range.

### 3.3.2 Equations-of-motion coupled-cluster methods

As described above in Section 3.2.3, EOM-CCSD methods may be used to calculate properties of electronically excited and open-shell species.<sup>161,162</sup> A multiconfigurational set of target states are described from a single reference formalism. However, unlike with EOM-IP-CCSD where the general operator removes an electron from the reference state, for the treatment of electronic excitations (EOM-EE-CCSD), the general operator  $R$  conserves the number of electrons and total spin ( $M_S$ ).<sup>161,178–180</sup> Hence, only  $\alpha \rightarrow \alpha$  or  $\beta \rightarrow \beta$  excitations may occur.

$$|\Phi_f(M_S = 0)\rangle = R_{M_S=0}(\Phi_f) |\Phi_0(M_S = 0)\rangle \quad (3.26)$$

Figure 3.2 illustrates the excitations included in  $R$  for a simple system within the EOM-EE-CCSD scheme. The EOM-EE-CCSD approach has proven to calculate VEEs of neutral and anionic chromophores with excellent agreement with experiment.<sup>72,166,181</sup> In Chapter 4, properties of singlet excited states of  $p\text{CA}^-$  in the gas phase are calculated using EOM-EE-CCSD. These calculations were performed with the aug-cc-pVDZ basis set within the Q-Chem software package. In Chapter 7,

EOM-EE-CCSD/6-31+G\* theory is used to perform excited state analysis of  $p\text{CE}^-$  in aqueous solution.

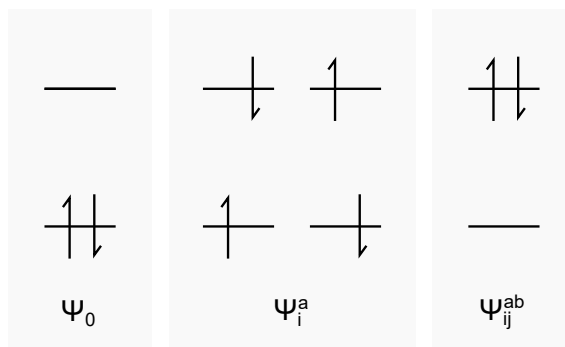


**Figure 3.2:** Example determinants included within the EOM-EE-CCSD method where  $|\Psi(M_S = 0)\rangle = R_{M_S=0}(\Psi) |\Psi_0(M_S = 0)\rangle$ .

### 3.3.3 Algebraic diagrammatic construction methods

The algebraic diagrammatic construction (ADC) scheme for the polarization propagator encompasses a series of *ab initio* methods based on perturbation theory for the calculation of excited states.<sup>182,183</sup> Much like EPT (Section 3.2.2), ADC originates from many-body Green's function theory. The polarisation propagator describes the polarisation of a many-electron system over a certain time or, rather, acts on the time-dependent ground state wavefunction and propagates time-dependent density fluctuations of the many-body system. The ground state wavefunction is described by  $n$ th order Møller-Plesset perturbation theory as the starting point for the ADC( $n$ ) calculation. ADC(1) would represent the ground-state wavefunction by a non-correlated Hartree-Fock system but with increasing order  $n$ , ADC methods converge to full-CI. The second-order scheme, ADC(2) is perhaps most popular due to its accuracy and computational expense in the calculation of excited states.<sup>184</sup>

As described in later chapters, ADC(2) calculations were used to calculate electronically excited states of anionic PYP chromophore analogues in the gas phase and were performed within the Q-Chem software package.

## 3.4 Inclusion of an environment

Performing accurate *ab initio* calculations on chromophores in bulk solution are much more challenging than those on isolated chromophores. However, there are many approaches designed to model solvation effects. Such methods vary in complexity, computational expense and accuracy. It would not be feasible to model all atoms within a bulk system explicitly with quantum mechanics and outlined below are three common approaches used to simplify such a complex system.

### 3.4.1 Microsolvation

Microsolvation approaches involve reducing the bulk solvation to a small number of water molecules, usually fewer than the second solvation shell. This allows for all atoms in this truncated system to be treated using quantum mechanics. Such calculations are inherently interesting to compare with experiments investigating clusters and also provide information on the bridge between gas and bulk media. However, microsolvation studies are susceptible to magic numbers in cluster sizes and so careful consideration of the number of solvent molecules included is required to mimic bulk behaviour. An example of a microsolvated system in which a phenol molecule is surrounded by five water molecules is shown in Figure 3.3.

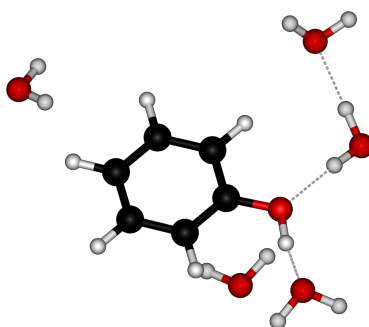


**Figure 3.3:** An example construction of a microsolvation calculation for phenol surrounded by five water molecules.

Ghosh *et al.* used a microsolvation approach to calculate the ionisation energy of phenol with successive additions of water molecules within the cluster.<sup>165</sup> Their

results are summarised in Table 3.1. It can be seen that the experimental measurements indicate there is a shift of  $-0.94$  eV upon bulk solvation and the microsolvated cluster that provides the best agreement with this shift is phenol( $\text{H}_2\text{O}$ ) and not the largest cluster. It is difficult to extrapolate from these small cluster sizes to bulk media because there is no general trend but it is interesting to consider the effect of an inclusion of a local environment. Microsolvation techniques also provide powerful comparisons for benchmarking purposes, which was the aim of this work by Ghosh *et al.*

	EOM-IP-CCSD	Experiment
phenol	8.35	8.74 <sup>a</sup>
phenol( $\text{H}_2\text{O}$ )	7.82	
phenol( $\text{H}_2\text{O}$ ) <sub>2</sub>	8.28	
phenol( $\text{H}_2\text{O}$ ) <sub>3</sub>	8.11	
phenol( $\text{H}_2\text{O}$ ) <sub>4</sub>	8.12	
phenol( $\text{H}_2\text{O}$ ) <sub>bulk</sub>		7.8

**Table 3.1:** VIEs (in eV) calculated for phenol and microsolvated clusters of phenol using EOM-IP-CCSD with the 6-31+G\* basis set, taken from Reference 165. These are compared with experimental values for gas-phase phenol (<sup>a</sup>Reference 185) and phenol in bulk solvation (Reference 165).

### 3.4.2 Implicit solvent models

Implicit solvation involves representing the solvent as a continuous homogeneous medium instead of by explicit solvent molecules. Polarisable continuum model (PCM) approaches<sup>186</sup> are one of the most popular types of continuum solvation methods and involve modelling the solvent as a polarisable dielectric continuum. The degree of polarisability of the implicit solvent medium is governed by the dielectric constant. The implicit solvent surrounds the solute which resides within a solvent-free cavity, often defined by the van der Waals surface of the solute. The charge density of the solute interacts with the dielectric field of the solvent continuum, polarising the solvent, which then causes a change in the polarisation of the solute. This recursive polarisation response is iterated to self-consistency.

PCM models are incredibly popular due to their ease of use, availability in software packages, versatility and low expense.<sup>187</sup> However, treatment of the solvent in

this way misses directional interactions such as hydrogen bonding. Hydrogen bonds are pertinent in aqueous solvents and particularly so with anionic solutes. Hence, using an implicit solvent model to calculate the electronic structure of a chromophore in aqueous solution is useful to provide a low-cost qualitative indication of the solvent shift but is generally not able to provide quantitative accuracy. Combining an implicit solvent model with microsolvation can be useful to reduce harsh boundary effects at the surface of the cluster while including hydrogen bonding interactions locally with the chromophore.

### 3.4.3 Quantum mechanics/molecular mechanics

A popular approach to simulate a bulk explicit solvent system is to describe the solvent by molecular mechanics (MM) which requires very low computational expense. To describe the full system with MM would acquire low accuracy results, particularly for complex anionic systems. However, hybrid quantum mechanics/molecular mechanics (QM/MM) approaches balance accuracy and cost by describing a small subsystem of interest (*e.g.* the chromophore solute) by QM and another, surrounding subsystem by MM (*e.g.* the solvent). An example QM/MM construction is illustrated in Figure 3.4 with the QM (purple) region containing a phenol molecule and the MM (blue) region containing all water molecules.

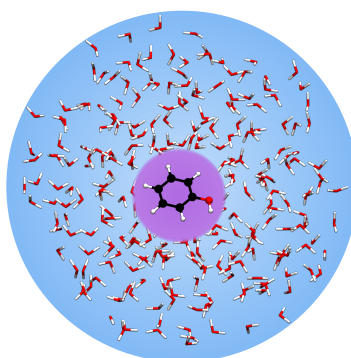


**Figure 3.4:** An example QM/MM calculation for phenol in an aqueous solvent with possible QM and MM levels highlighted in purple and blue, respectively.

The QM level section is described by methods such as Hartree-Fock or DFT, for example. The MM region is instead described by a particular forcefield that provides

molecular parameters that govern the bonding and non-bonding interactions of the atoms under classical mechanics. A popular forcefield is CHARMM22 (chemistry at Harvard macromolecular mechanics, version 22) in which the energy function, dependent on the coordinates of the atoms  $\mathbf{r}$ , may be written as the following.<sup>188</sup>

$$\begin{aligned}
 U(\mathbf{r}) = & \sum_{\text{bonds}} K_b (b - b_0)^2 + \sum_{\text{UB}} K_{\text{UB}} (S - S_0)^2 + \sum_{\text{angles}} K_{\theta} (\theta - \theta_0)^2 \\
 & + \sum_{\text{dihedrals}} K_{\chi} (1 + \cos(n\chi - \chi_0)) + \sum_{\text{impropers}} K_{\text{imp}} (\psi - \psi_0)^2 \\
 & + \sum_{\text{nonbond}} \epsilon \left[ \left( \frac{r_{\min}}{r_{ij}} \right)^{12} - 2 \left( \frac{r_{\min}}{r_{ij}} \right)^6 \right] + \frac{q_i q_j}{\epsilon_1 r_{ij}}
 \end{aligned} \tag{3.27}$$

Here,  $K_b$ ,  $K_{\text{UB}}$ ,  $K_{\theta}$ ,  $K_{\chi}$  and  $K_{\text{imp}}$  are the bond, Urey-Bradley angle, angle, dihedral angle and improper dihedral angle force constants, respectively.  $b$ ,  $S$ ,  $\theta$ ,  $\chi$  and  $\psi$  are the bond length, Urey-Bradley 1,3-distance, bond angle, dihedral angle and improper torsion angle, respectively, with subscript zero representing the equilibrium values for each term. The non-bonded terms are a Lennard-Jones potential and an electrostatic Coulombic potential which are summed over all pairs of atoms separated by three or more covalent bonds,  $(i, j)$ .  $\epsilon$  is the Lennard-Jones minimum,  $r_{\min}$  is the distance between atoms  $i$  and  $j$  at the Lennard-Jones minimum energy,  $q_x$  is the partial charge on atom  $x$ ,  $\epsilon_1$  is the effective dielectric constant and  $r_{ij}$  is the distance between atoms  $i$  and  $j$ . The CHARMM22 forcefield partial charges were derived from quantum chemical calculations between model compounds and water and other parameters from fitting to empirical datasets. The water model used was the TIP3P (transferable intermolecular potential with 3 points) which defines each water molecule by three interaction points at the three atom positions.<sup>189</sup>

The outer boundary of the system may be embedded within a PCM or defined by a set of periodic boundary conditions to reduce any unwanted surface effects. QM regions can also be extended beyond simply the chromophore, as shown in Figure 3.4, to include some solvent molecules, similar to a microsolvated system. Hybrid methods like QM/MM are often used to calculate properties of solutes in solutions<sup>190</sup> but careful consideration of the composition of the QM and MM regions needs to be considered to accommodate the coupling between the two regions appropriately.



In addition, the construction of the system is difficult to assemble using chemical intuition alone due to the vast number of degrees of freedom. Instead, an MM/MM simulation may be used to find a configuration (or series of configurations) of the complex system through equilibration over time-evolution (molecular dynamics) or averaging over a sufficient number of states (Monte Carlo). Full MM simulations are very inexpensive relative to QM/MM approaches and so provide a good starting point for a simulation. However, thoroughly benchmarked forcefield parameters are not always readily available for chromophores of interest. There are methods available for the approximate parametrisation of custom structures using information from *ab initio* calculations.

### 3.4.4 Effective fragment potential methods

The effective fragment potential (EFP) method is a computationally inexpensive way of modelling intermolecular interactions and environmental effects in non-bonded systems without any empirical parameterisation.<sup>191,192</sup> QM/EFP methods differ from typical QM/MM approaches in that hybrid QM/EFP methods may be employed without relying on an empirically-derived forcefield. EFP was originally formulated to describe the solvent effects in complex chemical systems. A library of standard solvent fragments is available which includes water but one may also construct user-defined EFP potentials.

The total energy of a QM/EFP system consists of the interaction energy of effective fragments ( $E^{\text{ef-ef}}$ ) and the energy of the QM region in the field of the EFP fragments. The EFP interaction energy includes electrostatic, polarisation, dispersion and exchange-repulsion contributions:

$$E^{\text{ef-ef}} = E_{\text{elec}} + E_{\text{pol}} + E_{\text{disp}} + E_{\text{ex-rep}} \quad (3.28)$$

The QM-EFP interactions are calculated such that the electrostatic and polarisation potentials perturb the QM one-electron Hamiltonian.

$$H'_{pq} = H_{pq} + \langle p | \hat{V}^{\text{elec}} + \hat{V}^{\text{pol}} | q \rangle \quad (3.29)$$

Whereas, the dispersion and exchange-repulsion components of the QM-EFP interaction energy are treated as additive corrections to the total energy.

The electrostatic component of the EFP energy accounts for Coulombic interactions and is the major contribution to the total intermolecular interaction energy in hydrogen-bonded or polar systems.<sup>193</sup> Multipoles up to and including octupoles are included at sites of high electron density, *i.e.* at the atom centres and bond mid-points. The fragment-fragment interactions included are charge-charge, charge-dipole, charge-quadrupole, charge-octupole, dipole-dipole, dipole-quadrupole and dipole-octupole in addition to terms describing the interactions between multipoles and the nuclei and the nuclear repulsion energy. The QM-EFP electrostatic interactions, introduced by  $\hat{V}^{\text{elec}}$ , consists as a sum of contributions from the multipole site locations of the fragments. Each fragment multipole site includes four terms corresponding to each multipole (charge, dipole, quadrupole and octupole).

The multipole expansion representation used breaks down when the fragments become too close as the interactions are too repulsive with significant electron density overlap and charge-penetration. The charge-penetration energy can be significant, particularly in systems with weak electrostatic interactions.<sup>194</sup> To overcome this, an exponential decay damping of the charge-charge term is introduced.<sup>194,195</sup>

The polarisation energy of a QM/EFP system is computed with the induced ( $\mu^k$ ) and conjugated induced ( $\bar{\mu}^{-k}$ ) dipole at a distributed point  $k$ .<sup>191</sup>

$$E^{\text{pol}} = -\frac{1}{2} \sum_k \mu^k (F^{\text{mult},k} + F^{\text{QM,nuc},k}) + \frac{1}{2} \sum_k \bar{\mu}^{-k} F^{\text{QM,elec},k} \quad (3.30)$$

Here,  $F^{\text{mult},k}$  is the external field due to the static multipoles and nuclei of other fragments,  $F^{\text{QM,elec},k}$  is the field due to the electronic density of the QM system and  $F^{\text{QM,nuc},k}$  is the field of the QM nuclei. The induced dipoles are calculated using the total field including  $F^{\text{mult},k}$ ,  $F^{\text{QM,nuc},k}$  and  $F^{\text{QM,elec},k}$  fields in addition to the field of the other induced dipoles. Therefore, the induced dipoles on a particular fragment depend on the induced dipoles of all other fragments. Furthermore, the induced dipoles of the fragments depend on the QM electron density which is itself affected by the field created by the EFP induced dipoles as described by the  $\hat{V}^{\text{pol}}$  pertur-

bation of the one-electron Hamiltonian. Hence, the polarisation energy is solved self-consistently to account for the many-body interaction effects. The fragment-fragment polarisation energies are augmented by Gaussian-like damping functions applied to the total field.<sup>196</sup>

The exchange-repulsion energy originates from the Pauli exclusion principle and is inherently a quantum effect. In MM forcefields, such as CHARMM22, the exchange-repulsion energy is included as a repulsive term within the  $R^{-12}$  Lennard-Jones potential. Within an EFP calculation, a wavefunction-based formalism is used to introduce the exchange-repulsion energy.<sup>197,198</sup> The exchange-repulsion energy is the only non-classical component of EFP and is derived as an expansion of the intermolecular overlap. A basis set is necessary for each effective fragment to calculate this overlap and kinetic one-electron integrals for each interacting pairs of fragments. This makes the exchange-repulsion term the most computationally expensive component of the EFP energy in calculations of moderately-sized systems.

QM/EFP calculations are available within software packages such as QChem or Firefly. Currently, QChem supports single point calculations such as the calculation of energies or excited states with EOM-CCSD/EFP approaches, for example. Firefly has perhaps the widest range of supported calculation types with which EFP may be used. Firefly allows for both vibrational frequency calculations as well as geometry optimisations with QM/EFP. In a QM/EFP geometry optimisation calculation, all atoms within the QM region are adjusted while the EFP fragments reorientate such that the internal coordinates of each fragment remain fixed but with free rotational and translational movement.

Hybrid QM/EFP calculations are widely used to represent bulk solute-solvent interactions and when compared to traditional QM/MM techniques, provide more accurate results.<sup>199,200</sup> In Chapters 6 and 7, the results are discussed of QM/EFP calculations used to model anionic chromophores in aqueous solutions.

## 3.5 Summary

This chapter describes some of the common quantum chemistry calculation approaches used to predict electronic and nuclear structures of chromophores isolated in the gas phase and how these methods could be extended to include an aqueous environment. A description of the methods used later in this thesis to calculate detachment energies and electronic excitation energies is provided. Later chapters discuss the results of such calculations, illustrating how useful theoretical methods are for the interpretation of results in addition to highlighting the differences in performance between the various methods used and their agreement with experimental measurements.

## Chapter 4

# Electronic structure and dynamics of torsion-locked photoactive yellow protein chromophores

As discussed in Chapter 1, the photocycle of photoactive yellow protein (PYP) begins with small-scale nuclear motions at the chromophore level that amplify to large-scale movements of the surrounding protein manifold, thus creating a long-lived signalling state to which the host organism responds. The importance of single-bond rotations (*i.e.* torsional motions) within the chromophore in the early steps in the photocycle are still not understood fully. The work described in this Chapter sought to address this by employing a combination of anion photoelectron spectroscopy and quantum chemistry to investigate the effect of locking torsional motion at either single bond site adjacent to the double bond within the PYP chromophore.

### 4.1 Introduction

Briefly, to put the work in this chapter into context, the chromophore found at the heart of PYP is the deprotonated *trans-para*-coumaric acid anion ( $pCA^-$ ) which is bound to the surrounding protein *via* a thioester link to a cysteine residue, as

shown in Figure 4.1. Upon photoexcitation of UV light, PYP undergoes a *trans-cis* isomerisation. Although this photoisomerisation is of key importance in entering the photocycle, this movement also couples with other nuclear motions of the chromophore to allow the isomerisation within the confined protein cavity. Hence, there is some resultant torsional motion about the single bonds adjacent to the central double bond.<sup>67</sup> However, without the protein environment, it has been suggested that it is single bond and not double bond rotation that dominates in the first excited state.<sup>61,62</sup> It is well-understood that this is the case for the methyl thioester analogue of the chromophore in an aqueous environment where rotation about the phenolate-ethene single bond ( $\alpha$ -rotation) is the key coordinate in the relaxation pathway following excitation with  $\sim 400$  nm light.<sup>44,201</sup>

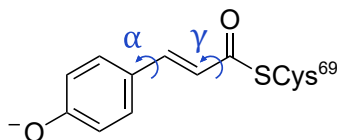


**Figure 4.1:** Structure of the deprotonated PYP chromophore with the relevant single bond rotations labelled.

Theoretical studies have suggested that this single bond rotation also dominates when the chromophore is isolated in the gas phase,<sup>62</sup> or in a mutant protein environment (R52Q).<sup>61</sup> It was suggested that the global minimum on the excited state surface is a double-bond twisted structure with a dihedral angle across the double bond of  $90^\circ$ . In addition, a local minimum structure was found with a dihedral angle of  $90^\circ$  about the single bond joining the phenoxide and ethene moieties ( $\alpha$ -rotation). It was proposed that a role of the protein scaffold is to restrict this competing single bond rotation and hence promote *trans-cis* isomerisation by stabilising the twisted double bond global minimum structure and lowering the barrier to isomerisation on the excited state potential energy surface. On the other hand, some experimental studies have contradicted this. A time-resolved spectroscopy study probing the photophysics of wild-type PYP and a reconstructed PYP with a chromophore rotation-locked across the phenolate-ethene single bond by an ethane bridge<sup>51</sup> reported that the excited state dynamics of the locked chromophore were accelerated but that the isomerisation yield was reduced by  $\sim 60\%$ , implying that the pheno-

late rotation is not an alternative to *trans-cis* isomerisation but that it does help facilitate the isomerisation with some coupled movement. This contrasts with the conclusions of an earlier gas-phase time-resolved photoelectron spectroscopy study of a ketone analogue of the PYP chromophore which did not show any evidence for a single-bond twisted intermediate in the excited state and revealed isomerisation times similar to those in the protein.<sup>32</sup>

Efforts have also been made to understand the importance of other single bond rotations in the chromophore. Some studies focussed on the  $C_{C=O}-S_{Cys}$  bond, the connection between the chromophore and the protein.<sup>202-204</sup> In a Fourier-transform infrared spectroscopy study it was found that PYP derivatives with locked chromophores were unable to undergo isomerisation but were still able to produce intermediates of the PYP photocycle.<sup>204</sup> Hence, the authors deemed the *trans-cis* isomerisation process dispensable for photoactivity in PYP and instead suggested that rotation of the carbonyl group is more significant. Thus, it is clear that the roles of the various torsional motions in the early stages of the PYP photocycle are not completely understood.

Non-radiative electronic relaxation pathways such as internal conversion (IC), intersystem crossing, intramolecular vibrational redistribution and photodetachment (PD) of electrons can compete with the *trans-cis* isomerisation process. In order to understand the role of the protein in minimising these competing processes, it is important to understand the intrinsic photochemistry of the isolated chromophores. Following excitation of a ketone analogue of  $pCA^-$  in the gas-phase, at 400 nm (3.1 eV), Lee *et al.* reported that 20% of the excited state population was found to undergo autodetachment and it was deduced that one of the roles of the protein environment is to funnel excited state population through the conical intersection (CI) seam towards the *cis* isomer to impede radical formation.<sup>32</sup>

The work in this chapter extends previous studies by employing structural analogues of  $pCA^-$  designed to allow us to test the importance of torsional motions on the electronic relaxation dynamics of the PYP chromophore in the gas phase following photoexcitation of the first excited state and higher lying excited states. Specifically, anion photoelectron spectroscopy and quantum chemistry calculations

were used to investigate the electronic structure and dynamics of four model PYP chromophores (Figure 4.2):  $p\text{CA}^-$ , its methyl ester  $p\text{CE}^-$ , and two analogues of  $p\text{CE}^-$  with aliphatic carbon bridges hindering single-bond torsional motion at either site adjacent to the unsaturated bond, denoted here as  $Pp\text{CE}^-$  and  $Np\text{CE}^-$  due to the pyranone and (tetrahydro)naphthalene motifs, respectively. By comparing the locked and unlocked chromophores, we may then determine the electronic structure and relaxation pathways available to the chromophores and how these are influenced by locking the single bond rotations.

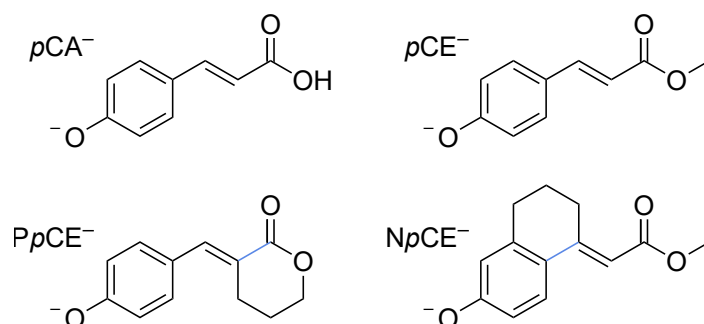


**Figure 4.2:** Structures of the deprotonated PYP chromophores used in this study with conformationally-locked bonds shown in blue.

## 4.2 Methods

### 4.2.1 Chromophores

$p\text{CA}$  (*para*-coumaric acid) was purchased from Sigma-Aldrich and  $p\text{CE}$  (methyl *trans*-*p*-coumarate) was purchased from Tokyo Chemical Industry, both were used without further purification. (*E*)-3-(4-hydroxybenzylidene)tetrahydro-2*H*-pyran-2-one ( $Pp\text{CE}$ ) and methyl (*E*)-2-(6-hydroxy-3,4-dihydronaphthalen-1(2*H*))-ylidene acetate ( $Np\text{CE}$ ) were synthesised using standard chemistry techniques by collaborators at UCL.<sup>205</sup>

### 4.2.2 Photoelectron spectroscopy

Anion photoelectron spectra were recorded using the anion photoelectron spectrometer described in Chapter 2. Specifically, argon was used as the collision gas in



the ion trap. Nanosecond laser pulses of wavelength 310–346 nm were generated by frequency-doubling the output of a Nd:YAG pumped dye laser. Femtosecond laser pulses ( $>50$  fs, 250 Hz) with wavelength centred at 400 nm were produced by frequency-doubling the output of a commercial amplified Ti:Sapphire femtosecond laser system. Electron kinetic energy (eKE) spectra were obtained by calibrating the radial photoelectron velocity distribution against the photoelectron spectrum of iodide<sup>117</sup> (310–346 nm) and *p*-HBDI<sup>-119</sup> (400 nm). The energy resolution,  $\Delta E/E$ , of the 310–346 nm spectra were  $<5\%$  and around 14% for the 400 nm spectra.

### 4.2.3 Calculations

As described in Chapter 3, the structures of the anionic chromophores and their corresponding neutral radicals were optimised at the B3LYP/6-311++G(3df,3pd) level. Vibrational analysis was performed to ensure the optimisations resulted in true minima.

VEEs of the singlet electronic excited states of the anionic chromophores were calculated using TD-DFT and ADC(2) methods. TD-DFT calculations were performed using CAM-B3LYP/6-311++G(3df,3pd) and ADC(2) calculations were performed with the 6-31+G\*\* basis set. These approaches were benchmarked against VEEs calculated for *p*CA<sup>-</sup> with EOM-EE-CCSD/aug-cc-pVDZ calculations and values from the literature, as presented in (Table 4.1).

**Table 4.1:** Vertical excitation energies (VEEs) of *p*CA<sup>-</sup> calculated using various methods compared with SA-CASSCF(14,12)-PT2/cc-pVDZ calculated values<sup>42</sup> and experimental values.<sup>33</sup> VEEs are given in eV and oscillator strengths are shown in brackets.

Method	Basis set	S <sub>1</sub> (1 <sup>1</sup> $\pi\pi^*$ )	S <sub>2</sub> (1 <sup>1</sup> $n\pi^*$ )	S <sub>3</sub> (2 <sup>1</sup> $\pi\pi^*$ )
TD-CAM-B3LYP	6-311++G(3df,3pd)	3.45 (0.91)	4.10 (0.00)	4.33 (0.11)
EOM-EE-CCSD	aug-cc-pVDZ	3.15 (1.06)	4.02 (0.00)	4.23 (0.10)
ADC(2)	cc-pVDZ	3.17 (1.01)	3.41 (0.00)	4.34 (0.09)
	aug-cc-pVDZ	2.96 (0.96)	3.33 (0.00)	4.05 (0.11)
	6-31+G**	2.96 (1.00)	3.35 (0.00)	4.13 (0.09)
	6-311+G**	2.96 (0.99)	3.33 (0.00)	4.11 (0.09)
SA-CASSCF(14,12)-PT2	cc-pVDZ	2.96	3.65	3.82
Experiment		2.89	-	-

VDEs were calculated using various methods to compare to the measured values we have obtained: the energy difference method at the B3LYP/6-311++G(3df,3pd) level, EPT/6-311++G(3df,3pd) and EOM-IP-CCSD/aug-cc-pVDZ approaches. Geometry optimisations, vibrational frequencies, TD-DFT and EPT calculations were performed using the Gaussian09 software suite, while EOM-CCSD and ADC(2) calculations were carried out using the Q-Chem software package.

## 4.3 Results and discussion

### 4.3.1 Photoelectron spectra

Anion photoelectron spectra were recorded for each of the four chromophores (Figure 4.2) using wavelengths of 400, 346, 330, 318, 315 and 310 nm. The wavelengths were chosen to probe various electronic excited states, with guidance from the action-absorption measurements reported elsewhere for  $pCA^-$  and  $pCE^-$  (see Figures 1.9 and 1.14).<sup>31,34</sup> At 400 nm, the photon energy (3.10 eV) is close to resonant with the first electronically excited state while wavelengths between 330 and 310 nm probe higher-lying electronically excited states in the detachment continuum. At 346 nm, the photon energy lies near the minimum in the action-absorption spectra. Hence, photoelectron spectra recorded at 346 nm are likely to be dominated by direct photodetachment with minimal contribution from indirect photodetachment processes.

The anion photoelectron spectra are presented as a function of eKE and eBE ( $h\nu - \text{eKE}$ ) for each of the four chromophores in Figure 4.3. Vertical lines on the spectra mark the calculated VDEs and VEEs. There are many trends and differences to be taken from this data. First, consider the sharp low eBE edges of the spectra. For each of the chromophores, this edge lies at the same eBE as photon energy is changed and so this feature is assigned to direct detachment to  $D_0$ . We can use the maximum of this feature in the 346 nm spectra to provide an experimental estimate for the vertical detachment energy for each of the chromophores. These are listed in Table 4.2 alongside the calculated values. The VDEs for all four chromophores lie in the 2.7–3.0 eV range in the order:  $NpCE^- < pCE^- < PpCE^- < pCA^-$ . There

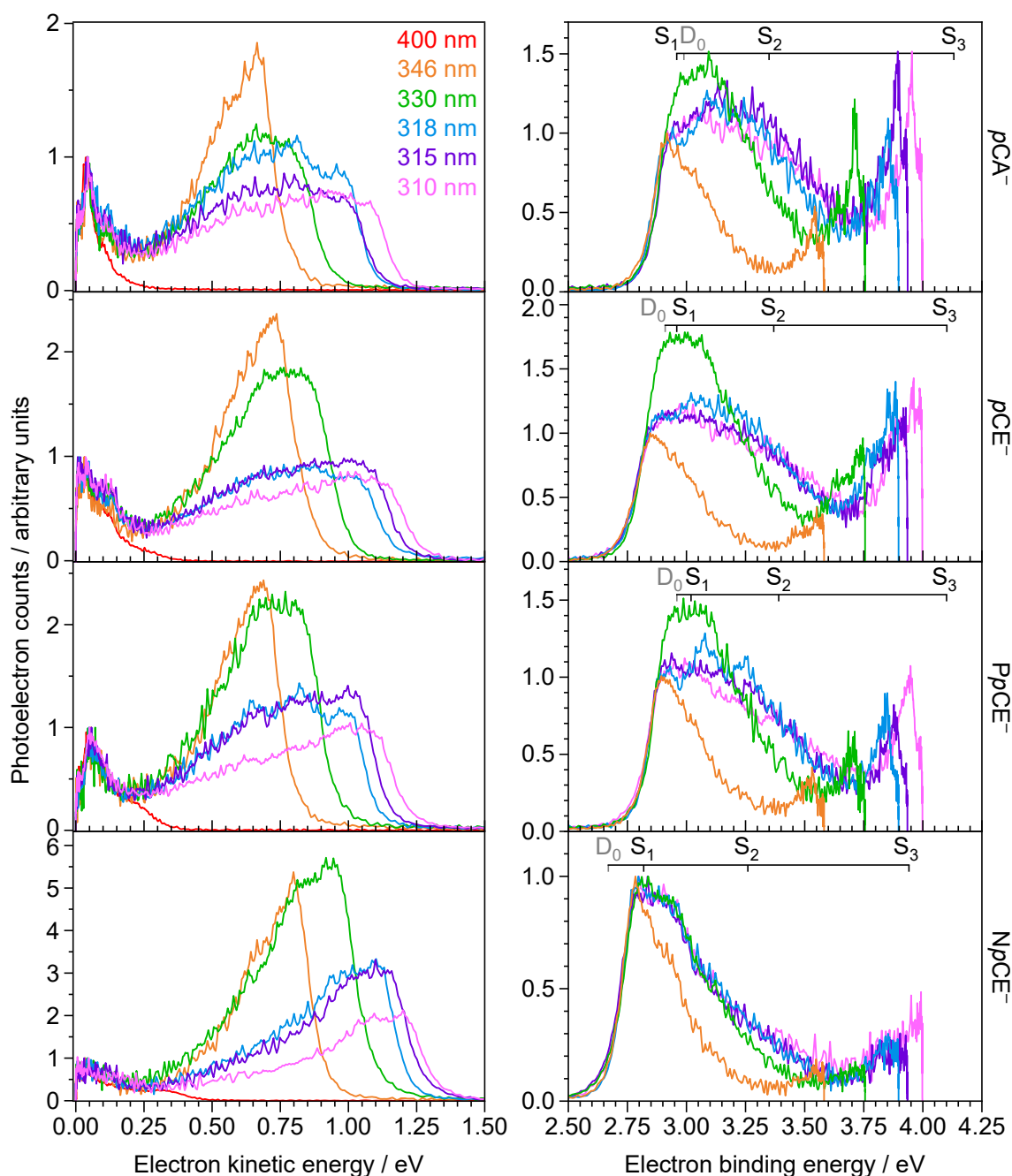


**Figure 4.3:** Photoelectron spectra of  $pCA^-$ ,  $pCE^-$ ,  $PpCE^-$  and  $NpCE^-$  recorded at 310 nm (4.00 eV), 315 nm (3.94), 318 nm (3.90), 330 nm (3.76 eV), 346 nm (3.58 eV) and 400 nm (3.10 eV). Intensities of the spectra plotted as a function of eKE (left) are normalised to the maximum of the low eKE feature. Intensities of the spectra plotted as a function of eBE (right) have been scaled to align the rising edges and are normalised to the maximum of the rising edges of the 346 nm spectra. The 400 nm spectra are plotted as a function of eBE in Figure 4.4. Combs mark the EPT calculated VDEs (grey) and the first three singlet excited states of the anion calculated using ADC(2)/6-31+G\*\* (black).

appears to be no other features that remain at a constant eBE with increasing photon energy and so this suggests that only one direct photodetachment channel is observed in the wavelength range used.

For each chromophore, the high eBE edge of this direct detachment feature broadens as photon energy is increased. This is due to an underlying resonant autodetachment feature (similar to the blue feature in Figure 1.5). However, this broadening is much less pronounced for  $NpCE^-$ . In previous anion photoelectron spectroscopy studies of PYP chromophores, this underlying resonant feature has been assigned to autodetachment from the  $S_3$  ( $2^1\pi\pi^*$ ) state.<sup>37,38</sup> There is also a feature at  $eKE \approx 0$  ( $eBE \approx h\nu$ ) in all the recorded spectra which has a shape unique to each chromophore that remains similar across the wavelength range used. The intensity of this low eKE feature increases with respect to direct detachment as photon energy is increased. This low eKE feature is much less intense in the spectra of  $NpCE^-$ .

Figure 4.4 shows the spectra recorded at 400 nm as a function of eBE and how these compare to the 346 nm spectra. Similarly to the eBE plots in Figure 4.3, the spectra are normalised to the maximum of the 346 nm spectra and scaled to align the rising edges. At 400 nm, the photon energy is not high enough to access high-lying excited states and so the available electronic relaxation pathways are much more limited than those observed in the 310-346 nm spectra. At 400 nm, the spectra have very little contribution from direct photodetachment, which is expected as the photon energy is close to the detachment threshold. Most of the photoelectron signal measured at 400 nm forms part of the low eKE feature that was also seen in the spectra recorded at shorter wavelengths. This is illustrated by the maximum intensity of the 400 nm spectra shown in Figure 4.4 given relative to the intensity of the direct detachment feature (at approx. unity in intensity).

The spectra presented in this chapter were all recorded using the VMI spectrometer described in Chapter 2 and so angular information is obtained in addition to the eKE distributions. The VMI images recorded are presented in Figure 4.5 and, by observation, the angular distributions appear largely isotropic. The exception being the outermost peak in the  $NpCE^-$  images. This could be due to the rigidity of

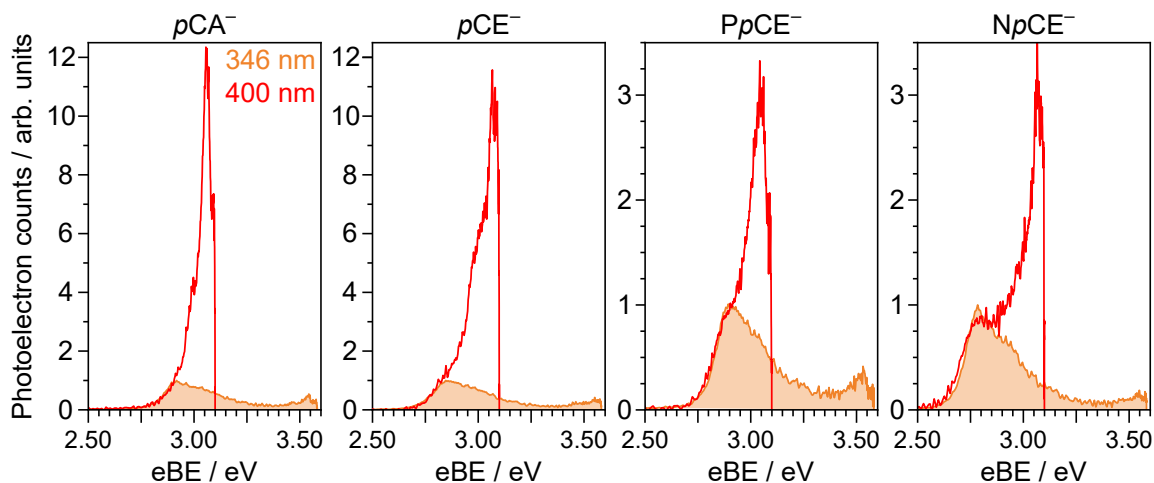


**Figure 4.4:** Photoelectron spectra of  $pCA^-$ ,  $pCE^-$ ,  $PpCE^-$  and  $NpCE^-$  recorded at 346 nm (3.58 eV) and 400 nm (3.10 eV). Intensities of the spectra have been scaled to align the rising edges and are normalised to the maximum of the rising edges of the 346 nm spectra. The 346 nm spectra have been shaded to illustrate the contribution of direct PD to the 400 nm spectra.

the  $NpCE^-$  anion afforded by the tether across the conjugated vinylphenol moiety, while the other chromophores are more flexible.

Figure 4.6 shows the anisotropy parameters determined from the angular distributions measured for  $NpCE^-$  recorded at wavelengths of 346, 330 and 310 nm. The  $\beta_2$  values are presented as five-point averages over the main intensity peak with  $\beta_2 \sim -0.25$  across the peak in the 346 and 330 nm spectra but in the 310 nm spectrum, the angular distribution is more isotropic. This is perhaps due to the involvement of a resonance at 310 nm, obscuring the anisotropy to a more averaged, isotropic  $\beta_2$  closer to zero.

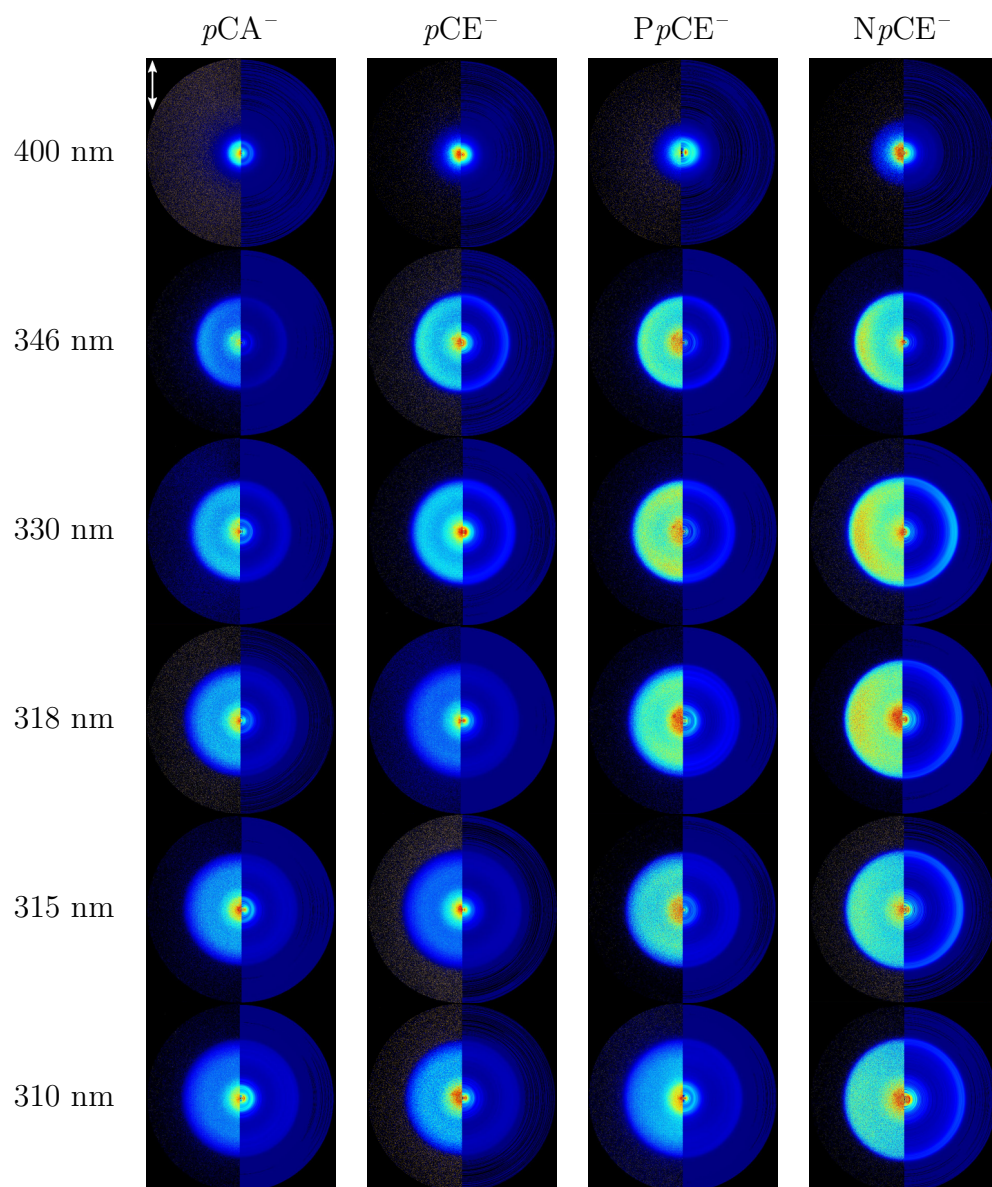


**Figure 4.5:** Photoelectron images recorded for each chromophore (left halves: raw VMI images; right halves: pBasex inverted images). In all images the polarisation axis of the laser is parallel to the double-headed arrow (top left).

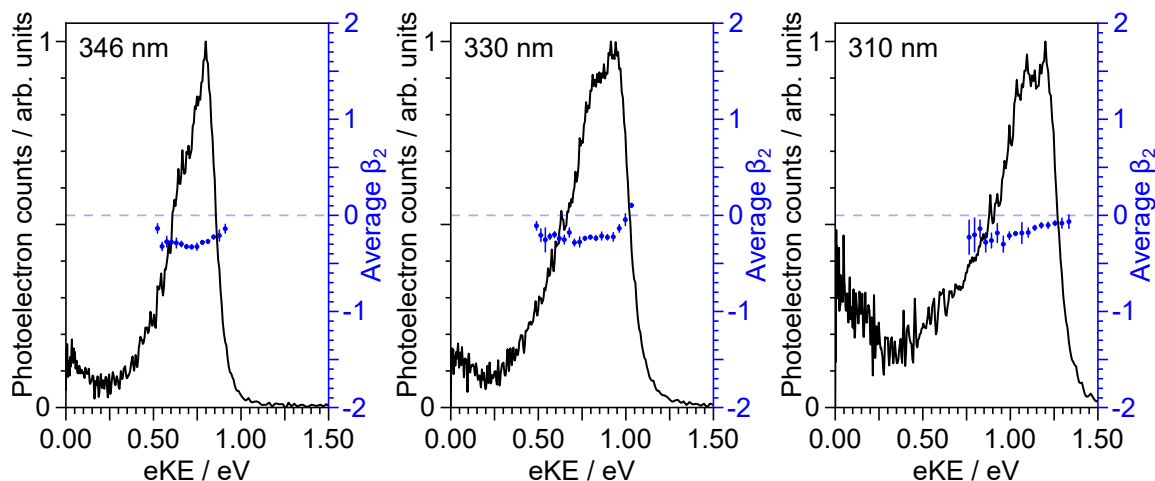


**Figure 4.6:** Photoelectron spectra of  $NpCE^-$  recorded at 346 nm (3.58 eV), 330 nm (3.76 eV) and 310 nm (4.00 eV). Intensities of the spectra plotted as a function of eKE and are normalised to the peak maxima. Anisotropy parameters  $\beta_2$  are shown as five-point averages over the main peak. The horizontal dashed line indicates  $\beta_2 = 0$ , an isotropic distribution.

### 4.3.2 Computational results

To help outline the electronic structures of the chromophores, ADEs, VDEs and VEEs were calculated for each of the species. Table 4.2 lists the calculated VDEs and ADEs along with the maxima of the 346 nm spectra. For  $D_0$ , the calculated VDEs and ADEs share the same trend as the experimental estimates; they increase in the order  $NpCE^- < pCE^- < PpCE^- < pCA^-$ . This trend can be interpreted in terms of the electronic effects of the acyl substituents and structural strain on the resonant stabilisation of the anion. The slight difference between the  $pCA^-$  and  $pCE^-$  detachment thresholds can be attributed to the hydroxyl group of  $pCA^-$  being a slightly weaker electron donor than the OMe group, as was reported previously.<sup>38</sup> This is intuitive as the methyl group is electron releasing and in this instance can be shown by the sum of the ChelpG<sup>206</sup> partial charges on the OH group (-0.296  $e$ ) compared to that of the OMe group (-0.275  $e$ ). In  $pCE^-$  the effect of  $n_{O(sp^2)} \rightarrow \sigma^*_{C=O}$  donation will destabilise the anion. This stereoelectronic effect is not possible with  $PpCE^-$  so it is surprising that the VDEs of  $PpCE^-$  and  $pCE^-$  are so similar. The expected greater stabilising effect of the lactone ring in  $PpCE^-$  may be offset by the destabilising effect of the planarity being compromised due to the conformation

induced by the tether with respect to the simple ester in  $p\text{CE}^-$ . The detachment threshold of  $\text{NpCE}^-$  is most likely lowered by the ring strain introduced by the rotation lock (half-chair conformation) inducing a small reduction in the planarity (see Figure 4.7) and thus hindering resonant stabilisation of the anion.

**Table 4.2:** Vertical detachment energies (VDEs), B3LYP/6-311++G(3df,3pd)  $\text{D}_0\text{-S}_0$  adiabatic detachment energies (ADEs) (0-0 transition) and maxima of the experimental 346 nm photoelectron spectra in eV for each chromophore. VDEs were calculated using EPT/6-311++G(3df,3pd) (pole strengths in parentheses), EOM-IP-CCSD/aug-cc-pVDZ and B3LYP/6-311++G(3df,3pd). EPT and EOM-IP-CCSD have two values listed pertaining to detachment to the  $\text{D}_0$  and  $\text{D}_1$  states.

	Vertical detachment energy			ADE (0-0)	Experiment
	EPT	EOM-IP-CCSD	DFT		
$p\text{CA}^-$	2.99 (0.879)	2.97	3.10	2.99	$2.92 \pm 0.05$
	5.25 (0.872)	5.45			
$p\text{CE}^-$	2.91 (0.879)	2.78	3.01	2.91	$2.85 \pm 0.05$
	5.18 (0.873)	4.42			
$\text{PpCE}^-$	2.96 (0.878)	2.83	3.03	2.93	$2.89 \pm 0.05$
	5.23 (0.871)	4.48			
$\text{NpCE}^-$	2.67 (0.879)	2.71	2.93	2.82	$2.78 \pm 0.05$
	5.02 (0.868)	4.33			

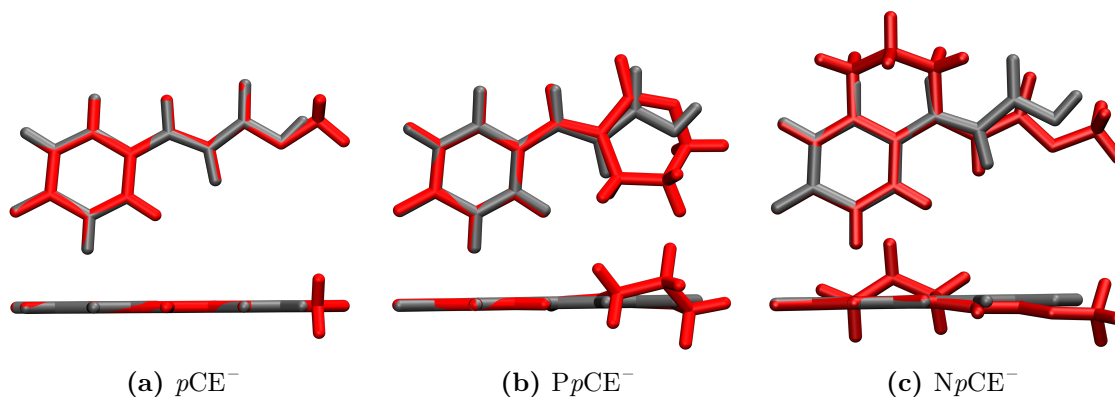


**Figure 4.7:** Structures of  $p\text{CE}^-$ ,  $\text{PpCE}^-$  and  $\text{NpCE}^-$  (each shown in red) superimposed on the  $p\text{CA}^-$  structure (grey) with the positions of the carbon atoms in the phenol ring overlapped. All chromophores are in their anionic form and have been optimised at the B3LYP/6-311++G(3df,3pd) level. Comparisons are viewed from above (top) and the side (bottom).

It is worth noting that  $p\text{CA}$  can deprotonate to form either the carboxylate or phenolate isomers of  $p\text{CA}^-$ , as discussed in Section 1.2.2. In these calculations, only



the phenolate isomer is considered because the spectra of  $pCA^-$  and  $pCE^-$  are so similar and the calculated VDE agrees with the experimental value very well. In addition, the carboxylate  $pCA^-$  isomer has a much higher detachment threshold (4.68 eV),<sup>37</sup> inaccessible with the photon energies used here ( $h\nu < 4$  eV). Hence, should there be a significant proportion of carboxylate  $pCA^-$  produced within the ion source, we would not observe photoelectrons from it but instead solely photoelectrons from phenolate  $pCA^-$ , the biologically-relevant form.

The VDEs calculated using DFT are close to the ADEs suggesting that the geometries of the anions and their corresponding neutral forms (following photodetachment) are similar, in agreement with previous work on PYP chromophore analogues.<sup>37,38</sup> The small difference between the VDEs and ADEs can also be seen in the spectra as the rising edge of the direct detachment feature is sharp.

The EPT method has calculated the first VDEs of  $pCA^-$ ,  $pCE^-$  and  $PpCE^-$  to be slightly higher than the experimental maxima ( $\sim 0.05$  eV) and slightly lower for  $NpCE^-$  (0.115 eV). The EPT/6-311++G(3df,3pd) approach was employed elsewhere<sup>37</sup> on the phenolate anion to find the first VDE to be within 1% of the experimental value of Gunion *et al.*<sup>207</sup> Here, there is a 2% difference between the EPT VDE and the experimental maxima for  $pCA^-$ ,  $pCE^-$  and  $PpCE^-$  and a 4% difference for  $NpCE^-$ . The VDEs calculated with the energy difference method with DFT are systematically higher than the experimental maxima by approximately 0.15 eV. The EOM-IP-CCSD calculations have predicted the VDEs within  $\sim 0.06$  eV of the experimental maxima, albeit the deviations are less systematic than those found with DFT; for example, the EOM-IP-CCSD VDE of  $pCA^-$  is higher than the experimental maximum whereas the calculated VDE of  $pCE^-$  is an underestimation of the experimental maximum. Note that the uncertainty of the measurements is  $\pm 0.05$  eV and that the high density of vibrational transitions contributing to these unresolved spectra can obscure the peak maximum from the true VDE. Hence, the calculated VDEs are in good agreement with the experiment and interestingly, the simple computationally-cheap DFT approach has performed very well. The calculated VDEs for the  $S_0$  to  $D_1$  transitions all lie above the highest photon energy, 310 nm (4 eV). Hence, it is unlikely we would measure direct detachment to  $D_1$ , or

higher detachment continua.

The first three singlet excited states of the chromophores were calculated using TD-DFT and ADC(2) for each of the four chromophores. The orbital contributions to each transition are presented in Tables 4.3 to 4.6. The three electronically excited states are found to be largely of  $1^1\pi\pi^*$ ,  $1^1n\pi^*$  and  $2^1\pi\pi^*$  character, involving the  $n$  (HOMO-1),  $\pi$  (HOMO),  $\pi_1^*$  and  $\pi_2^*$  orbitals. These orbitals along with any others that are involved in the calculated transitions are presented for each of the species in Figures 4.8 to 4.11. The ADC(2) orbitals appear to have more diffuse character than those calculated with TD-DFT and this is expected for two different basis sets and methods. The locked chromophores have greater contributions from diffuse orbitals which is intuitive as the molecular systems are larger allowing the electron density to expand further and the number of orbitals (or electrons) has increased so in turn, the number of diffuse orbitals and states has also increased.

**Table 4.3:** Excited states calculated with TD-CAM-B3LYP/6-311++G(3df,3pd) and ADC(2)/6-31+G\*\* for  $pCA^-$ . The vertical excitation energies (VEEs), main orbital contributions,  $c^2 > 10\%$  and oscillator strengths ( $f$ ) for each transition are listed.

Method	State	VEE / eV	Main contribution(s)		$c^2$	$f$
TD-CAM-B3LYP	S <sub>1</sub>	3.447	43→45	$\pi \rightarrow \pi_1^*$	0.956	0.910
	S <sub>2</sub>	4.098	42→45	$n \rightarrow \pi_1^*$	0.811	0.000
	S <sub>3</sub>	4.333	43→51	$\pi \rightarrow \pi_2^*$	0.900	0.102
ADC(2)	S <sub>1</sub>	2.959	43→47	$\pi \rightarrow \pi_1^*$	0.814	1.000
	S <sub>2</sub>	3.346	41→47	$n \rightarrow \pi_1^*$	0.739	0.000
	S <sub>3</sub>	4.134	43→55	$\pi \rightarrow \pi_2^*$	0.501	0.091

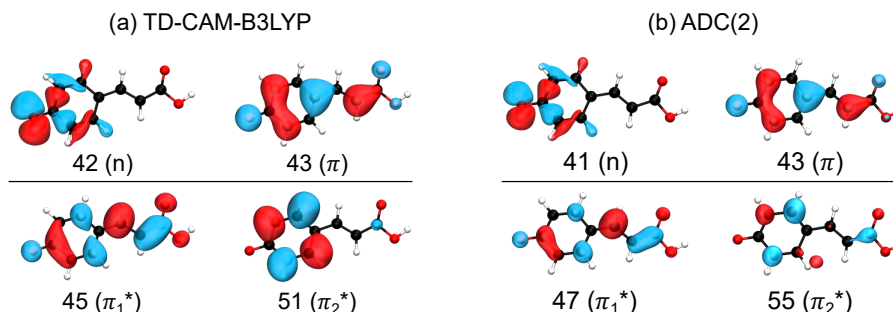


**Figure 4.8:** Relevant orbitals contributing to the electronic transitions of  $pCA^-$  listed in Table 4.3 determined from (a) TD-CAM-B3LYP/6-311++G(3df,3pd) and (b) ADC(2)/6-31+G\*\* calculations.

**Table 4.4:** Excited states calculated with TD-CAM-B3LYP/6-311++G(3df,3pd) and ADC(2)/6-31+G\*\* for  $p\text{CE}^-$ . The vertical excitation energies (VEEs), main orbital contributions,  $c^2 > 10\%$  and oscillator strengths ( $f$ ) for each transition are listed.

Method	State	VEE / eV	Main contribution(s)		$c^2$	$f$
TD-CAM-B3LYP	S <sub>1</sub>	3.434	47→49	$\pi \rightarrow \pi_1^*$	0.954	0.949
	S <sub>2</sub>	4.124	46→49	$n \rightarrow \pi_1^*$	0.832	0.000
	S <sub>3</sub>	4.311	47→57	$\pi \rightarrow \pi_2^*$	0.894	0.110
ADC(2)	S <sub>1</sub>	2.957	47→54	$\pi \rightarrow \pi_1^*$	0.527	1.021
			47→51		0.378	
	S <sub>2</sub>	3.368	45→54	$n \rightarrow \pi_1^*$	0.484	0.000
			45→51		0.250	
	S <sub>3</sub>	4.101	47→60	$\pi \rightarrow \pi_2^*$	0.476	0.097
			47→62		0.098	

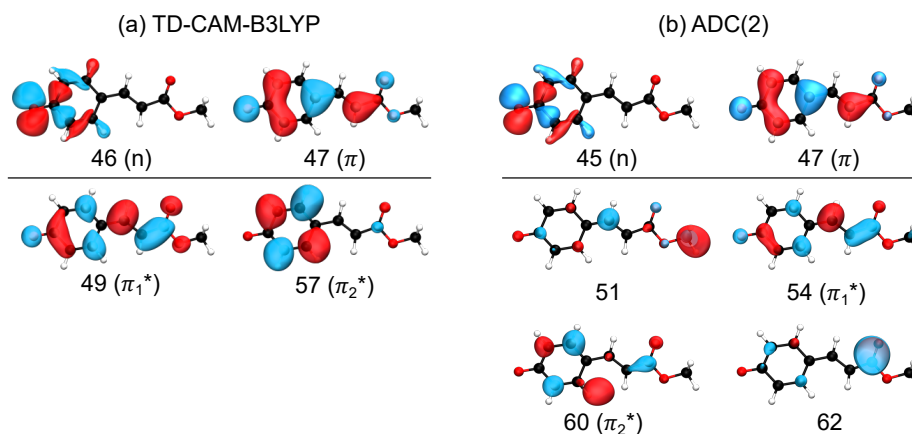


**Figure 4.9:** Relevant orbitals contributing to the electronic transitions of  $p\text{CE}^-$  listed in Table 4.4 determined from (a) TD-CAM-B3LYP/6-311++G(3df,3pd) and (b) ADC(2)/6-31+G\*\* calculations.

**Table 4.5:** Excited states calculated with TD-CAM-B3LYP/6-311++G(3df,3pd) and ADC(2)/6-31+G\*\* for PpCE<sup>-</sup>. The vertical excitation energies (VEEs), main orbital contributions,  $c^2 > 10\%$  and oscillator strengths ( $f$ ) for each transition are listed.

Method	State	VEE / eV	Main contribution(s)		$c^2$	$f$
TD-CAM-B3LYP	S <sub>1</sub>	3.488	54→57	$\pi \rightarrow \pi_1^*$	0.594	0.952
			54→58		0.199	
			54→56		0.162	
	S <sub>2</sub>	4.151	53→57	$n \rightarrow \pi_1^*$	0.493	0.000
			53→58		0.188	
			53→56		0.135	
	S <sub>3</sub>	4.340	54→66	$\pi \rightarrow \pi_2^*$	0.760	0.056
ADC(2)	S <sub>1</sub>	3.019	54→60	$\pi \rightarrow \pi_1^*$	0.611	1.032
	S <sub>2</sub>	3.389	51→60	$n \rightarrow \pi_1^*$	0.671	0.000
	S <sub>3</sub>	4.103	54→68	$\pi \rightarrow \pi_2^*$	0.242	0.061
			54→70		0.204	

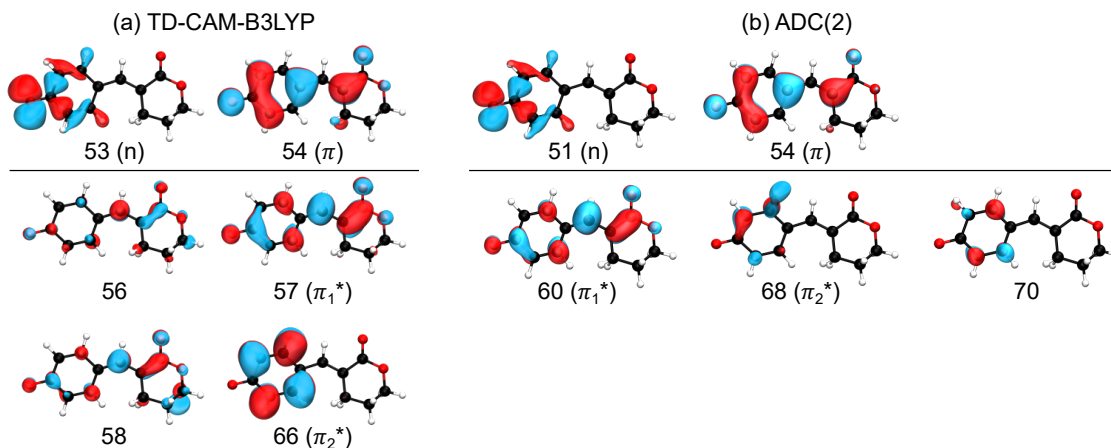


**Figure 4.10:** Relevant orbitals contributing to the electronic transitions of PpCE<sup>-</sup> listed in Table 4.5 determined from (a) TD-CAM-B3LYP/6-311++G(3df,3pd) and (b) ADC(2)/6-31+G\*\* calculations.

**Table 4.6:** Excited states calculated with TD-CAM-B3LYP/6-311++G(3df,3pd) and ADC(2)/6-31+G\*\* for  $NpCE^-$ . The vertical excitation energies (VEEs), main orbital contributions,  $c^2 > 10\%$  and oscillator strengths ( $f$ ) for each transition are listed.

Method	State	VEE / eV	Main contribution(s)		$c^2$	$f$
TD-CAM-B3LYP	S <sub>1</sub>	3.356	58→61	$\pi \rightarrow \pi_1^*$	0.876	0.812
	S <sub>2</sub>	4.103	57→61	$n \rightarrow \pi_1^*$	0.790	0.000
	S <sub>3</sub>	4.402	58→73	$\pi \rightarrow \pi_2^*$	0.320	0.026
			58→63		0.177	
			58→70		0.120	
			54→67		0.082	
			ADC(2)	S <sub>1</sub>	2.822	58→67
			58→63		0.216	
	S <sub>2</sub>	3.258	55→67	$n \rightarrow \pi_1^*$	0.464	0.000
			55→63		0.180	
	S <sub>3</sub>	3.936	58→64	$\pi \rightarrow \pi_2^*$	0.173	0.065
			58→76		0.137	

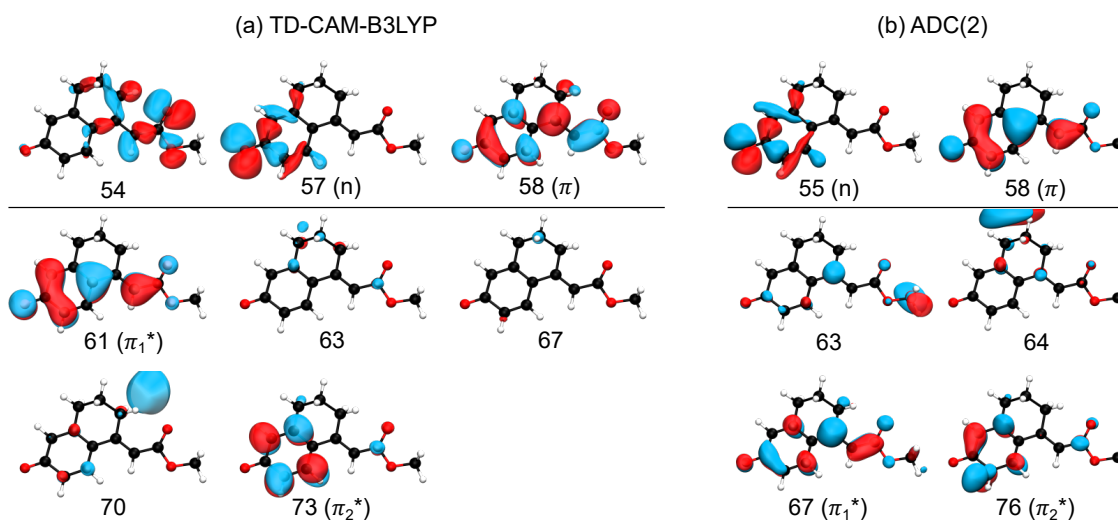


**Figure 4.11:** Relevant orbitals contributing to the electronic transitions of  $NpCE^-$  listed in Table 4.6 determined from (a) TD-CAM-B3LYP/6-311++G(3df,3pd) and (b) ADC(2)/6-31+G\*\* calculations.

Overall, the three transitions have similar characters and orbital contributions across the four chromophores. Hence, a comparison of the excited state calculations for the four chromophores is presented in Table 4.7 and Figure 4.12 illustrates a simplified depiction of the orbital transitions alongside the orbitals calculated for  $pCA^-$ . The  $\pi$  and  $\pi_1^*$  orbitals are delocalised across the whole chromophore whereas

the  $n$  and  $\pi_2^*$  orbitals are more localised on the phenoxide end of the anion. Hence, the  $S_3(2^1\pi\pi^*)$  and the  $S_2(1^1n\pi^*)$  transitions have significant charge transfer character. The delocalised  $\pi$  orbital is the highest occupied molecular orbital and the electronic configuration of the  $D_0$  state of the neutral radical has a hole in this orbital, as shown.

**Table 4.7:** Vertical excitation energies (VEEs) calculated using CAM-B3LYP/6-311++G(3df,3pd) and ADC(2)/6-31+G\*\* compared with SA-CASSCF(14,12)-PT2/cc-pVDZ<sup>42</sup> calculated values and experimental values.<sup>33</sup> VEEs are given in eV and oscillator strengths are shown in brackets.

		$pCA^-$	$pCE^-$	$PpCE^-$	$NpCE^-$
CAM-B3LYP 6-311++G(3df,3pd)	$S_1: 1^1\pi\pi^*$	3.45 (0.910)	3.43 (0.949)	3.49 (0.952)	3.36 (0.812)
	$S_2: 1^1n\pi^*$	4.10 (0.000)	4.12 (0.000)	4.15 (0.000)	4.10 (0.000)
	$S_3: 2^1\pi\pi^*$	4.33 (0.071)	4.31 (0.110)	4.34 (0.056)	4.40 (0.026)
ADC(2) 6-31+G**	$S_1: 1^1\pi\pi^*$	2.96 (1.000)	2.96 (1.021)	3.02 (1.032)	2.82 (0.885)
	$S_2: 1^1n\pi^*$	3.35 (0.000)	3.37 (0.000)	3.39 (0.000)	3.26 (0.000)
	$S_3: 2^1\pi\pi^*$	4.13 (0.091)	4.10 (0.097)	4.10 (0.061)	3.94 (0.065)
SA-CASSCF (14,12)-PT2 cc-pVDZ	$S_1: 1^1\pi\pi^*$	2.96	2.94	-	-
	$S_2: 1^1n\pi^*$	3.65	3.65	-	-
	$S_3: 2^1\pi\pi^*$	3.82	3.82	-	-
Experiment	$S_1: 1^1\pi\pi^*$	2.89	2.88	-	-

The calculated oscillator strength for the  $S_0 \rightarrow S_1$  transition is near unity for each of the chromophores whereas that for the  $S_0 \rightarrow S_2$  transition is zero. The  $S_0 \rightarrow S_3$  transition has a non-zero oscillator strength for each chromophore of approximately 0.1. From Tables 4.2 and 4.7, and the VDEs and VEEs plotted in Figure 4.3, it is clear that the  $D_0$  and  $S_1$  states lie close in energy, particularly for  $pCA^-$ ,  $pCE^-$  and  $PpCE^-$ . Due to the good agreement between the literature and ADC(2) methods, the ADC(2) values are plotted on the spectra in Figure 4.3. The CAM-B3LYP VEEs are similar to those calculated for PYP chromophores in earlier work using the same method;<sup>38</sup> however, the VEEs for  $pCA^-$  and  $pCE^-$  are consistently  $\sim 0.5$  eV higher than those calculated using higher level theory<sup>42</sup> and obtained from action absorption spectra.<sup>33</sup> The VEEs calculated using the ADC(2)/6-31+G\*\* method for  $pCA^-$  and  $pCE^-$  are in good agreement with those calculated using the SA-CASSCF(14,12)-PT2/cc-pVDZ method<sup>42</sup> and with the available experimental

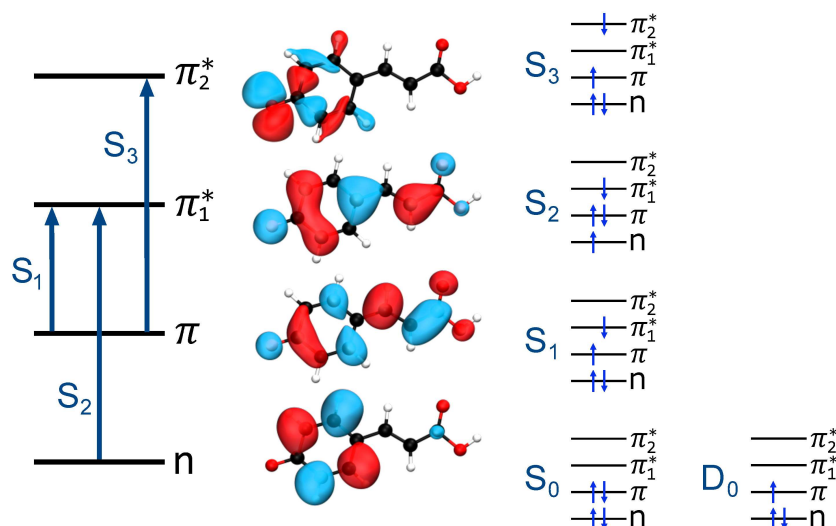


**Figure 4.12:** Left: The main molecular orbitals involved in the transitions to the first three singlet excited states of the anion. Although the MOs plotted are those calculated for  $pCA^-$ , they are similar for all the chromophores (see Figures 4.8 to 4.11). Right: The dominant electron configurations associated with the ground state of the anion ( $S_0$ ) and neutral radical ( $D_0$ ) and the first three singlet excited states of the anion for all the chromophores.

measurements,<sup>33</sup> so we use the VEEs calculated with this method to assist with the interpretation of our experimental measurements.

The electron configurations of the accessible electronic excited states of the anions and the corresponding neutral radicals (Figure 4.12) are useful in the consideration of coupling strengths of the excited states of the anion to the detachment continua (see Section 1.6). Indirect PD from the  $S_1$  state to the  $D_0$  continuum involves removing a single electron from the  $\pi_1^*$  orbital to yield the  $D_0$  electron configuration. Vibrational states of  $S_1$  that lie in the  $D_0$  continuum have shape resonance character and are coupled strongly to the continuum. Indirect PD from  $S_3$  involves removing an electron from the  $\pi_2^*$  orbital to afford the electronic configuration of  $D_0$ . The  $S_3$  state has excited shape resonance character with respect to the  $D_0$  continuum and electron detachment through this channel is expected to be very fast. In contrast, indirect PD from the dark  $S_2$  state to the  $D_0$  continuum involves removing a  $\pi_1^*$  electron and making the  $n \rightarrow \pi$  electronic transition. Thus  $S_2$  has Feshbach resonance character with respect to the  $D_0$  continuum and indirect detachment from this state is expected to be relatively slow. Although the  $D_1$  VDEs are higher than the photon energies employed in this work, adiabatic detachment

to  $D_1$  from the  $S_2$  and  $S_3$  states cannot be ruled out. The  $D_1$  state has electronic configuration  $n^1\pi^2\pi_1^{*0}\pi_2^{*0}/n^1\pi^1\pi_1^{*1}\pi_2^{*0}$  so the  $S_3$  state has Feshbach resonance character with respect to the  $D_1$  continuum. This suggests that indirect PD from  $S_3$  to  $D_1$  will not be able to compete with indirect PD to  $D_0$  or ultrafast IC to lower-lying states. The  $S_2$  state is an excited shape resonance with respect to  $D_1$ , indicating that indirect PD from  $S_2$  to  $D_1$  is possible; however, there would still be competition from internal conversion to  $S_1$  or  $S_0$ . Overall, it seems most likely that the photoelectron spectra are dominated by direct and indirect electron emission to the  $D_0$  continuum.

### 4.3.3 Interpreting the spectra

On the whole, the calculated electronic structures of the four chromophores differ very little, suggesting that the chromophores have the same electronic relaxation pathways available. This is perhaps expected for four chromophores carefully designed to retain the major conjugated backbone. Hence, the spectra of the locked chromophores can be compared very closely with those of the unlocked chromophores. If we first consider only the spectra of  $pCA^-$ , it is possible to simplify the 346–310 nm spectra to be only a combination of three features pertaining to three relaxation pathways. Possible direct and indirect photodetachment processes were discussed in Chapter 1 for PYP chromophore analogues and are illustrated in the Jablonski diagram presented in Figure 1.4. Figure 4.13 shows the anion photoelectron spectra of  $pCA^-$  recorded with wavelengths 310–346 nm both as a function of eKE and eBE. Each plot shows how the spectrum could be reconstructed from some combination of three features, analogous to the cartoon representation in Fig 1.5 where it can be seen that as photon energy is increased, the indirect features shift linearly in eBE but remain at constant eKE. Additionally, the direct detachment feature remains at constant eBE but shifts linearly in eKE.

First consider the 346 nm spectrum of  $pCA^-$  (bottom panel of Figure 4.13). It is possible to obtain an intensity profile to model the direct detachment and low eKE features, shown by the purple and grey areas, respectively. These profiles may then be fitted to the spectra recorded at higher photon energies and the remaining



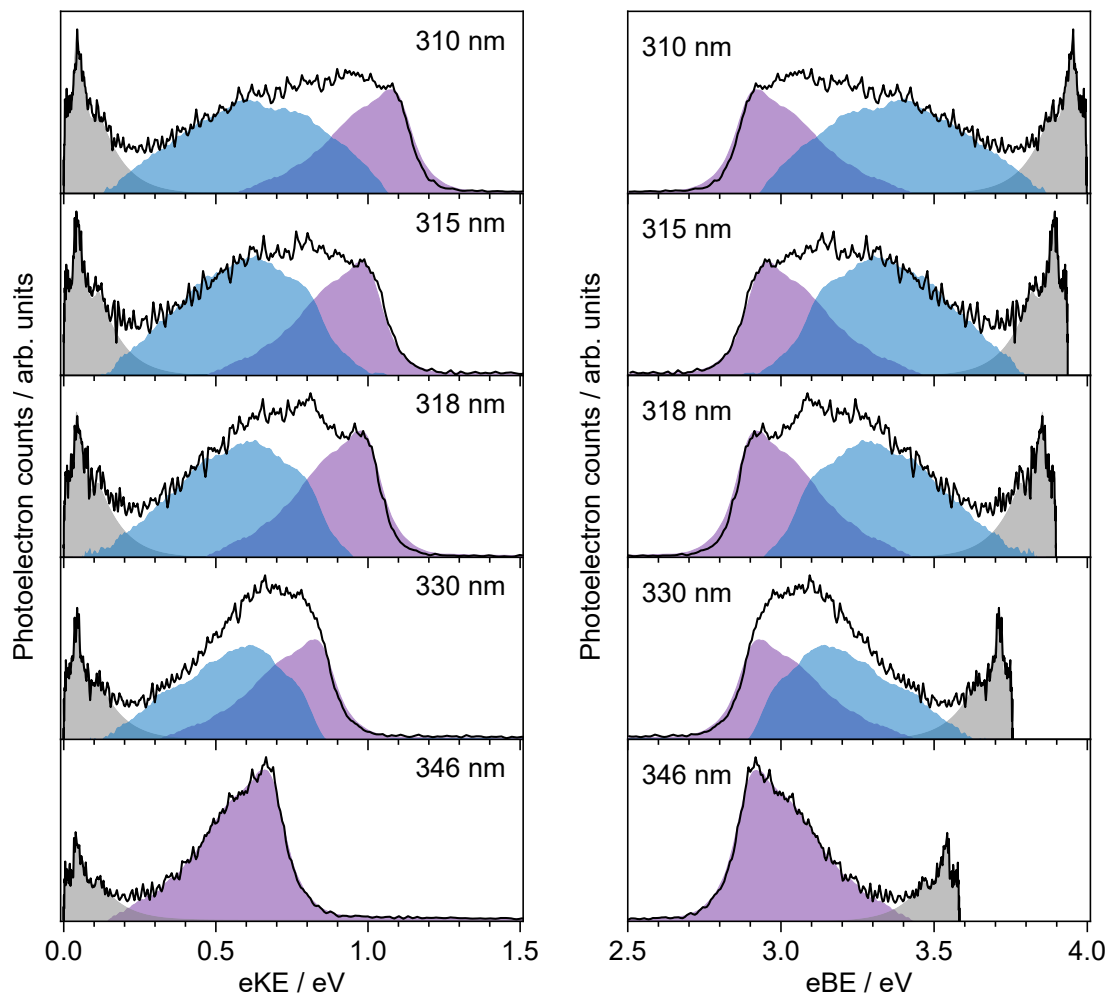


**Figure 4.13:** Photoelectron spectra of  $p\text{CA}^-$  recorded at wavelengths 310–346 nm plotted as a function of eKE and eBE. Purple shading indicates direct photodetachment from  $S_0$  to  $D_0$ , blue shading shows indirect photodetachment from  $S_3$  and the grey shading indicates thermionic emission. Direct and thermionic emission profiles are obtained from the 346 nm spectrum and then scaled to fit the other wavelengths. These areas are then subtracted from the total intensity to give the  $S_3$  indirect detachment.

signal extracted by subtraction. This allows us to isolate a third feature, shown in blue, that we assign to autodetachment from the high-lying  $S_3(2^1\pi\pi^*)$  state. The eKE at the maxima of this indirect photodetachment feature corresponds to  $E(S_3) - E(D_0) \sim 0.6$  eV where  $E(S_3)$  and  $E(D_0)$  denote the adiabatic excitation energy to  $S_3$  and  $D_0$  ADE, respectively. Hence, assuming the  $VDE(\sim ADE) = 2.92$  eV,  $E(S_3)$  may be approximated to 3.5 eV which is in agreement with the onset of the second band in the action-absorption spectrum of  $pCE^-$ .<sup>34</sup>

The analysis of the photoelectron spectra recorded for the other chromophores may be considered in a similar way. *I.e.* as some combination of three spectral features: direct detachment at low eBE, indirect detachment from  $S_3$  broadening the direct detachment peak and a low eKE feature. The 400 nm spectra include no indirect detachment from  $S_3$  but rather are dominated by the low eKE feature with small contributions from direct detachment.

#### 4.3.4 The role of torsional motion

The photoelectron signal forming the low eKE signal could be autodetachment from a low-lying electronically excited state such as  $S_1$  which could be populated directly at 400 nm, or *via* internal conversion from the higher  $S_3$  state at shorter wavelengths. Alternatively, this feature could be attributed to thermionic emission from a vibrationally-hot ground state following internal conversion from an excited state of the anion back to the ground state. It could also be a combination of these processes. For the feature to pertain fully to  $S_1$  autodetachment, one would expect a marked difference in the spectral profile measured at various wavelengths. At higher photon energies, one would expect broader features in the spectra as more vibrational transitions are available in the photodetachment process. Hence this suggests that the dominant electronic relaxation mechanism forming the low eKE features is IC to  $S_0$  followed by TE. However, the ratio of photoelectrons attributed to TE compared with those attributed to direct PD at 400 nm decreases in the order  $pCA^- \approx pCE^- \gg PpCE^- > NpCE^-$ . This suggests that torsional motions around both single bonds adjacent to the alkene group are involved in steering the PYP chromophore towards the  $S_1/S_0$  conical intersection but that rotation around

the single bond between the alkene moiety and the phenoxide group plays a more important role.

Photoexcitation at 346 nm results predominantly in direct detachment from  $S_0$ ; however, the observation of  $eKE \approx 0$  ( $eBE \approx h\nu$ ) photoelectrons with an overall exponential decay profile suggests that there could be some contribution from resonant excitation of excited states of the anion followed by IC to  $S_0$  and subsequent TE. The resonant excitation process cannot be assigned to any particular excited state of the anion, but could be to the high vibrational levels of  $S_1$ , low vibrational levels of  $S_3$  or the  $S_2$  state, through vibronic mixing with a bright state. In terms of the role of torsional motions, the ratio of photoelectrons attributed to TE compared with those from direct PD is lower for  $NpCE^-$  than the other three chromophores, supporting the idea that rotation around the single bond between the alkene moiety and the phenoxide group plays an important role in IC from  $S_1$  to  $S_0$ .

Increasing the photon energy from 330 to 310 nm results in a significant contribution from indirect PD from  $S_3$  and TE from  $S_0$  for  $pCA^-$ ,  $pCE^-$  and  $PpCE^-$ . In contrast, indirect PD is far less pronounced for  $NpCE^-$  and the contribution from TE only increases slightly with increasing photon energy. The most likely explanation for these observations is that as the photon energy increases, increasing population of  $S_3$  followed by internal conversion to  $S_1$  occurs and subsequent autodetachment to  $D_0$  or IC to  $S_0$  followed by TE. Locking the rotation around the single bond between the alkene moiety and the phenoxide group in  $NpCE^-$  inhibits these pathways, which suggests that rotation around the single bond between the alkene moiety and the phenoxide group also plays a role in IC from  $S_3$  to  $S_1$ .

Since reporting this work, Bull *et al.* have published femtosecond time-resolved anion photoelectron spectroscopy measurements of the model PYP chromophore  $pCE^-$  in which they report that the low  $eKE$  feature is not attributed to thermionic emission from  $S_0$  but is instead largely autodetachment from  $S_1$ .<sup>41</sup> In addition, they report evidence for autodetachment from a dipole bound state that is populated through internal conversion from the  $S_1$  state, possibly with single bond rotation about the phenolate moiety as a key coupling mode. In their experiments, they populate the  $S_1$  state directly with a 2.83 eV pump pulse and, following a delay,

photodetach an electron using a 1.55 eV probe pulse. The authors find stark differences in the potential energy surface of the  $S_1$  state for the  $pCE^-$  anion used in their work when compared to that found for the ketone analogue reported in previous time-resolved measurements by Zewail and coworkers<sup>32</sup> and subsequent measurements by their own group.<sup>17</sup> This leads the authors to highlight how sensitive the  $S_1$  potential energy surface can be to slight differences in molecular structure and how ambiguous single-colour nanosecond photoelectron spectroscopy measurements can be to details in the low eKE features. This brings uncertainty to the assignment of the low eKE signal found in the spectra for the PYP chromophores presented in this Chapter. For example, by comparing the  $D_0$  VDEs and  $S_1$  VEEs (see the combs in Figure 4.3), it can be seen that for  $pCA^-$  the  $S_1$  state is slightly bound but with the other chromophores, the  $S_1$  state lies in the continuum with varying degrees. Hence, despite the similarity in the characters of the  $S_1$  states, there could be vast differences in the potential energy surfaces of those states leading to differences in the photodetachment pathways available from  $S_1$ . However, there is much still to consider in the similarities found in the shape of the spectrum at low eKE across the 400–310 nm range. Subsequently, Bull *et al.* also presented single-colour photoelectron spectra of  $pCE^-$  probing the first three singlet excited states.<sup>208</sup> They assign the low eKE signal recorded at higher photon energies to also be autodetachment from  $S_1$  or a dipole bound state by comparison with the profiles of the lower photon energy spectra. The photoelectron spectra probing at wavelengths resonant with the  $S_2$  and  $S_3$  bands show complex and vibrational mode-specific behaviours in how the excited state population converts to the  $S_1$  state indicating the need for cry-cooled ions, high-level simulation of the potential energy surfaces and time-resolved photoelectron spectroscopy measurements.

Regarding the possibility of dipole-bound states present with the chromophores discussed in this chapter, the permanent dipoles have been calculated for each chromophore in its neutral radical ( $D_0$ ) state as shown in Table 4.8. For each chromophore, the dipole is larger than 2.5 D, the minimum dipole moment required to bind an electron in a dipole-bound state, as determined experimentally.<sup>209,210</sup> In addition, the energies of the first excited states are similar to the detachment energies

(and thus dipole bound states) and so it seems likely that the first excited state could couple to dipole bound states. It would very interesting to study the dynamics of the first excited states for the locked chromophores discussed here in terms of how they access these dipole bound states. In particular, the dipole moments of chromophores  $pCE^-$  and  $NpCE^-$  are similar in both magnitude and direction and it has been proposed that the single bond rotation locked in  $NpCE^-$  is an important coupling mode for internal conversion from the first excited state to the dipole bound state.<sup>41</sup> Hence, with careful calculation of the excited state surfaces and high-resolution time-resolved photoelectron spectroscopy measurements, locked chromophores such as  $NpCE^-$  could help unravel the nuclear coordinates central to the internal conversion process to the dipole bound state.

**Table 4.8:** Permanent dipole moments of each chromophore in its neutral radical ( $D_0$ ) state, calculated using B3LYP/6-311++G(3df,3pf). The direction of the dipoles are illustrated by the purple arrows and the magnitudes are shown in Debye calculated with the optimised  $S_0$  geometries (FC) and optimised  $D_0$  geometries (relaxed).

	$pCA^-$	$pCE^-$	$PpCE^-$	$NpCE^-$
FC	2.258	3.293	4.637	3.821
relaxed	2.923	3.944	5.048	3.821

## 4.4 Outlook and conclusion

From a combination of photoelectron spectroscopy measurements and computational chemistry calculations, it was found that the torsional motions around the single bonds either side of the alkene moiety play an important role in the electronic relaxation of isolated PYP chromophores in the gas phase. It was found that both single bond rotations are involved in steering the PYP chromophore towards the  $S_1/S_0$  CI and that rotation around the single bond between the alkene moiety and the phenoxide group plays a particularly important role. From measurements at higher photon energies, it was also found that rotation around this single bond

between the alkene moiety and the phenoxide group plays a key role in IC from  $S_3$  to  $S_1$ . This suggests that torsional motions around the single bonds, and particularly around the one between the alkene and phenoxide groups are not restricted in the protein. This supports the conclusion of the earlier time-resolved study by Lee *et al.* on the ketone analogue of the PYP chromophore in which isomerisation occurred on a similar time scale to the protein, suggesting entry into the photocycle must be unhindered by torsional motion.<sup>32</sup>

The photoelectron spectra described in this Chapter were recorded using single-colour laser pulses and so given the information available at the time, the assignment of thermionic emission to the low eKE features was appropriate. Subsequent time-resolved measurements of  $pCE^-$  have since been performed elsewhere,<sup>41</sup> which highlight the difficulty in distinguishing the nature of the photodetachment pathway(s) leading to low eKE signal using purely static single-colour measurements. It has been noted how sensitive the  $S_1$  potential energy surface may be to slight differences in the structure of the chromophore. In the other measurements of  $pCE^-$ , the authors found no evidence of  $S_1$  to  $S_0$  conversion, while in a previous time-resolved study of a ketone analogue, repopulation of the ground state was reported.<sup>32</sup> Hence, it is difficult to assume an  $S_1/S_0$  CI is accessible for all the chromophores discussed in this chapter without pump-probe measurements and simulation of the excited state surfaces. This makes PYP chromophores interesting targets to study how slight systematic differences in the structure of the chromophore may cause marked differences in the excited state dynamics and photodetachment pathways using computational simulations and time-resolved photoelectron spectroscopy techniques.

## Chapter 5

# The role of photoisomerisation on the photodetachment of the photoactive yellow protein chromophore

Photoisomerisation is of key importance for successful entry into the photocycle of the photoactive yellow protein. Following photoexcitation, the protein microenvironment steers the excited state population towards isomerisation and away from other competing relaxation pathways such as electron emission. The work in this Chapter aimed to investigate the effect of locking the double bond (preventing isomerisation) on the competition of these photochemical pathways using a combination of anion photoelectron spectroscopy (400–310 nm) and quantum chemistry calculations.

### 5.1 Introduction

As described in Chapter 1, the chromophore that lies at the core of PYP is a deprotonated *trans-para*-coumaric acid anion, covalently-bound to the protein *via* a thioester linkage. The first steps of the photocycle of PYP begin following photoexcitation of the first excited singlet state of the chromophore ( $\lambda_{\text{max}} \approx 400 \text{ nm}$ )

which induces a *trans-cis* isomerisation about the central C=C bond.<sup>3</sup> In the protein, isomerisation proceeds *via* a bicycle-pedal or hula-twist motion rather than a simple one-bond flip, to conserve volume in the tight pocket within the protein microenvironment.<sup>211</sup> In addition to the functional photochemical pathway, alternative, competing processes such as internal conversion (IC) and electron emission may occur.<sup>37,38,48,63,205</sup> Studying the photophysical behaviour of the isolated chromophore in the gas phase, free from solvent interactions, provides an understanding of the intrinsic dynamics of the chromophore and hence allows us to infer the role the protein environment plays in guiding the excited state dynamics away from these competing pathways.

There have been many studies of PYP and isolated PYP chromophores in solution investigating the role of torsional motions and isomerisation in the chromophore. These have included isolated chromophores with conformational locks over the single<sup>51</sup> and double-bond rotations.<sup>47,48,204</sup> Hellingwerf and co-workers reconstructed PYP with non-isomerising analogues of the PYP chromophore in which an ester linkage was introduced to tether across the double bond, or in which the C=C linkage was replaced with a C≡C bond.<sup>204</sup> The authors reported that both reconstructed PYP systems showed evidence of successful entry into the photocycle, which led to the suggestion that isomerisation was not necessary for the function of PYP. Later work reported that absorption for the ester-bridged chromophore was blue-shifted and the excited state lifetime lengthened (3 ns compared to 2 ps for the unlocked chromophore), hence suggesting that isomerisation facilitated fast internal conversion to the ground state.<sup>48</sup> Our understanding of the excited-state dynamics of the PYP chromophore has benefited significantly from these studies. However, the chromophores used all had additional functional groups which could possibly have obscured the subtle differences in the excited-state behaviour, intrinsically or through interactions with the protein or solvent. Furthermore, the relevance of double-bond rotation on competing photoionisation processes is relatively unexplored.

The work described in this chapter follows on from previous studies in which anion photoelectron spectroscopy and quantum chemistry calculations were employed to explore the photophysics of PYP chromophore analogues.<sup>37,38,205</sup> In the previ-



ous chapter, the PYP chromophore analogues employed included two torsion-locked species and aimed to investigate the importance of the single-bond rotations at either site adjacent to the C=C bond. This chapter reports on a similar study aimed to better understand the role of isomerisation in the chromophore on the electron emission processes following photoexcitation. To do so, the measured spectra and computational results are compared for two chromophores: the unlocked, methyl-ester analogue described in the previous chapter,  $p\text{CE}^-$ , and a carefully-designed locked analogue with an ethane bridge inhibiting double bond rotation,  $\text{EB}p\text{CE}^-$  (Figure 5.1).  $\text{EB}p\text{CE}^-$  is unique in that no additional functionality has been introduced and the ring strain is minimised by employing a six-membered ring. The single bond connecting the alkene to the ester moiety is also locked (similar to  $\text{P}p\text{CE}^-$  in the previous chapter). However, this rotation was found to be of less importance than the single bond connecting the alkene and phenolate moieties.<sup>205</sup>

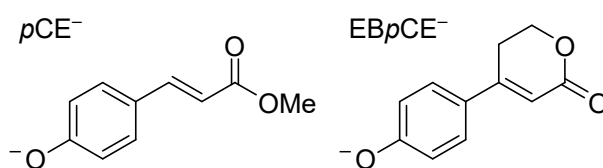


**Figure 5.1:** Structures of the deprotonated PYP chromophores used in this study.

## 5.2 Methods

### 5.2.1 Chromophores

$p\text{CE}$  (methyl *trans*- $p$ -coumarate) was purchased from Tokyo Chemical Industry and used without further purification. 4-(4-hydroxyphenyl)-5,6-dihydro-2H-pyran-2-one ( $\text{EB}p\text{CE}^-$ ) was prepared by collaborators at UCL using methods described in detail in the supporting material of Reference 212.

### 5.2.2 Photoelectron spectroscopy

Anion photoelectron spectra were recorded using the spectrometer described in Chapter 2. Specifically, nanosecond laser pulses of wavelength 310–346 nm were

generated by frequency-doubling the output of a Nd:YAG pumped dye laser. Femtosecond laser pulses ( $>50$  fs, 250 Hz) with wavelength centred at  $\sim 400$  nm were produced by frequency-doubling the output of a commercial amplified Ti:Sapphire femtosecond laser system. Electron kinetic energy spectra were obtained by calibrating the radial photoelectron velocity distribution against the photoelectron spectrum of iodide<sup>117</sup> (310–346 nm), deprotonated indole<sup>118</sup> (397.85 nm) and *p*-HBDI<sup>-119</sup> (400 nm). The energy resolution,  $\Delta E/E$ , was  $<5\%$  for the 310–346 nm spectra and around 14% for the 400 nm spectra. The temporal window used to collect electrons at the detector was 75 ns.

### 5.2.3 Calculations

The computational methods used here are as described in the previous chapter and in more detail in Chapter 3. Briefly, the structures were optimised and vibrational analyses were performed to confirm that the structures were true minima at the B3LYP/6-311++G(3df,3pd) level of theory. VEEs were calculated for singlet states of the anions with both TD-CAM-B3LYP/6-311++G(3df,3pd) and ADC(2)/6-31+G\*\*. A description of the benchmarking of these methods, using PYP chromophores *p*CA<sup>-</sup> and *p*CE<sup>-</sup>, is presented in Table 4.1. VDEs were calculated to compare to the measured values using various methods: the energy difference method at the B3LYP/6-311++G(3df,3pd) level, EPT/6-311++G(3df,3pd) and EOM-IP-CCSD/aug-cc-pVDZ approaches. Canonical heat capacities were obtained from frequency calculations to estimate the temperature of the neutral radical following thermionic emission. Geometry optimisations, vibrational frequencies, TD-DFT and EPT calculations were performed using the Gaussian09 software suite, while EOM-IP-CCSD and ADC(2) calculations were carried out using the Q-Chem software package.

## 5.3 Results and discussion

### 5.3.1 Photoelectron spectra

Anion photoelectron spectra of  $\text{EB}p\text{CE}^-$  are presented alongside those of the unlocked reference chromophore  $p\text{CE}^-$  in Figure 5.2 as a function of eKE and eBE ( $\text{eBE} = h\nu - \text{eKE}$ ). Combs marked on the eBE plots indicate the calculated VDEs and VEEs. Note that the data presented here for  $p\text{CE}^-$  is as shown in the previous chapter. The composition of each of the spectra may be considered as a combination of three processes, similar to the  $p\text{CA}^-$  spectra presented in Chapter 4 (Figure 4.13). Firstly, a sharp rising edge at low eBE, which remains at a constant eBE with increasing photon energy representing direct detachment to the  $\text{D}_0$  continuum. Secondly, an underlying feature that appears as a broadening of this direct detachment peak towards higher eBE with increasing photon energy attributed to autodetachment from a high-lying electronically excited state of the anion. Finally, a feature at low eKE that could result from autodetachment from a low lying electronically excited state of the anion or thermionic emission from a vibrationally hot ground state of the anion. With the higher photon energies used here, it is most likely that these low lying electronic states are not populated by direct photoexcitation, but are instead accessed through internal conversion process(es) from higher-lying electronically excited states of the anion. Such relaxation pathways are illustrated in a Jablonski diagram in Figure 1.4.

The 346 nm spectra contain the lowest contributions from indirect detachment processes and so are most dominated by direct detachment to  $\text{D}_0$ . Hence, the maxima of the 346 nm spectra were used as an estimate of the VDEs. This gives VDE values in a similar range to other PYP chromophores: 2.85 eV for  $p\text{CE}^-$  and 3.02 eV for  $\text{EB}p\text{CE}^-$ . These VDEs are listed together with the calculated VDEs later in Table 5.1.

Photoelectron spectra were also recorded at a wavelength of  $\sim 400$  nm and these are shown in the eKE plots in Figure 5.2 and in greater detail, later, in Figure 5.7. The photon energy at 400 nm is much closer to the detachment thresholds of the chromophores and so direct detachment is much less significant. Instead, these

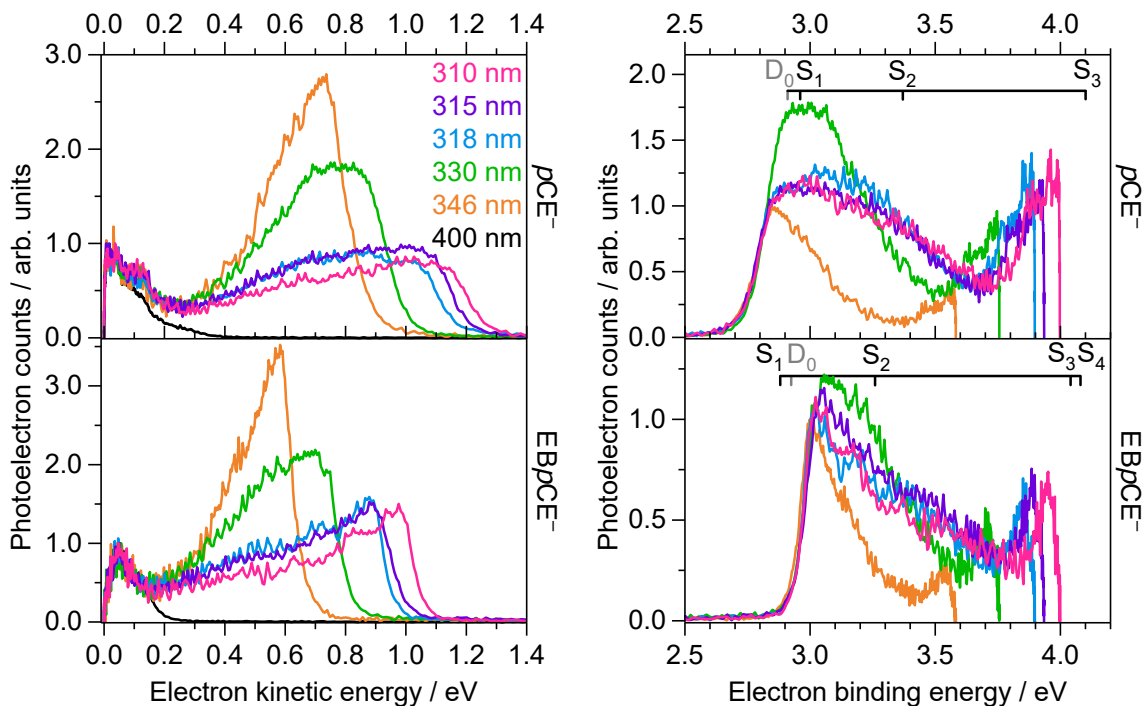
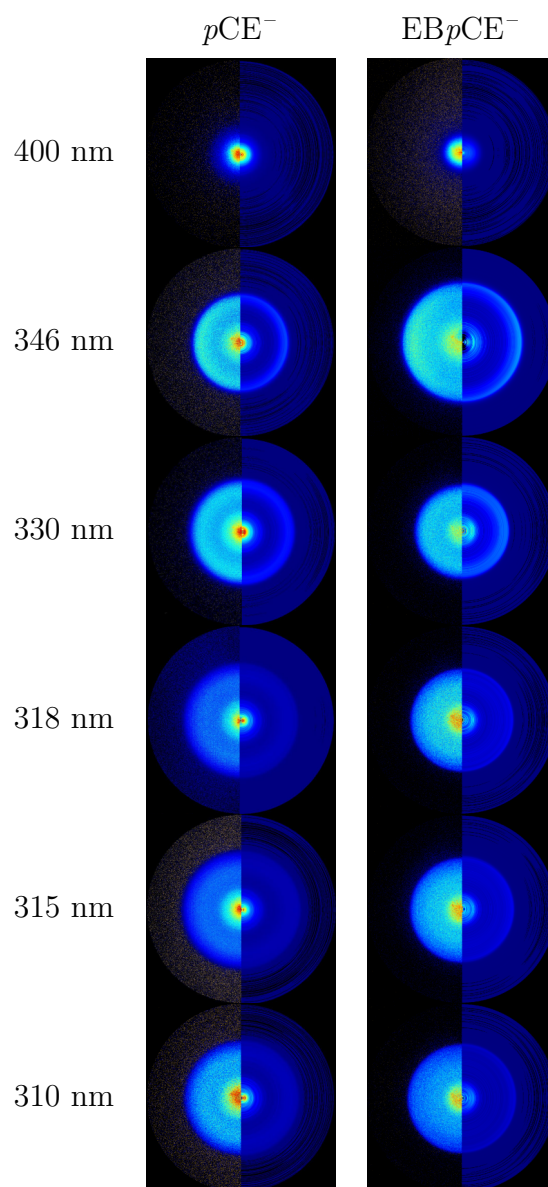


**Figure 5.2:** Photoelectron spectra of  $pCE^-$  and  $EBpCE^-$  recorded at 310 nm (4.00 eV), 315 nm (3.94 eV), 318 nm (3.90 eV), 330 nm (3.76 eV), 346 nm (3.58 eV) and 400 nm (3.10 eV). Intensities of the spectra plotted as a function of eKE (left) are normalised to the maximum of the low eKE feature. Intensities of the spectra plotted as a function of eBE (right) have been scaled to align the rising edges and are normalised to the maximum of the rising edges of the 346 nm spectra. The 400 nm spectra are shown in greater detail later in Figure 5.7. Combs mark the EPT calculated VDEs (grey) and VEEs calculated using  $ADC(2)/6-31+G^{**}$  (black).

spectra are dominated by indirect photodetachment and form very similar spectral shapes to the low eKE features observed in the spectra recorded at higher photon energies.

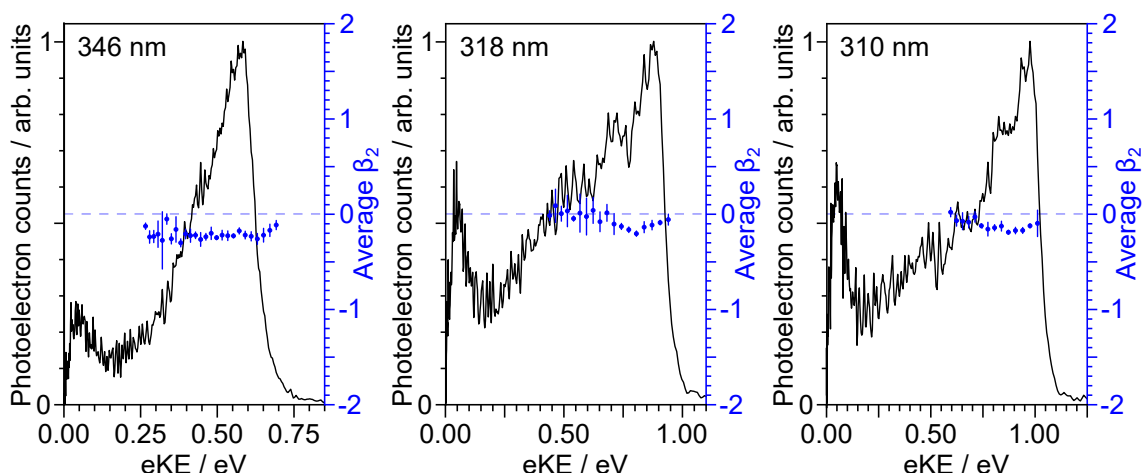
The photoelectron images recorded for  $pCE^-$  and  $EBpCE^-$  are presented in Figure 5.3. The angular distributions are largely isotropic, although there appears to be some weak (perpendicular) anisotropy in some of the images for  $EBpCE^-$ . This is perhaps most evident in the 346 nm image. This is similar to  $NpCE^-$  in the previous chapter, another locked chromophore that also showed weak anisotropy in the measured photoelectron images. Analogously,  $EBpCE^-$  is also a very rigid structure when compared to the unlocked  $pCE^-$  chromophore and so this could explain the anisotropy observed here in the  $EBpCE^-$  images.

Figure 5.4 shows the anisotropy parameters determined from the measured an-



**Figure 5.3:** Photoelectron images recorded for  $p\text{CE}^-$  and  $\text{EB}p\text{CE}^-$  (left halves: raw VMI images; right halves: pBASEX inverted images). In all images the polarisation axis of the laser is vertical with respect to the images.

gular distributions for  $\text{EBpCE}^-$  recorded at wavelengths of 346, 318 and 310 nm. The  $\beta_2$  values are presented as five-point averages over the main intensity peak with  $\beta_2 \sim -0.25$  across the peak in the 346 nm spectrum and approximately  $-0.15$  in the 318 and 310 nm spectra. This decrease in anisotropy could be due to the involvement of a resonance at the higher photon energies.



**Figure 5.4:** Photoelectron spectra of  $\text{EBpCE}^-$  recorded at 346 nm (3.58 eV), 318 nm (3.90 eV) and 310 nm (4.00 eV). Intensities of the spectra plotted as a function of eKE and are normalised to the peak maxima. Anisotropy parameters  $\beta_2$  are shown as five-point averages over the main peak. The horizontal dashed line indicates  $\beta_2 = 0$ , an isotropic distribution. Images in the top left are reproduced from Figure 5.3 for convenience.

### 5.3.2 Computational results

As noted earlier, by observation of the onset of the photoelectron spectra, the detachment thresholds of both chromophores are similar. The VDEs are estimated by the maxima of the 346 nm spectra and are listed in Table 5.1 along with calculated values for the detachment energies using various methods. The DFT VDEs and ADEs of  $\text{EBpCE}^-$  are close to one another, suggesting that the optimised geometries of the anion and neutral radical are similar, in agreement with previous work on other model PYP chromophores.<sup>37,38,205</sup> The calculated VDEs are all within  $\sim 0.1$  eV of the experimental maximum. The EPT method has provided the closest agreement with the experimental values and so these VDEs are plotted on the spectra in Figure 5.2. The calculated  $D_1$  VDEs are all significantly higher than the

Method	$p\text{CE}^-$		$\text{EB}p\text{CE}^-$	
	$D_0$	$D_1$	$D_0$	$D_1$
EPT	2.91 (0.88)	5.18 (0.87)	3.05 (0.99)	5.25 (0.87)
EOM-IP-CCSD	2.78	4.42	2.93	4.50
B3LYP VDE	3.01		3.15	
B3LYP ADE (0-0)	2.91		3.05	
Experiment	$2.85 \pm 0.05$		$3.02 \pm 0.05$	

**Table 5.1:** Vertical detachment energies (VDEs), B3LYP/6-311++G(3df,3pd)  $D_0$ - $S_0$  adiabatic detachment energies (ADEs) (0-0 transition) and maxima of the experimental 346 nm photoelectron spectra given in eV for  $p\text{CE}^-$  and  $\text{EB}p\text{CE}^-$ . VDEs were calculated using EPT/6-311++G(3df,3pd) (pole strengths in parentheses), EOM-IP-CCSD/aug-cc-pVDZ and B3LYP/6-311++G(3df,3pd).

photon energies used ( $\leq 4$  eV). Hence, it is unlikely that there is any contribution from detachment processes to higher lying  $D_{n>0}$  continua.

The detachment thresholds found for  $\text{EB}p\text{CE}^-$  are consistently a little higher than those of  $p\text{CE}^-$ . Differences in VDEs like this are generally understood by considering the relative stabilities of the anions and so at first, it may seem non-intuitive that the locked chromophore has a higher VDE (more stable anion) because there is extra ring strain from the molecular tether. However, there are several weak stereoelectronic effects to consider that stabilise  $\text{EB}p\text{CE}^-$  relative to  $p\text{CE}^-$ . First, consider the orientation of the non-bonding orbitals at the ester oxygen site in each chromophore; in  $p\text{CE}^-$ , this orbital is able to overlap with the  $\text{C}=\text{O}$   $\sigma^*$  and hence destabilise the anion. Conversely, this effect is not possible in  $\text{EB}p\text{CE}^-$  and so this stabilises the locked chromophore in reference to  $p\text{CE}^-$ . Secondly, in  $\text{EB}p\text{CE}^-$ , hyperconjugation between the  $\text{C}-\text{H}$   $\sigma$  orbitals in the ring and the non-bonding orbitals of the ester oxygen stabilises the anion and this effect is not present with  $p\text{CE}^-$ . Similar effects were discussed in the previous chapter when comparing  $p\text{CE}^-$  and  $\text{P}p\text{CE}^-$  but the VDEs were very similar in that case due to this stereoelectronic stabilisation also being offset by destabilising ring strain effects. Here, with  $\text{EB}p\text{CE}^-$ , there is a small  $\sim 0.1$  eV difference in the VDEs and so, by comparison with  $\text{P}p\text{CE}^-$ , the extra stabilisation of  $\text{EB}p\text{CE}^-$  could be attributed to these stereoelectronic stabilising effects with minimal destabilising effects due to ring strain. A structural comparison of the two anionic structures is provided in Figure 5.5.

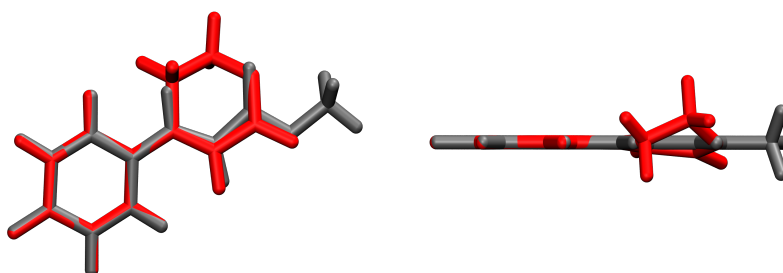


**Figure 5.5:** Optimised anion structure of  $\text{EBpCE}^-$  (red) superimposed on the optimised  $\text{pCE}^-$  structure (grey) with the positions of the carbon atoms in the phenolate ring overlapped. Comparisons are viewed from above (left) and the side (right).

VEEs to singlet states of the anion within the photon energy range used were calculated using TD-CAM-B3LYP/6-311++G(3df,3pd) and ADC(2)/6-31+G\*\*. For  $\text{pCE}^-$  these results are detailed in Table 4.4 and the relevant orbitals are shown in Figure 4.9. For  $\text{EBpCE}^-$ , the VEEs are listed in Table 5.2 and the relevant orbitals are represented in Figure 5.6. Tables 4.4 and 5.2 are truncated to form a simpler comparison of the two chromophores later in Table 5.3. As described in the previous chapter, the ADC(2)/6-31+G\*\* approach has been shown to provide VEEs in excellent agreement with experiment<sup>33</sup> and high-level theory<sup>42</sup> for  $\text{pCA}^-$  and  $\text{pCE}^-$  (see Table 4.1 for a comparison).

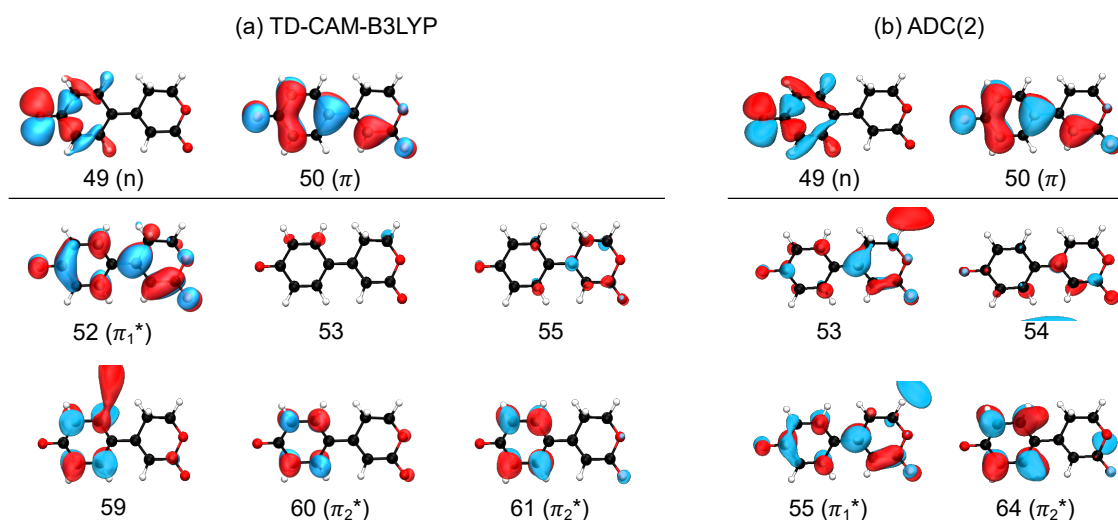


**Figure 5.6:** Relevant orbitals contributing to the electronic transitions of  $\text{EBpCE}^-$  listed in Table 5.2 determined from (a) TD-CAM-B3LYP/6-311++G(3df,3pd) and (b) ADC(2)/6-31+G\*\* calculations.



**Table 5.2:** Excited states calculated with TD-CAM-B3LYP/6-311++G(3df,3pd) and ADC(2)/6-31+G\*\* for EBpCE<sup>-</sup>. The vertical excitation energies (VEEs), main orbital contributions, weighting ( $c^2$ ) of each contribution and oscillator strengths ( $f$ ) for each transition are listed.

Method	State	VEE / eV	Main contribution(s)	$c^2$	$f$
TD-CAM-B3LYP	S <sub>1</sub>	3.381	50→52 $\pi_{(\text{HOMO})} \rightarrow \pi_1^*$	0.929	0.765
		4.086	49→52 $n \rightarrow \pi_1^*$	0.633	0.001
	S <sub>3</sub>	4.258	50→53	0.137	0.024
			50→55 $\pi_{(\text{HOMO})} \rightarrow \pi_2^*$	0.458	
			50→59	0.152	
			50→61	0.085	
			50→60	0.078	
	S <sub>4</sub>	4.339	50→55 $\pi_{(\text{HOMO})} \rightarrow \pi_2^*$	0.316	0.090
			50→59	0.215	
			50→61	0.184	
			50→60	0.143	
ADC(2)	S <sub>1</sub>	2.883	50→55 $\pi_{(\text{HOMO})} \rightarrow \pi_1^*$	0.307	0.871
			50→53	0.276	
	S <sub>2</sub>	3.261	48→55 $n \rightarrow \pi_1^*$	0.305	0.000
			48→53	0.236	
	S <sub>3</sub>	4.041	50→64 $\pi_{(\text{HOMO})} \rightarrow \pi_2^*$	0.213	0.024
			50→54	0.196	
	S <sub>4</sub>	4.076	50→54 $\pi_{(\text{HOMO})} \rightarrow \pi_2^*$	0.250	0.025
			50→64	0.191	

Both the TD-CAM-B3LYP and ADC(2) approaches find the first three singlet states of pCE<sup>-</sup> and EBpCE<sup>-</sup> to be of  $1\pi\pi^*$ ,  $1n\pi^*$  and  $2\pi\pi^*$  characters as the main contributions and so these are summarised in Table 5.3. However, there is some configurational mixing; most notably with the ADC(2) calculations of EBpCE<sup>-</sup>. Unlike pCE<sup>-</sup>, for EBpCE<sup>-</sup>, the  $\pi \rightarrow \pi_2^*$  transition was found to be the main contribution in the calculated transitions to both the S<sub>3</sub> and S<sub>4</sub> states. However, the ADC(2) VEEs and oscillator strengths to these states are very close suggesting that these states are strongly coupled. Hence, transitions to these states are both denoted here by the transition ( $S_0 \rightarrow 2\pi\pi^*$ ). Oscillator strengths for both chromophores have been calculated to be near unity for the  $1\pi\pi^*$  state and zero for the  $1n\pi^*$  state. The oscillator strengths for transitions to the  $2\pi\pi^*$  states are low, yet significant.

Overall, the calculated electronic structures and orbitals of the two chromophores are similar to one another, and also to those of other PYP chromophores described

		$1\pi\pi^*$ ( $S_1$ )	$1n\pi^*$ ( $S_2$ )	$2\pi\pi^*$ ( $S_3$ )	$2\pi\pi^*$ ( $S_4$ )
$p\text{CE}^-$	TD-DFT	3.43 (0.949)	4.12 (0.000)	4.31 (0.110)	
	ADC(2)	2.96 (1.021)	3.37 (0.000)	4.10 (0.097)	
$\text{EB}p\text{CE}^-$	TD-DFT	3.38 (0.765)	4.09 (0.001)	4.26 (0.024)	4.34 (0.090)
	ADC(2)	2.88 (0.871)	3.26 (0.000)	4.04 (0.024)	4.08 (0.025)

**Table 5.3:** Calculated VEEs at the TD-CAM-B3LYP/6-311++G(3df,3pd) and ADC(2)/6-31+G\*\* levels of theory, given in eV. Oscillator strengths are shown in parentheses.

in the previous chapter. Hence, the nature of the electronic excitations and the electronic configurations of the relevant electronic states may be considered for  $p\text{CE}^-$  and  $\text{EB}p\text{CE}^-$  as represented for  $p\text{CA}^-$  in Figure 4.12. Further, the  $\pi\pi^*$  states are coupled strongly to the  $D_0$  continuum, whereas the  $n\pi^*$  state is a Feshbach resonance with respect to the  $D_0$  continuum. Hence, autodetachment from either  $1\pi\pi^*$  or  $2\pi\pi^*$  is expected to be fast and autodetachment from  $1n\pi^*$  will be much slower. Thus it is likely that population in this state could undergo internal conversion to lower energy electronic states. It is worth noting that the autodetachment lifetime not only depends on the correlation of the electronic configurations, but also the coupling of vibrational modes between the electronically excited state and the continuum.

### 5.3.3 The importance of double bond rotation

In the photoelectron spectra recorded at 346–310 nm (Figure 5.2), the low eBE peak broadens out towards higher eBE with increasing photon energy and this effect is seen for both chromophores. Thus, locking the double bond rotation appears to have very little effect on autodetachment from the high-lying  $2\pi\pi^*$  state. In the eKE distributions of both chromophores there are intensities in the low eKE region (0 to 0.4 eV) that are consistent in both shape and peak position for all wavelengths in the range 346–310 nm. Due to the constant peak position in eKE, these low eKE features can be attributed to indirect detachment process(es) such as autodetachment from the low lying  $1\pi\pi^*$  state, or thermionic emission from a vibrationally hot ground state. By comparing the intensities of the peaks in the spectra, it can be seen that with increasing photon energy, both chromophores exhibit higher intensities of this low eKE feature relative to the high eKE (low eBE) feature assigned to direct

photodetachment. Hence, as photon energy is increased, the internal conversion to lower lying electronic states of the anion becomes more prominent. For  $p\text{CE}^-$ , the profile of this low eKE signal is a structured exponential decay and so this may be assigned to predominantly thermionic emission from a vibrationally-hot ground state of the anion. Conversely, the low eKE signal observed in the  $\text{EB}p\text{CE}^-$  spectra have a much more broad shape without the distinct exponential profile indicative of thermionic emission. Hence, it seems unlikely that this feature can be attributed to thermionic emission but is instead a result of autodetachment from the low-lying  $1\pi\pi^*$  state.

The shape of the low eKE features remains constant in the 400 nm spectra for both chromophores (Figure 5.7). At 400 nm (3.10 eV) the photon energy is resonant with the  $1\pi\pi^*$  state and is close to the detachment thresholds of both chromophores. Hence, the spectra are dominated by indirect detachment processes and have only a small amount of direct detachment in the spectra. At 400 nm, the direct detachment in eKE would peak at  $eKE = h\nu - VDE = 0.25$  eV for  $p\text{CE}^-$  and 0.10 eV for  $\text{EB}p\text{CE}^-$  and these values are shown in the lower plots of Figure 5.7 by vertical blue lines. The expected eKE position for autodetachment from  $1\pi\pi^*$  may be estimated as  $eKE = E(1\pi\pi^*) - VDE \approx 0.1$  eV for  $p\text{CE}^-$  and this could explain the shelf seen in the eKE spectra at  $eKE \sim 0.1$  eV. This combination of thermionic emission and autodetachment from  $1\pi\pi^*$  is in accordance with previous work by Zewail and coworkers in which they report that 20% of the  $1\pi\pi^*$  population of a ketone PYP chromophore analogue underwent autodetachment.<sup>32</sup>

The shape of the low eKE features are strikingly different for the two chromophores. For  $p\text{CE}^-$ , the overall profile is characteristic of thermionic emission from the anion ground state. The eKE distribution of electrons emitted through thermionic emission has been shown to be modelled well by Klots' formula (Equation 1.3).<sup>8,9</sup> The canonical heat capacities of both chromophores in their neutral radical states were estimated using vibrational analyses (B3LYP/6-311++G(3df,3pd) in Gaussian09). Hence the microcanonical heat capacities ( $C_V$ ) may be estimated from these canonical heat capacities ( $C_{\text{canonical}}$ ) as  $C_V \approx C_{\text{canonical}} - k_B$ . These microcanonical heat capacities are then used to calculate the temperature of the resulting

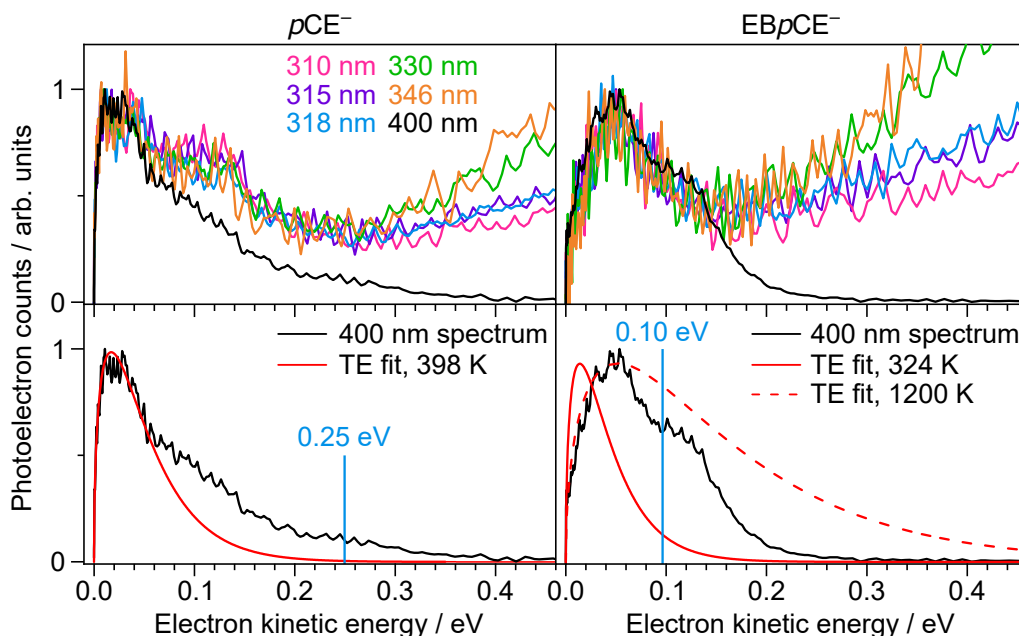


**Figure 5.7:** Photoelectron spectra presented as a function of eKE for unlocked chromophore  $pCE^-$  (left) and isomerisation-locked chromophore  $EBpCE^-$  (right). The top panels show the  $\sim 400$  nm spectra overlaid on the spectra recorded at shorter wavelengths (346–310 nm) in the low eKE region.  $\sim 400$  nm spectra were recorded with  $\lambda_{\max}$  as 400 nm (3.10 eV) for  $pCE^-$  and 397.85 nm (3.12 eV) for  $EBpCE^-$ . The bottom panels show the 400 nm spectra with modelled thermionic emission profiles using Klots’ formula plotted at the temperatures specified. Intensities of the spectra are normalised to the maximum intensity and vertical blue lines mark the eKEs corresponding to direct detachment ( $h\nu - \text{VDE}$ ).

neutral radical ( $T_{M\bullet}$ ) using Equation 1.1 and assuming the initial temperature of the anions is 298 K. Hence, a model eKE distribution for thermionic emission may be plotted for each chromophore. For  $pCE^-$ ,  $T_{M\bullet}$  was estimated as 398 K and for  $EBpCE^-$  it was estimated as 324 K. The corresponding Klots’ distributions are shown in Figure 5.7 using these temperatures. The model distribution fits well to the measured eKE distribution of the unlocked chromophore but poorly for the locked chromophore. The dashed line shows an attempt to fit the low eKE edge (eKE  $\sim 0$  eV) which still forms a poor fit with the measured distribution and suggests an unreasonably high temperature of 1200 K for the neutral radical. Thus, it seems that while the unlocked chromophore undergoes internal conversion from  $1\pi\pi^*$  to the ground state, followed by thermionic emission, this pathway is not possible for the locked chromophore. This same observation is made following photoexcitation

at shorter wavelengths.

The dominant contribution to the 400 nm photoelectron spectrum of  $\text{EB}p\text{CE}^-$  is then attributed to autodetachment from the  $1\pi\pi^*$  state. The broad, approximately statistical line shape suggests that the population is trapped in the  $1\pi\pi^*$  state long enough to populate the vibrational modes that couple strongly with the  $\text{D}_0$  continuum. Similarly, from the spectra recorded at shorter wavelengths resonant with the  $2\pi\pi^*$  state, it appears that population in the  $2\pi\pi^*$  state undergoes internal conversion to the  $1\pi\pi^*$  state where is then trapped long enough to allow vibrational redistribution followed by autodetachment. This may seem non-intuitive at first as the vibrational levels of the  $1\pi\pi^*$  state that lie above the detachment threshold have shape resonance character with respect to the  $\text{D}_0$  continuum. However, consider the propensity for conserving vibrational energy during autodetachment that results in the emission of photoelectrons with  $eKE \approx E(1\pi\pi^*) - VDE$ . For  $\text{EB}p\text{CE}^-$ ,  $E(1\pi\pi^*) < VDE$  which makes it impossible to conserve vibrational energy during the detachment process and indicates the vibrational overlap between the excited state and the  $\text{D}_0$  continuum is small. This gives time for vibrational redistribution to populate the modes that strongly couple the  $1\pi\pi^*$  state to the  $\text{D}_0$  continuum that are not populated directly at 400 nm, nor indirectly following internal conversion from the  $2\pi\pi^*$  state at shorter wavelengths. This highlights the importance of considering both the electronic and vibrational coupling with the detachment continuum. It would be interesting to employ high level quantum chemistry calculations to model the Franck-Condon overlap and identify the key coupling modes.

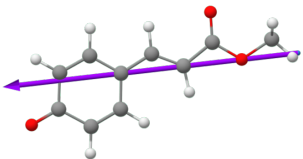
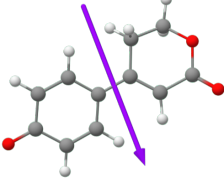
Since the work described in this chapter was published,  $p\text{CE}^-$  has been studied by Verlet and co-workers using time-resolved photoelectron spectroscopy to study the dynamics of the first excited state.<sup>41</sup> As noted in Section 4.3.4, the authors found that the low eKE signal is not attributed to thermionic emission from the ground state but rather pertains largely to autodetachment from the first excited state. They also find evidence for autodetachment from a dipole-bound state, accessed *via* internal conversion from the first excited state. Notably, the authors contrast their spectra with earlier time-resolved photoelectron spectroscopy measurements of the ketone PYP chromophore analogue studied by Zewail and co-workers<sup>32</sup> and find

that the photodetachment pathways differ markedly. This indicates how sensitive the potential energy surface is to small structural differences in the chromophore and how distinguishing between the various detachment processes that can form low eKE signal is difficult with only single-colour nanosecond photoelectron spectroscopy measurements. With all this considered, it now seems difficult to form such a like-for-like comparison of the relaxation pathways for the two chromophores discussed in this chapter as it would be wrong to assume that both chromophores have similar excited state potential energy surfaces. However, the consistency in the shape and position of the low eKE features across the 400–310 nm range still requires some consideration. Verlet and co-workers have also reported recently on photoelectron spectroscopy measurements of  $p\text{CE}^-$  using higher photon energies to probe the higher lying electronically excited states.<sup>208</sup> They observed the same low eKE as was seen in their time-resolved measurements and so they assign this low eKE feature to the same photodetachment pathways; largely autodetachment from the first excited state but with some contribution from autodetachment from a dipole-bound state. Thus, the interpretation of the electronic structure and dynamics of PYP chromophore analogues, requires careful consideration of how slight nuances in the structure may cause more dramatic effects in the shape and dynamics of the potential energy surfaces and so highlights the need for time-resolved measurements and accurate simulation of the excited state surfaces.

It would be interesting to investigate the internal conversion process from the electronically excited states to the dipole bound state with  $p\text{CE}^-$  in greater detail, with regards to the differences in initial photoexcitation of the lower or higher energy states and also in finding which coupling coordinates have conical intersections to the dipole bound state. It seems that locked chromophores, such as  $\text{EB}p\text{CE}^-$ , could play a key role in unravelling the important coupling modes if the potential energy surfaces are similar to those of  $p\text{CE}^-$  in the other coordinates. Interestingly, the neutral radical states of both  $p\text{CE}^-$  and  $\text{EB}p\text{CE}^-$  have permanent dipole moments that are comparable in magnitude yet quite different in geometry, as shown in Table 5.4. This would lead to significant differences in the distribution of the electron densities for the dipole bound states in either chromophore, which tend to be localised

at the positive end of the dipole moment. For  $p\text{CE}^-$ , calculations have predicted that much of the density lies at the ester end of the chromophore,<sup>41</sup> whereas with  $\text{EB}p\text{CE}^-$ , the positive end of the dipole moment lies in close proximity to the carbon and hydrogen atoms in the rings. Hence, it could be that the oscillator strengths for direct photoexcitation of dipole bound states for either chromophore will be significantly different and possibly photodetachment from these states could lead to interesting differences in the anisotropy parameters. Overall, there is much yet to be explored in the excited state dynamics of dipole bound states and how they are accessed. Hence, isolated PYP chromophore analogues are great candidates for future studies due to their strong dipole moments and the proximity of the energies of the first excited state and the detachment energy.

**Table 5.4:** Permanent dipole moments of each chromophore in its neutral radical ( $\text{D}_0$ ) state, calculated using B3LYP/6-311++G(3df,3pf). The direction of the dipoles are illustrated by the purple arrows and the magnitudes are shown in Debye calculated with the optimised  $\text{S}_0$  geometries (FC) and optimised  $\text{D}_0$  geometries (relaxed).

	$p\text{CE}^-$	$\text{EB}p\text{CE}^-$
		
FC	3.293	3.558
relaxed	3.944	3.805

## 5.4 Conclusions and outlook

This chapter described a study employing anion photoelectron spectroscopy and quantum chemistry calculations aimed to investigate the effect of locking double bond rotation on the electronic relaxation pathways following photoexcitation at 400–310 nm. It was found that inhibiting isomerisation in the isolated PYP chromophore anion effectively turns off the ultrafast internal conversion to the ground state and traps population in the  $1\pi\pi^*$  state. This is consistent with observations of PYP chromophores in solution by Larsen *et al.* in which the authors reported that

locking the double bond rotation increased the lifetime of the  $1\pi\pi^*$  state from 2 ps to 3 ns.<sup>86</sup> It is also in line with the theoretical predictions made by Groenhof *et al.* in which they proposed that both the global minimum and the  $S_1/S_0$  conical intersection lie in the double bond rotation coordinate on the potential energy surface of the first excited state of the PYP protein.<sup>61,62</sup>

The measurements reported here were recorded using single-colour nanosecond laser pulses and so it was appropriate at the time to assign the low eKE features observed in the photoelectron spectra to predominantly thermionic emission in the case of  $pCE^-$  and autodetachment from the first electronically excited state for  $EBpCE^-$ . Subsequent time-resolved photoelectron spectroscopy measurements of  $pCE^-$  performed elsewhere have highlighted how difficult it is to assign specific photodetachment processes to low eKE features using single-colour measurements.<sup>41</sup> The authors also find a large contrast in their measurements of  $pCE^-$  when comparing to an earlier time-resolved study of a different PYP chromophore analogue<sup>32</sup> and hence bring attention to how sensitive the potential energy surface of the first electronically excited state can be to slight differences in the structure of the chromophore. Thus, highlighting the need for accurate simulation of the potential energy surfaces and time-resolved pump-probe measurements in order to fully interpret the excited state dynamics of isolated PYP chromophores. However, this makes isolated PYP chromophores fantastic candidates to conduct future experiments on in order to explore a wide breadth of different photophysical processes while keeping the backbone of the chromophore the same. Hence, such chromophore analogues could be reintroduced to the protein manifold to provide new opportunities for the engineering of proteins with specific photoactive properties.



## Chapter 6

# A procedure for calculating the electronic structure of an anionic solute in aqueous solution

This Chapter illustrates how the photodetachment of an anionic chromophore in a bulk aqueous environment may be simulated using the phenolate anion as an example, a common molecular motif in nature. The approach uses a classical molecular dynamics simulation to sample an ensemble of conformations at room temperature which is then used in subsequent quantum-mechanical/effective-fragment potential (QM/EFP) calculations. Following a representative sampling step, selected snapshot structures are then relaxed within a QM/EFP description and detachment energies are calculated using high-level theory. The procedure provides a wealth of information useful for the study of charged solutes in aqueous solutions and investigating photodetachment processes in solution, which is of central importance to understanding electron transfer reactions.

### 6.1 Introduction

Electron detachment is a fundamental physical process underpinning electron transfer mechanisms such as redox reactions or ionic bond formation. Numerous biological processes involve photodetachment of electrons including radiation damage of DNA

and photosynthesis. Studying electron detachment in complex natural environments such as within a protein or in aqueous solution can be very challenging, both experimentally and computationally. Simulating photodetachment from a solute in bulk solution is complicated by the need for high-level quantum-mechanical approaches for accurate representation, a large number of degrees of freedom, long-range interactions and the inhomogeneity in the conformations of the local environment surrounding the solute at finite temperatures.

Hybrid quantum-mechanics/molecular-mechanics (QM/MM) methods allow explicit treatment of all atoms in a large system by balancing accuracy with computational expense. A small local region of interest is described by more accurate QM theory while the rest of the system is described by an inexpensive MM force-field. Hence, multiscale QM/MM approaches allow for the simulation of solutes in bulk solution. In QM/MM calculations, most commonly an empirical force-field is used to describe the MM region which may be improved upon by using a polarisable force-field derived from first principles, as in the effective fragment potential (EFP) approach.<sup>165,192,194,213,214</sup> QM/EFP methods provide a rigorous yet efficient way to describe interactions at the solute-solvent interface.<sup>192,199,213</sup> The QM/EFP approach has been used with equation-of-motion coupled-cluster methods with single and double excitations (EOM-CCSD) as the QM method to calculate accurate solvatochromic shifts in absorption bands<sup>166,199,200,215–217</sup> and ionisation energies<sup>165,200,216,218–226</sup> of solutes in aqueous solvent. In order to model the inhomogeneous environment surrounding the solute, often an ensemble of solute-solvent configurations are sampled and hence numerous structures are used in subsequent electronic structure calculations. The EOM-CCSD calculations scale unfavourably with system size ( $\sim N^6$ ), however it is often important to expand the QM system to include some solvent molecules to accurately represent the chemical behaviour of charged solutes. Hence, it is preferable to perform these intensive calculations using the smallest number of conformations required to converge an average value of the property of interest.

Bose *et al.* demonstrated a computationally efficient method for sampling a smaller number of geometries in the configurational space which involved first cal-

culating approximate solute-solvent Coulombic interaction energies over a large ensemble of configurations and from the distribution of interaction energies, configurations with energies close to the average interaction energy were selected first.<sup>224</sup> For example, the authors calculated the first vertical detachment energy (VDE) of the green fluorescent protein chromophore anion in bulk water and found that randomly sampling the configurational space required 100 configurations to reach convergence while with the biased sampling only 45 configurations were required to converge the VDE. Recently, Mukherjee *et al.* have presented a different biased sampling scheme to efficiently calculate QM/MM ionisation energies of a base-pair complex in aqueous solution.<sup>227</sup> In their approach, vertical ionisation energies (VIEs) are first calculated using Hartree-Fock (HF) theory for 200 snapshot geometries extracted directly from an MD simulation and then twenty configurations with VIEs close to the average VIE are selected to use in subsequent EOM-CCSD calculations. They found that their biased sampling technique with twenty snapshot geometries gave the same result as the average calculated using 200 randomly sampled snapshots. Hence, the computational time may be significantly reduced by including a biased sampling approach.

Ghosh *et al.* presented a protocol for calculating ionisation and detachment energies of aqueous phenol and phenolate using QM/EFP methods which they benchmarked with experimental liquid-microjet photoelectron measurements.<sup>165</sup> The vertical ionisation energies (VIEs) and VDEs were calculated by averaging the results of EOM-IP-CCSD/EFP calculations (EOM-CCSD for the calculation of ionisation potentials) performed on 100 snapshot geometries taken directly from a classical molecular dynamics (MD) simulation. The VIEs calculated for phenol were in excellent agreement with experiment but this was not the case for phenolate where the first VDE was overestimated by 0.6 eV. It was suggested that this discrepancy in accuracy between the phenol system and the more complex phenolate system was a result of sampling the configurational space using a classical MM force-field, which perhaps poorly describes the charged solute, or due to an approximation of the solvent polarisation surrounding the chromophore since only the solute was included within the QM description which is expected to be more significant for a charged solute.

In previous work, we reported an approach for calculating VIEs of phenol in bulk aqueous solution using a different biased sampling approach and similar EOM-IP-CCSD/EFP techniques.<sup>228</sup> In our biased sampling, QM/EFP energies were calculated for a large number of conformations taken directly from an MD trajectory and snapshot geometries were chosen with QM/EFP energies close to the mean energy to use in geometry optimisation and EOM-IP-CCSD calculations with QM/EFP. It was found that VIEs calculated using QM/EFP-optimised structures were in closer agreement to experiment than snapshot geometries extracted directly from an MD trajectory. The work in this Chapter extends on this phenol study by simulating the photodetachment of the phenolate anion in bulk aqueous solution with hybrid QM/EFP methods. The results presented here are compared with those of Ghosh *et al.*<sup>165</sup> to test the importance of including solvent molecules within the QM description and relaxing the geometry of the system within a QM/EFP framework. In nature, the phenolate motif is a key component of many biological molecules including tyrosine and the chromophores within green fluorescent protein and photoactive yellow protein (Figure 6.1). Hence, this work on aqueous phenolate also outlines an effective procedure that could be applied to study more complex solutes in future work.

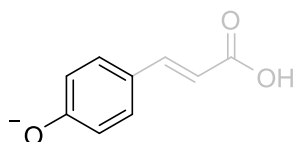


**Figure 6.1:** Structure of the photoactive yellow protein chromophore,  $p\text{CA}^-$ , with the phenolate anion shown in black.

## 6.2 Methods

QM/EFP methods were used to simulate a phenolate anion in bulk water using the method developed from our earlier work investigating aqueous phenol.<sup>228</sup> Several steps were involved in sampling conformations of the complex system before performing electronic structure calculations as outlined in the flowchart in Figure 6.2

and described in greater detail later in this Chapter. Initially, a classical MD simulation was performed within the NAMD software<sup>229</sup> (developed by the Theoretical and Computational Biophysics Group in the Beckman Institute for Advance Science and Technology at the University of Illinois at Urbana-Champaign). Snapshot geometries were extracted from the MD trajectory to sample an ensemble of conformations of phenolate in bulk water at room temperature. In the MD simulation, a phenolate anion was positioned at the centre of a large cube of water (length  $\sim 102$  Å, 34181 water molecules). The faces of the cube formed periodic boundary conditions for a canonical ensemble (*i.e.*  $NVT$  - constant number of particles, volume and temperature). CHARMM force-field parameters<sup>230</sup> were used to describe the phenolate anion and water molecules were described by the TIP3P model.<sup>189</sup> Snapshot geometries of the system were saved every 500 fs after an equilibration period to provide 500 snapshot geometries of the solute-solvent system at room temperature.

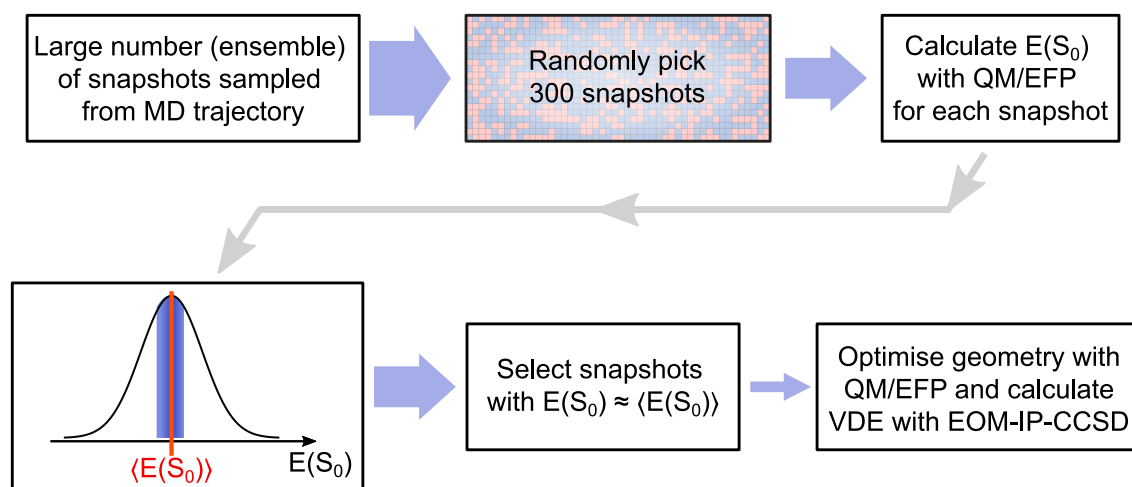


**Figure 6.2:** Flowchart outlining the major steps made in sampling the configurational space of the solute in bulk solvent. The width of the blue arrows indicate qualitatively the number of sampled snapshots taken forward at each step.

The construction of the QM/EFP geometries was carefully considered by calculating the VDE as the size of the QM or EFP subsystems were increased. The VDEs were calculated using the energy difference method with B3LYP/6-31+G\* representing the QM and ultimately an appropriate QM/EFP construction was found to involve a QM system containing a phenolate anion and the five water molecules closest to any atom within the solute and the EFP system containing any water

molecule within 16 Å of any atom within the solute. All other water molecules were discarded. Extraction of the QM and EFP geometries was performed within the VMD software<sup>231</sup> with a script similar to that in Appendix D. 300 of the 500 potential configurations from the MD trajectory were then randomly selected and used within DFT/EFP calculations constructed in this way to find the ground state energy of the anion ( $S_0$ ), the ground state energy of the neutral radical ( $D_0$ ) and hence the VDE as the difference.

Various DFT functionals and two basis sets (6-31+G\* and 6-311++G\*\*) were tested for ten randomly-picked snapshots and the average VDEs are listed in Table 6.1. There is only a small difference in the VDEs calculated with the different functionals ( $\sim 0.1$  eV) and extending to a triple-zeta basis set with polarisation and diffuse functions on the hydrogen atoms has made a marginal effect (0.03 eV). Therefore, B3LYP/6-31+G\*//EFP was employed within these energy calculations.

	B3LYP	$\omega$ -B97x-D	CAM-B3LYP
6-31+G*	7.73	7.83	7.80
6-311++G**	7.76	7.86	7.83

**Table 6.1:** DFT/EFP VDEs (in eV) calculated for phenolate in water with the various exchange-correlation functionals and basis sets specified. Calculated as an average over ten randomly-picked snapshot geometries constructed with the QM region phenolate and the five water molecules closest to the chromophore and an EFP region including any water molecules within 16 Å of the chromophore (not described by QM).

The distribution of the 300  $S_0$  energies were used in a second sampling step to collect a small subset of 10-50 configurations to represent the full ensemble. Snapshots with  $S_0$  energies closest to the energy at the centre of the Gaussian fit to the full distribution were selected first. The subset of selected configurations was then used in more expensive calculations such as QM/EFP geometry optimisations and the calculation of VDEs using EOM-IP-CCSD. A smaller EFP subsystem including exactly 300 water molecules was used within the geometry optimisation calculations and any subsequent calculations performed using the optimised structures.

Geometry optimisations were performed within the Firefly quantum chemistry package,<sup>152</sup> which is partially based on the GAMESS (US) source code.<sup>153</sup> All other QM/EFP calculations were performed within the QChem software package.<sup>156</sup> Stan-

dard EFP parameters were used to represent water in QM/EFP calculations within the QChem<sup>232</sup> and Firefly<sup>233</sup> libraries. Photodetachment cross-sections were calculated using ezDyson version 4.0<sup>234</sup> with a charge of zero on the neutral core following detachment and so the ejected electron is modelled as a plane wave.

## 6.3 Results and discussion

### Collecting an ensemble of conformations

At ambient temperature, the complex solute-solvent system may sample a continuous distribution of conformations over the many degrees of freedom. Hence, a temperature-dependent ensemble of geometries of phenolate in bulk water were extracted from a molecular dynamics trajectory evolving at a temperature of 300 K. The simulation cell used in the MD trajectory is shown in Figure 6.3 and is constructed as a single phenolate anion at the centre of a large cube of water (34,181 water molecules). This large simulation cell was defined such that the solute-solute distance remains at 100 Å throughout the trajectory (*i.e.* using a cube of length  $\sim 102$  Å). The  $\sim 50$  Å distance from the chromophore to the boundary of the simulation cell ensures a bulk representation and enables easy extraction of the smaller snapshot geometries used in later QM/EFP calculations without any unwanted surface effects.

In the MD simulation, all atoms were allowed to relax without any fixed coordinates. The simulation comprised of an initial minimisation over 2000 steps (making up 2 ps in the trajectory), an equilibration period at 300 K (20 ps) and then the sampling trajectory (250 ps). The initial minimisation is not strictly necessary but helps to reduce any frustration in the system generated during construction of the input geometry which could artificially heat the system. The molecular dynamics begin after this minimisation step and the system is allowed to evolve at 300 K for the remainder of the simulation, with the initial equilibration period (20 ps) discarded. Snapshots from the sampling trajectory were saved every 500 fs affording 500 potential conformations of the solute-solvent system to use in subsequent hybrid QM/EFP calculations. Figure 6.4 shows the total potential energy (the sum

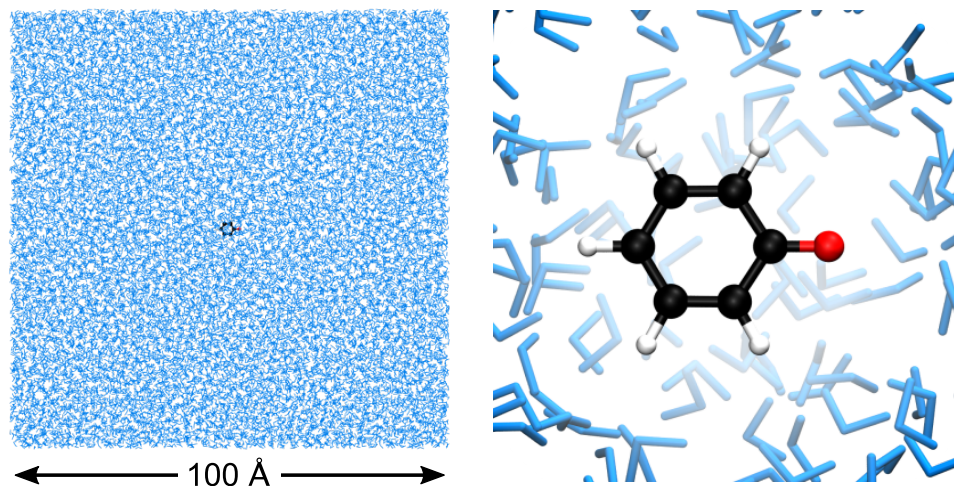


**Figure 6.3:** Left: full model system used in the molecular dynamics simulation of phenolate (centre) in bulk water (blue). Right: close-up of the solute within the simulation cell.

shown in Equation 3.27) calculated over the MD trajectory from the beginning of the equilibration period to the end of the sampling period. Notably there is only a correlation between time and potential energy at the very beginning of the equi-

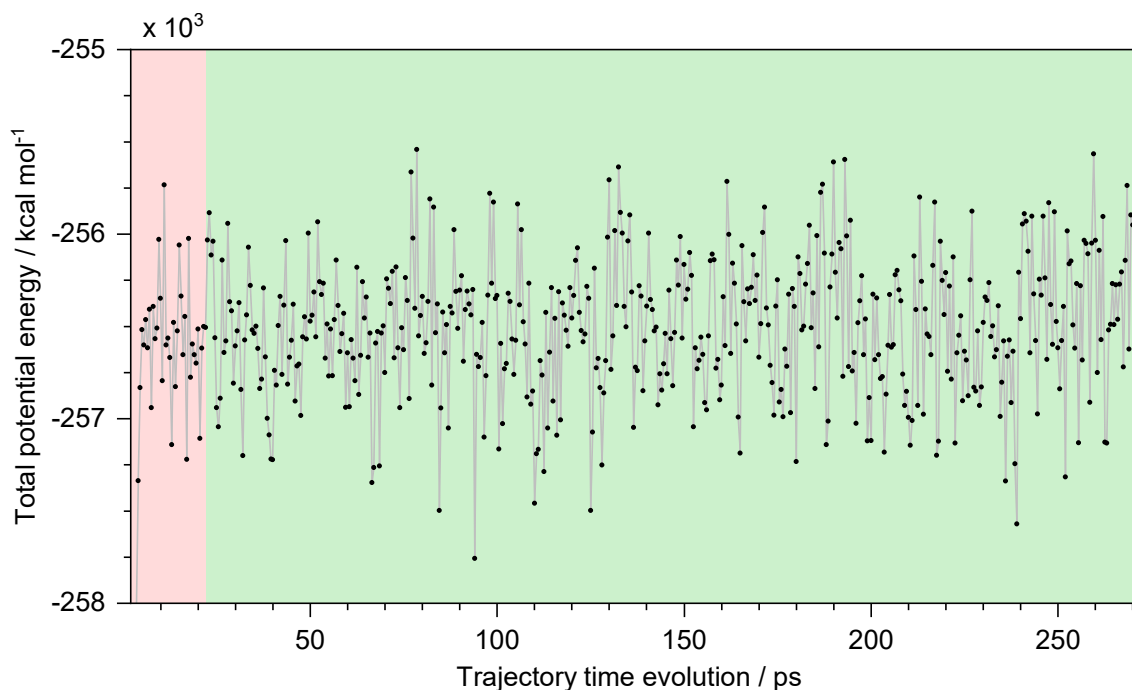


**Figure 6.4:** Total potential energy calculated over the time evolution in the MD simulation. Scale shows the equilibration period (red, 2-22 ps) and the sampling period (green, 22-272 ps).



libration period, indicating that the system has equilibrated within 20 ps and the geometry of the system is evolving stochastically in the sampling region. Hence, the sampling trajectory is appropriate for extracting a series of conformations to represent the full ensemble.

### Constructing QM/EFP configurations

Structures were extracted from the MD trajectory to construct geometries for the hybrid QM/EFP calculations with careful consideration of the size of both the QM and EFP components, accounting for the computational expense of such a complex system. First, the number of solvent molecules to include in the construction of the QM region was considered. For each of the 500 snapshots taken from the MD simulation, the number of water molecules hydrogen bonded with the chromophore was determined using the default criteria within the VMD software (a donor-acceptor distance within 3 Å and a donor-H-acceptor angle of  $180 \pm 20^\circ$ ). These results are summarised in the column chart in Figure 6.5. Across the total 500 snapshot geometries, the greatest number of solute-solvent hydrogen bonds was found to be five and most commonly three water molecules were hydrogen-bonded to the chro-

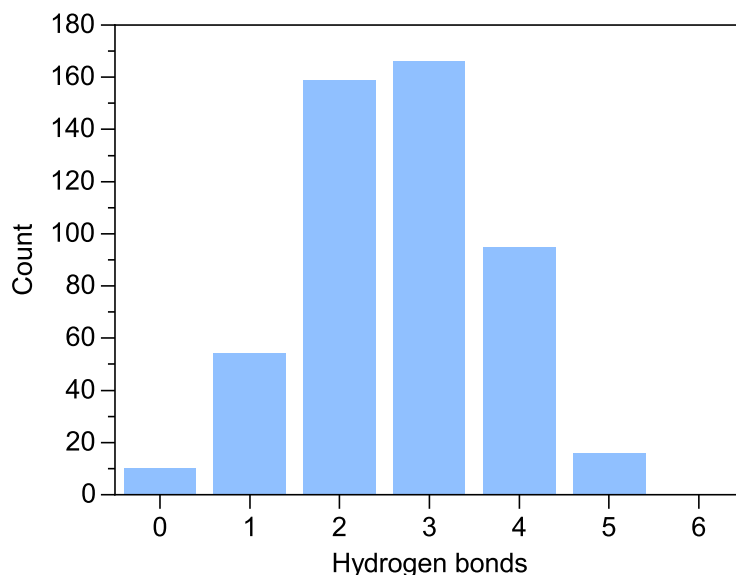


**Figure 6.5:** Column chart illustrating the distribution in the number of water molecules forming direct hydrogen bonds with phenolate determined over the 500 snapshots extracted from the MD simulation.

mophore. Hence, constructing the QM region of the hybrid QM/EFP calculations to be the chromophore and the five water molecules closest to the chromophore ensures that all water molecules forming direct hydrogen bonds with the chromophore are described by QM level theory.

Alternatively, the cut-off of five water molecules may be understood in the context of solvation shells. Figure 6.6 shows radial distribution functions (RDFs) surrounding the phenolate oxygen atom for both water oxygen and water hydrogen atoms. The hydrogen RDF relates more to the hydrogen-bonding interactions but the oxygen RDF provides a more intuitive measure of how many discrete solvent molecules lie within a particular radius. *i.e.* the hydrogen RDF has a second peak at  $\sim 3$  Å not present in the oxygen RDF which arises due to the second hydrogen atom within each water molecule, whereas there is only a single oxygen atom per water molecule. The average cut-off radius for five atoms may be determined from the integration plots (inset) and it can be seen that this filled area within the oxygen RDF includes the first solvation shell entirely and some of the second.

To test the number of water molecules required in the QM region, VDEs were calculated with the energy difference method using QM/EFP (QM = B3LYP/6-31+G\*) in which the QM region was increased to incrementally include up to twenty water molecules within the QM region. This was performed for ten randomly-selected snapshots with an EFP region constructed to include all water molecules within a 10 Å radius of any atom within the chromophore (that were not included within the QM region). The results of these calculations are presented in Figure 6.7 for each of the ten snapshots and for the average over the ten snapshots. Overall there is a difference of  $< 0.25$  eV between the simplest QM system (in which only the chromophore is described by QM) and the most complex system with twenty QM water molecules. The difference in the average VDE calculated between the 5-water system and the 10-water system is only 0.13 eV. The computational expense increases steadily as the QM region is expanded, as expected for DFT, but the increase will be more dramatic for later EOM-IP-CCSD calculations. Therefore, a compromise between accuracy and computational expense was made by including exactly five solvent molecules within the QM region.

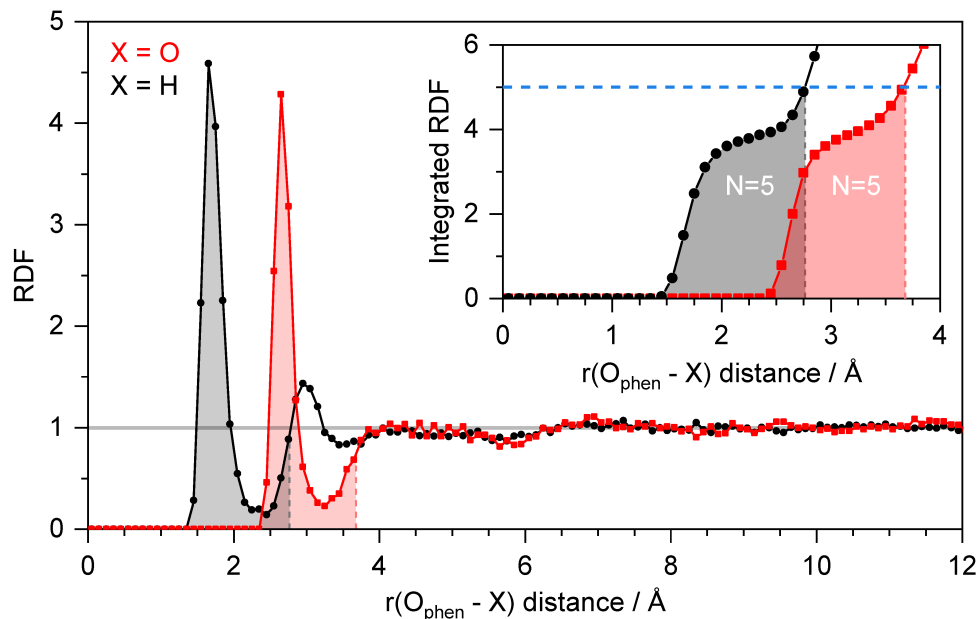


**Figure 6.6:** Radial distribution functions (RDFs) determined from the phenolate oxygen atom to oxygen (red) and hydrogen (black) atoms within water over the 500 snapshots extracted from the MD simulation. Inset: integrated RDFs with shaded areas indicating the average radius surrounding the phenolate oxygen atom that contains five of the nearest solvent atom (oxygen or hydrogen) sites. This same radius is used as the cut-off in the filled areas in the main RDF plots.

To determine an appropriate size of the EFP subsystem, a similar approach was employed. Again, ten randomly-selected snapshots were used to calculate the VDE employing the energy difference method with QM/EFP (QM = B3LYP/6-31+G\*) but this time with a QM region including the chromophore and its five nearest water molecules and an increasing EFP region size. The EFP selections were made using a cut-off radius such that any solvent molecules that form an interatomic distance to the chromophore equal to or within a given radius were included. EFP radii from 0, *i.e.* a pure QM calculation, to 30 Å were tested, as shown in Figure 6.7. There is a dramatic difference between the VDEs calculated using a pure QM microsolvated system and the EFP radii  $>10\text{\AA}$ , indicating the necessity for a surrounding solvent model to represent bulk solvation. However, the increase in the number of EFP fragments also increases the computational expense significantly. Notably these single-point DFT energy calculations performed here to calculate the VDEs are much cheaper than the geometry optimisations or EOM-IP-

CCSD calculations discussed later. Hence, with this considered, a compromise on EFP radius was made between the computational expense and convergence and an EFP radius of 16 Å was chosen.

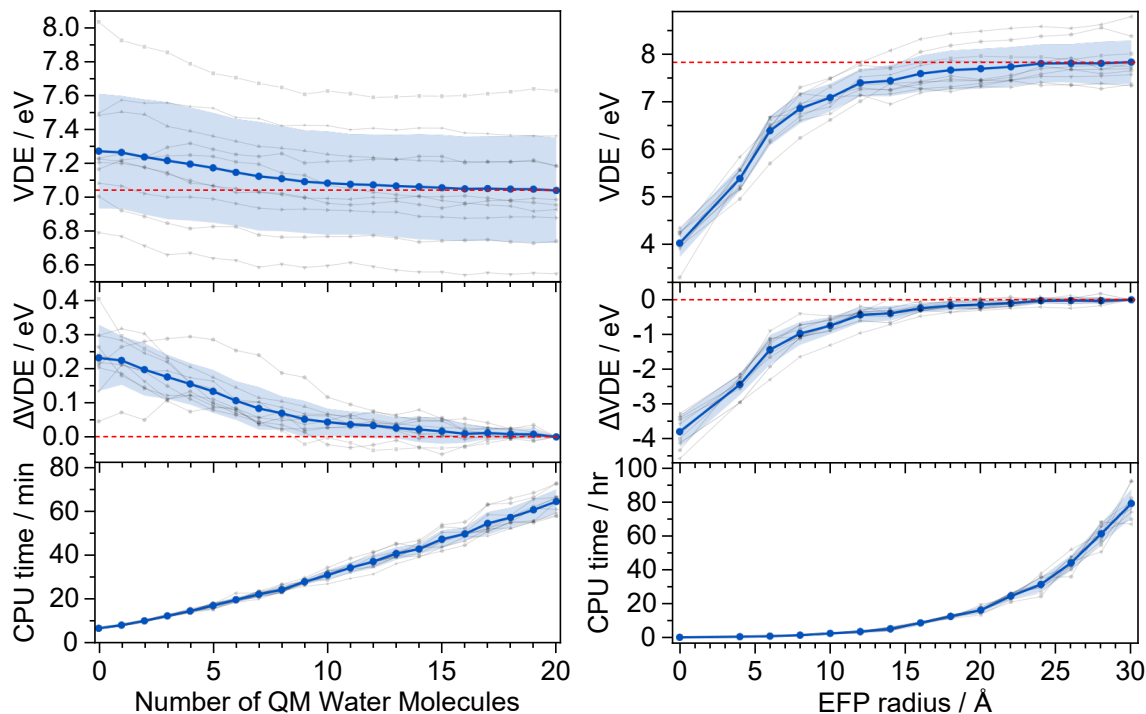


**Figure 6.7:** Top: QM/EFP VDEs calculated for ten randomly-selected snapshot geometries with the number of water molecules incrementally increased in the QM region (left) and with an increasing EFP region size described by a cut-off radius surrounding the chromophore (right). Dashed red lines indicate the VDE calculated using the largest QM/EFP construction in each case. Middle:  $\Delta$ VDE here is the difference between the VDE calculated with a specific QM/EFP construction and the largest QM/EFP construction in both cases. Bottom: CPU time as the system size is increased in each region. Averages for each system size are shown by the blue circles and the shaded areas indicate a single standard deviation each side of the mean.

An example of a QM/EFP construction with an EFP radius of 16 Å is shown in Figure 6.8A. In the particular snapshot used in this example, the 16 Å radius contains 810 EFP fragments. In calculations discussed later in which the geometries are optimised at a QM/EFP level, a smaller EFP subsystem is used, restricted by software requirements. In such cases, exactly 300 water molecules were included within the EFP region as illustrated in the example in Figure 6.8B.

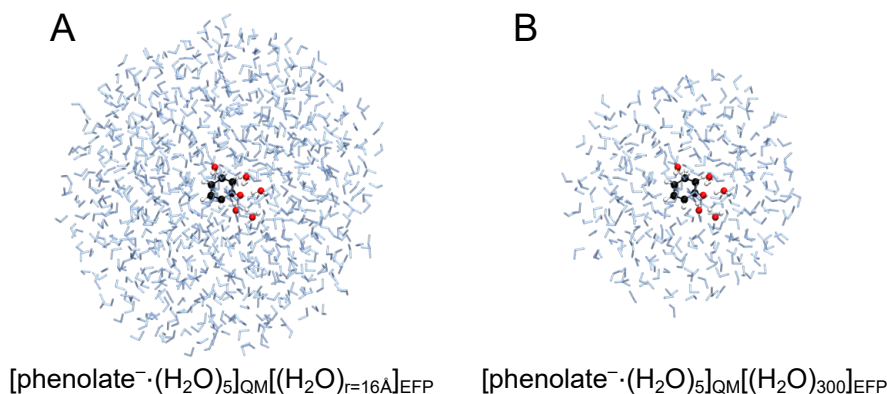


**Figure 6.8:** Example QM/EFP constructions with an EFP radius of 16 Å (A) and a truncated EFP region including exactly 300 solvent fragments (B). The larger system is used in subsequent QM/EFP calculations in which the geometries have not been optimised using QM/EFP. The smaller system is used in the QM/EFP geometry optimisation calculations and any further calculations using those optimised geometries.

### Averaging QM/EFP calculations over the ensemble

300 snapshot geometries were selected randomly from the MD sampling trajectory and for each snapshot, the QM and EFP structures were extracted to form a  $[\text{phenolate}^{\cdot-}(\text{H}_2\text{O})_5]_{\text{QM}}[(\text{H}_2\text{O})_{r=16\text{\AA}}]_{\text{EFP}}$  construction, similar to that shown in Figure 6.8A. The electronic energy of each of these configurations was calculated using QM/EFP (QM=B3LYP/6-31+G\*) for both the anionic ground state,  $S_0$  and the ground state of the neutral radical,  $D_0$ . These single point energy calculations are relatively quick allowing for the 600 calculations performed at this stage. Figure 6.9 shows the  $S_0$  QM/EFP energies plotted against the corresponding MM/MM energies (of the full MD simulation cell) and it can be seen that both sets of energies are approximately normally-distributed although, interestingly, there is little correlation between the methods.

Figure 6.10 shows the energies of the  $S_0$  and  $D_0$  states calculated for each snapshot and the distribution of these energies. The spread of these energies are similar in both states and they overlap significantly. The full-width half maxima (FWHM) of the  $S_0$  and  $D_0$  Gaussian distributions are both 14.6 eV. The average VDE may be taken as the energy difference between these Gaussian peaks as 7.64 eV. Alternatively, the average VDE may be found by first calculating the VDE for each

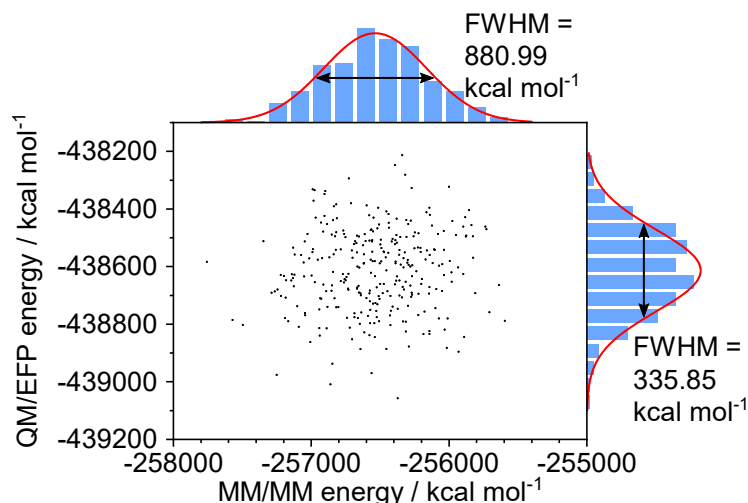


**Figure 6.9:** Energies of the ground state anionic system calculated for 300 randomly-selected configurations taken from the MD trajectory using QM/EFP (QM=B3LYP/6-31+G\*) and MM/MM energies (total potential energies) taken from the MD simulation.

snapshot, as shown in the bottom panel. The rolling average plateaus within  $\sim 50$  snapshots and averaging over 300 snapshots gives a value of 7.64 eV. The distribution of the VDEs is significantly more narrow than found for the component energies with a FWHM of 0.85 eV. This suggests the  $S_0$  and  $D_0$  potential energy surfaces are effectively parallel on the scale of the deviation of each surface. The peak of the Gaussian fit to the distribution of VDEs also affords an average VDE of 7.64 eV. The agreement between these three approaches to determine the average VDE indicates that, within the central limit theorem, the sample size of 300 snapshots is sufficiently large to form a Normal distribution and obtain an average.

### Sampling representative conformations

In the QM/EFP calculations presented so far, the geometries of the solute-solvent system have been extracted directly from the MD simulation and so the atomic positions have only relaxed within a Newtonian force field description. A much more accurate representation of the system geometry is obtained by describing the complex anionic molecule by QM theory. However, to optimise the geometry of each of the 300 snapshots would not be feasible and so it is important to select a subset of the snapshots to be used in QM/EFP geometry optimisation calculations. Snapshots

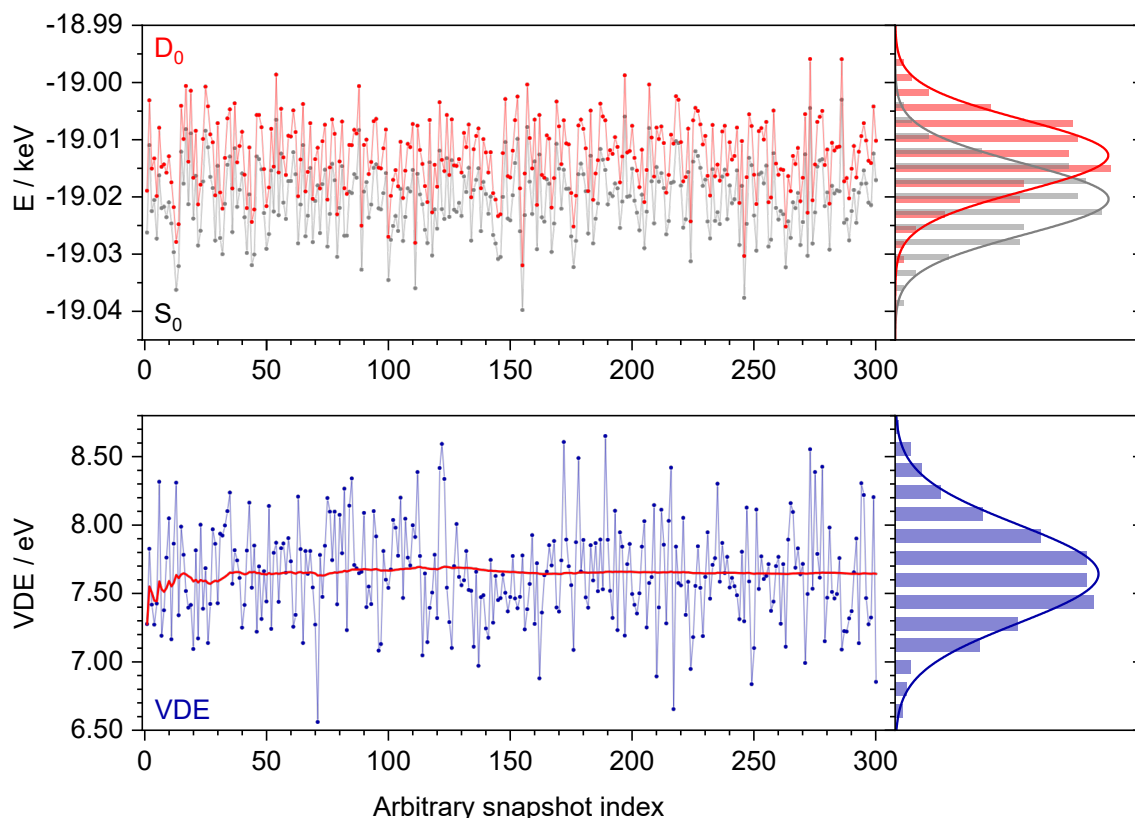


**Figure 6.10:** Top: energies of the  $S_0$  and  $D_0$  states calculated with QM/EFP (QM=B3LYP/6-31+G\*) for each of 300 randomly-selected snapshot geometries and the right panel shows the distribution of these energies collected into a histogram. Bottom: VDEs calculated for each of the snapshots using the difference of the energies in the plot above. A rolling average is shown in red and the distribution of the VDEs is shown in the histogram in the right panel. A Gaussian distribution has been fit to each histogram.

were selected by prioritising those with QM/EFP energies that lie closest to the peak of the Gaussian profile fit to the full distribution - *i.e.* are most representative of the full 300 K ensemble, as shown in Figure 6.11. Subsets of 10, 20, 30, 40 and 50 snapshots were selected in this way to illustrate the convergence in the sampling method.

The snapshots selected in this sampling stage were used within geometry optimisations using QM/EFP (QM=B3LYP/6-31+G\*) with a smaller EFP region similar to that shown in Figure 6.8B. Within these geometry optimisation calculations, the positions of all QM atoms (the chromophore and five water molecules) are adjusted freely and the 300 water molecules modelled by EFP are reorientated such that the internal geometry remains fixed but the rotational and translational degrees of

freedom are relaxed.

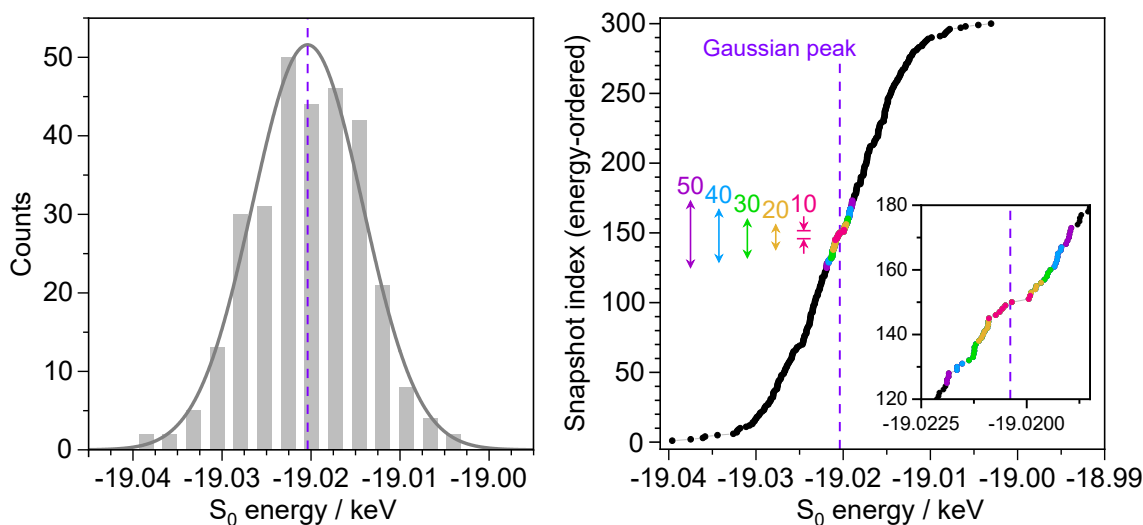


**Figure 6.11:** Left: histogram of  $S_0$  energies calculated with QM/EFP (QM=B3LYP/6-31+G\*) over the 300 randomly-selected snapshots with a Gaussian distribution (bin widths are 2.66 eV). The centre of the Gaussian peak is indicated by the vertical dashed line. Right: energies in increasing order highlighting the 10-50 selected snapshots with energies closest to the average energy (Gaussian peak). Inset is an expansion of the scale in the selection region.

These large-scale simulations also provide key insight into the chemistry of the system at a molecular level. The first VDE of gas-phase phenolate is 2.25 eV,<sup>235</sup> whereas in aqueous solution, this blue-shifts to 7.1 eV.<sup>165</sup> This huge solvent shift is a result of how effectively the polar solvent stabilises the anion. The water molecules form electron-accepting hydrogen bond interactions with the phenolate anion and this can be quantified within the QM/EFP calculations by studying the charge populations. Figure 6.12 illustrates the distribution of charge over the phenolate, water and phenolate oxygen atom ( $O_{\text{phenolate}}$ ) sites calculated for fifty unoptimised and optimised snapshot geometries in both the  $S_0$  and  $D_0$  states. Charges calculated at the same theory level for an isolated gas-phase phenolate anion optimised at the B3LYP/6-31++G(3df,3pd) level<sup>236</sup> are shown in black.

Generally, there is little difference between the unoptimised and optimised charge distributions for each part of the QM system, although the optimised structures have slightly narrower distribution widths and more charge is localised at the phenolate O atom. The isolated phenolate monoanion in the gas phase has a charge of -1,



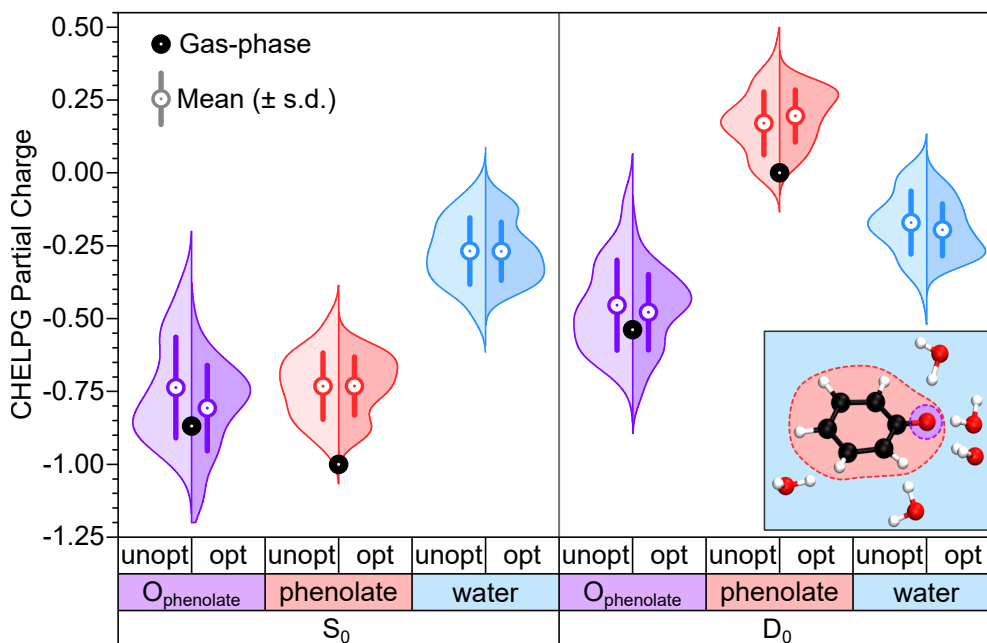


**Figure 6.12:** QM/EFP (QM=B3LYP/6-31+G\*) CHELPG atomic partial charges calculated for the phenolate oxygen atom (purple), the sum of the charges on each atom in the phenolate molecule (red) and the sum of the charges on each atom of the five QM water molecules (blue), as indicated by the diagram in the bottom right. Charges were calculated for each of fifty snapshot geometries taken directly from the MD trajectory (unopt) and following optimisation with QM/EFP (opt) in both  $S_0$  and  $D_0$  states. The charge distributions in each case are shown by the shaded areas (Kernel smooth violin plots) with the circle and bar describing the mean and a single standard deviation either side of the mean, respectively. Charges calculated for gas-phase phenolate (B3LYP/6-31+G\*) are shown as black circles.

whereas, on average, the phenolate anion in the QM/EFP systems was -0.73 (for both unoptimised and optimised structures). The remainder of the charge (-0.27 on average) lies across the five solvent molecules. The extent of charge transfer from solute to solvent relates to the strength of the solute-solvent interactions<sup>237,238</sup> and hence the overall stability of the system. The  $D_0$  charges are calculated vertically from the  $S_0$  geometries and now have an overall charge of zero. The phenolate oxygen atom remains partially negative upon instantaneous-ionisation but to a lesser extent than in the anionic  $S_0$  state. Curiously, the phenolate charges are slightly positive for the QM/EFP structures. However, the charge on the surrounding solvent molecules has changed very little on ionisation which is perhaps because the configuration of

the water molecules is significantly more stable with the surplus charge and the phenolate is slightly positively charged to compensate.

### Vertical detachment energies

Figure 6.10 illustrated how the first VDE may be calculated as an average over a large number of unoptimised snapshots taken directly from the MD simulation to be 7.64 eV. The VDE may also be calculated using this DFT-based energy difference method for the QM/EFP optimised structures and these results are shown in Table 6.2. These calculations were averaged over the 10-50 snapshots with ground state energies closest to the Gaussian peak, using the selection process illustrated in Figure 6.11. A comparison to the corresponding average VDEs obtained over the same subset of structures before QM/EFP optimisation are also provided. Optimising the structures has lowered the average VDEs by  $\sim 1.1$  eV for each of the sample sizes. This brings the average VDEs closer to the experimental values measured using x-ray liquid-microjet photoelectron spectroscopy.<sup>165</sup> Additionally, there is little difference in the average VDEs for the different sample sizes which suggests that it is sufficient to average over a sample size as small as ten configurations within this representative sampling approach.

QM/EFP calculations using EOM-IP-CCSD/6-31+G\* were performed to calculate VDEs with an *ab initio* wavefunction-based approach and also find the VDE to the second detachment continuum ( $S_0$ - $D_1$  transition). However, such calculations are much more expensive and so to calculate over a large number of snapshots would be infeasible. Table 6.10 lists the VDEs for the first two detachment states,  $D_0$  and  $D_1$ , calculated as an average over the different subsets of sampled snapshots. These calculations were performed on the structures before and after optimisation to investigate the effect that optimising the geometry with QM/EFP has on the EOM-IP-CCSD VDEs. As with the DFT calculations, geometry optimisation decreases the average VDEs by roughly 1 eV and provides a better agreement with the experimental measurements. The EOM-IP-CCSD method has calculated the first VDE to be slightly closer to the experimental estimate than the DFT approach and, notably, the VDE to  $D_1$  is in very good agreement with experiment.

**Table 6.2:** QM/EFP VDEs calculated with B3LYP or EOM-IP-CCSD with the 6-31+G\* basis set. Averages are calculated over the number of specified QM/EFP structures constructed as  $[\text{phenolate}^- \cdot (\text{H}_2\text{O})_5]_{\text{QM}}[(\text{H}_2\text{O})_X]_{\text{EFP}}$  where X, the size of the EFP system, is an EFP radius of 16 Å for the unoptimised (unopt.) structures and 300 fragments for the optimised structures (opt.). Example QM/EFP constructions are illustrated in Figure 6.8 for the unopt. (A) and opt. (B) systems. Also listed are experimental and calculated values from the literature.<sup>165</sup> All VDEs are given in eV.

QM level	Averaged over	S <sub>0</sub> -D <sub>0</sub>		S <sub>0</sub> -D <sub>1</sub>	
		unopt.	opt.	unopt.	opt.
B3LYP/ 6-31+G*//EFP	1	7.55	6.66		
	10	7.66	6.55		
	20	7.66	6.54		
	30	7.63	6.53		
	40	7.62	6.49		
	50	7.64	6.49		
	300	7.64			
EOM-IP-CCSD/ 6-31+G*//EFP	1	7.88	6.88	9.26	8.45
	10	7.98	6.77	9.35	8.32
	20	7.71	6.76	9.12	8.29
	30	7.76	6.75	9.19	8.28
	40	7.80	6.71	9.21	8.24
	50	7.85	6.71	9.26	8.25
EOM-IP-CCSD/EFP <sup>165</sup>		7.75		9.25	
Experimental <sup>165</sup>		7.1 ± 0.1		8.5 ± 0.1	

The EOM-IP-CCSD/EFP VDEs reported by Ghosh *et al.* used the same QM theory level (EOM-IP-CCSD/6-31+G\*) with different QM/EFP constructions such that just the phenolate anion was described by QM and a larger, 35 Å diameter sphere of EFP water molecules surrounded the solute.<sup>165</sup> These VDEs were taken from an average of 100 VDEs calculated using geometries extracted directly from an MD simulation. Hence, it is not surprising that these VDEs are comparable to the VDEs presented here in Table 6.2 using unoptimised snapshot geometries.

The convergence of the calculated VDEs is illustrated in Figure 6.13 with a rolling average for each calculation set. Clearly, the optimised structures give more narrow distributions in the VDEs and provide closer agreement to experiment (dashed lines). The rolling averages plateau within 40 snapshots but within a much smaller sample for the optimised structures.

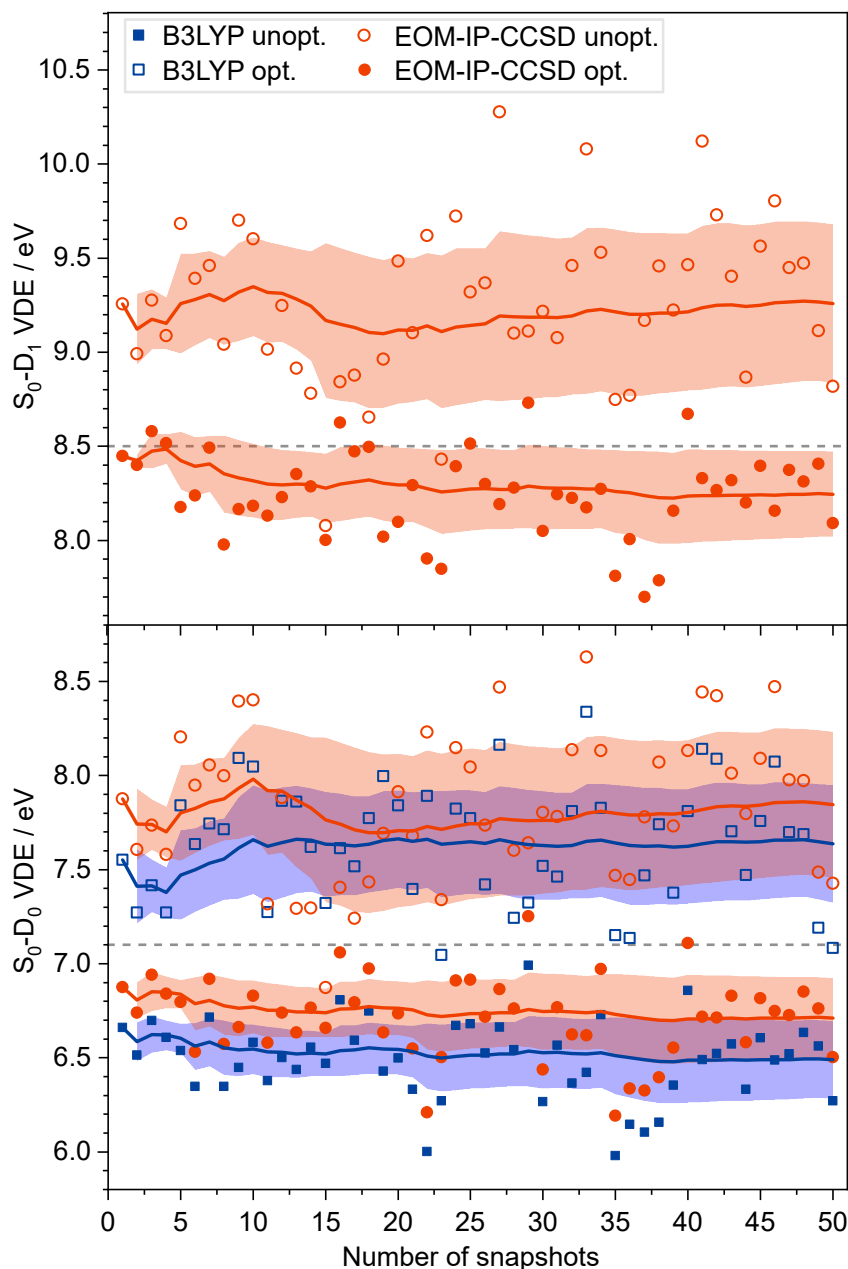


**Figure 6.13:**  $S_0$ - $D_1$  (top) and  $S_0$ - $D_0$  (bottom) VDEs calculated using QM/EFP methods (B3LYP/6-31+G\* or EOM-IP-CCSD/6-31+G\*) for the unoptimised and optimised structures sampled as illustrated in Figure 6.11. Rolling averages are shown by the solid lines and the shaded areas mark a single standard deviation either side of this average. The horizontal dashed lines mark the experimental measurements<sup>165</sup> at 7.1 and 8.5 eV for  $D_0$  and  $D_1$ , respectively.

The difference between the DFT and EOM-IP-CCSD  $D_0$  VDEs calculated using the optimised structures appears to be almost constant across the range. This strong correlation between the two methods is illustrated in Figure 6.14. Hence,

perhaps the first VDEs of EOM-IP-CCSD level accuracy could be estimated by simply applying a linear shift to the values calculated with the much cheaper DFT approach. However, additive schemes like this need to be used with caution and require thorough benchmarking to employ with certainty, particularly if applied to other chemical systems.

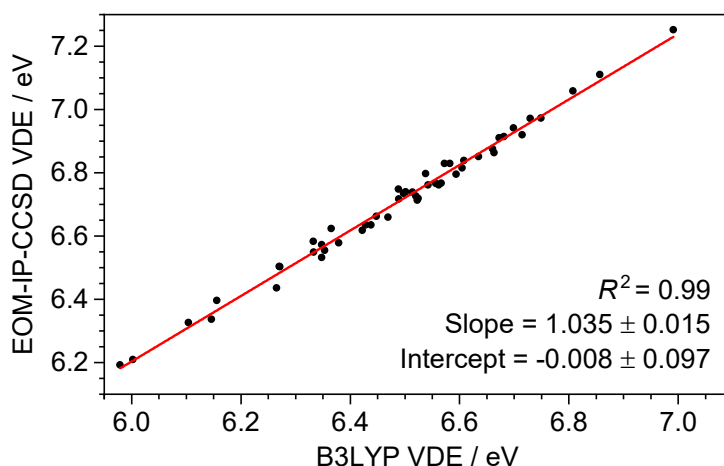


**Figure 6.14:**  $S_0$ - $D_0$  VDEs calculated with EOM-IP-CCSD plotted against those calculated using B3LYP for fifty optimised QM/EFP snapshot geometries. A line of best fit is shown in red and the fit parameters listed in the lower right.

Hole orbitals for the  $D_0$  and  $D_1$  electron configurations are shown in Tables 6.3 and 6.4 as calculated using the EOM-IP-CCSD/6-31+G\*\*/EFP method. Hole orbitals are presented from the EOM-IP-CCSD calculations performed using the single snapshot structure with  $S_0$  energy closest to the mean  $S_0$  energy (B3LYP/6-31+G\*\*/EFP) both before and following optimisation with QM/EFP. For all of the EOM-IP-CCSD calculations using both the unoptimised and optimised systems, the  $S_0$ - $D_0$  transition is dominated by an electron leaving the HOMO  $\pi$  orbital with amplitude  $> 0.94$ . The similarity between the HF and Dyson orbitals indicates a single-electron transition. The orbitals shown in Table 6.3 are representative of the HOMOs calculated for all of the structures.

For the unoptimised structures, there were varied contributions of both the HOMO-1 ( $\pi$ -character) and HOMO-2 (non-bonding) orbitals to the hole orbitals calculated for the  $S_0$ - $D_1$  transitions. For example, for the unoptimised structure shown in Table 6.4, the  $S_0$ - $D_1$  transition includes significant contributions of electron

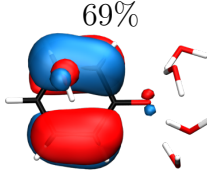
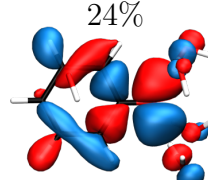
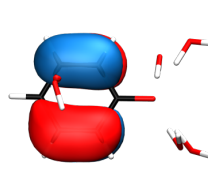
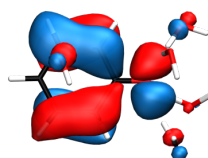
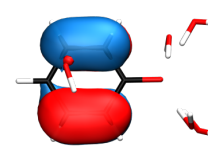
**Table 6.3:** HF hole orbitals and Dyson orbitals for the  $S_0$ - $D_0$  transition calculated with EOM-IP-CCSD/6-31+G\*\*/EFP using a single geometry both before and after optimisation with QM/EFP. Leading HF orbitals each have amplitudes close to unity ( $> 0.94$ ).

	$S_0$ - $D_0$	
	unoptimised	optimised
HF hole		
Dyson		

detachment from both the  $\pi$ -character HOMO-1 (69%) and n-character HOMO-2 (24%) orbitals and the combination is represented in the Dyson orbital. The other unoptimised snapshot geometries gave contributions from these orbitals in varied quantities; in some cases one of the orbitals dominated but generally significant mixing was found. This could explain the broad range of EOM-IP-CCSD  $S_0$ - $D_1$  VDEs for the unoptimised structures (Figure 6.13). The  $S_0$ - $D_1$  transition calculated using the optimised structures was found to be the ejection of a HOMO-1  $\pi$ -character orbital in almost all cases but in two of the fifty calculations, the hole orbital was calculated to be the HOMO-2 n-character orbital. In each of these cases, there was no significant mixing but a single dominant hole orbital with amplitude  $> 0.95$ .

The significant involvement of both the HOMO-1 and HOMO-2 orbitals in the calculated  $S_0$ - $D_1$  transitions suggests that the VDEs for detachment from either orbital are similar and the relative energies of these orbitals (and corresponding VDEs) depend strongly on the structure. To investigate the VDE for electron detachment from the n-character HOMO-2 orbital, the first four VDEs were calculated using a single optimised QM/EFP geometry with EOM-IP-CCSD/6-31+G\*\*/EFP. The first three VDEs and the corresponding Dyson orbitals are shown in Figure 6.15

**Table 6.4:** HF hole orbitals and Dyson orbitals for the  $S_0$ - $D_1$  transition calculated with EOM-IP-CCSD/6-31+G\*\*/EFP using a single geometry both before and after optimisation with QM/EFP. Percentage contributions are included for the unoptimised HF hole orbitals, whereas there is a single significant HF orbital for the optimised geometry (amplitude  $> 0.95$ ).

$S_0$ -D <sub>1</sub>			
	unoptimised		optimised
HF hole	69% 	24% 	
Dyson			

while the  $S_0$ - $D_3$  VDE was calculated to be much higher in energy (10.26 eV) and so not discussed here. As expected, the  $S_0$ - $D_1$  and  $S_0$ - $D_2$  VDEs are very close (within 0.1 eV). VDEs and Dyson orbitals for equivalent photodetachment processes from phenolate isolated in the gas phase were also calculated using the same QM theory level with a structure optimised with B3LYP/6-311++G(3df,3pd).<sup>236</sup> Note that the  $D_1$  and  $D_2$  panels have been reordered for the gas-phase calculations to provide a direct comparison with detachment processes from similar orbitals to those in the QM/EFP calculation. The photodetachment cross-sections for each of the electron detachment processes were calculated for photon energies from the QM/EFP VDEs to 225 eV using ezDyson.

The Dyson orbitals are very similar for detachment to  $D_0$  in both the gas and QM/EFP calculations, with only minor orbital coefficients on the water molecules. Hence, the calculated detachment cross-sections are very similar. As is the case for electron detachment from the  $\pi$ -character HOMO-1 orbital ( $S_0$ - $D_2$  in the gas phase and  $S_0$ - $D_1$  in the QM/EFP calculation). Conversely, electron detachment from the non-bonding HOMO-2 orbital ( $S_0$ - $D_1$  in the gas phase and  $S_0$ - $D_2$  in the QM/EFP calculations) have similar Dyson orbitals across the phenolate anion but there are significant coefficients on the water molecules in the QM/EFP Dyson orbital. In this

case the QM/EFP cross-section is more complex than that in the gas phase with added structure due to interference of the orbital density on the water molecules.

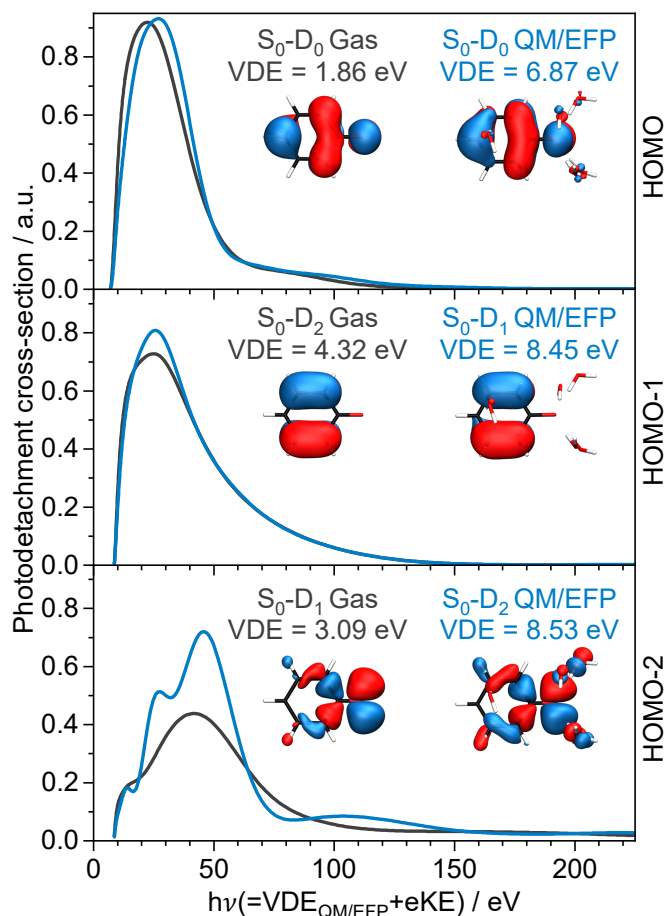


**Figure 6.15:** One-photon photodetachment cross-sections for isolated gas-phase phenolate (black lines) and a single optimised QM/EFP snapshot geometry (blue lines) for photodetachment from the HOMO, HOMO-1 and HOMO-2 HF orbitals. Cross-sections were calculated using the illustrated Dyson orbitals which are highly correlated with the HF orbitals. VDEs and Dyson orbitals were calculated with EOM-IP-CCSD/6-31+G\*. Photon energies ( $x$ -axis) were calculated using the QM/EFP VDEs for easier comparison.

With the calculated  $S_0$ - $D_1$  and  $S_0$ - $D_2$  QM/EFP VDEs being so close, it seems likely that electron detachment to  $D_1$  and  $D_2$  could overlap significantly in a photoelectron spectrum. This was not reported in the work by Ghosh *et al.* in which the x-ray photoelectron spectrum ( $h\nu = 200$  eV) of aqueous phenolate was fit using two Gaussian profiles (for  $D_0$  and  $D_1$ ).<sup>165</sup> However, it would be challenging to separate contributions from strongly overlapping features in their fitting analysis. At the high photon energy used (200 eV) the  $S_0$ - $D_2$  QM/EFP cross-section is much greater than



the  $S_0$ - $D_1$  equivalent and so at binding energies around  $\sim 8.5$  eV in an experimental spectrum, one would expect electron detachment from the non-bonding character HOMO-2 orbital to be much more significant. Hence, perhaps the two-Gaussian fit is appropriate but this could be describing the electron detachment processes from the HOMO and HOMO-2 orbitals with negligible contribution from HOMO-1 electron detachment. It would be interesting to measure the photodetachment of aqueous phenolate using UV pulses which could separate the  $S_0$ - $D_1$  and  $S_0$ - $D_2$  detachment processes as the cross-sections for the two transitions are markedly different with photon energies of  $\sim 10$  eV (Figure 6.15). In addition, UV photon energies probe resonant-enhanced photodetachment processes which will access certain detached states depending on the character of the excited resonant state.

## 6.4 Conclusions and outlook

The work in this chapter described a new approach for calculating the electronic structure of an organic anion in bulk aqueous solution using hybrid QM/EFP techniques. A large ensemble of phenolate - bulk water configurations was sampled using snapshots from a temperature-dependent MD simulation. A smaller subset of conformations was selected from the distribution of QM/EFP energies to represent the full ensemble at ambient temperature which were then used in more computationally-demanding geometry optimisation calculations at a QM/EFP level. EOM-IP-CCSD/EFP calculations were performed on the structures taken directly from the MD simulation (unoptimised) and following QM/EFP-optimisation to investigate the effect that relaxing the system within a QM description has on the transitions to the two lowest energy photodetached states ( $D_0$  and  $D_1$ ). The EOM-IP-CCSD/EFP VDEs calculated using the unoptimised structures were in agreement with those calculated elsewhere.<sup>165</sup> The EOM-IP-CCSD/EFP calculations performed on the QM/EFP optimised structures gave VDEs in closer agreement to experiment. On further inspection of the orbitals involved in the EOM-IP-CCSD transitions, the electronic configuration of the second photodetached state depends on the conformation of the solute-solvent system. It would be interesting to investigate

the higher energy photodetached states for a larger sample of configurations. The calculation of photodetachment energies in bulk media such as this are key to interpreting experimental measurements and simulating redox processes. The sampling approach could also be used to simplify other computationally expensive calculations such as transitions to electronically excited states or vibrational analysis. This work also validated an approach which may be used to study more complex anionic solutes in aqueous solution such as the PYP chromophore, as described in the following Chapter.

## Chapter 7

# Investigating the effect of solvation on the electron detachment from the photoactive yellow protein chromophore

The liquid-microjet valence x-ray photoelectron spectra presented in this Chapter were recorded by collaborators at BESSY, Berlin. All of the data analysis, including all fitting procedures, were performed by the author. Photoelectron spectra recorded in the gas phase provide useful insights into the intrinsic electronic structures of PYP chromophores (Chapters 4 and 5). Comparing these measurements and calculations to those performed with chromophores in bulk aqueous solution allows the interpretation of the effect of an environment on the chromophore. In this chapter, a valence x-ray photoelectron spectrum of the model PYP chromophore,  $p\text{CE}^-$ , in water is presented together with a computational analysis of the electronic structure of the chromophore in bulk water. Specifically, hybrid quantum mechanics/effective fragment potential (QM/EFP) techniques were employed to interpret the nature of the ionised states and explore potential approaches to model the absorption spectrum and hence make predictions for future UV photoelectron spectroscopy experiments.

## 7.1 Introduction

Photoinduced electron emission is an important competing process for many biological molecules and particularly so for anionic chromophores with detachment thresholds accessible with UV photons, such as the PYP chromophore. Understanding the electron emission from the PYP chromophore in aqueous solution can help disentangle the redox properties of the chromophore and indicate how it may undergo electron transfer chemistry in an aqueous environment. As demonstrated in Chapters 4 and 5, photoelectron spectroscopy studies of PYP chromophores isolated in the gas phase provide invaluable information on the intrinsic electronic structure and dynamics of isolated chromophores. By comparing these measurements made in the gas phase with those recorded in an aqueous solvent environment provides a valuable contrast and illustrates directly the effect an aqueous solvent environment has on the chromophore.

Microsolvated clusters of PYP chromophores have been studied both experimentally<sup>239</sup> and theoretically.<sup>45,181</sup> These studies have indicated a blueshift in the absorption maximum and threshold for electron detachment. Such studies provide useful insight into the effects of the micro-environment around the chromophore but are not representative of the bulk medium. No direct measurement or theoretical study of the electron detachment from a PYP chromophore in bulk water has been reported to date.

There have been numerous studies using transient absorption spectroscopy techniques to probe the excited state dynamics from both isolated PYP chromophore analogues and PYP in solution (see Chapter 1). Notably, evidence for the generation of solvated electrons has been reported following irradiation of high-intensity  $\sim 400$  nm light for both isolated chromophores<sup>85,86</sup> and the protein.<sup>63–65</sup> There is not a consensus on the mechanism for the electron detachment from PYP; resonant<sup>64</sup> and non-resonant<sup>63</sup> two-photon processes have been proposed. These studies indicate the presence of photodetachment but electron detachment has not been observed directly and they do not provide a quantitative analysis of the detachment energies. The aim of the work presented in this Chapter was to measure

the photodetachment directly and use computational techniques to model the PYP chromophore in solution to interpret the measurements at a molecular-level.

Employing photoelectron spectroscopy techniques with liquid samples has the potential to provide a powerful, direct comparison with the measurements made in the gas phase. Such measurements are challenging as the photoelectrons ejected from the sample must be collected in a vacuum which is difficult to achieve in the vicinity of an aqueous solution. This problem has been overcome through the development of liquid-microjet techniques.<sup>240–243</sup> Liquid-microjet photoelectron spectroscopy measurements are often performed using synchrotron radiation (100–200 eV) which probes almost exclusively direct photoionisation processes from the ground state. However, there are very few reported studies that have used these methods to investigate organic molecules in aqueous solutions<sup>220,242,244,245</sup> as generally the solubilities are very low ( $\sim$ mM). With such high photon energies, a workable signal-to-noise level of the analyte spectrum is difficult to acquire and instead the photoelectron spectrum of the solvent dominates.<sup>241</sup>

Accurate electronic structure calculations of an anionic chromophore in bulk solution are also very challenging. A large-scale molecular system is necessary to represent the diffuse charge and wide-spread hydrogen-bond network surrounding the chromophore. In addition, simulation of the inhomogeneous broadening observed in the experimental linewidths generally requires the inclusion of an ensemble of solute-solvent conformations, rather than just considering the geometry of the system at the minimum on the potential energy surface.

Several studies have employed hybrid quantum-mechanics/molecular-mechanics (QM/MM) methods to simulate the absorption spectrum of PYP chromophores in aqueous solution<sup>40,42,69,87,90,246–249</sup> or in the protein.<sup>45,61,62,66,67,83,245,250–259</sup> Aguilar and coworkers developed the averaged solvent electrostatic potential/molecular dynamics (ASEP/MD) method, a sequential QM/MM approach in which QM and MM descriptions are alternated and iterated until the charge distribution surrounding the solute has equilibrated.<sup>260</sup> Garcia-Prieto *et al.* have employed this ASEP/MD methodology with high-level multiconfigurational (CASSCF and CASPT2) methods to investigate the deprotonation site of the PYP chromophore,<sup>40</sup> the effect of func-

tionalisation at the carbonyl tail<sup>42</sup> and the energy profile of the first excited state surface.<sup>69,247</sup> From electronically excited state analysis using SA-CASSCF(14,12)-PT2/cc-pVDZ to describe the  $p\text{CE}^-$  chromophore within bulk water (1532 water molecules) described by an MM forcefield, the authors reported that the solvent shift for the  $n\pi^*$  state is more significant than for the  $\pi\pi^*$  states to such an extent that the states reorder from the gas phase (see Table 1.1).<sup>42</sup> Isborn and coworkers have simulated the absorption spectrum of PYP chromophores in solution using QM/MM with very large QM regions (solute and up to 400 water molecules) described by TD-DFT (TD- $\omega$ PBE/6-31+G\*) embedded within MM water molecules described by TIP3P point charges.<sup>248,249</sup> However, such large-scale calculations are only feasible for QM methods like DFT that scale well with the system size. The same group have also found that the inclusion of the vibronic Franck-Condon envelopes broadens the lineshape of the first absorption band obtained from vertical transitions to be in better agreement with experimental measurements, particularly on the blue edge.<sup>261</sup> This highlights the limitation of a spectrum obtained from purely vertical transitions.

Quantum-mechanics/effective-fragment potential (QM/EFP) methods provide a rigorous and computationally affordable way to include solute-solvent interactions.<sup>192,199,213</sup> QM/EFP is like QM/MM in that the model system is divided into subsystems described by different levels of theory but the bulk MM subsystem is not described by a classical and empirical forcefield. Instead the molecules in the low-level bulk subsystem are modelled as discrete effective fragments described by a non-empirical polarizable forcefield. Chapter 6 illustrated a procedure for modelling photodetachment from a phenolate anion in bulk aqueous solvent using QM/EFP methods. VDEs were calculated with a DFT/EFP approach and by employing the equation-of-motion coupled-cluster method with single and double excitation (EOM-CCSD) for ionisation potentials EOM-IP-CCSD/EFP. Configurational space of the solute-solvent system was sampled using a random-selection of snapshots taken from a temperature-dependent MD simulation and following a selection of representative configurations, a subset of snapshot geometries were relaxed within a QM/EFP description. The VDEs calculated using the QM/EFP-optimised structures were in

closer agreement with experiment than those extracted directly from the classical MD simulation.

In this chapter, a combined experimental and computational approach is used to study the electronic structure of the model PYP chromophore  $p\text{CE}^-$  in bulk water. A valence x-ray photoelectron spectrum of  $p\text{CE}^-$  in water is presented from which the VDE of the solvated chromophore may be obtained and compared to the gas-phase measurements described in Chapters 4 and 5 to reveal the effect of an aqueous environment on the photodetachment of the chromophore. To complement, a computational analysis of the chromophore in bulk water is also described in which a QM/EFP approach similar to that detailed in Chapter 6 was employed. The calculated results are used to interpret the nature of the ionised states, explore potential approaches to model the absorption spectrum and hence guide potential future experiments.

## 7.2 Methods

### 7.2.1 Experimental details

A solution of 5 mM  $p\text{CE}$  (methyl *trans*- $p$ -coumarate provided from TCI Chemicals, >98 % purity), 5.5 mM NaOH (Sigma-Aldrich, > 97.0 % purity) and 30 mM NaF (Sigma-Aldrich, > 99 % purity) in ultrapure water (18.2 M $\Omega$ cm resistivity at 25°C) was prepared. The solution was sonicated at 40°C for approximately 30 min to aid in dissolving the chromophore. A separate solution of 50 mM NaCl in ultrapure water was prepared to obtain a background subtraction.

Valence photoemission measurements from the aqueous solutions were performed at the U49/2 PGM-1 beamline (20×80  $\mu\text{m}^2$  focal size) of the synchrotron radiation facility BESSY II, Berlin. Details of the experimental apparatus have been detailed elsewhere.<sup>262</sup> The spectra were collected from a 25  $\mu\text{m}$  diameter liquid-microjet injected into vacuum with a velocity of approximately 20 m/s with a reservoir temperature of 12°C. Ejected photoelectrons were collected orthogonally to both the synchrotron beam polarisation and the liquid jet through a 500  $\mu\text{m}$  diameter opening which acts as an aperture to differentially pump the main chamber, containing the

liquid jet (low  $10^{-4}$  mbar) against the hemispherical electron analyser ( $\sim 10^{-6}$  mbar at the lens system), equipped with a multichannel detector (at  $10^{-8}$  mbar). The photon energy used in the experiments was 180 eV with a total resolution better than 125 meV. Energy resolution in the photoelectron detection was approximately 100 meV, achieved here using 20 eV pass energy (in sweep mode). The energy resolution for the beam line was approximately 100 meV (100  $\mu$ m beamline slit). The photoelectron spectra are calibrated to the  $1b_1$  peak of liquid water at 11.16 eV.<sup>263</sup> Given the low solute concentrations used, the shift in the water spectrum is expected to be minimal.<sup>264</sup>

An absorption spectrum was recorded using a PerkinElmer Lambda 365 spectrometer with an aqueous  $pCE^-$  solution consisting of 5 mM  $pCE$ , 50 mM NaOH and 30 mM NaF in distilled water. The addition of NaF did not change to the absorption spectrum within the 200-500 nm range. A 50 mM NaOH spectrum is subtracted from the sample spectrum and only contributes to intensities at photon energies  $< 225$  eV. The resulting absorption spectrum of aqueous  $pCE^-$  is comparable to those in the literature recorded in methanol (see Figure 1.19).<sup>33,34</sup>

## 7.2.2 Computational details

QM/EFP methods were used to simulate the  $pCE^-$  chromophore in bulk water using a multi-step approach to sample configurational space similar to that used in Chapter 6 to study aqueous phenolate. Initially, a classical molecular dynamics (MD) simulation was performed within the NAMD software<sup>229</sup> (developed by the Theoretical and Computational Biophysics Group in the Beckman Institute for Advance Science and Technology at the University of Illinois at Urbana-Champaign) to sample an ensemble of conformations of  $pCE^-$  in bulk water. In the MD simulation,  $pCE^-$  was positioned at the centre of a large cube of water (length  $\sim 102$  Å, 34,175 water molecules) as illustrated in Figure 7.1. A cube of  $\sim 100$  Å ensures a bulk solvation representation and provides ample flexibility in how the QM/EFP geometries may be extracted. The faces of the cube form periodic boundary conditions for a canonical ensemble (*i.e.*  $NVT$  - constant number of particles, volume and temperature).



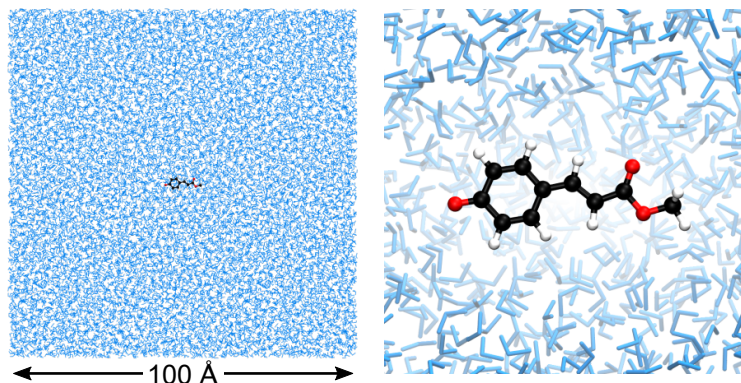


**Figure 7.1:** Left: full simulation cell used in the molecular dynamics simulation of  $p\text{CE}^-$  (centre) in bulk water (blue). Right: close-up of the chromophore within the simulation cell.

Approximate forcefield parameters for the chromophore were created using the SwissParam utility<sup>265</sup> with an isolated  $p\text{CE}^-$  optimised structure (Table B.2) and atomic partial charges (CHELPG<sup>206</sup>) calculated in the Gaussian09 software<sup>151</sup> at the B3LYP/6-311++G(3df,3pd) level. Water molecules were described by the TIP3P model.<sup>189</sup> The MD trajectory included an initial minimisation over 2000 steps (2 ps) before the the system was allowed to evolve at 300 K for 270 ps. The energy of the system equilibrated within 20 ps as shown in Appendix E.2. Geometries of the system were saved every 500 fs after the 20 ps equilibration period to provide 500 snapshot geometries of the solute-solvent system at room temperature to potentially sample in subsequent QM/EFP calculations.

The construction of the QM/EFP geometries was considered carefully by calculating the VDE as the size of the QM or EFP subsystems were increased, as illustrated in Appendices E.3 and E.4. All other water molecules were discarded. The VDEs were calculated using the energy difference method with B3LYP/6-31+G\* (benchmarked with aqueous phenolate in Table 6.1). There is only a minimal difference between the simplest QM system (in which only the chromophore is described by QM) and the most complex system with ten QM water molecules. The difference in the average VDE calculated between the five and ten-water systems was only 0.06 eV. Including five solvent molecules within the QM subsystem ensures that in almost all cases ( $\sim 93\%$ ), all water molecules forming direct hydrogen bonds with the chromophore were described by QM theory (Appendix E.5). There was a

dramatic difference between the VDEs calculated without the EFP system (a pure QM, microsolvated system) and VDEs calculated with EFP cut-off radii of  $> 10 \text{ \AA}$  but only a small difference ( $\sim 0.12 \text{ eV}$ ) between the average VDEs calculated for the  $16 \text{ \AA}$  and  $24 \text{ \AA}$  radii systems. Thus, an appropriate QM/EFP construction was found to include a QM system containing the chromophore and the five water molecules closest to any atom within the chromophore and the EFP system containing any water molecule within  $16 \text{ \AA}$  of any atom within the chromophore. An example of this system is shown in Figure 7.2A.

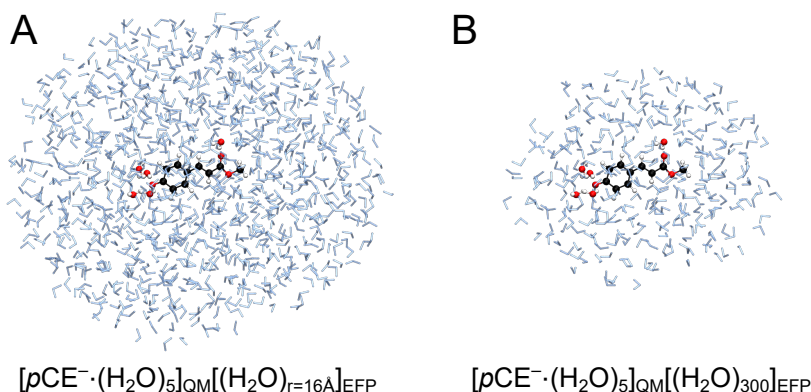


**Figure 7.2:** Example QM/EFP constructions with an EFP radius of  $16 \text{ \AA}$  (A) and a truncated EFP region including exactly 300 solvent fragments (B). The larger system is used in QM/EFP calculations in which the geometries have not been optimised using QM/EFP and in this example snapshot there are 985 water molecules included within the EFP subsystem. The truncated QM/EFP system is used in the QM/EFP geometry optimisation calculations and any further calculations using those optimised geometries.

300 of the 500 potential configurations from the MD trajectory were picked randomly and used within B3LYP/6-31+G\*//EFP calculations constructed as in Figure 7.2A to find the energies of the ground state energy of the anion ( $S_0$ ), the ground state energy of the neutral radical ( $D_0$ ) and hence the VDE as the difference. The distribution of the  $S_0$  energies were used in a second sampling step to collect a small subset of configurations to represent the full ensemble. Snapshots with  $S_0$  energies closest to the energy at the centre of the Gaussian fit to the distribution of the 300  $S_0$  energies were selected first.

The small subset of selected configurations was then used in more computationally-demanding calculations such as QM/EFP geometry optimisations, excited state analyses with TD-DFT and EOM-EE-CCSD (EOM-CCSD for excitation energies)

and the calculation of VDEs using EOM-IP-CCSD. A smaller EFP subsystem including exactly 300 water molecules was used within the geometry optimisation calculations and any subsequent calculations performed with the optimised structures. This was done to adhere to the requirements of the software and an example of this truncated QM/EFP system is shown in Figure 7.2B. In all TD-DFT calculations, eight singlet states were calculated. Geometry optimisations were performed within the Firefly quantum chemistry package,<sup>152</sup> which is partially based on the GAMESS (US) source code.<sup>153</sup> All other QM/EFP calculations were performed within the QChem software package.<sup>156</sup> Standard EFP parameters were used to represent water in QM/EFP calculations within the QChem<sup>232</sup> and Firefly<sup>233</sup> libraries.

## 7.3 Results and discussion

### 7.3.1 Experimental results

The valence x-ray photoelectron spectrum of an aqueous  $p\text{CE}^-$  solution in a liquid-microjet, recorded by collaborators at the BESSY facility in Berlin using a photon energy of 180 eV, is presented in Figure 7.3. It is not just the most weakly-bound  $p\text{CE}^-$  electrons that are detached but also those of liquid and gaseous water. At such low concentrations of  $p\text{CE}^-$ , the electron detachment signal from  $p\text{CE}^-$  is not visible on the full scale of the spectrum but can be seen in an expansion of the leading water edge (see inset). The water spectrum may be fit using a sum of Gaussian profiles for ionisation from the  $1b_1$ ,  $3a_1$  and  $1b_2$  orbitals of both gaseous and liquid water in a similar procedure to that used in previous studies of valence spectra of water.<sup>263,266–268</sup> The difference spectrum presented in the inset is obtained by subtracting the total water fit from the measured spectrum.

There is only a very small difference between two very high intensity lines and so confidence in the difference spectrum at binding energy  $> 8.5$  eV is limited and any subsequent fitting of this difference spectrum is highly sensitive to the shape of the reference spectrum in this region. Thus, many attempts were made to fit the leading  $1b_1$  peak to form the reference spectrum used in the subtraction, as shown in Figure 7.4. In Figure 7.3, the reference spectrum used was the sum of

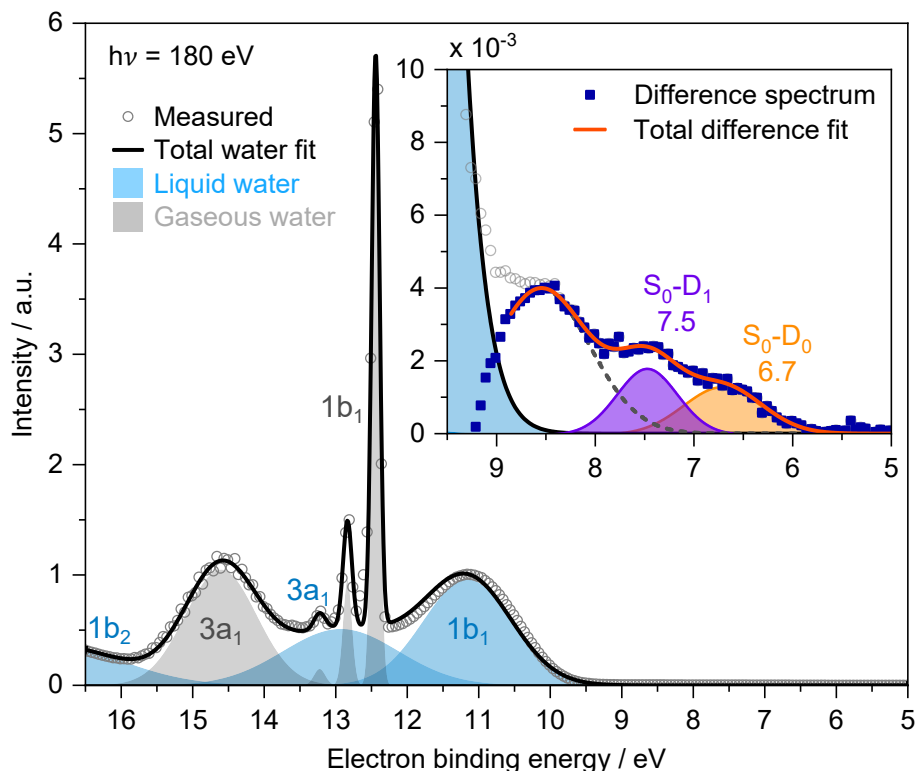


**Figure 7.3:** Valence photoelectron spectrum of a 5 mM  $p\text{CE}^-$  solution measured at 180 eV. Liquid and gaseous water ionisation are indicated by the Gaussian fits shown in solid blue and grey, respectively. Intensities are normalised to the  $1b_1$  liquid water peak. The inset shows an expansion of the onset of the spectrum with the difference (blue squares) between the measured spectrum and the total water fit. A fit of three Gaussian profiles to the difference spectrum is shown with the assignments and peak maxima of the two lower eBE peaks indicated.

the water peaks fit to the full spectrum in which the peak position and width of the leading  $1b_1$  Gaussian was constrained in the fit to be that reported previously for the liquid  $1b_1$  peak in pure water.<sup>263</sup> The water spectrum was also fit with these constraints lifted and both this and the constrained  $1b_1$  peaks are shown in Figure 7.4. Note that the only water peak with significant intensity in the  $< 10$  eV range is the liquid  $1b_1$  peak. A low concentration (50 mM) NaCl spectrum recorded under similar experimental conditions is also presented. The contribution of chloride detachment in this spectrum is expected to be minimal and so may serve as a background reference spectrum. This NaCl spectrum was smoothed (12 point quadratic Savitzky-Golay filter) before use in the subtraction to limit the effects of noise that could produce artefacts. Overall, the three different reference spectra

make little variation in the difference spectrum of  $pCE^-$ , particularly at binding energies below 8.5 eV which is the region of interest for the study of photodetachment from this chromophore.

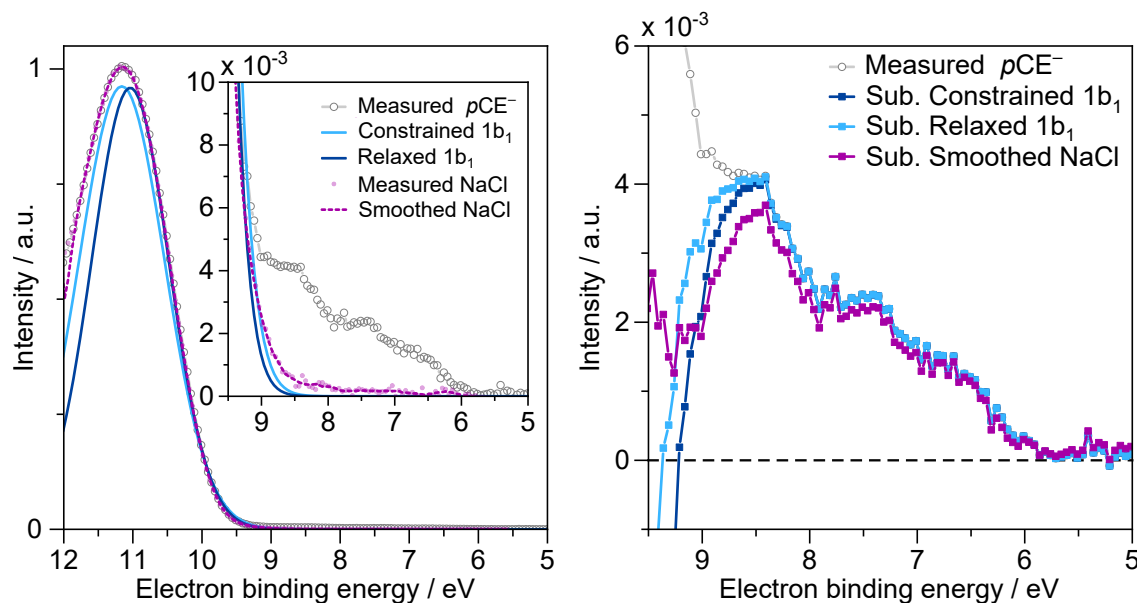


**Figure 7.4:** Attempts made to fit the reference spectrum used in the subtraction to give the difference spectrum of an aqueous  $pCE^-$  solution. Left: the various fitted reference spectra (inset shows an expansion of the onset). The constrained  $1b_1$  and relaxed water  $1b_1$  fits have been taken from a full fit to the water spectrum, as shown in Figure 7.3. In the constrained fit, the peak position and width are fixed to those reported in the literature.<sup>263</sup> The measured NaCl spectrum has been recorded under similar conditions to the  $pCE^-$  spectrum using a low concentration (50 mM) solution and has been smoothed before subtraction. Right: difference spectra generated by subtracting the different reference spectra from the aqueous  $pCE^-$  spectrum. Intensities of the measured spectra are normalised on the liquid  $1b_1$  peak.

The fit to the difference spectrum presented in Figure 7.3 has been constrained to binding energies below 8.85 eV, above which the overlap of the solute and water peaks becomes significant. Many fitting attempts of the difference spectrum were made by varying the fit cut-off, the number of Gaussians and the starting parameters. A representative selection of these attempts is presented in Figure 7.5. It can be seen that these attempts agree in the peak positions of the first two Gaussians and so, as presented in Figure 7.3, these two leading Gaussian peaks may be assigned to electron detachment from  $pCE^-$ . The third leading Gaussian at  $\sim 8.5$  eV is not assigned here as the sensitivity to the fit parameters and subtraction of the reference

data is too great to bring sufficient certainty. A fit of four Gaussians induces a small shift in the second leading feature but this is a poorer fit overall ( $R^2 = 0.90$ ) in which the extra fourth peak resides in the uncertain  $< 8.5$  eV region. The error in the fitting of the orange Gaussian is within the experimental error of 0.1 eV whereas there is more deviation in the position of the purple Gaussian in the fits so a conservative estimate of 0.2 eV is used for the error on this feature. Therefore,

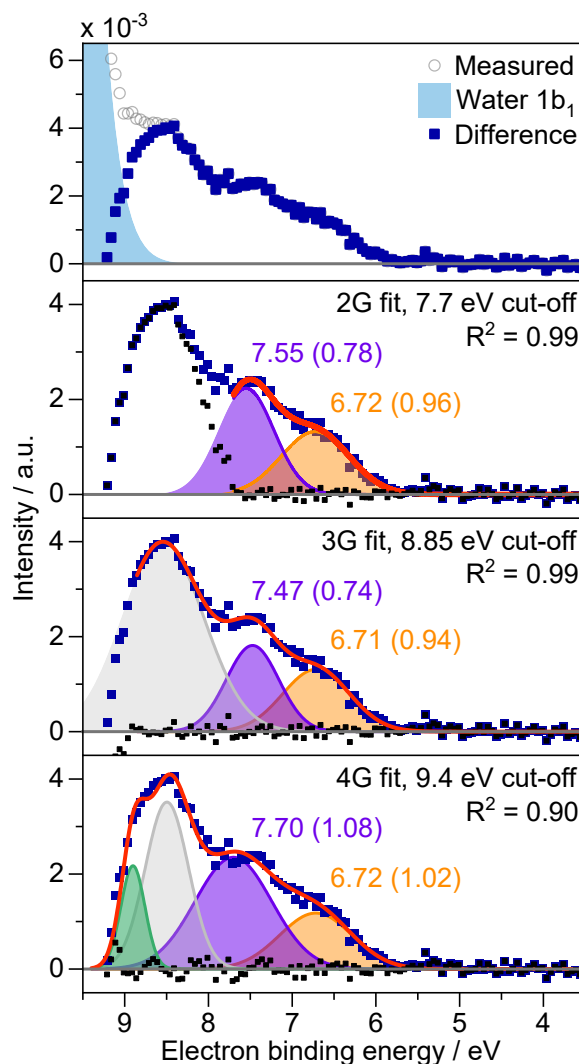


**Figure 7.5:** Various fit attempts made to the difference spectrum of an aqueous  $p\text{CE}^-$  solution. The top panel shows the difference spectrum and the lower panels show different fits to this difference spectrum using varied fitting parameters. The number of Gaussians (G) used in the fit, the cut-off of the fit in electron binding energy and the  $R^2$  values are noted for each plot. Additionally, the peak positions (and full-width-half-maxima in parentheses) are labelled for the leading two Gaussians in each fit. The total fit in each case is shown by the red line and the residuals are plotted as black squares. Intensities are normalised on the liquid  $1b_1$  peak.

the lowest energy VDE of  $pCE^-$  ( $S_0-D_0$ ) is determined as the peak of the orange Gaussian at  $6.7 \pm 0.1$  eV and the second VDE ( $S_0-D_1$ ) as the peak of the purple Gaussian at  $7.5 \pm 0.2$  eV.

The aqueous  $pCE^-$  solution was composed of 5 mM  $pCE$ , 5.5 mM NaOH and 30 mM NaF in water and the possibility of other components contributing to the spectrum shown in Figure 7.3 was also investigated. The ionisation of  $Na^+$  is beyond the scale of the water spectrum with an eBE of 35.4 eV.<sup>269</sup> Electron detachment from fluoride anions is expected to be a minimal contribution to the spectrum with an eBE of 11.58 eV.<sup>241</sup> This has not been included within the fits to the full water spectrum due to the overlap with the liquid  $1b_1$  and  $3a_1$  peaks in this region making fluoride detachment challenging to locate at such low concentrations. A slight excess (10%) of NaOH base was used to ensure full deprotonation of the chromophore in solution and so it is expected that some residual hydroxide anions would be in the solution ( $\sim 500 \mu M$ ). Winter *et al.* reported that electron detachment from 0.1 M hydroxide in water occurs with a peak at 8.8 eV eBE and a FWHM of 1.3 eV.<sup>270</sup> The authors also measured photoelectron spectra at stronger concentrations and found a linear dependence between the hydroxide concentration and the photoelectron signal of the hydroxide peak in reference to the liquid water  $1b_1$  photoelectron signal. Using this linear relationship, the photoelectron signal expected from the residual 0.5 mM hydroxide concentration in the solution may be estimated to have a peak height of  $\sim 1.2 \times 10^{-6}$  on the intensity scale in Figure 7.3. Hence, the hydroxide contribution to the spectrum lies within the amplitude of the experimental noise and has been disregarded from further analysis of this  $pCE^-$  spectrum. Overall, this leaves electron detachment from aqueous  $pCE^-$  to be the only contributing process to the spectrum at eBEs below the water  $1b_1$  peak.

### 7.3.2 Computational results

#### QM/EFP calculations performed on a large sample size

300 snapshots were randomly selected from an MD sampling trajectory and for each snapshot structure, the QM and EFP geometries were extracted to form a

$[p\text{CE}^- \cdot (\text{H}_2\text{O})_5]_{\text{QM}}[(\text{H}_2\text{O})_{r=16\text{\AA}}]_{\text{EFP}}$  construction, similar to that shown in Figure 7.2A. The electronic energy of each of these configurations was calculated using QM/EFP (QM=B3LYP/6-31+G\*) for both the anionic ground state,  $S_0$  and the ground state of the neutral radical,  $D_0$ . Figure 7.6 shows the energies of the  $S_0$  and  $D_0$  states calculated for each snapshot and the distribution of these energies.

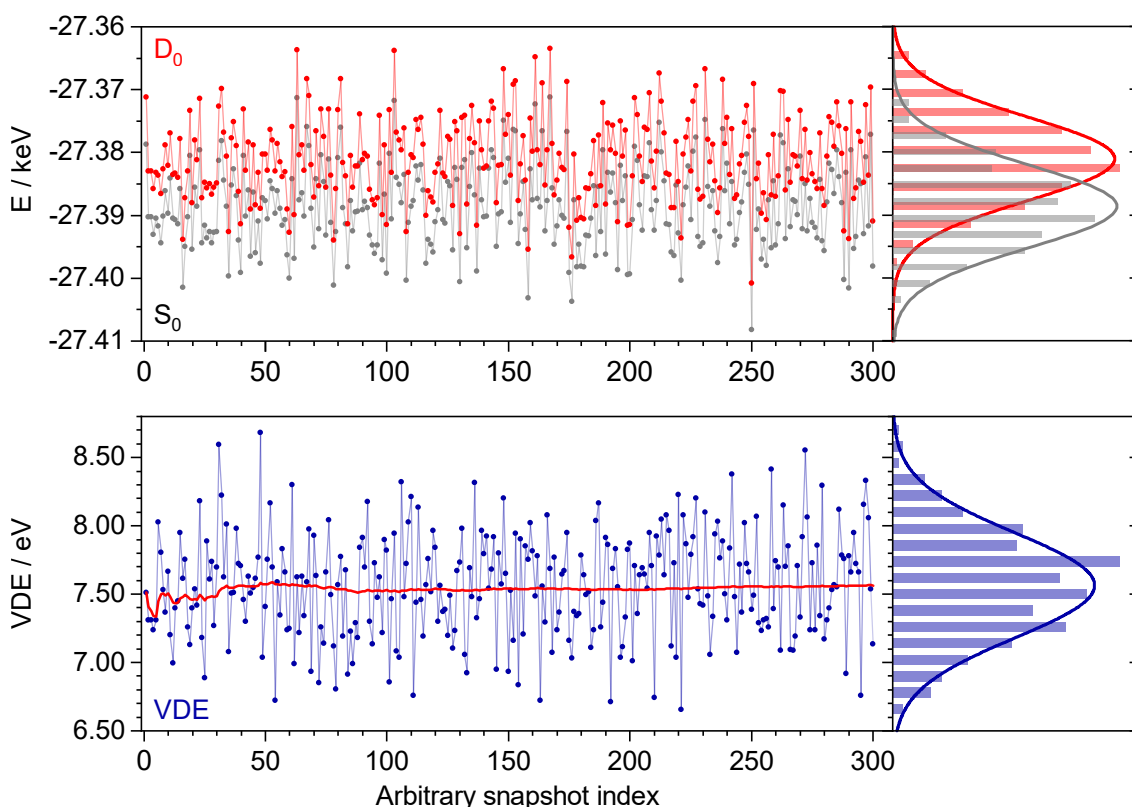


**Figure 7.6:** Top: energies of the  $S_0$  and  $D_0$  states calculated with QM/EFP (QM=B3LYP/6-31+G\*) over 300 randomly-selected snapshots and the right panel shows the distribution of these energies collected into a histogram. Bottom: VDEs calculated for each of the snapshots using the difference of the energies in the plot above. A rolling average is shown in red and the distribution of the VDEs is shown with the histogram in the right panel. Each of the histograms have been fit with a Gaussian distribution.

The spread of energies is similar for both states and there is significant overlap. The FWHM of the  $S_0$  and  $D_0$  Gaussian distributions are 15.6 and 15.7 eV, respectively. The average VDE may be taken as the energy difference between these Gaussian peaks as 7.56 eV. Alternatively, the average VDE may be found by first calculating the VDE for each snapshot, as shown in the bottom panel. The rolling average plateaus within  $\sim 100$  snapshots and at 300 snapshots has a value of 7.56 eV.



The distribution of the VDEs is significantly more narrow than found for the component energies with a FWHM of 0.90 eV. This suggests the  $S_0$  and  $D_0$  potential energy surfaces are effectively parallel on the scale of the deviation of each surface. The peak of the Gaussian fit to the distribution of VDEs also affords an average VDE of 7.56 eV. The agreement between these three approaches to determine the average VDE indicates that the sample size of 300 snapshots is sufficiently large to form a Normal distribution and obtain an average.

### Sampling representative conformations

Snapshot geometries were selected by first fitting a Gaussian curve to the distribution of B3LYP/6-31+G\*\*/EFP  $S_0$  energies and then choosing snapshots with energy close to the peak of the Gaussian, as shown in Figure 7.7. The sampling approach was used to select twenty structures that are representative of the full ensemble.

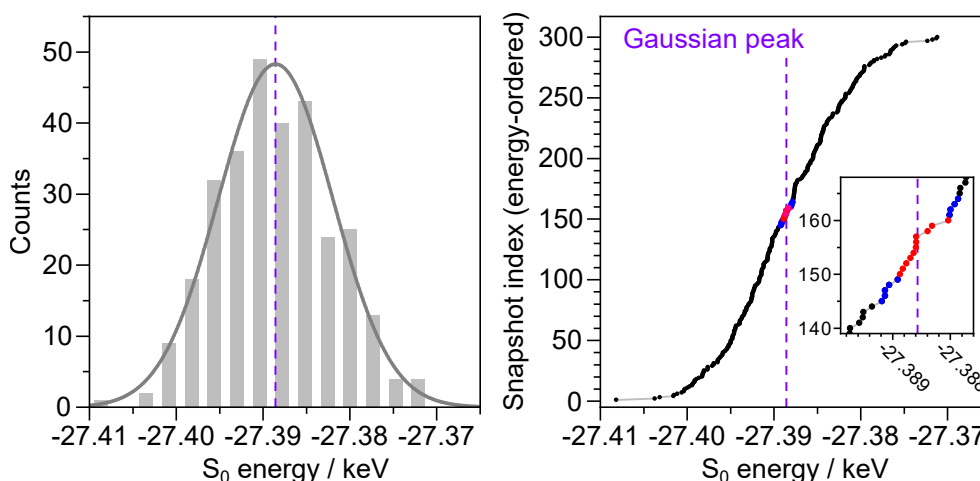


**Figure 7.7:** Left: histogram of  $S_0$  energies calculated with QM/EFP (QM=B3LYP/6-31+G\*) over the 300 randomly-selected snapshots with a Gaussian distribution (bin widths are 2.61 eV). The centre of the Gaussian peak is indicated by the vertical dashed line. Right: energies in increasing order highlighting the ten (red) or twenty (blue) selected snapshots with energies closest to the average energy (Gaussian peak). Inset is an expansion of the scale in the selection region.

The snapshots selected in this second sampling stage were used within geometry optimisations using QM/EFP (QM=B3LYP/6-31+G\*) with a smaller EFP region similar to that shown in Figure 7.2B. Within the geometry optimisation calculations, the positions of all QM atoms (the chromophore and five water molecules) are freely

adjusted and the 300 water molecules modelled by EFP are reorientated such that the internal geometries remain fixed but the rotational and translational degrees of freedom are relaxed.

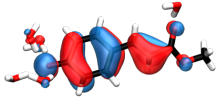
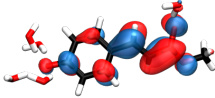
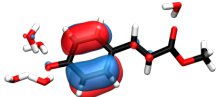
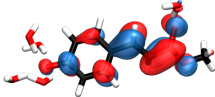
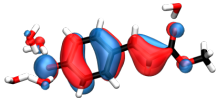
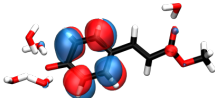
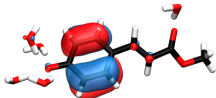
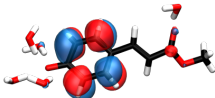
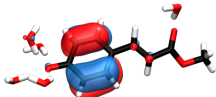
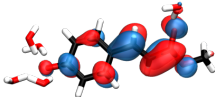
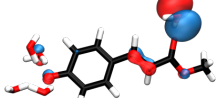
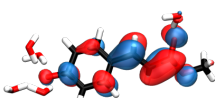
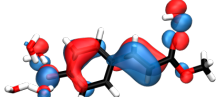
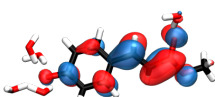
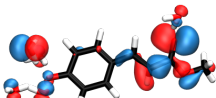
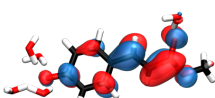
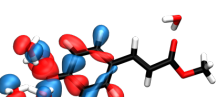
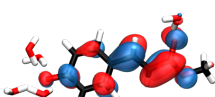
### Vertical excitation energies

Excited state analysis was performed employing TD-DFT and EOM-EE-CCSD approaches. TD-DFT calculations scale approximately with  $\sim N^{2.5}$  and so are more appropriate for the large-scale complex QM/EFP systems, particularly when calculating with many geometries. EOM-EE-CCSD calculations scale approximately with  $N^6$  and so are much more expensive but the method is not limited by empirical parametrisation like with the DFT functionals used here. Here, TD-DFT calculations have been used to illustrate how electronically excited state calculations with QM/EFP may be used to simulate an absorption spectrum and a preliminary EOM-EE-CCSD analysis is also presented. In theory, the EOM-EE-CCSD approach could be extended to simulate an absorption spectrum similar to that shown with the TD-DFT analysis.

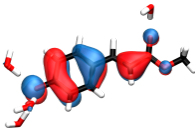
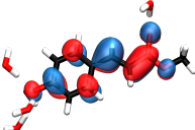
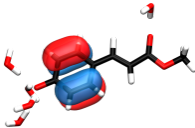
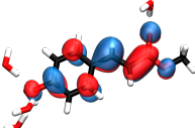
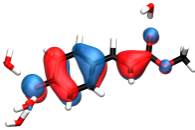
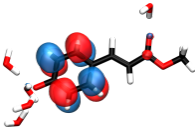
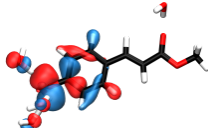
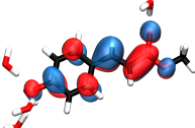
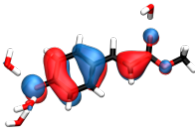
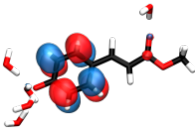
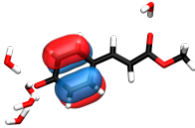
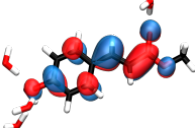
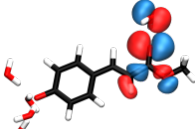
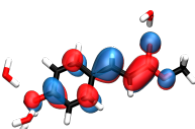
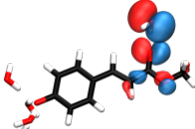
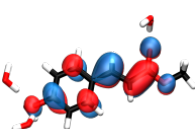
The first five electronically excited singlet states were calculated using TD-DFT/EFP (B3LYP/6-31+G\*) for the snapshot with the ground state energy closest to the peak of the Gaussian in Figure 7.7. This calculation was performed using both the unoptimised and optimised geometries, the results are shown in Tables 7.1 and 7.2, respectively. The orbital contributions to each transition are also included. With optimisation, the  $\pi\pi^*$  transitions change very little with only a small redshift ( $\sim 0.2$  eV). Conversely, the  $n_{\text{phen}}\pi_1^*$  transition redshifts more significantly by 0.74 eV. The relevant orbitals found for the optimised system are more localised to the chromophore and more similar to those found for the gas-phase chromophore reported in Chapter 4.

The maximum of the first band in the experimental absorption spectrum is found at  $\sim 3.5$  eV (Figure 7.8) and so the optimised geometry provides a slightly better agreement with the experimental measurement. Further TD-DFT calculations were performed using this same optimised geometry with various different theory levels as shown in Table 7.3. Three popular hybrid exchange-correlation functionals were

**Table 7.1:** Vertical excitation energies, oscillator strengths ( $f$ ) and orbital contributions to the first five singlet electronic excited states calculated using QM/EFP (QM=B3LYP/6-31+G\*) with an unoptimised geometry. Contributions above 7% are included.

VEE / eV ( $f$ )	Occupied	Unoccupied	Character	$c^2$ %
4.142 (0.777)		$\rightarrow$ 	$\pi_H \pi_1^*$	92
4.516 (0.052)		$\rightarrow$ 	$\pi_{H-1} \pi_1^*$	65
		$\rightarrow$ 	$\pi_H \pi_2^*$	29
5.142 (0.046)		$\rightarrow$ 	$\pi_{H-1} \pi_2^*$	56
		$\rightarrow$ 	$\pi_{H-1} \pi_1^*$	30
5.279 (0.007)		$\rightarrow$ 	$\pi_{\text{water}} \pi_1^*$	48
		$\rightarrow$ 	$n_{\text{CO}} \pi_1^*$	28
		$\rightarrow$ 	$n'_{\text{CO}} \pi_1^*$	15
5.312 (0.001)		$\rightarrow$ 	$n_{\text{phen}} \pi_1^*$	89

**Table 7.2:** Vertical excitation energies, oscillator strengths ( $f$ ) and orbital contributions to the first five singlet electronic excited states calculated using QM/EFP (QM=B3LYP/6-31+G\*) with an optimised geometry. Contributions above 7% are included.

VEE / eV ( $f$ )	Occupied	Unoccupied	Character	$c^2$ %
3.791 (1.226)			$\pi_H \pi_1^*$	94
4.314 (0.001)			$\pi_{H-1} \pi_1^*$	76
			$\pi_H \pi_2^*$	23
4.571 (0.000)			$n_{phen} \pi_1^*$	97
4.976 (0.065)			$\pi_H \pi_2^*$	59
			$\pi_{H-1} \pi_1^*$	18
4.987 (0.006)			$n_{CO} \pi_1^*$	79
			$n'_{CO} \pi_1^*$	11

used: B3LYP,  $\omega$ -B97X-D<sup>176,177</sup> and CAM-B3LYP, each with the 6-31+G\* and 6-311++G\*\* basis sets. The orbital contributions for the first five states calculated with any of the methods used here are found to be similar to those presented in Table 7.2 calculated with B3LYP/6-31+G\* but the ordering of these transitions changes between the methods. See Appendix E for detailed orbital contributions for each of the TD-DFT transitions. For each of the methods, the first state is calculated to be a bright state with a VEE of  $\sim 3.77$ -4.02 eV with the leading contribution being a transition from the HOMO  $\pi_{\text{H}}$  orbital to the LUMO  $\pi_1^*$  orbital. Similarly, the second state is found to be almost optically dark ( $f < 0.01$ ) with a transition energy of  $\sim 4.3 - 4.75$  eV with similar orbital contributions, regardless of the TD-DFT approach used. The higher lying states reorder in energy with the different theory levels used. In particular, the states with greater charge transfer characters (*i.e.*  $n\pi^*$  character states) reorder more significantly which is expected as the DFT functionals used here have varied representations of the long-range interactions.

**Table 7.3:** Vertical excitation energies (in eV), oscillator strengths ( $f$ ) and characters of the first five singlet electronically excited states calculated using QM/EFP at various QM levels with an optimised geometry. Contributing orbitals are similar to those presented in Table 7.2. Transitions to diffuse states have been omitted.

	1	2	3	4	5
B3LYP/ 6-31+G*	3.791 (1.226) $\pi_{\text{H}}\pi_1^*$	4.314 (0.001) $\pi_{\text{H}-1}\pi_1^*/\pi_{\text{H}}\pi_2^*$	4.571 (0.000) $n_{\text{phen}}\pi_1^*$	4.976 (0.065) $\pi_{\text{H}-1}\pi_1^*/\pi_{\text{H}}\pi_2^*$	4.987 (0.006) $n_{\text{CO}}\pi_1^*$
B3LYP/ 6-311++G**	3.774 (1.217) $\pi_{\text{H}}\pi_1^*$	4.294 (0.001) $\pi_{\text{H}-1}\pi_1^*/\pi_{\text{H}}\pi_2^*$	4.549 (0.000) $n_{\text{phen}}\pi_1^*$	4.934 (0.074) $\pi_{\text{H}-1}\pi_1^*/\pi_{\text{H}}\pi_2^*$	4.961 (0.001) $n_{\text{CO}}\pi_1^*$
$\omega$ -B97X-D/ 6-31+G*	4.040 (1.222) $\pi_{\text{H}}\pi_1^*$	4.747 (0.010) $\pi_{\text{H}-1}\pi_1^*/\pi_{\text{H}}\pi_2^*$	5.404 (0.000) $n_{\text{phen}}\pi_1^*$	5.565 (0.002) $n_{\text{CO}}\pi_1^*$	5.660 (0.175) $\pi_{\text{H}-1}\pi_1^*/\pi_{\text{H}}\pi_2^*$
$\omega$ -B97X-D/ 6-311++G**	4.018 (1.207) $\pi_{\text{H}}\pi_1^*$	4.712 (0.013) $\pi_{\text{H}-1}\pi_1^*/\pi_{\text{H}}\pi_2^*$	5.380 (0.000) $n_{\text{CO}}\pi_1^*$	5.539 (0.002) $n_{\text{phen}}\pi_1^*$	5.619 (0.173) $\pi_{\text{H}-1}\pi_1^*/\pi_{\text{H}}\pi_2^*$
CAM-B3LYP/ 6-31+G*	4.000 (1.225) $\pi_{\text{H}}\pi_1^*$	4.729 (0.009) $\pi_{\text{H}-1}\pi_1^*/\pi_{\text{H}}\pi_2^*$	5.425 (0.000) $n_{\text{CO}}\pi_1^*$	5.518 (0.003) $n_{\text{phen}}\pi_1^*$	5.603 (0.166) $\pi_{\text{H}-1}\pi_1^*/\pi_{\text{H}}\pi_2^*$
CAM-B3LYP/ 6-311++G**	3.979 (1.213) $\pi_{\text{H}}\pi_1^*$	4.694 (0.012) $\pi_{\text{H}-1}\pi_1^*/\pi_{\text{H}}\pi_2^*$	5.402 (0.001) $n_{\text{CO}}\pi_1^*$	5.493 (0.003) $n_{\text{phen}}\pi_1^*$	5.561 (0.162) $\pi_{\text{H}-1}\pi_1^*/\pi_{\text{H}}\pi_2^*$

Each of the various TD-DFT analyses shown in Table 7.3 are illustrated as stick spectra in Figure 7.8 together with the experimental absorption spectrum. With each of the theory levels used, the eight calculated states are included and a

Gaussian convolution of the stick spectrum (FWHM 0.5 eV) is shown to generate a simulated absorption spectrum. Generally, the simulated spectra consist of two bands and the shoulder in the experimental spectrum at  $\sim 4$  eV is not apparent in the simulated spectra. This suggests that this shoulder in the measured spectrum forms part of the vibrational structure of the first band which is not included in the purely electronic vertical spectra presented. This is in agreement with the *ab initio* MD simulations reported by Zuehlsdorff *et al.*<sup>261</sup> The position of the first band changes very little with the increase in basis set size. It is not clear which approach provides the most accurate results for the full spectrum but the B3LYP methods have given the closest agreement with the first experimental band.

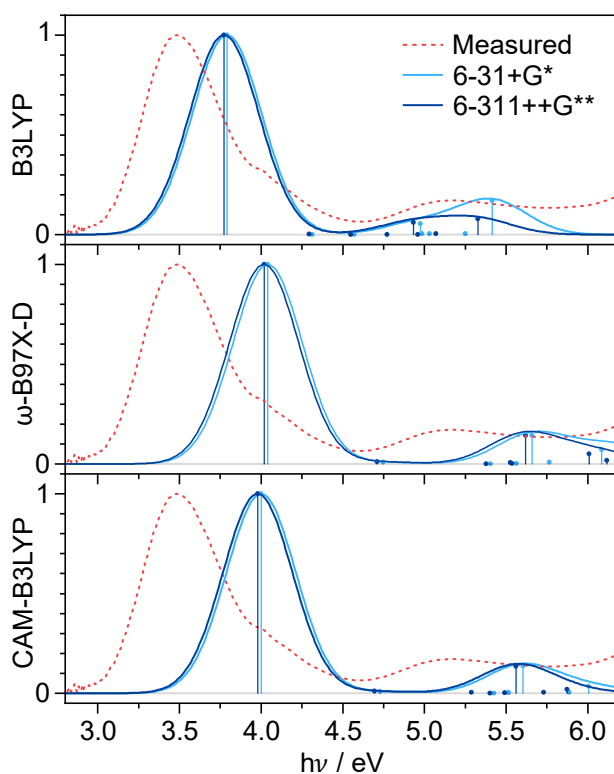


**Figure 7.8:** Measured absorption spectrum of  $p\text{CE}^-$  in water with simulated spectra calculated using TD-DFT/EFP with various exchange-correlation functionals and basis sets for a single optimised geometry. Calculated excitation energies and oscillator strengths (normalised to maxima) are shown by the vertical lines for eight singlet states calculated with two basis sets, 6-31+G\* in light blue and 6-311++G\*\* in dark blue. The full line spectra are the result of a Gaussian convolution of the stick spectra (0.5 eV FWHM).

Such TD-DFT calculations are inexpensive and so may be performed on a large number of snapshot geometries. A thorough analysis of the orbital contributions

is cumbersome when considering many geometries as the orbitals differ with the atomic positions. However, a simulated absorption spectrum may still be made using the oscillator strengths and VEEs to indicate the electronic structure. Figure 7.9 shows the B3LYP/6-31+G\* stick spectra calculated for each of the twenty optimised QM/EFP structures selected as shown in Figure 7.7. Eight states were calculated for each of the structures and each stick spectrum set is represented by a different colour. Gaussian convolutions of all 400 states are shown on the right with various Gaussian widths. Interestingly, the general shape of the spectrum is similar to that found for just one structure as shown in the top panel of Figure 7.8. Considering just the lowest energy transition, most of the geometries gave VEEs around 4 eV but a small proportion gave lower VEEs broadening this band in the simulated spectrum slightly towards the red. It would be interesting to investigate whether a more delocalised sampling approach could provide a width of the first band in better agreement with experiment.

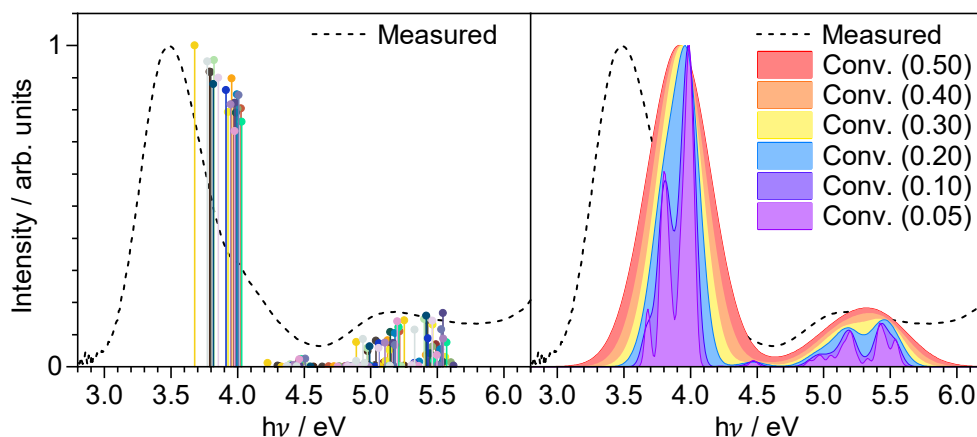


**Figure 7.9:** Left: simulated spectrum calculated using QM/EFP (QM=B3LYP/6-31+G\*). Left: calculated VEEs and oscillator strengths (normalised to maximum) for each of twenty optimised QM/EFP geometries are shown by the vertical lines with each geometry set represented by a different colour. Right: simulated spectra generated with a Gaussian convolution of all the stick spectra shown on the left with a FWHM specified in parentheses. Each panel presented with the measured absorption spectrum of  $p\text{CE}^-$  in water (dashed black line).

A similar approach may be used to simulate the absorption spectrum using high-level wavefunction methods rather than TD-DFT. Table 7.4 compares the excited state analysis performed using EOM-EE-CCSD/6-31+G\*//EFP to the B3LYP/6-

311++G\*\*//EFP analysis. The orbitals involved in the EOM-EE-CCSD transitions (Table 7.5) are similar to those calculated with the DFT approach but the higher energy unoccupied orbitals have more diffuse character. The structure used in these calculations is the snapshot with ground state energy closest to the Gaussian peak selected in Figure 7.7 that has been optimised using QM/EFP. Table 7.4 also lists SA-CASSCF(14,12)-PT2/cc-pVDZ//MM values reported by Garcia-Prieto *et al.*<sup>42</sup> and the maxima of the distinct bands in the experimental absorption spectrum. It is worth noting that the VEEs for the  $\pi_{\text{H}}\pi_1^*$  states calculated with TD-DFT, EOM-EE-CCSD and the SA-CASSCF method are in very close agreement. However, the other states vary in ordering, character and intensity. Both the DFT and EOM-EE-CCSD results share similar characters for the second electronically excited states but this is not the case for the SA-CASSCF result. It would be interesting to calculate a greater number of EOM-EE-CCSD transitions to see where the  $n_{\text{phen}}\pi_1^*$  VEE lies.

### Vertical detachment energies

Figure 7.6 illustrated how the first VDE may be calculated as an average over a large number of unoptimised snapshots taken directly from the MD simulation to be 7.56 eV. The VDE may also be calculated using this energy difference method for the optimised structures as shown in Table 7.6. This has been performed using an average of the ten and twenty snapshots with ground state energies closest to the Gaussian peak as selected in Figure 7.7. A comparison to the VDE averaged over the same subset of structures before QM/EFP optimisation is also provided. Optimising the structures has lowered the average VDEs by  $\sim 1.4$  eV for both the ten- and twenty-sample averages. This brings the average VDE closer to the experimental value taken from the peak of the leading Gaussian in the fit in Figure 7.3. Additionally, there is little difference in the 10, 20 or 300-sample averages suggesting that it is sufficient to average over ten configurations.

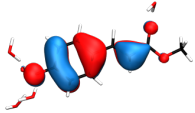
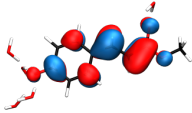
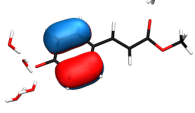
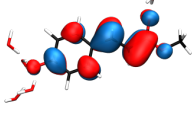
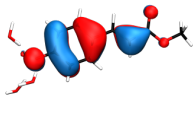
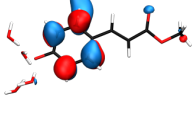
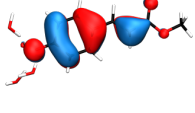
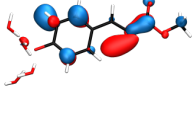
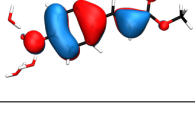
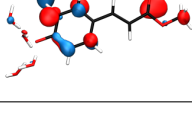
QM/EFP calculations using EOM-IP-CCSD/6-31+G\* were performed to calculate VDEs with an *ab initio* wavefunction-based approach and also find the VDE to the second detachment continuum ( $S_0$ -D<sub>1</sub> transition). However, such calculations are much more expensive and so to calculate over a large number of snapshots



**Table 7.4:** Vertical excitation energy (VEEs) calculated using QM/EFP with B3LYP/6-311++G\*\* or EOM-EE-CCSD/6-31+G\* for a single optimised geometry compared with QM/MM (QM = SA-CASSCF(14,12)-PT2/cc-pVDZ) calculated values<sup>42</sup> and the maxima of the distinct bands in the experimental absorption spectrum.

Method		VEE / eV ( <i>f</i> )	Contributions	
Experimental maxima		3.48		
		5.15		
QM/EFP	1	3.77 (1.22)	94 %	$\pi_H\pi_1^*$
B3LYP/ 6-311++G**	2	4.29 (0.00)	74 %	$\pi_{H-1}\pi_1^*$
			24 %	$\pi_H\pi_2^*$
	3	4.55 (0.00)	97 %	$n_{\text{phen}}\pi_1^*$
	4	4.93 (0.07)	61 %	$\pi_H\pi_2^*$
			21 %	$\pi_{H-1}\pi_1^*$
QM/EFP	1	3.86 (1.00)	83 %	$\pi_H\pi_1^*$
EOM-EE-CCSD/ 6-31+G*	2	4.59 (0.03)	26 %	$\pi_{H-1}\pi_1^*$
			22 %	$\pi_H\pi_2^*$
			12 %	$\pi_H\pi_2^*(\text{diff})$
			8 %	$\pi_H\pi_2^*(\text{diff})'$
QM/MM SA-CASSCF(14,12)-PT2/ cc-pVDZ <sup>42</sup>	1	3.76 (0.18)	39 %	$\pi_H\pi_2^*$
			18 %	$\pi_H\pi_1^*$
	2	3.81 (0.60)	49 %	$\pi_H\pi_1^*$
			13 %	$\pi_H\pi_2^*$
	3	5.00 ( $\sim 0$ )	76 %	$n_{\text{phen}}\pi_1^*$

**Table 7.5:** Vertical excitation energies, oscillator strengths ( $f$ ) and orbital contributions to the first two singlet electronic excited states calculated using QM/EFP (QM=EOM-IP-CCSD/6-31+G\*) with an optimised geometry. Contributions above 2% are included.

VEE / eV ( $f$ )	Occupied	Unoccupied	Transition	$c^2$ %
3.865 (0.996)			$\pi_H \pi_1^*$	83
4.586 (0.003)			$\pi_{H-1} \pi_1^*$	26
			$\pi_H \pi_2^*$	22
			$\pi_H \pi_2^*(\text{diff})$	12
			$\pi_H \pi_2^*(\text{diff})'$	8

would be unfeasible. Table 7.6 lists the VDEs for the first two detachment states,  $D_0$  and  $D_1$ , calculated as an average over the ten snapshots with ground state energies closest to the Gaussian peak as shown in Figure 7.7. These calculations were performed on the structures before and after optimisation to investigate the effect that optimising the geometry with QM/EFP has on the calculated VDEs. As with the DFT calculations, QM/EFP geometry optimisation decreases the average VDEs by roughly 1.5 eV and gives a better agreement with the experimental estimates. The EOM-IP-CCSD method has calculated the first VDE to be slightly closer to the experimental estimate than the DFT approach.

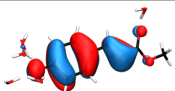
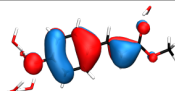
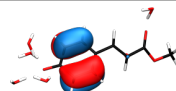
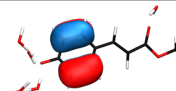
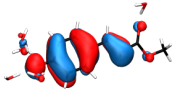
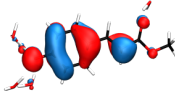
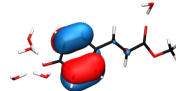
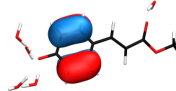
Representative hole orbitals for the  $D_0$  and  $D_1$  electron configurations are shown in Table 7.7 calculated using the EOM-IP-CCSD method on a single snapshot structure. Hole orbitals are presented from the EOM-IP-CCSD calculations performed using both the optimised and unoptimised structures. For all EOM-IP-CCSD calcu-

**Table 7.6:** QM/EFP VDEs calculated with B3LYP or EOM-IP-CCSD with the 6-31+G\* basis set. Averages are calculated over the number of specified QM/EFP structures constructed as  $[p\text{CE}^- \cdot (\text{H}_2\text{O})_5]_{\text{QM}}[(\text{H}_2\text{O})_X]_{\text{EFP}}$  where X, the size of the EFP system, is an EFP radius of 16 Å for the unoptimised (unopt.) structures and 300 fragments for the optimised structures (opt.). Example QM/EFP constructions are illustrated in Figure 7.2 for the unopt. (A) and opt. (B) systems. The experimental values are taken from the Gaussian peak positions from the fit in 7.3.

QM level	Averaged over	S <sub>0</sub> -D <sub>0</sub> VDE		S <sub>0</sub> -D <sub>1</sub> VDE	
		unopt.	opt.	unopt.	opt.
B3LYP	300	7.56			
B3LYP	20	7.58	6.21		
B3LYP	10	7.54	6.17		
EOM-IP-CCSD	10	8.04	6.34	9.57	8.16
Experimental		6.7 ± 0.1		7.5 ± 0.2	

lations, the S<sub>0</sub>-D<sub>0</sub> transition is dominated by an electron leaving the HOMO  $\pi$  orbital ( $\pi_{\text{H}}$ ) and the S<sub>0</sub>-D<sub>1</sub> transition is dominated by an electron leaving the HOMO-1  $\pi$  orbital ( $\pi_{\text{H}-1}$ ). The amplitudes for transitions of electrons leaving these HF orbitals are all close to unity ( $> 0.95$  eV). This indicates a single-electron transition and is further illustrated by the similarity between the HF orbitals and the Dyson orbitals.

**Table 7.7:** HF hole orbitals and Dyson orbitals found for the first two EOM-IP-CCSD/6-31+G\*//EFP transitions calculated for a single geometry both before and after optimisation with QM/EFP.

	S <sub>0</sub> -D <sub>0</sub>		S <sub>0</sub> -D <sub>1</sub>	
	unoptimised	optimised	unoptimised	optimised
HF				
Dyson				

The results of the S<sub>0</sub>-D<sub>0</sub> VDE calculations are illustrated in Figure 7.10 with a rolling average for each calculation set. The difference between the average DFT and EOM-IP-CCSD calculations appears to be almost constant for both optimised and unoptimised systems up to an average of ten. The EOM-IP-CCSD results were only calculated for the first ten snapshots but it appears that the rolling averages of the optimised structure calculations have settled within a sample of ten.

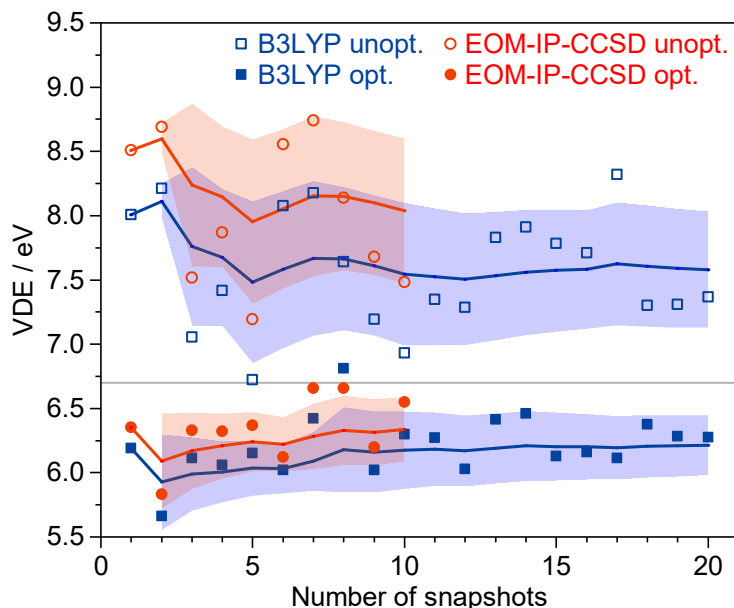


**Figure 7.10:**  $S_0$ - $D_0$  VDEs calculated using QM/EFP methods (B3LYP/6-31+G\* or EOM-IP-CCSD/6-31+G\*) for the unoptimised and optimised structures selected in 7.7. Rolling averages are shown by the solid lines and the shaded areas mark a single standard deviation either side of this average. The horizontal dashed line marks the experimental estimate at 6.7 eV.

### 7.3.3 Role of an aqueous environment

The solubility of  $p\text{CE}^-$  in water is poor and so even with solute concentrations close to saturation, the photoelectron spectrum signal intensities from solute electron detachment are much lower than the dominant water spectrum. Hence, to isolate the  $p\text{CE}^-$  signal from the water spectrum is challenging. Numerous attempts to carefully isolate and fit the  $p\text{CE}^-$  spectrum were made and ultimately, the onset of the spectrum was fit reproducibly by two Gaussian profiles centred at  $6.7 \pm 0.1$  and  $7.5 \pm 0.2$  eV. These values are assigned to the first and second VDEs of  $p\text{CE}^-$ , respectively.

The QM/EFP calculations performed using geometries of the complex solute-solvent system extracted directly from the classical simulation gave an average VDE over 300 configurations of 7.56 eV and a FWHM of 0.9 eV. The width of the distribution of these VDEs is comparable to that of the experimental fits ( $\sim 0.9$ -1 eV), despite poor agreement in the peak positions. VDEs in closer agreement to experiment are obtained using geometries relaxed within QM/EFP calculations in which the chromophore and nearby water molecules are described by QM methods (Table

7.6). Geometry optimisation calculations with QM/EFP are expensive and so a small subset of the 300 snapshots selected from the MD were chosen as shown in Figure 7.7 by prioritising snapshots with QM/EFP energies close to the mean of the distribution of the energies. A sample of ten or twenty snapshots provides average VDEs similar to the 300-sample average before optimisation indicating the subsets are representative of the larger 300-sample ensemble. The optimised geometry VDEs decrease and form better agreement with experiment. There is little difference between the ten and twenty sample averages and this convergence is shown graphically in Figure 7.10. Hence, the more expensive EOM-IP-CCSD approach was performed on a sample of ten. The difference in the EOM-IP-CCSD VDEs calculated on the unoptimised and optimised systems is even more dramatic than found with DFT. The spread in the VDEs for the optimised systems is much narrower than the unoptimised systems. Curiously, the small difference between the optimised DFT and EOM-IP-CCSD VDEs remains almost constant. However, extrapolating the average EOM-IP-CCSD VDE out to twenty snapshots would not differ significantly from the ten-sample average. This correlation between the two methods was also observed for phenolate (Figure 6.14) and it would be interesting to test how universal this apparent constant difference is in order to simplify similar supramolecular systems by shifting DFT-calculated results. In particular, this could enable the use of much larger QM systems. However, the application of such a linear shift requires more thorough testing and benchmarking to employ with certainty. The EOM-IP-CCSD calculations were also used to calculate the second VDE. Optimising the coordinates with QM/EFP improves the agreement with experiment significantly and an average over the ten results gave a VDE of 8.16 eV.

QM/EFP approaches were also used to perform a preliminary analysis of the electronic absorption spectrum of aqueous  $p\text{CE}^-$ . Much like with the VDE calculations, optimising the geometry of the system improved the agreement with experiment. The first VEE for the unoptimised and optimised systems were calculated using B3LYP/6-31+G\* to be 4.14 and 3.79 eV, respectively (*cf.* maximum of the experimental absorption spectrum lies at 3.48 eV). Various levels of TD-DFT were tested using an optimised system geometry, as shown in Table 7.3 and with a comparison

to experiment in Figure 7.8. In each calculation, eight states were included and so the first state will have converged but this may not be the case for the higher-lying states. Generally, regardless of the functional, increasing the basis set size makes very little difference to the VEEs, particularly to the lower-lying states. Adding diffuse functions to the hydrogen atoms in the basis set does invoke the addition of more diffuse continuum states. However, these generally have very low oscillator strength and so make very little difference to the simulated spectra created by convoluting the oscillator strengths with a Gaussian profile. For each of the functionals used, the first state is calculated to be a bright state with a VEE of  $\sim 3.77$ -4 eV with the leading contribution being a transition from the HOMO  $\pi_{\text{H}}$  orbital to the LUMO  $\pi_1^*$  orbital. The second state is found to be almost optically dark ( $f < 0.01$ ) with a transition energy of  $\sim 4.3 - 4.75$  eV with similar orbital contributions, regardless of the TD-DFT approach used. The higher lying states reorder in energy with the different theory levels used. In particular, the states with greater charge transfer characters (*i.e.*  $n\pi^*$  character transitions) reorder more significantly, which is expected as the DFT functionals used here differ in their treatment of long-range interactions.

Such TD-DFT/EFP calculations are inexpensive and so could potentially be performed with a large number of snapshots. However, optimising the geometries is still a key step in calculating accurate VEEs and so it is still important to sample a subset of snapshots from the ensemble of possible geometries. Additionally, detailed analysis of the electronically excited state characters becomes challenging with a large number of geometries. Figure 7.9 shows the distribution of the VEEs calculated for twenty optimised systems. The convolution is only slightly different from that found with a single snapshot geometry but there is a slight broadening on the red edge of the first band. It would be interesting to investigate whether increasing the number of snapshots included would broaden this peak significantly toward the experimental band.

An EOM-EE-CCSD analysis of the first two singlet states was performed on a single optimised geometry and similar orbitals, transition energies and oscillator strengths to the TD-DFT results were found (Table 7.4). The second state has more

diffuse orbital character with EOM-EE-CCSD than the TD-DFT approach but these diffuse orbitals share similar coefficients on the aromatic carbon atoms seen in the  $\pi_2^*$  orbital (Table 7.5). Hence, for such a transition, it would perhaps be preferable to consider the natural transition orbitals rather than the single-electron HF orbitals. Both the TD-DFT and EOM-EE-CCSD results compare favourably with the SA-CASSCF results of Garcia-Prieto *et al.*<sup>42</sup> for the states that are dominated by  $\pi_H\pi_1^*$  character. However, the ordering of the states is not shared across the methods. Notably, the  $\pi_{H-1}$  orbital found to be significantly involved in the results presented here is not reported to be significant in any of the transitions reported within the SA-CASSCF analysis. These differences are not necessarily a result of the theory level used but could be geometry-specific. The SA-CASSCF results were formed as an average of five geometries taken from a QM/MM trajectory. Hence, perhaps with more optimised geometries sampled in the QM/EFP calculations, a closer comparison could be made. However, overall the QM/EFP calculations have performed well to model the first band in the absorption spectrum and these preliminary results illustrate various methods available within the flexible QM/EFP framework to gain a molecular-level understanding of the absorption spectrum.

The experimentally-measured VDEs of  $pCE^-$  in solution are dramatically different from those recorded in the gas phase discussed in Chapters 4 and 5, and this is illustrated in Figure 7.11. The first VDE of  $pCE^-$  in water was measured from the valence XPS photoelectron spectrum in Figure 7.3 to be 6.5 eV. This is more than double that of  $pCE^-$  in the gas phase (2.85 eV). This is due to the significant stabilising effect that the solvent has on the anionic chromophore. The first VDE of the chromophore in its native environment within PYP is yet to be measured experimentally but electron emission from PYP in solution has been observed in TAS measurements following photoexcitation with 395 nm<sup>64,65</sup> or 400 nm light.<sup>63</sup> The electron detachment process has been proposed to be a two-photon process and so a rough estimate of the maximum VDE of PYP may be taken as the sum of two 400 nm photons (6.2 eV), as illustrated in Figure 7.11. The maxima of the first bands of the absorption spectra recorded in the three environments are also illustrated. The solvent shift of the absorption band is much less significant than

the change in VDE which may be easily explained by the difference in the dipole moments between the initial and final states in each transition. The first absorption band in all three media is of  $\pi_H\pi_1^*$  (HOMO-LUMO) character and by observation of the HOMO and LUMO orbitals, it is clear there is only a small difference in the charge distributions across the chromophore. Conversely, between the anion and neutral states of the chromophore, the charge distributions will differ significantly. Also, the anionic state is much more polar than the neutral radical and so with the inclusion of a polar solvent, the VDE blueshifts dramatically.

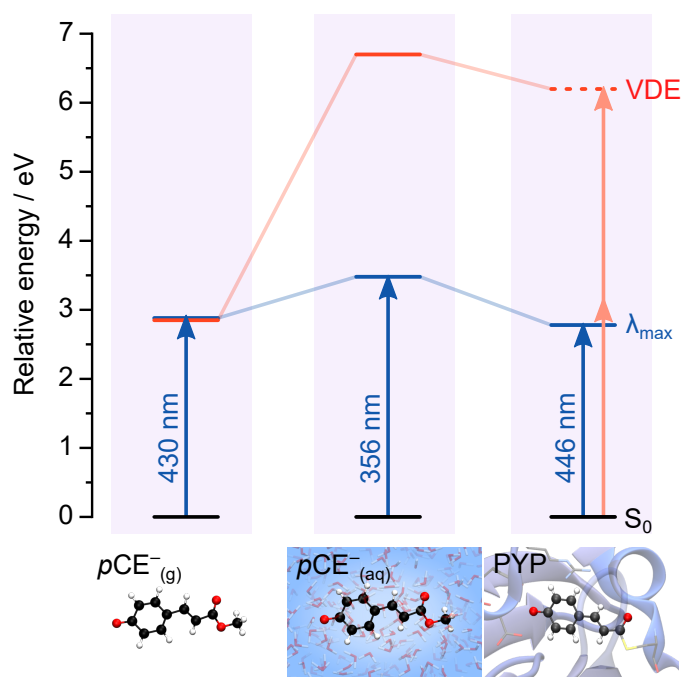


**Figure 7.11:** A comparison of the electronic structures of  $pCE^-$  in different environments. Left: isolated in the gas phase, middle: in aqueous solution and right: in the protein environment. Blue arrows mark the maxima of the first band in the experimental absorption spectrum ( $\lambda_{\max}$ ). PYP  $\lambda_{\max}$  from Reference 20. The first VDEs of  $pCE^-$  in the gas phase or aqueous solution are taken from experimental measurements presented in this thesis. The approximate maximum VDE of PYP is given as the sum of two 400 nm photons, in accordance with measurements reported by Zhu *et al.*<sup>63</sup>

The orbital analysis in the EOM-IP-CCSD indicates the valence orbitals from which the electrons are removed, as shown in Table 7.7. Intuitively, the  $D_0$  state has a hole in the HOMO orbital and the  $D_1$  state has a hole in the HOMO-1. The  $S_0$ - $D_0$  transition involves removing an electron from an orbital (HOMO) which is similar in character to that in the gas phase - also the HOMO. In the gas phase, the  $D_1$



state similarly has a hole in the HOMO-1 orbital but this orbital is non-bonding in character, rather than  $\pi$ . This reordering is perhaps due to the relative stabilisation gained by the more localised n-orbital in a polar solvent.

The EOM-EE-CCSD analysis may be useful for the interpretation of future photoelectron spectra of  $p\text{CE}^-$  in aqueous solution using UV sources as it may be used in conjunction with EOM-IP-CCSD to calculate ionisation potentials and cross-sections to various detachment continua from electronically excited states. In addition, the correlation between the electronic configurations calculated for the EE and IP states can indicate ionisation propensities under Koopmans' approximation for various resonance-enhanced detachment processes which are likely to dominate the UV photoelectron spectra. Figure 7.12 shows how such predictions could be made using the EOM-EE-CCSD and EOM-IP-CCSD calculations for the first two VEEs and VDEs. Electron detachment from  $S_0$  to the  $D_0$  and  $D_1$  states may occur through the ejection of an electron from the  $\pi_{\text{H}}$  or  $\pi_{\text{H}-1}$  orbitals, respectively, as measured in the x-ray photoelectron spectrum. The electronic configuration of  $S_1$  is strongly coupled to that of  $D_0$  as this transition only requires the removal of a  $\pi_1^*$  electron.  $S_0$ - $D_1$  detachment is expected to be much less likely as this transition would require a two-electron process. Hence, following excitation to  $S_1$ , photodetachment to  $D_0$  is more likely than to  $D_1$ . The electronic configuration of the  $S_2$  state is uncertain but the leading contributions found from the EOM-EE-CCSD analysis are shown. The  $\pi_{\text{H}-1}^2 \pi_{\text{H}}^1 \pi_1^{*0} \pi_2^{*1}$  configuration is very strongly coupled to  $D_0$  and weakly so to  $D_1$ . Conversely, the  $\pi_{\text{H}-1}^1 \pi_{\text{H}}^2 \pi_1^{*1} \pi_2^{*0}$  configuration is strongly coupled to  $D_1$  and not  $D_0$ .

Experimental investigation of these resonance-enhanced detachment processes would be very interesting to assist in benchmarking these calculations and also provide a better understanding of the electronic structure of aqueous  $p\text{CE}^-$ . Further, pump-probe photoelectron spectroscopy techniques could allow the study of the time evolution of the excited state dynamics and potentially probe the formation of solvated electrons.

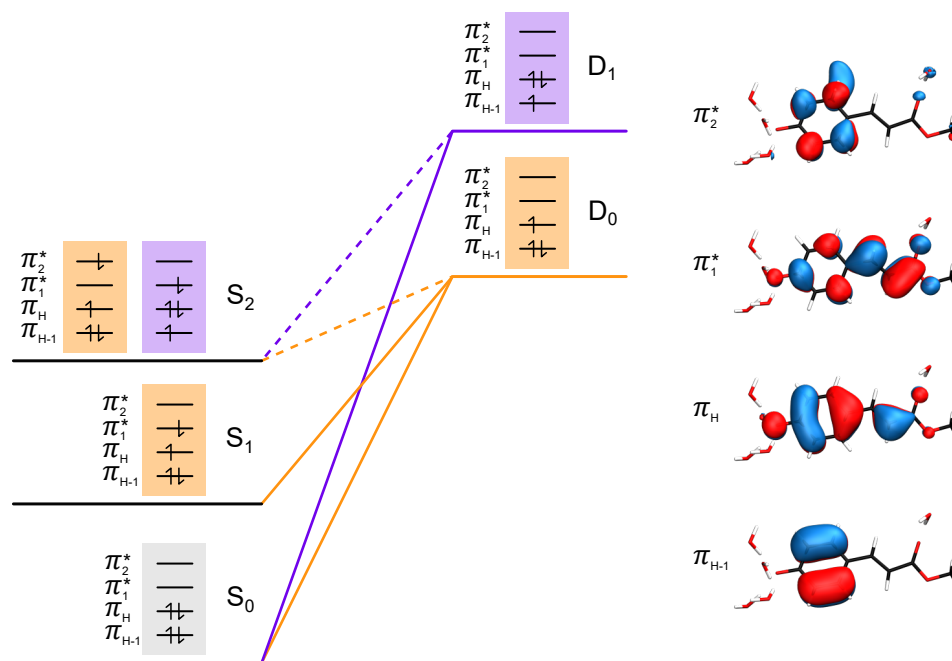


**Figure 7.12:** Electronic configurations and molecular orbitals contributing to the transitions to the first two electronically excited and photodetached states calculated using EOM-CCSD approaches.  $S_n$  and  $D_n$  states are linked to highlight which electronic configurations are strongly correlated and hence are expected to have high transition probabilities. Not to scale.

## 7.4 Conclusions and outlook

The electronic structure of a model PYP chromophore ( $pCE^-$ ) in bulk aqueous solvent was probed using x-ray valence photoelectron spectroscopy and hybrid QM/EFP calculations. This is the first x-ray valence photoelectron spectrum measured for a protein chromophore in aqueous solution. The experimental spectrum indicates VDEs for aqueous  $pCE^-$  to be  $6.7 \pm 0.1$  and  $7.5 \pm 0.2$  eV for the  $S_0$ - $D_0$  and  $S_0$ - $D_1$  transitions, respectively. This first VDE is more than double that in the gas phase due to the stabilisation of the anionic chromophore by the solvent. The absorption bands do not exhibit such dramatic solvent shifts and so, in solution, the low-lying electronically excited states are stable with respect to autodetachment, unlike that in the gas phase. The QM/EFP models have modelled the complex system well and optimisation of the structures using a QM description of the chromophore was found to improve the agreement with experiment. Various excited state QM/EFP approaches were trialled with TD-DFT and EOM-EE-CCSD methods to illustrate how the absorption spectrum may be modelled and developing

the procedures to include vibrational structure would be interesting for future work. The electronic configurations calculated for the first two electronically excited and photodetached states using EOM-CCSD/EFP theory were used to form some predictions in the propensities for different resonance-enhanced detachment processes. These predictions should prove valuable in the interpretation of future photoelectron spectroscopy measurements of PYP chromophores in solution using UV pulses. In addition, an understanding of the electron detachment processes in solution is key to understanding the mechanism for the formation of solvated electrons observed in transient absorption studies of PYP chromophores as well as the redox properties of the chromophore.

# Chapter 8

## Summary and Outlook

The work in this thesis aimed to investigate the electronic structure and dynamics of photoactive yellow protein (PYP) chromophores to help improve our understanding of how PYP functions at a molecular scale and also highlight the tunability of the chromophore, which could lead to new PYP-based materials for various photoresponsive applications. Specifically, photoelectron spectroscopy and computational approaches were employed to study isolated PYP chromophores in the gas phase and in solution. Chapters 4 and 5 probed the competing electronic relaxation pathways of five model PYP chromophores in the gas phase: two commonly-used freely-rotating analogues and three chromophores with aliphatic bridges hindering rotation about specific bonds in the chromophore. The gas-phase measurements ensure the intrinsic photophysics of the chromophore are studied without any complication from solvent-interactions. The dynamics of the rotationally-locked species were compared to the freely-rotating reference chromophores, thus indicating importance of torsional motion in accessing different relaxation pathways.

In later Chapters, efforts were focussed on simulating and interpreting measurements of electron detachment from anionic chromophores in aqueous solvent. Chapter 6 described a protocol for modelling photodetachment from aqueous phenolate as an example of a complex large-scale anionic solute-solvent system. A biased sampling approach was used to help reduce computational expense yet retain a representation of the finite temperature system. In Chapter 7, a similar computational approach was used to simulate photodetachment from a PYP chromophore in

aqueous solution and this was presented with a liquid-microjet photoelectron spectrum. These solution-phase studies were compared to the gas-phase measurements presented earlier in this thesis to help identify the effect of an aqueous solvent environment on the chromophore.

## 8.1 Anion photoelectron spectroscopy of photoactive yellow protein chromophore analogues

In its natural protein environment, the PYP chromophore initiates the photoreponse of process by photoisomerisation in the  $S_1$  state following absorption of blue light. The protein environment steers the excited state population along the isomerisation coordinate and away from competing relaxation pathways. The gas-phase anion photoelectron spectroscopy measurements presented in Chapter 4 of model PYP chromophores suggested that torsional motions play an important role in the electronic relaxation pathways following photoexcitation of 400–310 nm light. Rotation about the single bonds either side of the the central  $C=C$  moiety were found to assist in directing population in the  $S_1$  state to a conical intersection with the ground state. The single-bond rotation about the phenolate group was found to be particularly important. This phenolate rotation was also found to facilitate efficient  $S_4 \rightarrow S_1$  conversion. Chapter 5 described similar measurements aimed at probing the effect of locking the isomerisation coordinate on the competing relaxation pathways. It was found that inhibiting isomerisation in the isolated PYP chromophore anion effectively turned off the ultrafast internal conversion to the ground state and trapped population in the  $S_1$  state.

The inferences made from these static one-colour measurements with regards to the dynamics of the first electronically excited state were largely through interpretation of the low energy photoelectron signal. The low energy signal for each chromophore was assigned as thermionic emission from a vibrationally-hot ground state ( $S_0$ ), accessed *via* internal conversion from  $S_1$ . Since these studies were published, subsequent time-resolved photoelectron spectroscopy measurements of the methyl-ester analogue  $pCE^-$  have been performed elsewhere,<sup>41</sup> in which the authors

found no evidence of  $S_1$  to  $S_0$  conversion despite a previous time-resolved study of a ketone analogue reporting repopulation of the ground state.<sup>32</sup> Hence, this suggests that the excited state dynamics of the  $S_1$  state are very sensitive to slight changes in the chromophore and highlights the difficulty in assigning low energy signals using only static single-colour measurements. Thus, it is difficult to assume that a viable  $S_1/S_0$  conversion pathway exists for each of the chromophores studied in Chapters 4 and 5 without time-resolved pump-probe measurements and accurate simulation of the non-adiabatic dynamics to fully interpret the complex excited state dynamics of isolated PYP chromophores.

The intricate competition on the first excited state between autodetachment, conversion to a dipole-bound state and electronic relaxation to the ground state makes PYP chromophores interesting candidates for future work. Each of the five chromophores discussed in this thesis have dipole moments large enough to support a dipole-bound state. Hence, it is possible that the rotation-locked chromophores could help to determine which nuclear motions modulate conversion between the  $S_1$  state and the dipole-bound state. This would only be possible with sufficient knowledge of the excited state surfaces of the locked and unlocked chromophores to deem the shapes of each surface to be similar in all important modes orthogonal to the locked mode.

Further, evidence for autodetachment from a dipole-bound state, as opposed to detachment *via* thermionic emission, could be found if the photoelectron angular distributions at low energy are anisotropic. This was not explored with the analysis presented in this thesis as the measurements were not acquired over a long enough period to quantify the angular information at such low photoelectron energies. However, this could be rectified relatively simply by acquiring over a longer period or, perhaps more efficiently, by employing slow electron velocity map imaging (SEVI) techniques to obtain higher-resolution images for these low energy photoelectrons. A SEVI spectrometer is currently being built in our lab along with other instrumental developments promising for future work on PYP chromophores including cryocooling, microsolvation and clustering capabilities, in addition to the application of tunable ultrafast light sources enabling time-resolved measurements.

## 8.2 Photodetachment from chromophores in aqueous solutions

Gas phase photoelectron spectroscopy studies provide invaluable information on the intrinsic electronic structure and dynamics of an isolated chromophore. However, it is also of great interest and importance to investigate the effect a solvent environment may have on the chromophore. An understanding of the electron detachment processes in solution also gives key insight into electron transfer mechanisms, such as redox reactions or ionic bond formation. A liquid-microjet x-ray photoelectron spectrum of  $p\text{CE}^-$  in aqueous solution was presented within Chapter 7. This is the first measurement of this kind recorded with such a sparingly soluble photoactive chromophore and the data required careful analysis in order to isolate the solute spectrum from the water spectrum, due to the low solute concentration. It was found that the first vertical detachment energy (VDE) of  $p\text{CE}^-$  has a dramatic solvent shift of 4 eV in aqueous solution compared to the gas phase.

Liquid photoelectron spectroscopy measurements such as this require supporting theoretical modelling to provide a fully mechanistic understanding of the electron detachment.<sup>271</sup> Chapter 6 describes an approach for calculating the electronic structure of an organic anion in bulk aqueous solution using hybrid quantum-mechanical/effective fragment potential (QM/EFP) techniques, with aqueous phenolate as an example system. A similar protocol was applied to simulate the aqueous  $p\text{CE}^-$  system, as described in Chapter 7. The calculations provide molecular detail on the nature of the orbitals from which the electrons are detached which may be useful in the context of relative photodetachment cross-sections. This was illustrated for the phenolate system where it was found that the dominant orbital character of the  $S_0\text{-D}_1$  transition depended on system geometry. Electronic configurations were also used to predict relative detachment propensities from excited states which will be valuable when interpreting resonance-enhanced multi-photon detachment (REMPD) processes accessed with UV photoelectron spectroscopy. Preliminary UV-REMPD measurements were recorded during this PhD with an aqueous  $p\text{CE}^-$  solution but are not presented here. Repeated measurements are currently in progress, the anal-

ysis of which will certainly benefit from the x-ray valence spectrum and simulated results presented within this thesis. Further, plans are in place to measure time-resolved pump-probe measurements of aqueous  $p\text{CE}^-$  which could shed light on the excited state dynamics of the aqueous chromophore and help resolve the mechanism responsible for the production of solvated electrons observed in transient absorption spectroscopy measurements.<sup>85,86</sup> Analogous measurements of the protein itself in solution are also planned which provide a VDE of the chromophore in its native environment and form a powerful contrast between gas-phase, aqueous-phase and protein environments using the same photoelectron spectroscopy technique.

Promising future directions to further develop the theoretical simulations include expansion of the optimised EFP systems, the inclusion of vibrational structures and the inclusion of counterions. Recently, we have been testing the convergence of the calculated VDEs of the green fluorescent protein chromophore in aqueous solution and have found that a much larger EFP cut-off radius is required to reach convergence and form close agreement with experimental measurements.<sup>272</sup> Hence, we plan on investigating this for much larger systems with phenolate and  $p\text{CE}^-$  in solution. Excited state analysis of the chromophores in solution is valuable in the interpretation of future UV-REMPD measurements but also to support other widely-used techniques such as fluorescence or transient absorption spectroscopies. Finally, the simulations could be expanded to model the energy loss of the electron escaping the solvent which is essential for extracting genuine VDEs from liquid-microjet photoelectron spectroscopy measurements.<sup>273</sup>



# Appendices

## A Supporting material for Chapter 2

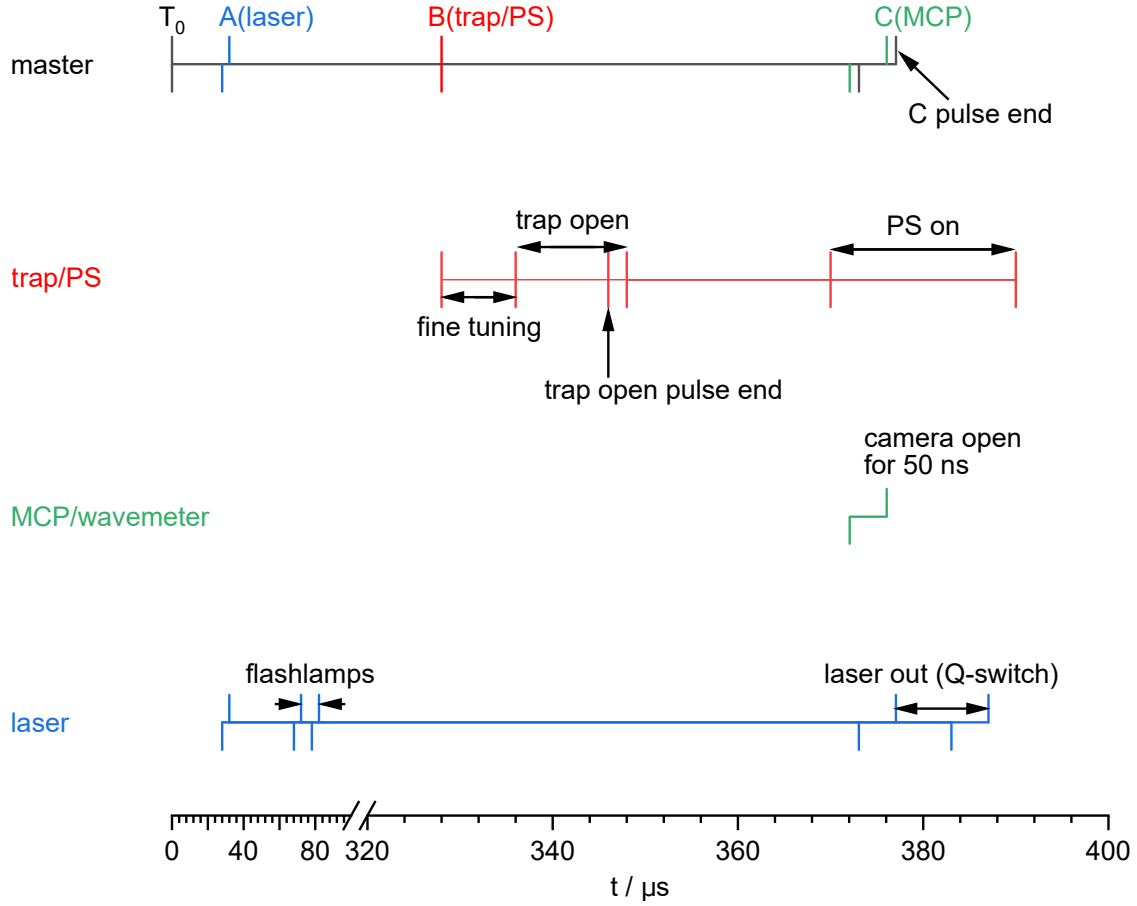


**Figure A.1:** Schematic of the times used in the delay generators for a 20 Hz experiment for iodide anions. The master delay generator connects to two other delay generators, one governing the timing of the potential switch and ion trap (trap/PS) and another the nanosecond laser system. The master trigger also sends a pulse to the camera and wavemeter after a certain delay. All delay generators use transistor-transistor logic. Delay times for both ion and electron detection are represented as vertical lines above and below the time lines for each of the delay generators and the camera trigger. Note there is a scale break from 100-320  $\mu\text{s}$ .

## B Supporting material for Chapter 4

### Coordinates of optimised structures

**Table B.1:** Cartesian coordinates of the anionic and neutral radical forms of deprotonated *p*CA optimised using B3LYP/6-311++G(3df,3pd).

Atom	Anion coordinates /Å			Neutral coordinates /Å		
	<i>x</i>	<i>y</i>	<i>z</i>	<i>x</i>	<i>y</i>	<i>z</i>
C	1.018412	-1.064838	-0.000039	0.997621	-1.075030	0.000084
C	0.430369	0.231492	-0.000022	0.442588	0.239254	0.000066
C	1.334833	1.328807	-0.000018	1.332794	1.349107	0.000018
C	2.692494	1.168728	0.000034	2.684188	1.180238	-0.000057
C	3.312270	-0.141529	0.000177	3.273448	-0.150401	-0.000178
C	2.370662	-1.249878	0.000010	2.341620	-1.271767	0.000010
H	0.368707	-1.932636	-0.000095	0.334390	-1.928733	0.000162
H	0.915051	2.330359	-0.000063	0.909348	2.345539	0.000050
H	3.355428	2.025466	0.000004	3.365451	2.019676	-0.000071
H	2.795100	-2.246788	-0.000033	2.772152	-2.263568	0.000044
O	4.551509	-0.311296	-0.000031	4.500182	-0.322802	-0.000064
C	-0.965424	0.468561	-0.000063	-0.969302	0.492960	0.000141
H	-1.261813	1.514094	-0.000059	-1.272483	1.534202	0.000142
C	-2.003486	-0.426630	-0.000124	-1.964757	-0.420544	0.000230
H	-1.841023	-1.494463	-0.000134	-1.787680	-1.485794	0.000238
C	-3.365566	0.015795	-0.000170	-3.370926	0.014994	0.000346
O	-4.263617	-1.041407	0.000126	-4.215052	-1.044908	-0.000263
H	-5.130141	-0.616203	0.000281	-5.115512	-0.690566	-0.000636
O	-3.806480	1.157343	0.000077	-3.761294	1.157258	-0.000159

**Table B.2:** Cartesian coordinates of the anionic and neutral radical forms of deprotonated *p*CE optimised using B3LYP/6-311++G(3df,3pd).

Atom	Anion coordinates /Å			Neutral coordinates /Å		
	<i>x</i>	<i>y</i>	<i>z</i>	<i>x</i>	<i>y</i>	<i>z</i>
O	5.040363	-0.421536	-0.000737	4.934763	-0.415475	-0.000628
C	3.807044	-0.209403	-0.000578	3.713587	-0.204842	0.000348
C	2.827955	-1.284227	-0.000534	2.746950	-1.296053	-0.000166
H	3.217527	-2.295342	-0.000655	3.146079	-2.300968	-0.000458
C	1.482221	-1.052785	-0.000351	1.409623	-1.057445	-0.000035
H	0.803334	-1.898061	-0.000328	0.720256	-1.890303	-0.000152
C	0.938949	0.262120	-0.000186	0.894959	0.273096	0.000219
C	1.880055	1.327220	-0.000223	1.820092	1.354066	0.000100
H	1.494985	2.342753	-0.000100	1.427931	2.363337	0.000079
C	3.232121	1.120653	-0.000404	3.165636	1.143047	-0.000031
H	3.923575	1.954610	-0.000424	3.872525	1.961090	-0.000230
C	-0.449818	0.547014	0.000006	-0.508664	0.570412	0.000350
H	-0.709146	1.602371	0.000115	-0.779359	1.620604	0.000452
C	-1.516524	-0.311322	0.000066	-1.531701	-0.311594	0.000342
H	-1.390724	-1.384198	-0.000025	-1.386422	-1.381795	0.000240
C	-2.866735	0.177323	0.000262	-2.927611	0.163775	0.000458
O	-3.263149	1.332272	0.000588	-3.279053	1.319820	0.000887
O	-3.777136	-0.869366	0.000573	-3.785242	-0.877072	0.000832
C	-5.142836	-0.485479	0.001035	-5.180067	-0.539599	0.001382
H	-5.715318	-1.411236	0.001222	-5.710313	-1.486266	0.001623
H	-5.389427	0.105727	0.884306	-5.430097	0.040398	0.887661
H	-5.390018	0.105737	-0.882064	-5.430802	0.040344	-0.884733

**Table B.3:** Cartesian coordinates of the anionic and neutral radical forms of deprotonated PpCE optimised using B3LYP/6-311++G(3df,3pd).

Atom	Anion coordinates /Å			Neutral coordinates /Å		
	<i>x</i>	<i>y</i>	<i>z</i>	<i>x</i>	<i>y</i>	<i>z</i>
C	3.512426	1.100380	-0.049477	3.502828	1.099786	-0.156930
C	2.178088	1.390385	-0.053311	2.177769	1.401511	-0.125727
C	1.158571	0.392942	0.005570	1.172244	0.399455	0.045449
C	1.627792	-0.952052	0.094465	1.608315	-0.947434	0.230676
C	2.959202	-1.263160	0.106850	2.929791	-1.273189	0.215701
C	4.004682	-0.260539	0.026791	3.963684	-0.269802	0.006903
H	4.253084	1.889454	-0.100122	4.257793	1.860477	-0.299670
H	1.860894	2.427091	-0.108685	1.854012	2.427623	-0.245041
H	0.918053	-1.761358	0.173716	0.884425	-1.724334	0.411857
H	3.281456	-2.294981	0.183938	3.262628	-2.291046	0.366229
O	5.222259	-0.548198	0.030887	5.166535	-0.567976	-0.019176
C	-0.191419	0.832920	-0.011936	-0.188975	0.845796	0.040765
H	-0.294410	1.912603	-0.001009	-0.306583	1.922488	0.061477
C	-1.406354	0.183549	-0.040829	-1.370087	0.168191	-0.008520
C	-2.584904	1.044476	-0.005074	-2.591646	1.045220	0.041444
O	-2.598793	2.258277	-0.077620	-2.544873	2.247752	-0.019993
C	-3.928693	-0.941593	0.413073	-3.940845	-0.963960	0.314467
H	-3.709763	-1.100980	1.476151	-3.801647	-1.209405	1.371261
H	-4.972944	-1.205916	0.241160	-4.973379	-1.177394	0.048457
C	-2.980079	-1.747951	-0.446133	-2.953500	-1.707565	-0.554281
H	-3.118628	-2.816637	-0.263974	-3.105220	-2.782638	-0.452352
H	-3.215203	-1.558474	-1.496640	-3.129823	-1.449515	-1.600511
O	-3.833828	0.447194	0.111548	-3.804373	0.458251	0.150871
C	-1.549974	-1.320393	-0.129932	-1.535701	-1.325035	-0.137761
H	-1.242205	-1.794182	0.810843	-1.311871	-1.800846	0.823736
H	-0.873480	-1.708592	-0.894251	-0.811915	-1.717464	-0.852168

**Table B.4:** Cartesian coordinates of the anionic and neutral radical forms of deprotonated NpCE optimised using B3LYP/6-311++G(3df,3pd).

Atom	Anion coordinates /Å			Neutral coordinates /Å		
	<i>x</i>	<i>y</i>	<i>z</i>	<i>x</i>	<i>y</i>	<i>z</i>
C	-1.219226	-1.510111	0.164766	-1.203935	-1.503055	0.328132
C	-0.868200	-0.135789	0.016059	-0.877619	-0.135663	0.076557
C	-1.963912	0.772699	-0.137207	-1.946623	0.777111	-0.204497
C	-3.262173	0.328396	-0.151006	-3.232921	0.318491	-0.272403
C	-3.634216	-1.060792	-0.016931	-3.581338	-1.071549	-0.052803
C	-2.507080	-1.957822	0.152541	-2.480236	-1.963309	0.271415
H	-0.430767	-2.235928	0.314077	-0.415375	-2.189024	0.599698
H	-4.074297	1.038092	-0.266632	-4.051314	0.992626	-0.489802
H	-2.729937	-3.010204	0.282479	-2.722693	-2.997191	0.474525
O	-4.821684	-1.457871	-0.032506	-4.753665	-1.473667	-0.121392
C	-1.681236	2.246884	-0.304145	-1.632790	2.235698	-0.415461
H	-1.520635	2.473706	-1.365847	-1.346221	2.404622	-1.459224
H	-2.552905	2.824447	0.009680	-2.527844	2.830693	-0.236130
C	-0.434473	2.643743	0.474188	-0.484582	2.655534	0.495603
H	-0.211862	3.706481	0.343531	-0.257605	3.714313	0.369087
H	-0.608851	2.480779	1.541893	-0.780816	2.515233	1.538336
C	0.755234	1.809942	0.012228	0.758015	1.829210	0.182492
H	1.639120	2.016946	0.609719	1.544802	2.009063	0.911788
H	1.031097	2.109628	-1.005899	1.185109	2.156343	-0.769653
C	0.496072	0.314106	0.006393	0.501646	0.337328	0.093895
C	1.570660	-0.555016	-0.028212	1.526781	-0.552471	-0.017060
H	1.389765	-1.616658	-0.075868	1.324339	-1.605463	-0.130166
C	2.961017	-0.212200	-0.028893	2.956578	-0.219165	-0.041381
O	3.515995	0.878824	-0.026014	3.458634	0.881879	-0.002543
O	3.737267	-1.368968	-0.042378	3.690723	-1.354772	-0.123875
C	5.138614	-1.158638	-0.058414	5.112307	-1.178000	-0.162451
H	5.590714	-2.148859	-0.072883	5.530366	-2.177571	-0.224879
H	5.448301	-0.595478	-0.940579	5.400358	-0.588254	-1.030936
H	5.471138	-0.611247	0.825308	5.459645	-0.673871	0.737610

## C Supporting material for Chapter 5

### Coordinates of optimised structures

Note that coordinates of the optimised  $p\text{CE}^-$  structures are listed in Table B.2.

**Table C.5:** Cartesian coordinates of the anionic and neutral radical forms of deprotonated EB $p\text{CE}$  optimised using B3LYP/6-311++G(3df,3pd).

Atom	Anion coordinates /Å			Neutral coordinates /Å		
	$x$	$y$	$z$	$x$	$y$	$z$
H	0.802746	-2.085713	0.327833	0.784536	-2.016948	0.639964
C	1.387028	-1.186578	0.178628	1.378764	-1.163081	0.348600
C	2.748417	-1.291566	0.184966	2.734579	-1.271193	0.343536
H	3.226878	-2.252178	0.334150	3.230634	-2.193307	0.613029
C	3.622207	-0.147510	-0.000728	3.582087	-0.145771	-0.016787
C	2.918492	1.103204	-0.188716	2.896645	1.089063	-0.357177
H	3.523058	1.989982	-0.336816	3.512679	1.933696	-0.633054
C	1.551604	1.185094	-0.181695	1.535290	1.174775	-0.328239
H	1.104986	2.159056	-0.337862	1.063623	2.109794	-0.594366
C	0.709529	0.053610	-0.000683	0.724769	0.058462	0.013036
C	-0.720943	0.148926	-0.017148	-0.725348	0.169483	0.010724
C	-1.588655	-0.917188	0.034349	-1.544320	-0.909235	-0.014946
C	-1.382268	1.506315	-0.145256	-1.388239	1.528352	-0.017817
C	-2.765253	1.483622	0.474964	-2.776545	1.441653	0.589626
H	-1.450339	1.786787	-1.201443	-1.446179	1.896009	-1.046509
H	-0.799772	2.279785	0.353411	-0.812435	2.257520	0.551639
O	-3.586454	0.441722	-0.048934	-3.573404	0.410173	-0.011977
H	-3.305263	2.410630	0.280859	-3.335882	2.361481	0.440340
H	-2.680589	1.354897	1.559940	-2.708936	1.246354	1.663004
C	-3.020308	-0.819049	-0.095666	-3.007850	-0.811817	-0.165559
H	-1.230740	-1.934048	0.068074	-1.176307	-1.922568	-0.046711
O	-3.777577	-1.756678	-0.267713	-3.692758	-1.757143	-0.461013
O	4.870272	-0.237854	0.003368	4.819823	-0.232551	-0.029174

## D Supporting material for Chapter 6

### Tcl QM/EFP coordinate abstraction

A Tcl/Tk script snippet used within the Tk Console of VMD to select QM and EFP regions from an MD trajectory and save out each set of coordinates for a given list of frames.

```
#recursive function to find the radius for selection that satisfies the required
    N water molecules
proc findQMsel {a b finalAtomN fram} {
    set c [expr ($a + $b)/2]
    #puts "a: $a , b: $b and c: $c "
    if { [info exists selQM ] } {
        $selQM delete
    }
    set selQM [atomselect top "resname LIG or same residue as solvent within
        $c of resname LIG" frame $fram]

    puts "# of atoms: [$selQM num] for frame $fram"

    if {[$selQM num] == $finalAtomN} {
        $selQM delete
        return $c
    }
    if {[$selQM num] > $finalAtomN} {
        $selQM delete
        return [findQMsel $a $c $finalAtomN $fram]
    }
    if {[$selQM num] < $finalAtomN} {
        $selQM delete
        return [findQMsel $c $b $finalAtomN $fram]
    }
}

#set list of frame #s randomly generated elsewhere
set list [list 79      147      163      402 ]
```



```
#set desired number of atoms in QM region (e.g. 27 -> 5 waters + phenolate)
set finalAtomN 27

#Note that in this case, the chromophore residue is labelled "LIG" in the pdb/psf
.

#Could change resname LIG to resid 0 to be more general.

#loop over each selected frame
foreach item $list {
    puts "frame: $item"
    set frame $item

    #set initial radii - if you have a radius around the chromophore bigger
    #than 50, you should change radB.
    set radA 0.0
    set radB 50.0

    puts "$radA $radB $finalAtomN $item"

    set radius [findQMsel $radA $radB $finalAtomN $item]

    puts "QM radius: $radius for frame $item"
    #specify QM selection using standard atomselect notation
    set selQM [atomselect top "resname LIG or same residue as solvent within
    $radius of resname LIG" frame $item]

    puts "selection QM: [$selQM text] "

    #specify EFP selection using standard atomselect notation
    # this selects any water (not already selected in the QM region) within 16
    # A of the chromophore.
    set seleFP [atomselect top "not (resname LIG or same residue as solvent
    within $radius of resname LIG) and same residue as solvent within 16
    of resname LIG" frame $item]

    #create new dir for each frame in the list
    file mkdir $item
```

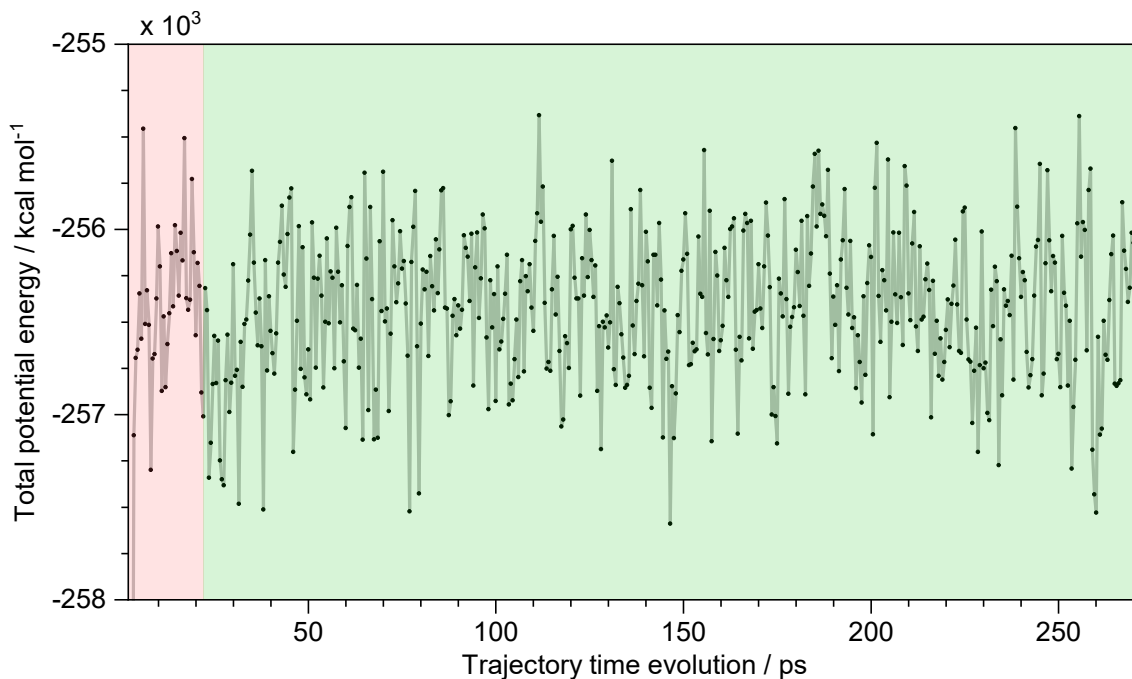
```
#Write the two files
$selQM writexyz ./${item}/QM_${item}.xyz
$selEFP writexyz ./${item}/EFP_${item}.xyz

#cleanup before next loop
$selQM delete
$selEFP delete

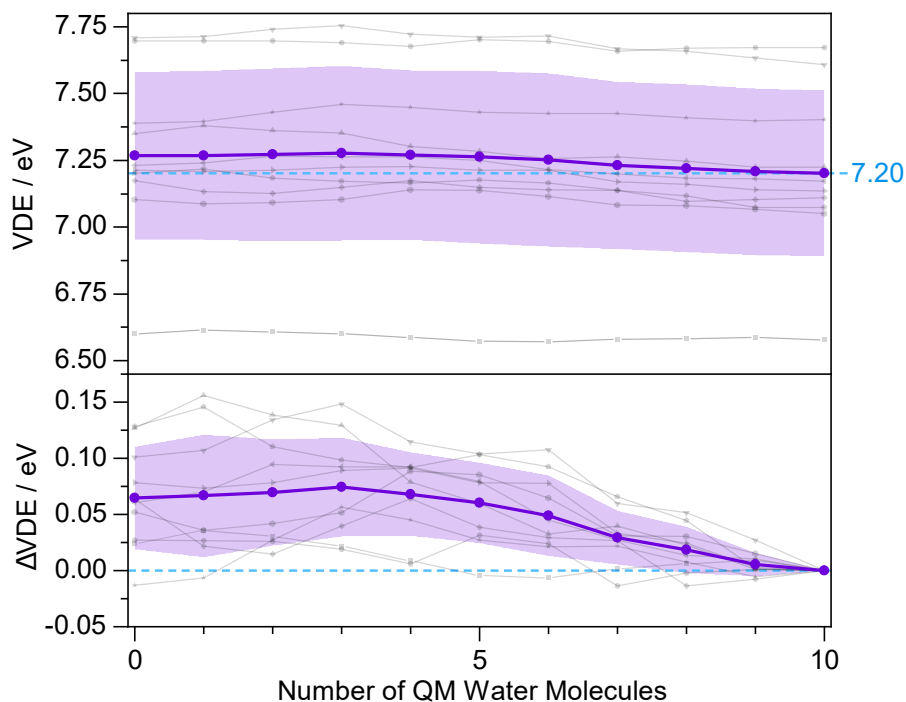
puts "file written see ./${item}/QM_${item}.xyz and ./${item}/EFP_${item}.
    xyz"
}
```

## E Supporting material for Chapter 7

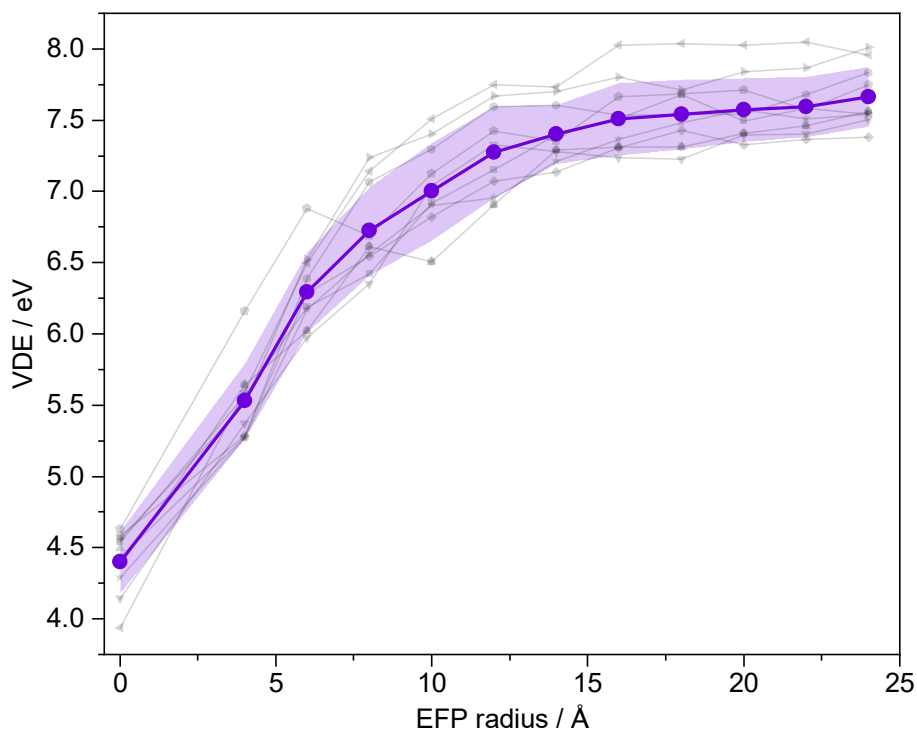
### Computational details



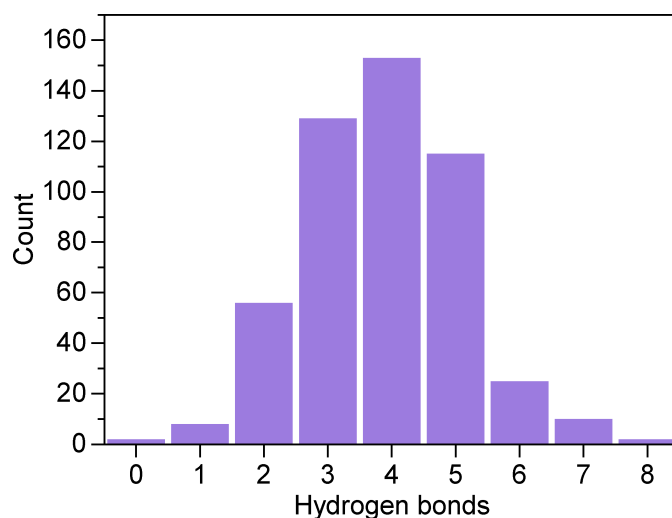
**Figure E.2:** Total potential energy (Equation 3.27) calculated over the time evolution in the MD simulation. Scale shows the equilibration period (red, 2-22 ps) and the sampling period (green, 22-272 ps). Note that the energy has equilibrated within 20 ps and the system geometry is evolving stochastically in the sampling region.



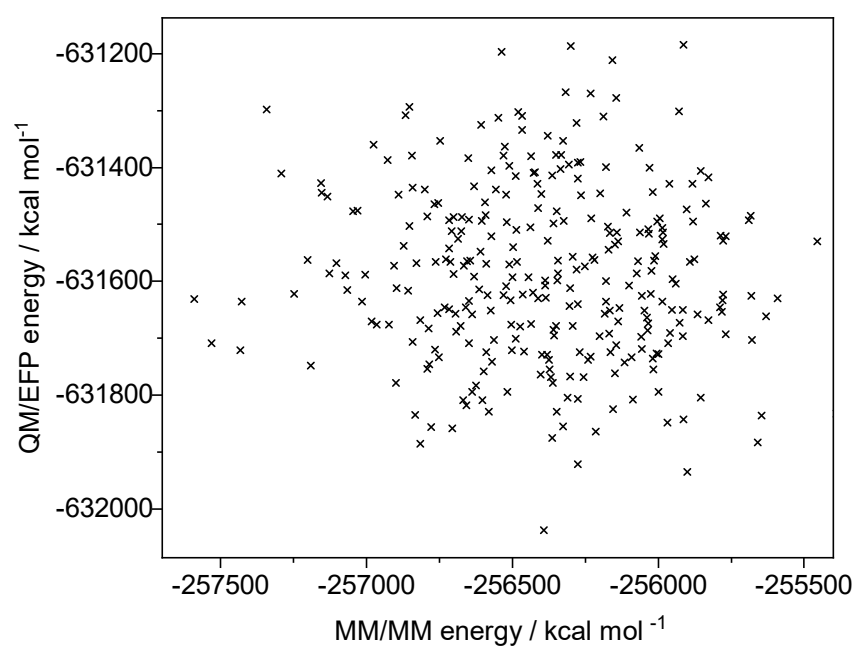
**Figure E.3:** Top: QM/EFP VDEs (B3LYP/6-31+G\*) calculated for ten randomly-selected conformations from the MD simulation with the number of water molecules included within the QM system incrementally increased. All solvent molecules within 10 Å of any atom within the chromophore were described by EFP. The purple circles show the average over the ten snapshots and the shaded area indicates a single standard deviation either side of the mean. The horizontal dashed blue line marks the average VDE calculated for the largest system. Bottom: Analogous to the top plot but  $\Delta$ VDE here is the difference between the VDE calculated with an  $n$ -water QM system and the largest 10-water calculation. Note the expanded energy scale.



**Figure E.4:** QM/EFP VDEs (B3LYP/6-31+G\*) calculated for ten randomly-selected conformations from the MD simulation with an increasing EFP region size described by the radius surrounding the chromophore forming the cut-off in the selection of the EFP solvent molecules. The QM region included the chromophore and five solvent molecules in each case. The purple circles show the average over the ten snapshots and the shaded area indicates a single standard deviation either side of the mean.



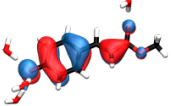
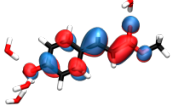
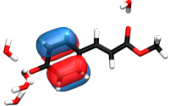
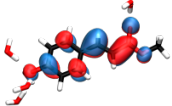
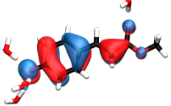
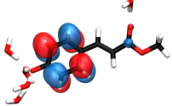
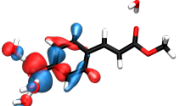
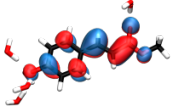
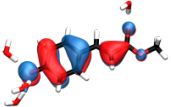
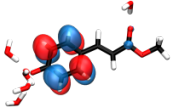
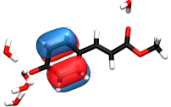
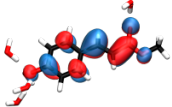
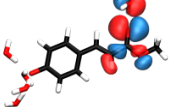
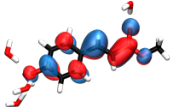
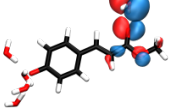
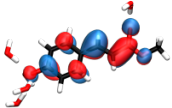
**Figure E.5:** Column chart illustrating the distribution in the number of water molecules forming direct hydrogen bonds with  $p\text{CE}^-$  determined over the 500 snapshots extracted from the MD sampling trajectory. Hydrogen bonds included any interaction with a donor-acceptor distance  $< 3 \text{ \AA}$  and donor-H-acceptor bond angle or  $160\text{--}200^\circ$ .  $\sim 93\%$  of the 500 conformations had five or fewer  $p\text{CE}^-$ -solvent H-bonds.



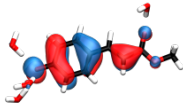
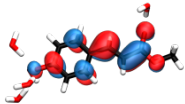
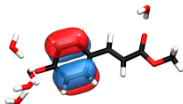
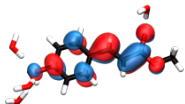
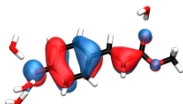
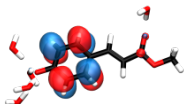
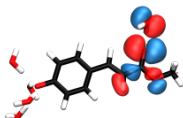
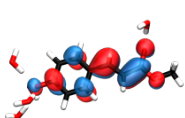
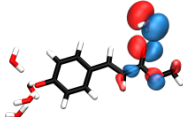
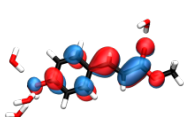
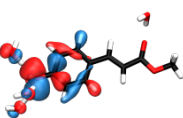
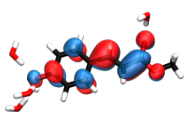
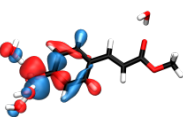
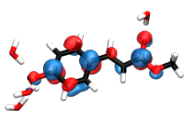
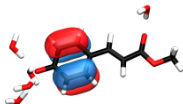
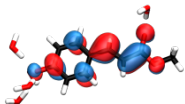
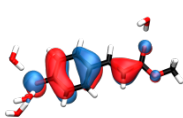
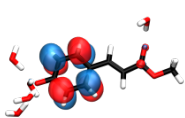
**Figure E.6:** Energies of the ground state anionic system calculated for 300 randomly-selected snapshot geometries taken directly from the MD trajectory using QM/EFP (QM=B3LYP/6-31+G\*) and MM/MM energies (total potential energies) taken from the MD simulation.

## Calculated TD-DFT transitions

**Table E.6:** Vertical excitation energies, oscillator strengths ( $f$ ) and orbital contributions to the first five singlet electronic excited states calculated using QM/EFP (QM=B3LYP/6-311++G\*\*) with an optimised geometry. Contributions above 7% are included.

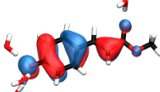
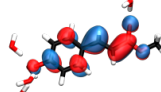
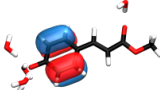
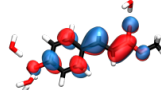
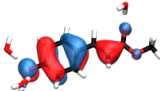
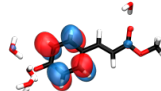
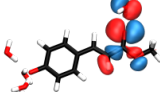
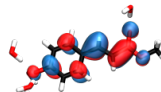
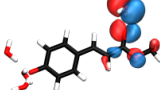
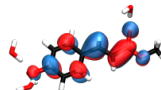
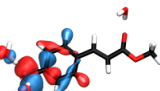
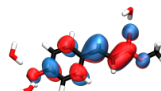
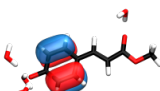
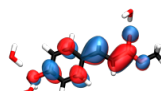
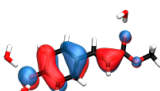
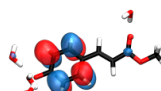
VEE / eV ( $f$ )	Occupied	Unoccupied	Character	$c^2$ %
3.774 (1.217)		→ 	$\pi_H\pi_1^*$	94
4.294 (0.001)		→ 	$\pi_{H-1}\pi_1^*$	74
		→ 	$\pi_H\pi_2^*$	24
4.549 (0.000)		→ 	$n_{phen}\pi_1^*$	97
4.934 (0.074)		→ 	$\pi_H\pi_2^*$	61
		→ 	$\pi_{H-1}\pi_1^*$	22
4.987 (0.006)		→ 	$n_{CO}\pi_1^*$	86
		→ 	$n'_{CO}\pi_1^*$	10

**Table E.7:** Vertical excitation energies, oscillator strengths ( $f$ ) and orbital contributions to the first five singlet electronic excited states calculated using QM/EFP (QM= $\omega$ -B97X-D/6-31+G\*) with an optimised geometry. Contributions above 7% are included.

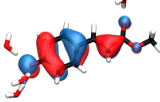
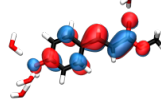
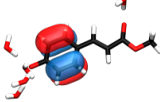
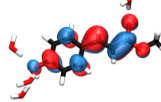
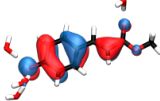
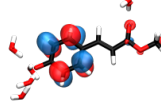
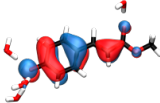
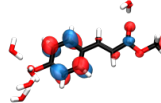
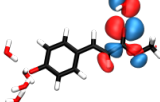
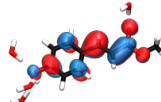
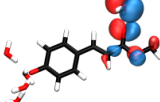
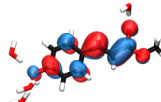
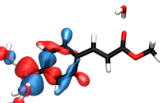
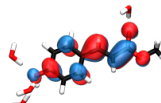
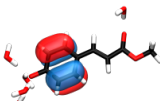
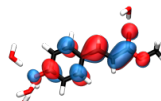
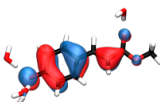
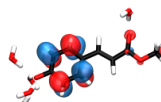
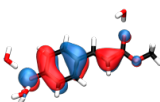
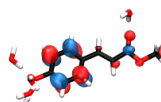
VEE / eV ( $f$ )	Occupied	Unoccupied	Character	$c^2$ %
4.040 (1.222)		$\rightarrow$ 	$\pi_H\pi_1^*$	93
4.747 (0.010)		$\rightarrow$ 	$\pi_{H-1}\pi_1^*$	46
		$\rightarrow$ 	$\pi_H\pi_2^*$	46
5.404 (0.000)		$\rightarrow$ 	$n_{CO}\pi_1^*$	69
		$\rightarrow$ 	$n'_{CO}\pi_1^*$	15
5.565 (0.002)		$\rightarrow$ 	$n_{phen}\pi_1^*$	78
		$\rightarrow$ 	$n_{phen}\pi_{diff}^*$	8
5.660 (0.175)		$\rightarrow$ 	$\pi_{H-1}\pi_1^*$	48
		$\rightarrow$ 	$\pi_H\pi_2^*$	43



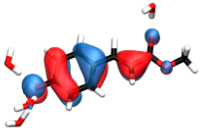
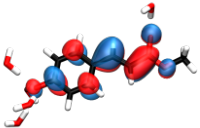
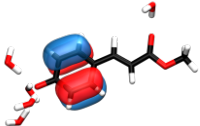
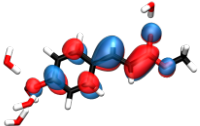
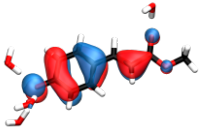
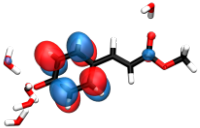
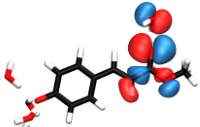
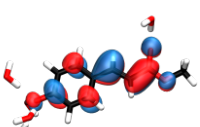
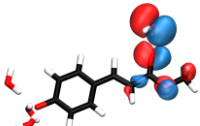
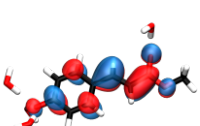
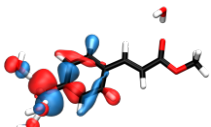
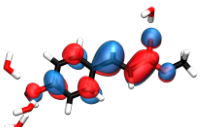
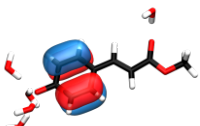
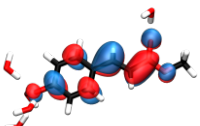
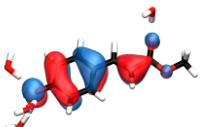
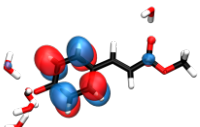
**Table E.8:** Vertical excitation energies, oscillator strengths ( $f$ ) and orbital contributions to the first five singlet electronic excited states calculated using QM/EFP (QM= $\omega$ -B97X-D/6-311++G\*\*) with an optimised geometry. Contributions above 7% are included.

VEE / eV ( $f$ )	Occupied	Unoccupied	Character	$c^2$ %
4.018 (1.207)		$\rightarrow$ 	$\pi_H\pi_1^*$	93
4.712 (0.013)		$\rightarrow$ 	$\pi_{H-1}\pi_1^*$	44
		$\rightarrow$ 	$\pi_H\pi_2^*$	43
5.380 (0.000)		$\rightarrow$ 	$n_{CO}\pi_1^*$	71
		$\rightarrow$ 	$n'_{CO}\pi_1^*$	14
5.539 (0.002)		$\rightarrow$ 	$n_{phen}\pi_1^*$	76
5.619 (0.173)		$\rightarrow$ 	$\pi_{H-1}\pi_1^*$	50
		$\rightarrow$ 	$\pi_H\pi_2^*$	37

**Table E.9:** Vertical excitation energies, oscillator strengths ( $f$ ) and orbital contributions to the first five singlet electronic excited states calculated using QM/EFP (QM=CAM-B3LYP/6-31+G\*) with an optimised geometry. Contributions above 7% are included.

VEE / eV ( $f$ )	Occupied	Unoccupied	Character	$c^2$ %
4.000 (1.225)		→ 	$\pi_H\pi_1^*$	94
4.729 (0.009)		→ 	$\pi_{H-1}\pi_1^*$	48
		→ 	$\pi_H\pi_2^*$	32
		→ 	$\pi_H\pi_{2'}^*$	13
5.425 (0.000)		→ 	$n_{CO}\pi_1^*$	69
		→ 	$n'_{CO}\pi_1^*$	13
5.518 (0.003)		→ 	$n_{phen}\pi_1^*$	70
5.603 (0.166)		→ 	$\pi_{H-1}\pi_1^*$	47
		→ 	$\pi_H\pi_2^*$	32
		→ 	$\pi_H\pi_{2'}^*$	12

**Table E.10:** Vertical excitation energies, oscillator strengths ( $f$ ) and orbital contributions to the first five singlet electronic excited states calculated using QM/EFP (QM=CAM-B3LYP/6-311++G\*\*) with an optimised geometry. Contributions above 7% are included.

VEE / eV ( $f$ )	Occupied	Unoccupied	Character	$c^2$ %
3.979 (1.213)			$\pi_H \pi_1^*$	93
4.694 (0.012)			$\pi_{H-1} \pi_1^*$	46
			$\pi_H \pi_2^*$	44
5.402 (0.001)			$n_{CO} \pi_1^*$	71
			$n'_{CO} \pi_1^*$	11
5.493 (0.003)			$n_{phen} \pi_1^*$	79
5.561 (0.162)			$\pi_{H-1} \pi_1^*$	47
			$\pi_H \pi_2^*$	40

# Bibliography

- [1] B. Valeur and M. N. Berberan-Santos, *Molecular Fluorescence Principles and Applications*, Wiley-VCH, 2012.
- [2] D. Hu, L. Yao, B. Yang and Y. Ma, *Phil. Trans. R. Soc. A.*, 2015, **373**, 20140318.
- [3] K. J. Hellingwerf, J. Hendriks and T. Gensch, *J. Phys. Chem. A*, 2003, **107**, 1082–1094.
- [4] W. Lee, G. Kodali, R. J. Stanley and S. Matsika, *Chem. Eur. J.*, 2016, **22**, 11371–11381.
- [5] E. D. Getzoff, K. N. Gutwin and U. K. Genick, *Nat. Struct. Biol.*, 2003, **10**, 663–8.
- [6] T. Koopmans, *Physica*, 1934, **1**, 104–113.
- [7] C. L. Adams, H. Schneider and J. M. Weber, *J. Phys. Chem. A*, 2010, **114**, 4017–4030.
- [8] C. E. Klots, *J. Chem. Phys.*, 1993, **98**, 1110–1115.
- [9] C. E. Klots, *J. Chem. Phys.*, 1994, **100**, 1035–1039.
- [10] R. Mabbs, E. Surber and A. Sanov, *Analyst*, 2003, **128**, 765–772.
- [11] J. B. Wills, F. Pagliarulo, B. Baguenard, F. Lépine and C. Bordas, *Chem. Phys. Lett.*, 2004, **390**, 145–150.

- [12] B. Climen, F. Pagliarulo, A. Ollagnier, B. Baguenard, B. Concina, M. A. Lebeault, F. Lépine and C. Bordas, *Eur. Phys. J. D*, 2007, **43**, 85–89.
- [13] K. L. Reid, *Ann. Rev. Phys. Chem.*, 2003, **54**, 397–424.
- [14] A. Sanov, *Annu. Rev. Phys. Chem.*, 2014, **65**, 341–363.
- [15] C. S. Anstöter, J. N. Bull and J. R. Verlet, *Int. Rev. Phys. Chem.*, 2016, **35**, 509–538.
- [16] C. S. Anstöter, C. R. Dean and J. R. Verlet, *J. Phys. Chem. Lett.*, 2017, **8**, 2268–2273.
- [17] C. S. Anstöter, B. F. Curchod and J. R. Verlet, *Nat. Commun.*, 2020, **11**, 2827.
- [18] E. P. Wigner, *Phys. Rev*, 1948, **73**, 1002–1009.
- [19] U. Fano and D. Dill, *Phys. Rev. A*, 1972, **6**, 185–192.
- [20] T. E. Meyer, *Biochim. Biophys. Acta*, 1985, **806**, 175–183.
- [21] T. E. Meyer, E. Yakali, M. A. Cusanovich and G. Tollin, *Biochemistry*, 1987, **26**, 418–423.
- [22] W. D. Hoff, P. Düx, K. Hård, B. Devreese, I. M. Nugteren-Roodzant, W. Crielaard, R. Boelens, R. Kaptein, J. Van Beeumen and K. J. Hellingwerf, *Biochemistry*, 1994, **33**, 13959–13962.
- [23] W. W. Sprenger, W. D. Hoff, J. P. Armitage and K. J. Hellingwerf, *J. Bacteriol.*, 1993, **175**, 3096–3104.
- [24] R. Brudler, R. Rammelsberg, T. T. Woo, E. D. Getzoff and K. Gerwert, *Nat. Struct. Biol.*, 2001, **8**, 265–70.
- [25] W. D. Hoff, P. Düx, K. Hård, B. Devreese, I. M. Nugteren-Roodzant, W. Crielaard, R. Boelens, R. Kaptein, J. Van Beeumen and K. J. Hellingwerf, *Biochemistry*, 1994, **33**, 13959–13962.

- [26] M. Baca, G. E. Borgstahl, M. Boissinot, P. M. Burke, D. W. R. Williams, K. A. Slater and E. D. Getzoff, *Biochemistry*, 1994, **33**, 14369–14377.
- [27] T. E. Meyer, G. Tollin, J. H. Hazzard and M. A. Cusanovich, *Biophys. J.*, 1989, **56**, 559–564.
- [28] L. A. Baker, M. D. Horbury, S. E. Greenough, F. Allais, P. S. Walsh, S. Habershon and V. G. Stavros, *J. Phys. Chem. Lett.*, 2016, **7**, 56–61.
- [29] C. M. Fraser and C. Chapple, *Arabidopsis Book*, 2011, **9**, e0152.
- [30] F. Gao, T. Gao, K. Zhou and W. Zeng, *Molecules*, 2016, **21**, 1163.
- [31] I. Nielsen, S. Boyé-Péronne, M. El Ghazaly, M. Kristensen, S. Brøndsted Nielsen and L. Andersen, *Biophys. J.*, 2005, **89**, 2597–2604.
- [32] I.-R. Lee, W. Lee and A. H. Zewail, *Proc. Natl. Acad. Sci. U. S. A.*, 2006, **103**, 258–262.
- [33] T. Rocha-Rinza, O. Christiansen, J. Rajput, A. Gopalan, D. B. Rahbek, L. H. Andersen, A. V. Bochenkova, A. A. Granovsky, K. B. Bravaya, A. V. Nemukhin, K. L. Christiansen and M. B. Nielsen, *J. Phys. Chem. A*, 2009, **113**, 9442–9449.
- [34] T. Rocha-Rinza, O. Christiansen, D. B. Rahbek, B. Klærke, L. H. Andersen, K. Lincke and M. Brøndsted Nielsen, *Chem. Eur. J.*, 2010, **16**, 11977–11984.
- [35] S. Smolarek, A. Vdovin, D. L. Perrier, J. P. Smit, M. Drabbels and W. J. Buma, *J. Am. Chem. Soc.*, 2010, **132**, 6315–6317.
- [36] M. Almasian, J. Grzetic, J. Van Maurik, J. D. Steill, G. Berden, S. Ingemann, W. J. Buma and J. Oomens, *J. Phys. Chem. Lett.*, 2012, **3**, 2259–2263.
- [37] C. R. S. Mooney, M. A. Parkes, A. Iskra and H. H. Fielding, *Angew. Chem., Int. Ed.*, 2015, **54**, 5646–5649.
- [38] M. A. Parkes, C. Phillips, M. J. Porter and H. H. Fielding, *Phys. Chem. Chem. Phys.*, 2016, **18**, 10329–10336.

- [39] E. V. Gromov and T. Domratcheva, *Phys. Chem. Chem. Phys.*, 2020, **22**, 8535–8544.
- [40] F. F. García-Prieto, I. F. Galván, A. Muñoz-Losa, M. A. Aguilar and M. E. Martín, *J. Chem. Theory Comput.*, 2013, **9**, 4481–4494.
- [41] J. N. Bull, G. D. Silva, M. S. Scholz, E. Carrascosa and E. J. Bieske, *J. Phys. Chem. A*, 2019, **123**, 4419–4430.
- [42] F. F. García-Prieto, M. A. Aguilar, I. F. Galván, A. Muñoz-Losa, F. J. Olivares del Valle, M. L. Sánchez and M. E. Martín, *J. Phys. Chem. A*, 2015, **119**, 5504–5514.
- [43] M. Vengris, D. S. Larsen, M. A. Van Der Horst, O. F. Larsen, K. J. Hellingwerf and R. Van Grondelle, *J. Phys. Chem. B*, 2005, **109**, 4197–4208.
- [44] A. Espagne, P. Changenet-Barret, P. Plaza and M. M. Martin, *J. Phys. Chem. A*, 2006, **110**, 3393–3404.
- [45] E. V. Gromov, I. Burghardt, J. T. Hynes, H. Köppel and L. S. Cederbaum, *J. Photochem. Photobiol. A Chem.*, 2007, **190**, 241–257.
- [46] A. Espagne, D. H. Paik, P. Changenet-Barret, P. Plaza, M. M. Martin and A. H. Zewail, *Photochem. Photobiol. Sci.*, 2007, **6**, 780–787.
- [47] M. Vengris, M. A. van der Horst, G. Zgrablić, I. H. M. van Stokkum, S. Haacke, M. Chergui, K. J. Hellingwerf, R. van Grondelle and D. S. Larsen, *Biophys. J.*, 2004, **87**, 1848–1857.
- [48] D. S. Larsen, M. Vengris, I. H. van Stokkum, M. A. van der Horst, F. L. de Weerd, K. J. Hellingwerf and R. van Grondelle, *Biophys. J.*, 2004, **86**, 2538–2550.
- [49] H. El-Gezawy, W. Rettig, A. Danel and G. Jonusauskas, *J. Phys. Chem. B*, 2005, **109**, 18699–18705.

- [50] M. A. Van Der Horst, T. P. Stalcup, S. Kaledhonkar, M. Kumauchi, M. Hara, A. Xie, K. J. Hellingwerf and W. D. Hoff, *J. Am. Chem. Soc.*, 2009, **131**, 17443–17451.
- [51] A. D. Stahl, M. Hospes, K. Singhal, I. van Stokkum, R. van Grondelle, M. L. Groot and K. J. Hellingwerf, *Biophys. J.*, 2011, **101**, 1184–1192.
- [52] G. Ahamed, S. Batuta, D. Ghosh, N. A. Begum and D. Mandal, *J. Photochem. Photobiol., A*, 2017, **335**, 86–93.
- [53] W. L. Ryan, D. J. Gordon and D. H. Levy, *J. Am. Chem. Soc.*, 2002, **124**, 6194–6201.
- [54] M. de Groot, E. V. Gromov, H. Köppel and W. J. Buma, *J. Phys. Chem. B*, 2008, **112**, 4427–4434.
- [55] P. J. Morgan, D. M. Mitchell and D. W. Pratt, *Chem. Phys.*, 2008, **347**, 340–345.
- [56] E. M. Tan, S. Amirjalayer, P. Mazzella, B. H. Bakker, J. H. Van Maarseveen, H. Beraugel and W. J. Buma, *J. Phys. Chem. B*, 2014, **118**, 12395–12403.
- [57] M. E. van Brederode, T. Gensch, W. D. Hoff, K. J. Hellingwerf and S. E. Braslavsky, *Biophys. J.*, 1995, **68**, 1101–1109.
- [58] U. K. Genick, S. M. Soltis, P. Kuhn, I. L. Canestrelli and E. D. Getzoff, *Nature*, 1998, **392**, 206–209.
- [59] L. J. G. W. van Wilderen, M. A. van der Horst, I. H. M. van Stokkum, K. J. Hellingwerf, R. van Grondelle and M. L. Groot, *Proc. Natl. Acad. Sci. U. S. A.*, 2006, **103**, 15050–15055.
- [60] P. D. Coureux, Z. P. Fan, V. Stojanoff and U. K. Genick, *Structure*, 2008, **16**, 863–872.
- [61] G. Groenhof, L. V. Schäfer, M. Boggio-Pasqua, H. Grubmüller and M. A. Robb, *J. Am. Chem. Soc.*, 2008, **130**, 3250–3251.



- [62] G. Groenhof, M. Bouxin-Cademartory, B. Hess, S. P. de Visser, H. J. C. Berendsen, M. Olivucci, A. E. Mark and M. A. Robb, *J. Am. Chem. Soc.*, 2004, **126**, 4228–4233.
- [63] J. Zhu, L. Paparelli, M. Hospes, J. Arents, J. T. M. Kennis, I. H. M. Van Stokkum, K. J. Hellingwerf and M. L. Groot, *J. Phys. Chem. B*, 2013, **117**, 11042–11048.
- [64] D. S. Larsen, I. H. M. van Stokkum, M. Vengris, M. A. van der Horst, F. L. de Weerd, K. J. Hellingwerf and R. van Grondelle, *Biophys. J.*, 2004, **87**, 1858–1872.
- [65] C. N. Lincoln, A. E. Fitzpatrick and J. J. Thor, *Phys. Chem. Chem. Phys.*, 2012, **14**, 15752–15764.
- [66] T. S. Zhang, Y. G. Fang, X. F. Song, W. H. Fang and G. Cui, *J. Phys. Chem. Lett.*, 2020, **11**, 2470–2476.
- [67] K. Pande, C. D. M. Hutchison, G. Groenhof, A. Aquila, J. S. Robinson, J. Tenboer, S. Basu, S. Boutet, D. P. DePonte, M. Liang, T. A. White, N. A. Zatsepin, O. Yefanov, D. Morozov, D. Oberthuer, C. Gati, G. Subramanian, D. James, Y. Zhao, J. Koralek, J. Brayshaw, C. Kupitz, C. Conrad, S. Roy-Chowdhury, J. D. Coe, M. Metz, P. L. Xavier, T. D. Grant, J. E. Koglin, G. Ketawala, R. Fromme, V. Šrajer, R. Henning, J. C. H. Spence, A. Ourmazd, P. Schwander, U. Weierstall, M. Frank, P. Fromme, A. Barty, H. N. Chapman, K. Moffat, J. J. van Thor and M. Schmidt, *Science*, 2016, **352**, 725–729.
- [68] E. V. Gromov, *J. Chem. Phys.*, 2014, **141**, 224308–224308.
- [69] F. F. García-Prieto, A. Muñoz-Losa, I. Fdez. Galván, M. L. Sánchez, M. A. Aguilar and M. E. Martín, *J. Chem. Theory Comput.*, 2017, **13**, 737–748.
- [70] M. Boggio-Pasqua and G. Groenhof, *J. Phys. Chem. B*, 2011, **115**, 7021–7028.
- [71] C. Ko, A. M. Virshup and T. J. Martínez, *Chem. Phys. Lett.*, 2008, **460**, 272–277.

- [72] D. Zuev, K. B. Bravaya, T. D. Crawford, R. Lindh and A. I. Krylov, *J. Chem. Phys.*, 2011, **134**, 034310.
- [73] J. L. Beltrán, N. Sanli, G. Fonrodona, D. Barrón, G. Özkan and J. Barbosa, *Anal. Chim. Acta*, 2003, **484**, 253–264.
- [74] V. R. Cunha, V. R. Constantino and R. A. Ando, *Vib. Spectrosc.*, 2012, **58**, 139–145.
- [75] M. Putschögl, P. Zirak and A. Penzkofer, *Chem. Phys.*, 2008, **343**, 107–120.
- [76] A. Espagne, D. H. Paik, P. Changenet-Barret, M. M. Martin and A. H. Zewail, *ChemPhysChem*, 2006, **7**, 1717–1726.
- [77] A. Espagne, P. Changenet-Barret, J. B. Baudin, P. Plaza and M. M. Martin, *J. Photochem. Photobiol., A*, 2007, **185**, 245–252.
- [78] D. S. Larsen, M. Vengris, I. H. van Stokkum, M. A. van der Horst, R. A. Cordfunke, K. J. Hellingwerf and R. van Grondelle, *Chem. Phys. Lett.*, 2003, **369**, 563–569.
- [79] P. Changenet-Barret, A. Espagne, S. Charier, J. B. Baudin, L. Jullien, P. Plaza, K. J. Hellingwerf and M. M. Martin, *Photochem. Photobiol. Sci.*, 2004, **3**, 823–829.
- [80] P. Changenet-Barret, A. Espagne, P. Plaza, K. J. Hellingwerf and M. M. Martin, *New J. Chem.*, 2005, **29**, 527.
- [81] A. Espagne, P. Changenet-Barret, P. Plaza and M. M. Martin, *J. Phys. Chem. A*, 2006, **110**, 3393–3404.
- [82] H. Kuramochi, S. Takeuchi and T. Tahara, *J. Phys. Chem. Lett.*, 2012, **3**, 2025–2029.
- [83] S. Mustalahti, D. Morozov, H. L. Luk, R. R. Pallerla, P. Myllyperkiö, M. Pettersson, P. M. Pihko and G. Groenhof, *J. Phys. Chem. Lett.*, 2020, **11**, 2177–2181.

- [84] P. Changenet-Barret, F. Lacombat and P. Plaza, *J. Photochem. Photobiol., A*, 2012, **234**, 171–180.
- [85] P. Changenet-Barret, P. Plaza and M. M. Martin, *Chem. Phys. Lett.*, 2001, **336**, 439–444.
- [86] D. S. Larsen, M. Vengris, I. H. van Stokkum, M. A. van der Horst, F. L. de Weerd, K. J. Hellingwerf and R. van Grondelle, *Biophys. J.*, 2004, **86**, 2538–2550.
- [87] S. Frutos-Puerto, A. Muñoz-Losa, M. E. Martín and M. A. Aguilar, *Comput. Theor. Chem.*, 2014, **1040-1041**, 287–294.
- [88] E. V. Gromov, *J. Chem. Phys.*, 2014, **141**, 224308.
- [89] E. V. Gromov, I. Burghardt, H. Köppel and L. S. Cederbaum, *J. Phys. Chem. A*, 2011, **115**, 9237–9248.
- [90] M. Boggio-Pasqua, M. A. Robb and G. Groenhof, *J. Am. Chem. Soc.*, 2009, **131**, 13580–13581.
- [91] C. R. S. Mooney, *PhD thesis*, Department of Chemistry, University College London, United Kingdom, 2015.
- [92] A. R. McKay, M. E. Sanz, C. R. S. Mooney, R. S. Minns, E. M. Gill and H. H. Fielding, *Rev. Sci. Instrum.*, 2010, **81**, 123101.
- [93] J. B. Fenn, *Angew. Chem., Int. Ed.*, 2003, pp. 3871–3894.
- [94] Z. Nie, Y.-K. Tzeng, H.-C. Chang, C.-C. Chiu, C.-M. C.-Y. Chang, C.-M. C.-Y. Chang and M.-H. Tao, *Angew. Chem., Int. Ed.*, 2006, **45**, 8131–8134.
- [95] J. Fenn, M. Mann, C. Meng, S. Wong and C. Whitehouse, *Science*, 1989, **246**, 64–71.
- [96] H. Wang and S. Hanash, *Mass Spectrom. Rev.*, 2005, **24**, 413–426.
- [97] S. Banerjee and S. Mazumdar, *Int. J. Anal. Chem.*, 2012, **2012**, 40.

- [98] G. I. Taylor, *Proc. R. Soc. London, Ser. A*, 1964, **280**, 383–397.
- [99] L. Konermann, E. Ahadi, A. D. Rodriguez and S. Vahidi, *Anal. Chem.*, 2013, **85**, 2–9.
- [100] S. Bajic, *US Pat.* 5 756 994, 1998.
- [101] P. E. Miller and M. B. Denton, *J. Chem. Educ.*, 1986, **63**, 617.
- [102] E. Mathieu, *J. Math. Pures Appl.*, 1868, **13**, 137–203.
- [103] R. E. March, *J. Mass Spectrom.*, 1997, **32**, 351–369.
- [104] A. T. J. B. Eppink and D. H. Parker, *Rev. Sci. Instrum.*, 1997, **68**, 3477.
- [105] L. Montgomery Smith, D. R. Keefer and S. I. Sudharsanan, *J. Quant. Spectrosc. Radiat. Transfer*, 1988, **39**, 367–373.
- [106] S. M. Candel, *Comput. Phys. Commun.*, 1981, **23**, 343–353.
- [107] F. D. Nunes, J. Santos and M. E. Manso, *Rev. Sci. Instrum.*, 1999, **70**, 1047.
- [108] S. Manzhos and H. P. Loock, *Comput. Phys. Commun.*, 2003, **154**, 76–87.
- [109] C. Bordas, F. Paulig, H. Helm and D. L. Huestis, *Rev. Sci. Instrum.*, 1996, **67**, 2257–2268.
- [110] M. J. Vrakking, *Rev. Sci. Instrum.*, 2001, **72**, 4084.
- [111] V. Dribinski, A. Ossadtchi, V. A. Mandelshtam and H. Reisler, *Rev. Sci. Instrum.*, 2002, **73**, 2634.
- [112] G. A. Garcia, L. Nahon, I. Powis, G. A. Garcia, L. Nahon and I. Powis, *Rev. Sci. Instrum.*, 2004, **75**, 4989–4996.
- [113] B. Dick, *Phys. Chem. Chem. Phys.*, 2014, **16**, 570–580.
- [114] G. R. Harrison, J. C. Vaughan, B. Hidle and G. M. Laurent, *J. Chem. Phys.*, 2018, **148**, 194101.

- [115] D. D. Hickstein, S. T. Gibson, R. Yurchak, D. D. Das and M. Ryazanov, *Rev. Sci. Instrum.*, 2019, **90**, 065115.
- [116] B. Dick, *Phys. Chem. Chem. Phys.*, 2019, **21**, 19499–19512.
- [117] R. J. Peláez, C. Blondel, C. Delsart and C. Drag, *J. Phys. B: At., Mol. Opt. Phys.*, 2009, **42**, 125001.
- [118] M. A. Parkes, J. Crellin, A. Henley and H. H. Fielding, *Phys. Chem. Chem. Phys.*, 2018, **20**, 15543–15549.
- [119] C. McLaughlin, M. Assmann, M. A. Parkes, J. L. Woodhouse, R. Lewin, H. C. Hailes, G. A. Worth and H. H. Fielding, *Chem. Sci.*, 2017, **8**, 1621–1630.
- [120] J. L. Woodhouse, *PhD thesis*, Department of Chemistry, University College London, United Kingdom, 2019.
- [121] E. Schrödinger, *Ann. Phys. (Berlin, Ger.)*, 1926, **384**, 489–527.
- [122] M. Born and R. Oppenheimer, *Ann. Phys. (Berlin, Ger.)*, 1927, **389**, 457–484.
- [123] D. R. Hartree, *Math. Proc. Cambridge Philos. Soc.*, 1928, **24**, 426–437.
- [124] D. R. Hartree, *Math. Proc. Cambridge Philos. Soc.*, 1929, **25**, 225–236.
- [125] V. Fock, *Z. Physik*, 1930, **61**, 126–148.
- [126] R. Krishnan, J. S. Binkley, R. Seeger and J. A. Pople, *J. Chem. Phys.*, 1980, **72**, 650–654.
- [127] P. Hohenberg and W. Kohn, *Phys. Rev.*, 1964, **136**, B864.
- [128] W. Kohn and L. J. Sham, *Phys. Rev.*, 1965, **140**, A1133.
- [129] J. P. Perdew and K. Schmidt, *AIP Conf. Proc.*, 2003, pp. 1–20.
- [130] A. D. Becke, *J. Chem. Phys.*, 2014, **140**, 18–301.
- [131] J. C. Slater, *Phys. Rev.*, 1951, **81**, 385–390.
- [132] S. H. Vosko, L. Wilk and M. Nusair, *Can. J. Phys.*, 1980, **58**, 1200–1211.

- [133] C. Lee, W. Yang and R. G. Parr, *Phys. Rev. B*, 1988, **37**, 785–789.
- [134] A. D. Becke, *Phys. Rev. A*, 1988, **38**, 3098–3100.
- [135] B. Miehlich, A. Savin, H. Stoll and H. Preuss, *Chem. Phys. Lett.*, 1989, **157**, 200–206.
- [136] P. M. Gill, B. G. Johnson, J. A. Pople and M. J. Frisch, *Int. J. Quantum Chem.*, 1992, **44**, 319–331.
- [137] P. J. Stephens, F. J. Devlin, C. F. Chabalowski and M. J. Frisch, *J. Phys. Chem.*, 1994, **98**, 11623–11627.
- [138] R. Van Noorden, B. Maher and R. Nuzzo, *Nature*, 2014, **514**, 550–553.
- [139] T. Schwabe and S. Grimme, *Phys. Chem. Chem. Phys.*, 2007, **9**, 3397–3406.
- [140] D. H. Ess and K. N. Houk, *J. Phys. Chem. A*, 2005, **109**, 9542–9553.
- [141] K. Kim and K. D. Jordan, *J. Phys. Chem.*, 1994, **98**, 10089–10094.
- [142] A. A. El-Azhary and H. U. Suter, *J. Phys. Chem.*, 1996, **100**, 15056–15063.
- [143] S. Grimme, *J. Comput. Chem.*, 2004, **25**, 1463–1473.
- [144] C. R. S. Mooney, M. E. Sanz, A. R. McKay, R. J. Fitzmaurice, A. E. Aliev, S. Caddick and H. H. Fielding, *J. Phys. Chem. A*, 2012, **116**, 7943–7949.
- [145] C. R. S. Mooney, M. A. Parkes, L. Zhang, H. C. Hailes, A. Simperler, M. J. Bearpark and H. H. Fielding, *J. Chem. Phys.*, 2014, **140**, 205103.
- [146] R. Beekmeyer, M. A. Parkes, L. Ridgwell, J. W. Riley, J. Chen, B. L. Feringa, A. Kerridge and H. H. Fielding, *Chem. Sci.*, 2017, **8**, 6141–6148.
- [147] J. L. Woodhouse, M. Assmann, M. A. Parkes, H. Grounds, S. J. Pacman, J. C. Anderson, G. A. Worth and H. H. Fielding, *Phys. Chem. Chem. Phys.*, 2017, **19**, 22711–22720.
- [148] M. A. Parkes, A. Bennett and H. H. Fielding, *Mol. Phys.*, 2019, **117**, 3027–3035.

- [149] T. Clark, J. Chandrasekhar, G. W. Spitznagel and P. V. R. Schleyer, *J. Comput. Chem.*, 1983, **4**, 294–301.
- [150] M. J. Frisch, J. A. Pople and J. S. Binkley, *J. Chem. Phys.*, 1984, **80**, 3265–3269.
- [151] M. J. Frisch, G. W. Trucks, H. B. Schlegel, G. E. Scuseria, M. A. Robb, J. R. Cheeseman, G. Scalmani, V. Barone, B. Mennucci, G. A. Petersson, H. Nakatsuji, M. Caricato, X. Li, H. P. Hratchian, A. F. Izmaylov, J. Bloino, G. Zheng, J. L. Sonnenberg, M. Hada, M. Ehara, K. Toyota, R. Fukuda, J. Hasegawa, M. Ishida, T. Nakajima, Y. Honda, O. Kitao, H. Nakai, T. Vreven, J. A. Montgomery, J. E. Peralta, F. Ogliaro, M. Bearpark, J. J. Heyd, E. Brothers, K. N. Kudin, V. N. Staroverov, R. Kobayashi, J. Normand, K. Raghavachari, A. Rendell, J. C. Burant, S. S. Iyengar, J. Tomasi, M. Cossi, N. Rega, J. M. Millam, M. Klene, J. E. Knox, J. B. Cross, V. Bakken, C. Adamo, J. Jaramillo, R. Gomperts, R. E. Stratmann, O. Yazyev, A. J. Austin, R. Cammi, C. Pomelli, J. W. Ochterski, R. L. Martin, K. Morokuma, V. G. Zakrzewski, G. A. Voth, P. Salvador, J. J. Dannenberg, S. Dapprich, A. D. Daniels, Ö. Farkas, J. B. Foresman, J. V. Ortiz, J. Cioslowski and D. J. Fox, *Gaussian 09, Revision D.01*, 2009.
- [152] Alex A. Granovsky, Firefly version 8.2.0,  
<http://classic.chem.msu.su/gran/firefly/index.html>.
- [153] M. W. Schmidt, K. K. Baldridge, J. A. Boatz, S. T. Elbert, M. S. Gordon, J. H. Jensen, S. Koseki, N. Matsunaga, K. A. Nguyen, S. Su, T. L. Windus, M. Dupuis and J. A. Montgomery Jr, *J. Comput. Chem.*, 1993, **14**, 1347–1363.
- [154] T. H. Dunning, *J. Chem. Phys.*, 1989, **90**, 1007–1023.
- [155] R. A. Kendall, T. H. Dunning and R. J. Harrison, *J. Chem. Phys.*, 1992, **96**, 6796–6806.

- [156] Y. Shao, Z. Gan, E. Epifanovsky, A. T. B. Gilbert, M. Wormit, J. Kussmann, A. W. Lange, A. Behn, J. Deng, X. Feng, D. Ghosh, M. Goldey, P. R. Horn, L. D. Jacobson, I. Kaliman, R. Z. Khaliullin, T. Kuś, A. Landau, J. Liu, E. I. Proynov, Y. M. Rhee, R. M. Richard, M. A. Rohrdanz, R. P. Steele, E. J. Sundstrom, H. L. Woodcock III, P. M. Zimmerman, D. Zuev, B. Albrecht, E. Alguire, B. Austin, G. J. O. Beran, Y. A. Bernard, E. Berquist, K. Brandhorst, K. B. Bravaya, S. T. Brown, D. Casanova, C.-M. Chang, Y. Chen, S. H. Chien, K. D. Closser, D. L. Crittenden, M. Diedenhofen, R. A. DiStasio Jr., H. Do, A. D. Dutoi, R. G. Edgar, S. Fatehi, L. Fusti-Molnar, A. Ghysels, A. Golubeva-Zadorozhnaya, J. Gomes, M. W. D. Hanson-Heine, P. H. P. Harbach, A. W. Hauser, E. G. Hohenstein, Z. C. Holden, T. C. Jagau, H. Ji, B. Kaduk, K. Khistyayev, J. Kim, J. Kim, R. A. King, P. Klunzinger, D. Kosenkov, T. Kowalczyk, C. M. Krauter, K. U. Lao, A. D. Laurent, K. V. Lawler, S. V. Levchenko, C. Y. Lin, F. Liu, E. Livshits, R. C. Lochan, A. Luenser, P. Manohar, S. F. Manzer, S.-P. Mao, N. Mardirossian, A. V. Marenich, S. A. Maurer, N. J. Mayhall, E. Neuscamman, C. M. Oana, R. Olivares-Amaya, D. P. O'Neill, J. A. Parkhill, T. M. Perrine, R. Peverati, A. Prociuk, D. R. Rehn, E. Rosta, N. J. Russ, S. M. Sharada, S. Sharma, D. W. Small, A. Sodt, T. Stein, D. Stück, Y.-C. Su, A. J. Thom, T. Tsuchimochi, V. Vanovschi, L. Vogt, O. Vydrov, T. Wang, M. A. Watson, J. Wenzel, A. White, C. F. Williams, J. Yang, S. Yeganeh, S. R. Yost, Z.-Q. You, I. Y. Zhang, X. Zhang, Y. Zhao, B. R. Brooks, G. K. L. Chan, D. M. Chipman, C. J. Cramer, W. A. Goddard III, M. S. Gordon, W. J. Hehre, A. Klamt, H. F. Schaefer III, M. W. Schmidt, C. D. Sherrill, D. G. Truhlar, A. Warshel, X. Xu, A. Aspuru-Guzik, R. Baer, A. T. Bell, N. A. Besley, J.-D. Chai, A. Dreuw, B. D. Dunietz, T. R. Furlani, S. R. Gwaltney, C.-P. Hsu, Y. Jung, J. Kong, D. S. Lambrecht, W. Liang, C. Ochsenfeld, V. A. Rassolov, L. V. Slipchenko, J. E. Subotnik, T. V. Voorhis, J. M. Herbert, A. I. Krylov, P. M. Gill and M. Head-Gordon, *Mol. Phys.*, 2015, **113**, 184–215.
- [157] J. Linderberg and Y. Öhrn, *Propagators in Quantum Chemistry*, John Wiley



- & Sons, Inc., Hoboken, NJ, USA, 2004, p. 79.
- [158] V. G. Zakrzewski, O. Dolgounitcheva, A. V. Zakjevskii and J. V. Ortiz, *Annu. Rep. Comput. Chem.*, Elsevier, 2010, vol. 6, pp. 79–94.
- [159] J. V. Ortiz, *WIREs Comput. Mol. Sci.*, 2013, **3**, 123–142.
- [160] J. V. Ortiz, *J. Chem. Phys.*, 2020, **153**, 070902.
- [161] J. F. Stanton and R. J. Bartlett, *J. Chem. Phys.*, 1993, **98**, 7029–7039.
- [162] A. I. Krylov, *Ann. Rev. Phys. Chem.*, 2008, **59**, 433–462.
- [163] D. Sinha, S. K. Mukhopadhyay, R. Chaudhuri and D. Mukherjee, *Chem. Phys. Lett.*, 1989, **154**, 544–549.
- [164] J. F. Stanton and J. Gauss, *J. Chem. Phys.*, 1994, **101**, 8938–8944.
- [165] D. Ghosh, A. Roy, R. Seidel, B. Winter, S. Bradforth and A. I. Krylov, *J. Phys. Chem. B*, 2012, **116**, 7269–7280.
- [166] S. Bose, S. Chakrabarty and D. Ghosh, *J. Phys. Chem. B*, 2016, **120**, 4410–4420.
- [167] J. W. Riley, B. Wang, J. L. Woodhouse, M. Assmann, G. A. Worth and H. H. Fielding, *J. Phys. Chem. Lett.*, 2018, 678–682.
- [168] V. A. Rassolov, J. A. Pople, P. C. Redfern and L. A. Curtiss, *Chem Phys. Lett.*, 2001, **350**, 573–576.
- [169] E. Runge and E. K. U. Gross, *Phys. Rev. Lett.*, 1984, **52**, 997–1000.
- [170] M. E. Casida, in *Time-Dependent Density Functional Response Theory for Molecules*, 1995, pp. 155–192.
- [171] C. A. Ullrich and Z.-h. Yang, *Braz. J. Phys.*, 2014, **44**, 154–188.
- [172] R. Van Leeuwen, *Phys. Rev. Lett.*, 1998, **80**, 1280–1283.
- [173] K. Burke, J. Werschnik and E. K. Gross, *J. Chem. Phys.*, 2005, **123**, 62206.

- [174] M. Casida and M. Huix-Rotllant, *Ann. Rev. Phys. Chem.*, 2012, **63**, 287–323.
- [175] T. Yanai, D. P. Tew and N. C. Handy, *Chem Phys. Lett.*, 2004, **393**, 51–57.
- [176] J. D. Chai and M. Head-Gordon, *J. Chem. Phys.*, 2008, **128**, 84106.
- [177] J. D. Chai and M. Head-Gordon, *Phys. Chem. Chem. Phys.*, 2008, **10**, 6615–6620.
- [178] H. Sekino and R. J. Bartlett, *Int. J. Quantum Chem.*, 1984, **26**, 255–265.
- [179] H. Koch, H. J. A. Jensen, P. Jørgensen and T. Helgaker, *J. Chem. Phys.*, 1990, **93**, 3345–3350.
- [180] A. I. Krylov, C. D. Sherrill and M. Head-Gordon, *J. Chem. Phys.*, 2000, **113**, 6509–6527.
- [181] D. Zuev, K. B. Bravaya, M. V. Makarova and A. I. Krylov, *J. Chem. Phys.*, 2011, **135**, 194304.
- [182] J. Schirmer, *Phys. Rev. A*, 1982, **26**, 2395–2416.
- [183] J. Schirmer and A. B. Trofimov, *J. Chem. Phys.*, 2004, **120**, 11449–11464.
- [184] A. Dreuw and M. Wormit, *WIREs Comput. Mol. Sci.*, 2015, **5**, 82–95.
- [185] J. H. Eland, *Int. J. Mass Spectrosc. Ion Phys.*, 1969, **2**, 471–484.
- [186] S. Miertuš, E. Scrocco and J. Tomasi, *Chem. Phys.*, 1981, **55**, 117–129.
- [187] F. Lipparini and B. Mennucci, *J. Chem. Phys.*, 2016, **144**, 160901.
- [188] A. D. MacKerell, D. Bashford, M. Bellott, R. L. Dunbrack, J. D. Evanseck, M. J. Field, S. Fischer, J. Gao, H. Guo, S. Ha, D. Joseph-McCarthy, L. Kuchnir, K. Kuczera, F. T. Lau, C. Mattos, S. Michnick, T. Ngo, D. T. Nguyen, B. Prodhom, W. E. Reiher, B. Roux, M. Schlenkrich, J. C. Smith, R. Stote, J. Straub, M. Watanabe, J. Wiórkiewicz-Kuczera, D. Yin and M. Karplus, *J. Phys. Chem. B*, 1998, **102**, 3586–3616.

- [189] W. L. Jorgensen, J. Chandrasekhar, J. D. Madura, R. W. Impey and M. L. Klein, *J. Chem. Phys*, 1983, **79**, 926–935.
- [190] R. E. Bulo, C. Michel, P. Fleurat-Lessard and P. Sautet, *J. Chem. Theory Comput*, 2013, **9**, 5567–5577.
- [191] P. N. Day, J. H. Jensen, M. S. Gordon, S. P. Webb, W. J. Stevens, M. Krauss, D. Garmer, H. Basch and D. Cohen, *J. Chem. Phys*, 1996, **105**, 1968–1986.
- [192] M. S. Gordon, M. A. Freitag, P. Bandyopadhyay, J. H. Jensen, V. Kairys and W. J. Stevens, *J. Phys. Chem. A*, 2001, **105**, 306–307.
- [193] A. D. Buckingham, *Q. Rev., Chem. Soc.*, 1959, **13**, 183–214.
- [194] L. V. Slipchenko and M. S. Gordon, *J. Comput. Chem.*, 2007, **28**, 276–291.
- [195] M. A. Freitag, M. S. Gordon, J. H. Jensen and W. J. Stevens, *J. Chem. Phys.*, 2000, **112**, 7300–7306.
- [196] L. V. Slipchenko and M. S. Gordon, *Mol. Phys.*, 2009, **107**, 999–1016.
- [197] J. H. Jensen and M. S. Nikkitan, *Mol. Phys.*, 1996, **89**, 1313–1325.
- [198] J. H. Jensen and M. S. Gordon, *J. Chem. Phys.*, 1998, **108**, 4772–4782.
- [199] L. V. Slipchenko, *J. Phys. Chem. A*, 2010, **114**, 8824–8830.
- [200] D. Ghosh, *J. Phys. Chem. A*, 2017, **121**, 741–752.
- [201] A. Baltuška, I. H. M. van Stokkum, A. Kroon, R. Monshouwer, K. J. Hellingwerf and R. van Grondelle, *Chem. Phys. Lett.*, 1997, **270**, 263–266.
- [202] L. Mendonça, F. Hache, P. Changenet-Barret, P. Plaza, H. Chosrowjan, S. Taniguchi and Y. Imamoto, *J. Am. Chem. Soc.*, 2013, **135**, 14637–14643.
- [203] A. Xie, W. D. Hoff, A. R. Kroon and K. J. Hellingwerf, *Biochemistry*, 1996, **35**, 14671–14678.

- [204] R. Cordfunke, R. Kort, A. Pierik, B. Gobets, G.-J. Koomen, J. W. Verhoeven and K. J. Hellingwerf, *Proc. Natl. Acad. Sci. U. S. A.*, 1998, **95**, 7396–7401.
- [205] A. Henley, M. E. Diveky, A. M. Patel, M. A. Parkes, J. C. Anderson and H. H. Fielding, *Phys. Chem. Chem. Phys.*, 2017, **19**, 31572–31580.
- [206] C. M. Breneman and K. B. Wiberg, *J. Comput. Chem.*, 1990, **11**, 361–373.
- [207] R. F. Gunion, M. K. Gilles, M. L. Polak and W. C. Lineberger, *Int. J. Mass Spectrom. Ion Processes*, 1992, **117**, 601–620.
- [208] J. N. Bull, C. S. Anstöter and J. R. R. Verlet, *J. Phys. Chem. A*, 2020, **124**, 2140–2151.
- [209] K. D. Jordan and F. Wang, *Annu. Rev. Phys. Chem.*, 2003, **54**, 367–396.
- [210] J. Simons, *J. Phys. Chem. A*, 2008, **112**, 6401–6511.
- [211] Y. O. Jung, J. H. Lee, J. Kim, M. Schmidt, K. Moffat, V. Šrajer and H. Ihee, *Nat. Chem.*, 2013, **5**, 212–220.
- [212] A. Henley, A. M. Patel, M. A. Parkes, J. C. Anderson and H. H. Fielding, *J. Phys. Chem. A*, 2018, **122**, 8222–8228.
- [213] D. Ghosh, D. Kosenkov, V. Vanovschi, C. F. Williams, J. M. Herbert, M. S. Gordon, M. W. Schmidt, L. V. Slipchenko and A. I. Krylov, *J. Phys. Chem. A*, 2010, **114**, 12739–12754.
- [214] I. A. Kaliman and L. V. Slipchenko, *J. Comput. Chem.*, 2013, **34**, 2284–2292.
- [215] D. Kosenkov and L. V. Slipchenko, *J. Phys. Chem. A*, 2011, **115**, 392–401.
- [216] D. Ghosh, *J. Chem. Phys.*, 2014, **140**, 094101.
- [217] K. D. Nanda and A. I. Krylov, *J. Chem. Phys.*, 2018, **149**, 164109.
- [218] D. Ghosh, O. Isayev, L. V. Slipchenko and A. I. Krylov, *J. Phys. Chem. A*, 2011, **115**, 6028–6038.

- [219] A. Defusco, N. Minezawa, L. V. Slipchenko, F. Zahariev and M. S. Gordon, *J. Phys. Chem. Lett.*, 2011, **2**, 2184–2192.
- [220] P. R. Tentscher, R. Seidel, B. Winter, J. J. Guerard and J. S. Arey, *J. Phys. Chem. B*, 2015, **119**, 238–256.
- [221] J. J. Guerard, P. R. Tentscher, M. Seijo and J. Samuel Arey, *Phys. Chem. Chem. Phys.*, 2015, **17**, 14811–14826.
- [222] A. Sadybekov and A. I. Krylov, *J. Chem. Phys.*, 2017, **147**, 14107.
- [223] L. V. Slipchenko and P. K. Gurunathan, *Fragmentation: Toward Accurate Calculations on Complex Molecular Systems*, John Wiley & Sons, Ltd, Chichester, UK, 2017, pp. 183–208.
- [224] S. Bose and D. Ghosh, *J. Comput. Chem.*, 2017, **38**, 2248–2257.
- [225] R. Chakraborty, S. Bose and D. Ghosh, *J. Comput. Chem.*, 2017, **38**, 2528–2537.
- [226] A. Barrozo, B. Xu, A. O. Gunina, M. I. Jacobs, K. Wilson, O. Kostko, M. Ahmed and A. I. Krylov, *J. Phys. Chem. Lett.*, 2019, **10**, 1860–1865.
- [227] M. Mukherjee, S. Haldar and A. K. Dutta, *Int. J. Quantum Chem.*, 2020, **120**, 1–14.
- [228] A. Henley, J. W. Riley, B. Wang and H. H. Fielding, *Faraday Discuss.*, 2020, **221**, 202–218.
- [229] J. C. Phillips, R. Braun, W. Wang, J. Gumbart, E. Tajkhorshid, E. Villa, C. Chipot, R. D. Skeel, L. Kalé and K. Schulten, *J. Comput. Chem.*, 2005, **26**, 1781–1802.
- [230] K. Vanommeslaeghe, E. Hatcher, C. Acharya, S. Kundu, S. Zhong, J. Shim, E. Darian, O. Guvench, P. Lopes, I. Vorobyov and A. D. Mackerell, *J. Comput. Chem.*, 2009, **31**, 671–690.
- [231] W. Humphrey, A. Dalke and K. Schulten, *J. Mol. Graphics*, 1996, **14**, 33–38.

- [232] D. Ghosh, D. Kosenkov, V. Vanovschi, J. Flick, I. Kaliman, Y. Shao, A. T. Gilbert, A. I. Krylov and L. V. Slipchenko, *J. Comput. Chem.*, 2013, **34**, 1060–1070.
- [233] P. N. Day, J. H. Jensen, M. S. Gordon, S. P. Webb, W. J. Stevens, M. Krauss, D. Garmer, H. Basch and D. Cohen, *J. Chem. Phys.*, 1996, **105**, 1968–1986.
- [234] S. Gozem and A. I. Krylov, *ezDyson*,  
<http://iopenshell.usc.edu/downloads/ezdyson>.
- [235] H.-T. Liu, C.-G. Ning, D.-L. Huang, P. D. Dau and L.-S. Wang, *Angew. Chem., Int. Ed.*, 2013, **52**, 8976–8979.
- [236] J. L. Woodhouse, A. Henley, M. A. Parkes and H. H. Fielding, *J. Phys. Chem. A*, 2019, **123**, 2709–2718.
- [237] P. A. Kollman and L. C. Allen, *Chem. Rev.*, 1972, **72**, 283–303.
- [238] A. Henley, M. Bound and E. Besley, *J. Phys. Chem. A*, 2016, **120**, 3701–3709.
- [239] J. Rajput, D. B. Rahbek, G. Aravind and L. H. Andersen, *Biophys. J.*, 2010, **98**, 488–492.
- [240] B. Winter and M. Faubel, *Chem. Rev.*, 2006, **106**, 1176–1211.
- [241] R. Seidel, B. Winter and S. E. Bradforth, *Ann. Rev. Phys. Chem.*, 2016, **67**, 283–305.
- [242] J. Hummert, G. Reitsma, N. Mayer, E. Ikonnikov, M. Eckstein and O. Kornilov, *J. Phys. Chem. Lett.*, 2018, **9**, 6649–6655.
- [243] T. Suzuki, *J. Chem. Phys.*, 2019, **151**, 104306.
- [244] N. Ottosson, K. J. Børve, D. Spångberg, H. Bergersen, L. J. Sæthre, M. Faubel, W. Pokapanich, G. Öhrwall, O. Björneholm and B. Winter, *J. Am. Chem. Soc.*, 2011, **133**, 3120–3130.

- [245] M. Nadal-Ferret, R. Gelabert, M. Moreno and J. M. Lluch, *J. Am. Chem. Soc.*, 2014, **136**, 3542–3552.
- [246] A. Toniolo, G. Granucci and T. J. Martínez, *J. Phys. Chem. A*, 2003, **107**, 3822–3830.
- [247] F. F. García-Prieto, A. Muñoz-Losa, M. Luz Sánchez, M. Elena Martín and M. A. Aguilar, *Phys. Chem. Chem. Phys.*, 2016, **18**, 27476–27485.
- [248] C. M. Isborn, A. W. Go, M. A. Clark, R. C. Walker, T. J. Martínez and B. Schlegel Festschrift, *J. Chem. Theory Comput.*, 2012, **8**, 8.
- [249] J. M. Milanese, M. R. Provorse, E. Alameda and C. M. Isborn, *J. Chem. Theory Comput.*, 2017, **13**, 2159–2171.
- [250] M. Kamiya, S. Saito and I. Ohmine, *J. Phys. Chem. B*, 2007, **111**, 2948–2956.
- [251] J. Gilmore and R. H. McKenzie, *J. Phys. Chem. A*, 2008, **112**, 2162–2176.
- [252] K. Saito and H. Ishikita, *Proc. Natl. Acad. Sci. U. S. A.*, 2012, **109**, 167–172.
- [253] M. Boggio-Pasqua, C. F. Burmeister, M. A. Robb and G. Groenhof, *Phys. Chem. Chem. Phys.*, 2012, **14**, 7912–7928.
- [254] L. Wei, H. Wang, X. Chen, W. Fang and H. Wang, *Phys. Chem. Chem. Phys.*, 2014, **16**, 25263–25272.
- [255] T. Graen, L. Inhester, M. Clemens, H. Grubmüller and G. Groenhof, *J. Am. Chem. Soc.*, 2016, **138**, 16620–16631.
- [256] P. J. Taenzler, K. Sadeghian and C. Ochsenfeld, *J. Chem. Theory Comput.*, 2016, **12**, 5170–5178.
- [257] S. Gozem, H. L. Luk, I. Schapiro and M. Olivucci, *Chem. Rev.*, 2017, **117**, 13502–13565.

- [258] L. T. Mix, E. C. Carroll, D. Morozov, J. Pan, W. R. Gordon, A. Philip, J. Fuzell, M. Kumauchi, I. Van Stokkum, G. Groenhof, W. D. Hoff and D. S. Larsen, *Biochemistry*, 2018, **57**, 1733–1747.
- [259] G. Groenhof, V. Modi and D. Morozov, *Curr. Opin. Struct. Biol.*, 2020, **61**, 106–112.
- [260] I. F. Galván, M. L. Sánchez, M. E. Martín, F. J. Olivares del Valle and M. A. Aguilar, *Comput. Phys. Commun.*, 2003, **155**, 244–259.
- [261] T. J. Zuehlsdorff, J. A. Napoli, J. M. Milanese, T. E. Markland and C. M. Isborn, *J. Chem. Phys.*, 2018, **149**, 24107.
- [262] R. Seidel, M. N. Pohl, H. Ali, B. Winter and E. F. Aziz, *Rev. Sci. Instrum.*, 2017, **88**, 73107.
- [263] B. Winter, R. Weber, W. Widdra, M. Dittmar, M. Faubel and I. V. Hertel, *J. Phys. Chem. A*, 2004, **108**, 2625–2632.
- [264] M. N. Pohl, E. Muchová, R. Seidel, H. Ali, Š. Sršen, I. Wilkinson, B. Winter and P. Slavíček, *Chem. Sci.*, 2019, **10**, 848–865.
- [265] V. Zoete, M. A. Cuendet, A. Grosdidier and O. Michielin, *J. Comput. Chem.*, 2011, **32**, 2359–2368.
- [266] K. Nishizawa, N. Kurahashi, K. Sekiguchi, T. Mizuno, Y. Ogi, T. Horio, M. Oura, N. Kosugi and T. Suzuki, *Phys. Chem. Chem. Phys.*, 2011, **13**, 413–417.
- [267] N. Kurahashi, S. Karashima, Y. Tang, T. Horio, B. Abulimiti, Y. I. Suzuki, Y. Ogi, M. Oura and T. Suzuki, *J. Chem. Phys.*, 2014, **140**, 174506.
- [268] S. Gozem, R. Seidel, U. Hergenbahn, E. Lugovoy, B. Abel, B. Winter, A. I. Krylov and S. E. Bradforth, *J. Phys. Chem. Lett.*, 2020, **11**, 5162–5170.
- [269] B. Winter, R. Weber, I. V. Hertel, M. Faubel, P. Jungwirth, E. C. Brown and S. E. Bradforth, *J. Am. Chem. Soc.*, 2005, **127**, 7203–7214.



- [270] B. Winter, M. Faubel, R. Vácha and P. Jungwirth, *Chem. Phys. Lett.*, 2009, **474**, 241–247.
- [271] E. Pluhařová, P. Slaviček and P. Jungwirth, *Acc. Chem. Res.*, 2015, **48**, 1209–1217.
- [272] R. Riley, A. Henley, A. N. Boichenko, N. N. Kleshchina, B. Wang, O. Tau, D. Winning, R. Lewin, J. M. Ward, H. C. Hailes, A. V. Bochenkova and H. H. Fielding, *submitted*.
- [273] D. Luckhaus, Y.-i. Yamamoto, T. Suzuki and R. Signorell, *Sci. Adv.*, 2017, **3**, e1603224.